Title

Plasmon-Enhanced Electrochemical Reduction of Carbon Dioxide

Author

Corson, Elizabeth

Publication Date

2020

Peer reviewed|Thesis/dissertation

Plasmon-Enhanced Electrochemical Reduction of Carbon Dioxide

By

Elizabeth R. Corson

A dissertation submitted in partial satisfaction of the
requirements for the degree of

Doctor of Philosophy

in

Chemical Engineering

in the

Graduate Division

of the

University of California, Berkeley

Committee Members

Professor Bryan D. McCloskey, Chair
Professor Nitash P. Balsara
Professor Kristin A. Persson

Fall 2020

Plasmon-Enhanced Electrochemical Reduction of Carbon Dioxide

Abstract

Plasmon-Enhanced Electrochemical Reduction of Carbon Dioxide

by

Elizabeth R. Corson

Doctor of Philosophy in Chemical Engineering

University of California, Berkeley

Professor Bryan D. McCloskey, Chair

Using inputs of only sunlight, electricity, carbon dioxide (CO_2), and water, photoelectrochemical CO_2 reduction could help mitigate climate change while producing valuable fuels or chemicals. Current CO_2 reduction technologies suffer from high overpotentials and low selectivity, producing a mixture of carbon monoxide (CO), methane, ethylene, formate, methanol, and other products. Plasmonic hot carriers and the strong local electric fields produced by plasmon excitation may open new mechanistic pathways for electrochemical reactions. Plasmon decay generates hot electrons that can be transferred selectively to an unoccupied electronic state of a surface molecule. Simultaneously, the enhanced electric fields can alter the electronic coupling with surface adsorbed molecules, thereby changing the binding energy of these species and the catalytic properties of plasmonic metals.

This dissertation aims to understand the mechanism of plasmon-enhanced electrocatalysis and how it can be used to direct the selectivity of CO_2 reduction at voltage-biased cathodes. First, the relatively new field of plasmon-enhanced electrochemical conversion (PEEC) is compared with the more established field of photoelectrochemistry (PEC). This chapter illustrates the best practices of PEC that can be applied to PEEC and the additional factors that must be considered. Special emphasis is placed on temperature control, light flux, and changes to the surface under reaction conditions.

With these considerations in mind, I developed the first front-illuminated, temperature-controlled electrochemical cell with features that allow for precise gas and liquid product analysis. The cell design maximizes the electrode surface area to electrolyte volume ratio to increase liquid product concentration for enhanced detection and quantification. Gas is bubbled through the catholyte during operation to maintain a saturated reactant concentration and to continuously mix the electrolyte. This cell was used for all of the product analysis experiments in the following chapters.

The first application of the temperature-controlled photoelectrochemical cell was to investigate CO_2 reduction at a plasmonic silver cathode. The silver thin film was electrochemically roughened to enhance the photocurrent and prevent further surface changes during electrochemical experiments. Illumination of this cathode selectively enhanced CO_2 reduction products (CO, formate, and methanol) while simultaneously suppressing undesired hydrogen evolution. Strikingly, methanol was produced only upon illumination, representing an improvement in

both selectivity and efficiency. CO_2 partial pressure experiments revealed that the reduction of CO_2 to CO has first-order behavior with respect to P_{CO_2} at all applied potentials in both the dark and the light, likely indicating no change in the rate-determining step upon illumination. The investigation of product distribution with temperature in both the dark and the light demonstrated that the selectivity changes observed upon illumination are not caused by local heating of the cathode surface.

To further understand the plasmonic mechanisms responsible for the enhanced CO_2 reduction and suppressed hydrogen evolution at the silver cathode, I conducted an in situ ATR–SEIRAS (attenuated total reflectance–surface-enhanced infrared absorption spectroscopy) study under both dark and illuminated conditions. The onset potential of CO_2 reduction to adsorbed CO on the silver surface was found to be -0.25 V versus the reversible hydrogen electrode (V_{RHE}) in both the light and the dark. As the production of gaseous CO was detected in the light near this onset potential but was not observed in the dark until -0.5 V_{RHE}, the light must be assisting the desorption of CO from the surface. This can be understood through a desorption induced by electronic transitions (DIET) mechanism, where a plasmonically excited hot electron temporarily transfers to an adsorbed species and increases the adsorbate energy level above the energy of desorption before decaying back to the metal Fermi level. The bicarbonate wavenumber and peak area were observed to increase immediately upon illumination, precluding a thermal effect. The enhanced local electric field that results from the localized surface plasmon resonance (LSPR) could be strengthening the bicarbonate bond, further increasing the local pH. This would account for the decrease of hydrogen formation and increase of CO_2 reduction products in the light.

Finally, I sought to combine the plasmonic properties of silver with the catalytic properties of copper, which is well known for its ability to form many two- and three-carbon CO_2 reduction products. Unlike the pure silver cathode where all CO_2 reduction products were enhanced in the light, the copper–silver cathode selectively promoted 5 of 15 products. At low overpotentials CO was promoted in the light while hydrogen was suppressed, and at high overpotentials ethylene, methane, formate, and allyl alcohol were enhanced upon illumination; generally C_1 products and C_2/C_3 products containing a double carbon bond were selectively promoted under illumination.

Dedication

To my family

Table of Contents

List of Figures

List of Tables

Acknowledgements

First I would like to thank my family. My husband Manuel was the first person to encourage me to get a doctorate degree when we were undergraduate students at the Illinois Institute of Technology. His love and support made graduate school a thoroughly enjoyable experience. My parents, Barbara and Forrest, also predicted that I would be back in graduate school before long. They taught me a love of reading, intellectual curiosity, and empathy. My sister Lena went through veterinary school at Iowa State University while I was at UC Berkeley and we enjoyed sharing our common experiences.

I thank my advisor Bryan McCloskey for his unfailing support for my myriad interests in research, teaching, and volunteering. Bryan always said yes to my ambitions, which took me to numerous conferences and workshops and to The Netherlands for three months. I couldn't have asked for a better advisor.

My time at Berkeley was brightened by all of my fellow graduate students in my cohort and in the years above and below me. I cherish the collaborative and supportive environment created by the graduate students, from prelims and qualifying exam assistance to ChemE kegs and summer softball, and I hope this spirit will continue. I appreciate GSAC and the opportunities to shape our department culture and improve the experiences of the graduate students.

I thank all of the members of the McCloskey lab for their support through each of the phases of my PhD. I am happy to see that our lab culture of kindness and willingness to help one another has continued even as we grow in numbers. I thank Erin Creel for being a fantastic partner in the lab and helping me maintain a positive outlook even when things didn't go as planned. I am so proud of the two undergraduate researchers I worked with, Matthew Liu and Ananya Subramani, and am excited to see their future accomplishments.

I appreciate my collaborators and informal advisors, Jeff Urban, Robert Kostecki, and Ruud Kortlever. I also acknowledge JCAP and the many researchers I have interacted with over the years. The incredible access to equipment and knowledgeable scientists within the field of CO_2 reduction and artificial photosynthesis greatly helped my research.

This work was supported by the National Science Foundation under grant no. CBET-1653430. This material is based upon work performed by the Joint Center for Artificial Photosynthesis, a DOE Energy Innovation Hub, supported through the Office of Science of the U.S. Department of Energy under award no. DE-SC0004993. Work at the Molecular Foundry was supported by the Office of Science, Office of Basic Energy Sciences of the U.S. Department of Energy under contract no. DE-AC02-05CH11231. Research performed in The Netherlands was supported by the Graduate Research Opportunities Worldwide (GROW) program with project number 040.15.067, which is partially financed by the National Science Foundation and the Dutch Research Council (NWO). I acknowledge support from the National Science Foundation Graduate Research Fellowship under grant no. DGE 1106400.

Chapter 1
Introduction

Carbon dioxide (CO_2) accounts for 76% of global greenhouse gas emissions, with the largest contribution (25%) coming from the burning of fossil fuels for electricity and heat production.[1] Technologies are being developed to capture CO_2 from the flue gas of power plants with the plan to geologically sequester the CO_2, effectively treating it as a waste product. However, if CO_2 were a feedstock rather than a waste it could help offset the cost of carbon capture.

CO_2 reduction can produce a variety of valuable fuels and chemicals. For example, CO_2 can be converted into ethanol, which is used as a transportation fuel. It can also be reduced to ethylene, which is currently derived from petrochemical sources and is used in many industrial applications including the synthesis of plastics. The potential impact of CO_2 reduction is tremendous as at least 16 distinct products have been reported.[2]

However, the scale of CO_2 emissions is staggering, with over 35 Gt of CO_2 emitted each year.[1] No single CO_2 reduction product has a global production that even approaches this value. For example, ethylene is produced globally at 150 Mt per year,[3] meaning that electrochemical ethylene production would consume not quite 1% of annual CO_2 emissions. While this number is small, electrochemical ethylene production would further offset CO_2 emissions by displacing the traditional fossil fuel-derived, themocatalytic method of ethylene production, which could account for a further reduction of 900 Mt of CO_2 emissions (2.5%).[3] To truly reduce CO_2 emissions through electrochemical CO_2 reduction, we must work in parallel to optimize different catalysts for different CO_2 reduction products. We can make a further impact by greatly expanding the global markets for CO_2 reduction products, such as replacing gasoline with ethanol as the dominant transportation fuel and developing fuel cells that consume methanol or formic acid.

Plasmon-enhanced electrochemical conversion (PEEC) can help achieve this goal by leading the CO_2 reduction reaction to greater selectivity and lower overpotentials. Plasmon-enhanced CO_2 reduction was first demonstrated when optically excited surface plasmons at the roughened surface of a silver (Ag) electrode in CO_2-containing solutions produced strong enhancement of the cathodic current.[4,5] With significantly improved nanofabrication and product detection techniques since this study was released, we can advance this proof-of-concept to more closely probe the mechanism of plasmon-enhanced CO_2 reduction and optimize the nanostructured electrodes for selective product formation.

1.1 Plasmon Excitation and Decay at Nanostructured Surfaces

Localized surface plasmon resonance (LSPR) occurs on a fast timescale (Figure 1.1). In the first 10 femtoseconds, irradiation at the LSPR frequency induces a collective oscillation of the free electron gas (plasmons) in plasmonic metals, which in turn generates a strong local electric field. When the negatively charged electrons are displaced relative to the positively charged nuclei, a restoring force arises between them that results in this oscillation. In nanoparticles significantly smaller than the incident wavelength, this oscillation can decay radiatively through the emission of a photon or can decay non-radiatively into hot electron–

hole pairs. Non-radiative decay dominates as nanoparticle size decreases. Over the next 500 femtoseconds, electron–electron scattering causes the electron distribution to thermalize at an electron temperature above the initial temperature, giving rise to the term "hot electron distribution." Within a picosecond, the electron energy dissipates to the lattice, unless the hot-carriers are transferred to an unoccupied state of a reactant at the surface.[6]

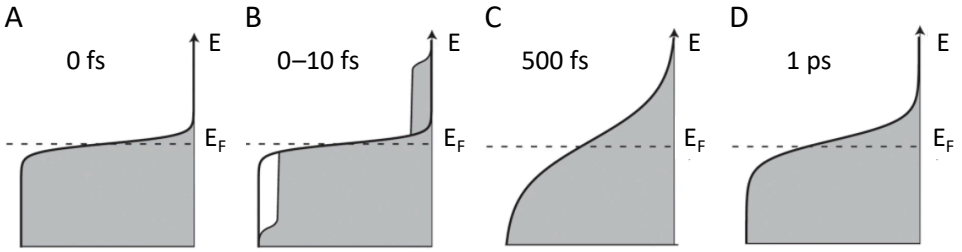

Figure 1.1: Plasmon excitation and decay in metals. Panels A–D depict the electronic energy distribution in the metal where E is the energy and E_F is the Fermi energy level. (A) Initially the electrons follow a Fermi-Dirac distribution. (B) Electrons are excited from filled states to unfilled states upon illumination. (C) A hot electron distribution is formed as electron–electron scattering causes the electron distribution to thermalize. (D) The electron energy dissipates to the lattice. Adapted with permission from ref. 6. Copyright 2015, Springer Nature.

The LSPR frequency is highly tunable through the manipulation of nanostructure shape, size, and composition and composition of the substrate. The resonant frequency, ω_{res}, of an isotropic sphere can be found by maximizing the polarizability

$$\omega_{res} = \frac{\omega_p}{\sqrt{1 + \left(\frac{\ell + 1}{\ell}\right)\epsilon_m}} \tag{1.1}$$

where ω_p is the Drude bulk plasmon frequency, ℓ is the angular momentum of the atomic orbital of the oscillating electrons, and ϵ_m is the dielectric constant of the surrounding media.[7]

Equation 1.1 shows how the LSPR can be affected by the size, shape, and material of the nanoparticles and their environment. As the dielectric constant of the surrounding media increases the ω_{res} decreases in value, causing the LSPR to red-shift. The angular momentum term in the denominator is determined by the electronic structure of the nanoparticle material and the nanoparticle size. Small nanoparticles are dominated by dipole excitation of electrons found in *sp* states ($\ell = 1$). Higher modes of plasmon excitation become more important as the nanoparticle size increases. Quadrupole oscillation is due to electrons in *d* orbitals ($\ell = 2$) and octupole resonances come from electrons in *f* states ($\ell = 3$). Thus is it clear from Equation 1.1 that as the nanoparticle size increases, the resonant frequency decreases. This red-shift in the LSPR is also accompanied by a broadening of the peak as the resonances of multiple modes of oscillation combine.[7] This has been measured experimentally; for example, in gold (Au) nanospheres the plasmon resonance wavelength red-shifted from 517 to 575 nm as the particle diameter was increased from 9 to 99 nm (Figure 1.2).[8] Similarly, the plasmon

resonance wavelength of Ag nanocubes shifted from 440 to 520 nm as the edge length was increased from 56 to 129 nm.[9]

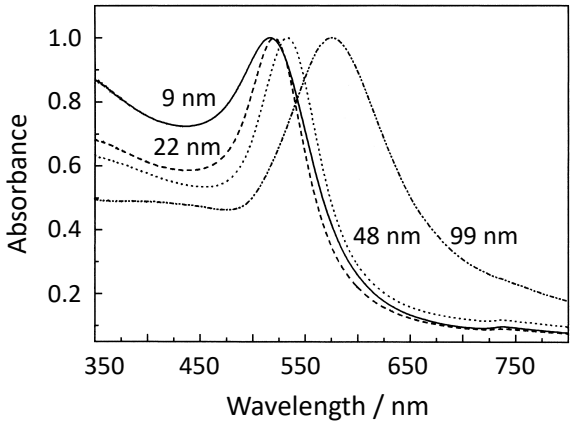

Figure 1.2: Peak plasmon resonance dependence on nanoparticle size. UV-visible absorption spectra of 9, 22, 48, and 99 nm gold nanoparticles in water. All spectra are normalized at their absorption maxima. Adapted with permission from ref. 8. Copyright 1999, American Chemical Society.

Nanoparticles with sharp corners experience charge accumulation, and the increased charge separation results in a reduction of the restoring force, shifting the resonance peak to lower energy. However, the shape effect is complicated by a potentially unique resonance along each axis of symmetry.[10] When comparing similarly sized Ag nanoparticles, nanowires were found to have a plasmon resonance at 380 nm, nanospheres at 420 nm, and nanocubes at 480 nm.[9]

1.2 Plasmonic Mechanisms

There are multiple plasmonic mechanisms that can influence reactions at the electrode surface. The first category of plasmonic mechanisms involves the *permanent* transfer of a hot electron into an unoccupied molecular orbital (MO) of an adsorbed species (Figure 1.3). This may occur through an indirect or direct charge-transfer mechanism. In the indirect charge-transfer mechanism, a hot electron distribution is formed through electron–electron scattering, as shown in Figure 1.1. Electrons with energy levels that match that of an unoccupied adsorbate orbital can transfer into that orbital, forming an excited adsorbate and potentially causing a chemical transformation. In the direct charge-transfer mechanism, a hot electron distribution is not formed. Rather, the decay of a resonant plasmon causes direct excitation of an electron to an unoccupied electronic state of an adsorbate, again possibly resulting in a chemical reaction.[6]

The second category of plasmonic mechanisms occurs through the *temporary* transfer of an excited electron (Figure 1.4). In this type of mechanism, the adsorbate is initially on its ground-state potential energy surface (PES). A plasmonically excited hot electron can temporarily transfer to an unoccupied MO of an adsorbate, forming an excited metal–adsorbate complex known as a transient negative ion (TNI) with a different PES. The adsorbate travels on the TNI PES and gains kinetic energy along the reaction coordinate. After a short time, the

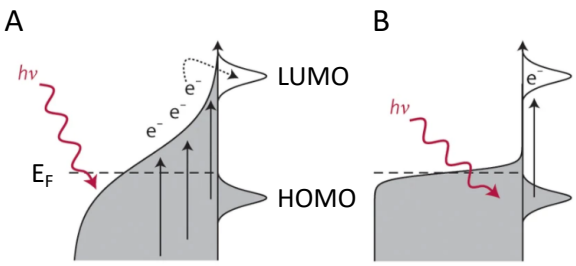

Figure 1.3: Indirect and direct charge-transfer mechanisms. (A) In the indirect charge-transfer mechanism, a hot electron distribution is formed through plasmon relaxation. Electrons at or above the energy level of the lowest unoccupied molecular orbital (LUMO) of an adsorbate can transfer into that orbital. (B) In the direct charge-transfer mechanism, decay of a resonant plasmon causes direct excitation of an electron to the LUMO of an adsorbate. HOMO refers to the highest occupied molecular orbital of an adsorbate. Adapted with permission from ref. 6. Copyright 2015, Springer Nature.

donated electron decays back to the metal E_F and the adsorbate returns to the ground state PES. If the energy transfer is sufficient to overcome the activation barrier (E_a), the chemical transformation will occur. The formation of a TNI may result in dissociation, desorption, or a chemical reaction. In the case of desorption, the mechanism is commonly referred to as desorption induced by electronic transitions (DIET).[9]

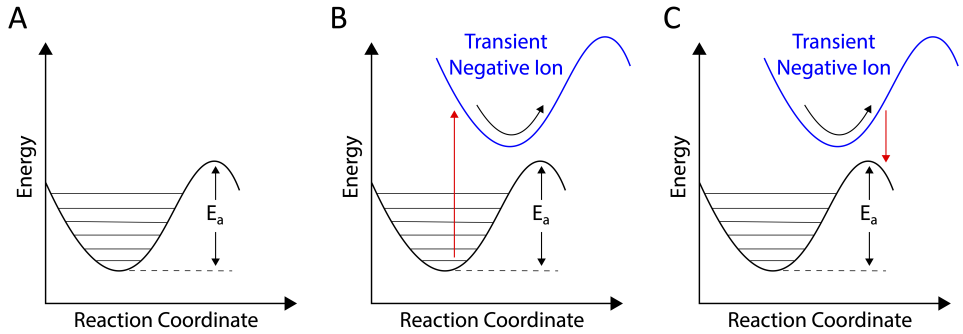

Figure 1.4: Transient negative ion (TNI) mechanism. (A) The adsorbate is initially on its ground-state potential energy surface (PES). (B) A hot electron can temporarily transfer to an unoccupied molecular orbital of an adsorbate, forming an excited metal–adsorbate complex known as a TNI with a different PES. On this new PES, the energy of the donated charge carrier is converted to the kinetic energy of the metal–adsorbate complex. (C) After a short time, the donated electron decays back to the metal E_F and the adsorbate returns to the ground state PES. If the energy transfer exceeds the activation barrier (E_a), a chemical transformation will occur. Adapted with permission from ref. 9. Copyright 2011, Springer Nature.

Plasmonic excitation may also result in an enhanced local electric field. The enhancement in electric field intensity may be up to 10^3 at the sharp corners of nanoparticles and more than 10^6 in the narrow space ($\sim$ 1 nm) between two nanoparticles.[9] This electric field can increase the rate of electron–hole formation and influence the bond strength and orientation of surface molecules.[6]

Finally, light-induced thermal heating of nanoparticles can occur when hot electrons transfer their energy to phonon modes (Figure 1.1D). This increased temperature could then influence the kinetics of the chemical reaction. However, significant heating is only expected for very high incident light intensity or for very small nanoparticles (< 5 nm), making it unlikely that plasmon-induced heating is the dominant mechanism for most systems.[6]

1.3 Plasmon-Enhanced Reactions

Reports of plasmon-enhanced reactions are more common in photocatalysis, where no external bias is applied. For example, the rate of hydrogen dissociation on Au nanospheres at room temperature increased instantaneously by 150X upon laser excitation (2.4 W cm^{-2}). As direct photodissociation of hydrogen would require laser intensities of 10^{13-14} W cm^{-2} and heating in the dark only resulted in a 3.7X increase in the rate, the authors concluded that hot electrons generated by plasmon decay must be reducing the barrier for hydrogen dissociation through a TNI mechanism.[11]

Ethylene epoxidation ($2\ C_2H_4 + O_2 \rightarrow 2\ C_2H_4O$) catalyzed by Ag nanocubes was found to have a fourfold increase in the reaction rate upon illumination. The authors suggested that the rate-limiting step, oxygen (O_2) dissociation, is facilitated through a TNI mechanism by the transfer of a plasmonically excited electron from Ag to the antibonding state of adsorbed O_2. This theory is supported by the reaction rate, which increases linearly with increasing light intensity rather than exponentially, as it would through heating.[12]

A few examples of PEEC have been reported. Shi et al. reported plasmon-enhanced O_2 reduction at Ag nanoparticles supported on graphene. Of the three types of nanoparticles that were studied—nanowires, nanospheres, and nanotriangles—the nanotriangles resulted in the greatest increase in O_2 reduction activity upon illumination. The authors concluded that this was a result of the larger absorption cross section and better alignment between the peak plasmon resonance and excitation laser wavelength (532 nm). The plasmonic mechanism was hypothesized to be enhanced O_2 adsorption due to hot electrons generated from Ag p–d interband transitions.[13]

Wilson et al. found that plasmonic excitation of Au nanoparticles enhanced the activity towards the hydrogen evolution reaction (HER) when compared to activity in the dark. The authors theorized that the electron–hole pairs generated by plasmon excitation resulted in a rise in the Fermi level of the Au nanoparticles, increasing the rate of electron transfer and decreasing the activation overpotential for the HER. Experiments performed in the dark from 22–30°C did not show a similar increase in HER activity, leading the authors to conclude that photothermal heating was not the primary plasmonic mechanism for HER enhancement.[14]

Clearly, plasmon-enhancement can influence a wide range of reactions through a variety of plasmonic mechanisms. To extract the most energy from sunlight it is desirable to use plasmonic metals with LSPR in the visible range to have the most overlap with the solar spectrum. Fortuitously, the three metals with the highest CO_2 reduction activity all have plasmon resonances at visible wavelengths: Ag (400 nm), Au (550 nm), and copper (Cu, 650 nm).[15]

1.4 CO_2 Reduction at Metals with Plasmon Resonances in the Visible Range

The high CO_2 reduction activity of Ag, Au, and Cu is attributed to their intermediate carbon monoxide (CO) binding strength as compared to other transition metals. Au has been shown to primarily produce CO and hydrogen (undesired reduction of water from the aqueous electrolyte) with formate and methanol as minor products.[16] Similarly, Ag mainly produces CO and hydrogen along with small quantities of formate and extremely small quantities of methane, methanol, and ethanol.[17] Cu is the most promising catalyst for valuable multi-carbon-containing products, but it suffers from low selectivity. Major products reported on Cu are hydrogen, methane, formate, CO, and ethylene; intermediate products are ethanol, n-propanol, and allyl alcohol; and minor products such as C_2 and C_3 alcohols and aldehydes have been detected.[2]

Of the three metals, Ag is best suited to plasmonically enhance reduction reactions. As shown in Figure 1.5, this is because the band structure permits transitions that result in highly energetic hot electrons. In comparison, Cu and Au result in hole-dominant energy distributions that would be better for oxidation reactions.[18]

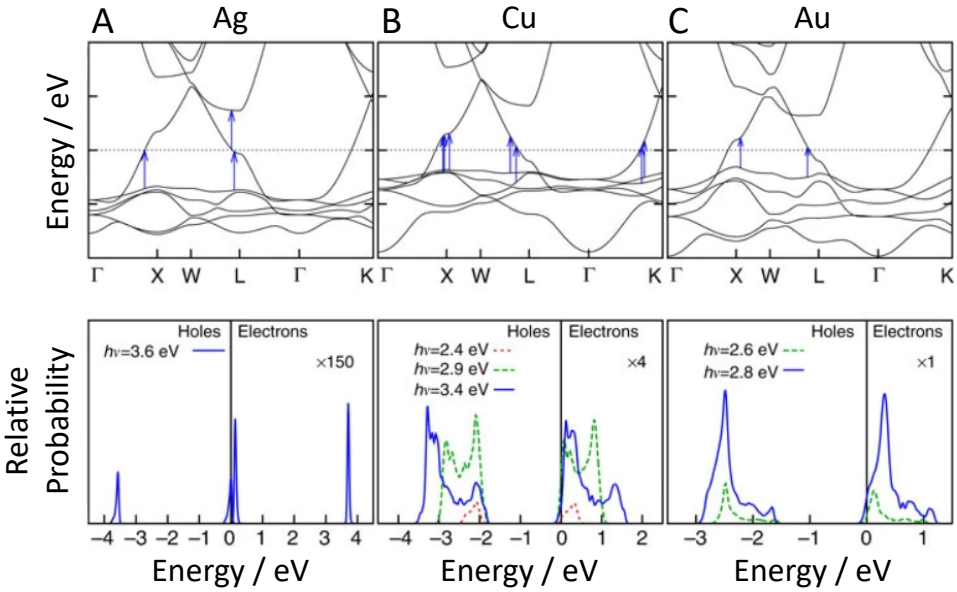

Figure 1.5: Theoretically calculated band structure and predicted hot-carrier energy distributions of (A) silver, (B) copper, and (C) gold. The top panels show the band structure and arrows mark the allowed transitions. The bottom panels show the energy distribution of hot electrons and holes relative to the Fermi level at 0 for various photon and plasmon energies, $h\nu$. Adapted with permission from ref. 18. Copyright 2014, Springer Nature.

Improving the efficiency of CO_2 reduction is an important aim of PEEC. While theoretical equilibrium potentials to produce these products range from -0.20 to 0.17 V vs. the reversible hydrogen electrode (V_{RHE}), the experimentally measured onset potentials are much larger and the applied potentials needed to achieve significant partial current densities are even greater. By subtracting the equilibrium potential from the applied potential we can find the

overpotential: the excess energy required for the reaction to proceed and an indication of the kinetic barriers in the reaction. These high energy barriers are one factor limiting the efficiency of CO_2 reduction. For example, the overpotential to simply begin producing CO on Cu is -0.21 V_{RHE}, ethylene is -0.82 V_{RHE}, and methane is -0.97 V_{RHE}.[19]

The magnitude of the overpotential directly influences the primary operating cost, electricity. As shown in Figure 1.6, how low the overpotential must be for economic feasibility depends on the CO_2 reduction product. For example, the high price of ethylene[3] permits overpotentials up to 1.4 V, assuming 100% Faradaic efficiency (FE) and considering only the cost of electricity (set at 6 cents per kWh[3]). However, a catalyst with only 50% FE towards ethylene would need to have an overpotential below 0.7 V by this simple economic analysis. In contrast, the currently low price of natural gas[20] means there is no economically feasible path to electrochemical methane production if the cost of electricity is 6 cents per kWh.

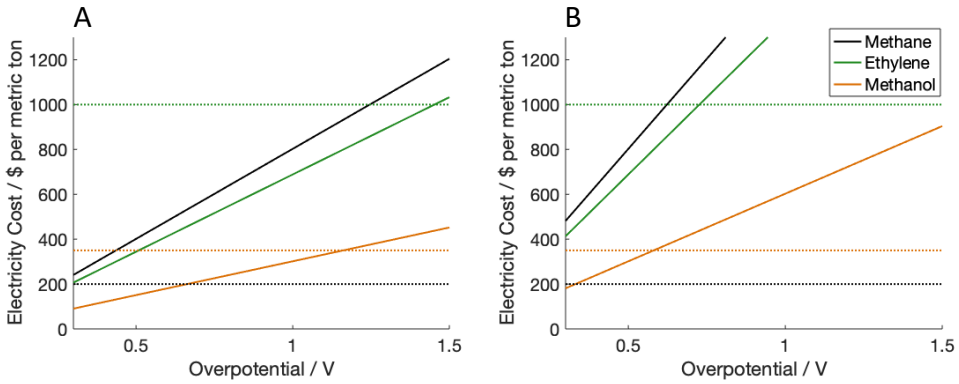

Figure 1.6: Electricity cost in $ per metric ton to produce methane, ethylene, and methanol at a given overpotential. Solid lines show the electricity cost and dashed lines show the commodity price in $ per metric ton. (A) Assumes a Faradaic efficiency (FE) of 100% and (B) assumes a FE of 50%. The electricity price is set at 6 cents per kWh.[3] The methane price is shown as $200 per metric ton,[20] the methanol price as $350 per metric ton,[20] and the ethylene price as $1,000 per metric ton.[3] The legend in (B) applies to both panels.

1.5 Organization of this Dissertation

This dissertation begins by defining plasmon-enhanced electrochemical conversion and comparing it to the more established field of photoelectrochemistry (Chapter 2). The following chapters present my research in CO_2 reduction and can be characterized by the dominant experimental method used in the study.

- Photoelectrochemical cell design (Chapter 3)
- Ex situ product analysis (Chapter 4 and 6)
- In situ spectroscopy (Chapter 5)

The final chapter explores my outlook on the field of plasmon-enhanced electrochemical CO_2 reduction with recommendations for future work (Chapter 7).

Chapter 2
Important Considerations in Plasmon-Enhanced Electrochemical Conversion at Voltage-Biased Electrodes*

2.1 Abstract

In this chapter we compare plasmon-enhanced electrochemical conversion (PEEC) with photoelectrochemistry (PEC). PEEC is the oxidation or reduction of a reactant at the illuminated surface of a plasmonic metal (or other conductive material) while a potential bias is applied. PEC uses solar light to generate photoexcited electron–hole pairs to drive an electrochemical reaction at a biased or unbiased semiconductor photoelectrode. The mechanism of photoexcitation of charge carriers is different between PEEC and PEC. Here we explore how this difference affects the response of PEEC and PEC systems to changes in light, temperature, and surface morphology of the photoelectrode.

2.2 Introduction

Plasmon-enhanced electrochemical conversion (PEEC) is performed by illuminating the surface of a plasmonic electrode while applying a potential to reduce or oxidize a reactant (Figure 2.1B). This underexplored field presents new opportunities for sustainable production of fuels and value-added chemicals. PEEC is related to the established field of photoelectrochemistry (PEC), where solar light is converted to electron–hole pairs at a biased or unbiased semiconductor photoelectrode to drive an electrochemical reaction, typically water splitting (Figure 2.1A). In this chapter we compare PEEC to PEC and discuss how standards developed in the field of PEC regarding temperature control, light flux measurement, and electrode stability characterization relate to the study of PEEC.

The origins of PEC and PEEC can be traced to the discovery of the photoelectric effect by Becquerel,[22] with pioneering advancements made on illuminated metal electrodes by Gerischer and Delahay.[23] The first reported PEC reaction was water splitting at an illuminated titanium dioxide (TiO_2) anode.[24,25] PEC water splitting has been extensively explored and reviewed[26–28] and, to a lesser extent, other PEC reactions like carbon dioxide (CO_2) reduction[29–31] and oxidation of organics.[32,33] The first report of PEEC was the extraction of plasmonically excited hot electrons and holes at a silver electrode.[34] Despite the comparable age, PEEC has been the subject of many fewer studies than PEC. Reported PEEC reactions include CO_2 reduction,[35,36] oxygen (O_2) reduction,[13,37] and hydrogen (H_2) evolution.[14,38,39]

The goal in PEC is to completely drive the reaction with sunlight, although an external potential bias is often needed to overcome the reaction activation barrier (Figure 2.1). In most semiconductor-driven PEC, there is little to no electrochemical activity observed under dark conditions. In contrast, the aim in PEEC is to couple illumination with an applied voltage to influence the catalyst selectivity and activity. In other words, there will be electrochemical

*This chapter was originally published in *iScience* and is adapted with permission from co-authors E. B. Creel, R. Kostecki, B. D. McCloskey, and J. J. Urban.[21]

activity without illumination in PEEC, and it is important to compare illuminated ("light") and unilluminated ("dark") performance to discern the impact of the light. In PEEC the total photocurrent can be distinguished from overall activity (often by chopped light experiments), but it can be difficult to precisely quantify how individual product formation changes upon illumination if products are formed in the dark and the light. The dark current may be quite high compared to the photocurrent which can make it challenging to detect subtle changes in product selectivity that are driven by the light. This need in PEEC to precisely compare dark and light performance motivates the essential use of temperature control.

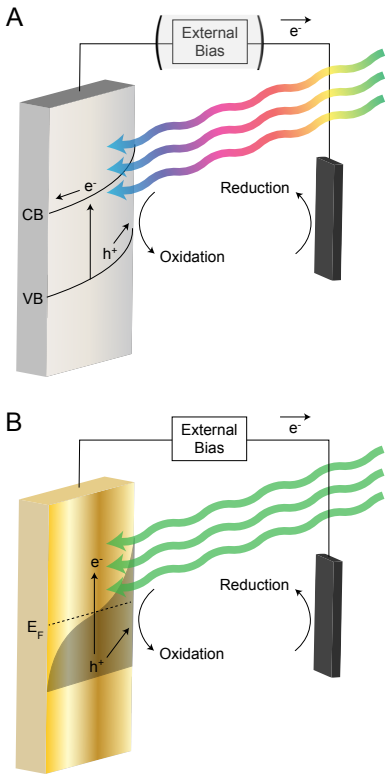

Figure 2.1: Comparison of the mechanism of photoexcitation of charge carriers in (A) photoelectrochemistry (PEC) and (B) plasmon-enhanced electrochemical conversion (PEEC). (A) In this PEC example the photoanode is an n-type semiconductor illuminated by solar light. When the energy of light exceeds the band gap, photoexcited electrons move from the valence band (VB) to the conduction band (CB) and through the external circuit to the cathode to drive the reduction reaction. Holes remaining in the VB propel the oxidation reaction. An external bias is optional in PEC. (B) In this PEEC example the photoanode is a plasmonic metal illuminated by a single wavelength of light matching the plasmonic resonance. The photoexcited electrons move from filled electronic states to higher energy unfilled states, resulting in an electron distribution with a higher population above the Fermi level (E_F). The holes with sufficient energy promote the oxidation reaction. An external bias is always applied in PEEC, in this case to tune the E_F of the plasmonic anode and provide electrons for the reduction reaction at the cathode.

2.3 Temperature Control

In PEC, temperature control is recommended to ensure that experiments performed at room temperature are comparable between labs.[40] PEC cells must be designed to withstand heating from a 100 mW cm^{-2} solar light source. In contrast, PEEC cells are often exposed to higher intensity light sources at a single wavelength to maximize photoccurrent. This difference is highlighted in Figure 2.1. Light absorption of water is low at ultraviolet (UV) and visible wavelengths and highest at infrared (IR) wavelengths.[41,42] IR wavelengths are present in solar light used in PEC while PEEC studies typically use light in the UV and visible wavelength ranges, so one might expect less cell heating in PEEC. However, light absorption of water can vary with ion concentration. Commonly used electrolyte salts such as potassium bicarbonate ($KHCO_3$) and sulfuric acid (H_2SO_4) absorb strongly in the near-UV, as shown in Figure 2.3B. In addition, cell heating can be caused by light absorption of the cell components and electrode, not just the electrolyte.

As shown in Figure 2.2A, continuous illumination of a PEEC cell by a single wavelength LED can lead to dramatic heating of the system. The unregulated temperature of the electrolyte in this cell,[43] which was designed with a low electrolyte volume to increase detectability of liquid products, rose by 12 K in 20 minutes—and would have continued to rise had the experiment not been terminated—under constant illumination by a 170 mW cm^{-2} 365 nm light-emitting diode (LED). This temperature rise demonstrates that PEEC cells are susceptible to heating whether the light source is a broadband incandescent bulb or a monochromatic beam.

In any catalytic system the Arrhenius equation predicts that reaction rate constants depend exponentially on temperature. As current is directly related to the reaction rate, one expects the current to increase with increasing temperature. However, there are multiple phenomena in PEC and PEEC beyond reaction kinetics that also depend on temperature and can influence the current density and product distribution.

A consideration that only affects PEC is the semiconductor bandgap, which may decrease with increasing temperature causing the photovoltage to decrease.[44] This decrease in the photovoltage may counteract the reaction rate increase, suppressing the overall increase in current density at a higher temperature. In contrast, for PEEC the rate of hot carrier generation is expected to increase with temperature due to the increase in phonon-assisted electronic transitions,[45] which would contribute to an increase in the photocurrent density.

Another reason for the importance of temperature regulation in PEC and PEEC is that increasing the electrolyte temperature typically causes the solubility of gases to decrease exponentially, as described by the van't Hoff equation. This can greatly decrease the reactant concentration for both PEC and PEEC systems where the reactant is a gas, as in CO_2 reduction or nitrogen (N_2) reduction, which may affect the product distribution. In addition, as each elementary reaction has a different temperature dependence according to their respective activation energies and pre-exponential factors, increasing the temperature may change the product distribution.[43]

An example of how the current is affected by changes in temperature can be seen in Figure 2.2B where linear sweep voltammetry is performed at a plasmonic silver cathode where CO_2 reduction and H_2 evolution are occurring. The magnitude of the current density increases

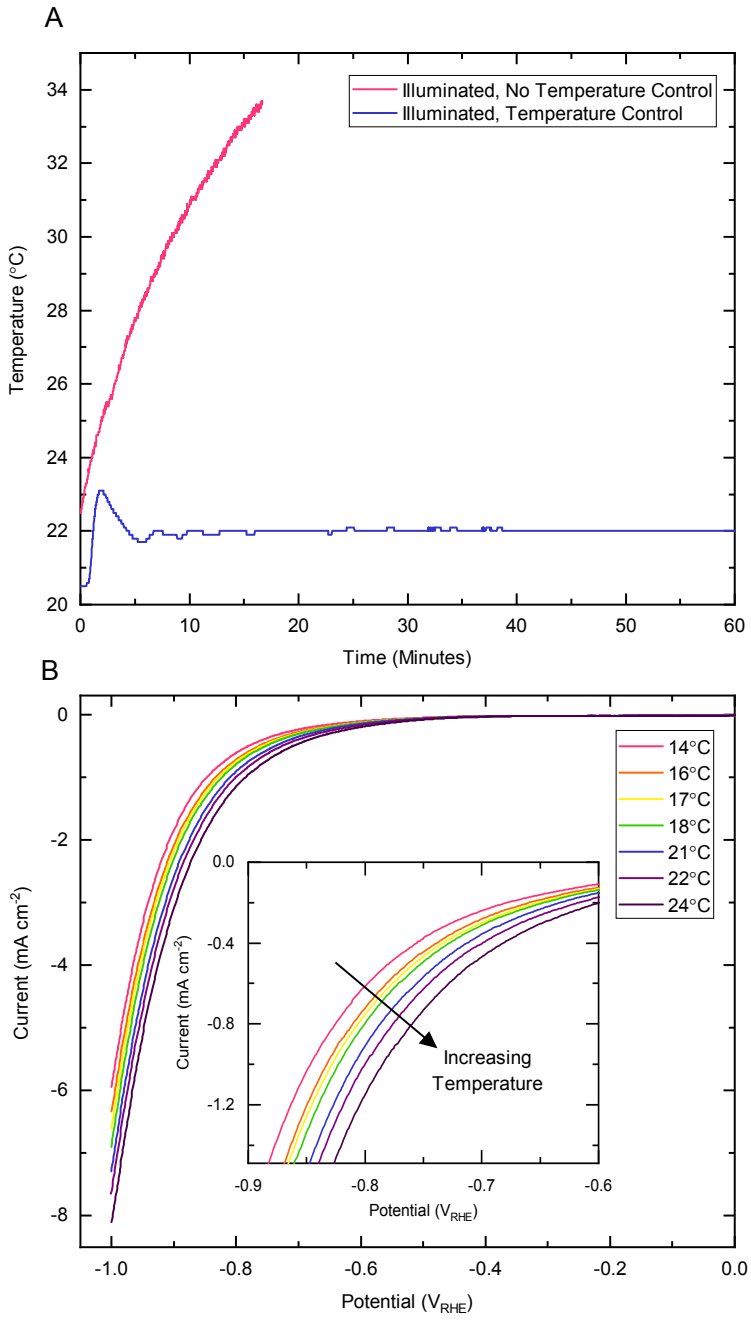

Figure 2.2: (A) Electrolyte temperature in a low-volume PEEC cell[43] over time with and without temperature control when illuminated with a 365 nm 2.5 W LED. (B) Linear sweep voltammetry at 100 mV s^{-1} at a plasmonic silver cathode in carbon dioxide-saturated (CO_2-saturated) 0.5 M potassium carbonate (K_2CO_3) electrolyte at various electrolyte temperatures. CO_2 flows continuously through the cell at 5 sccm. Inset is the same data in a smaller potential range to demonstrate activity increase with increasing temperature.

when the electrolyte temperature is increased by just 1 or 2 K from 14°C to 24°C. At -1.0 V versus the reversible hydrogen electrode (V_{RHE}) there is a 30% difference between the highest and lowest current densities across this modest 10 K temperature range, a range we have shown can easily be exceeded in an illuminated cell when the temperature is not controlled (Figure 2.2A). Similarly, Guo et al.[39] showed that the current density at plasmonic platinum/iron–gold (Pt/Fe–Au) nanorods during PEEC H_2 evolution increased by 33% when the temperature was raised from 20 to 30°C at -0.05 V_{RHE} while illuminated by a 808 nm laser. In comparison, Dias et al.[46] reported that the photocurrent density at a tungsten trioxide (WO_3) photoanode for PEC water splitting increased by 5% when the temperature was increased from 25 to 35°C at 1.7 V_{RHE}. This difference in the magnitude of the current density increase with a 10 K temperature rise between a PEC and PEEC system may reflect the opposing phenomena of bandgap decrease in PEC and increase in the rate of hot carrier generation in PEEC. When compared with PEC, the potentially greater impact of temperature makes it imperative in PEEC to use a temperature-controlled cell with precision of at least 1 K, especially when comparing light and dark activity and product distributions.

Effective cell temperature control requires incorporation of a temperature probe in contact with the electrolyte, ideally as close to the working electrode as possible, a cooling method, and a proportional-integral-derivative (PID) controller. The selection and sizing of the cooling method depends on the cell geometry and the maximum light intensity desired, as this will define the maximum heat removal needs of the system. While complete cell submersion in a water bath would make light incorporation difficult, a circulating bath connected to a cooling jacket or integrated heat-transfer channels within the cell can be designed to allow electrode illumination.[47] Another possible cooling system is a solid-state Peltier element with a heatsink and fan.[43]

2.4 Light Flux at the Electrode

An important figure of merit in PEC water splitting is the solar-to-hydrogen (STH) efficiency. While STH is not relevant for PEEC studies that use a non-solar light source or investigate reactions other than H_2 evolution, there are efficiency standards from the field of PEC that can be used in PEEC. The most applicable are the two ways to measure the quantum efficiency of light utilization for a given electrode: external quantum efficiency (EQE) and internal quantum efficiency (IQE).[48]

$$\mathrm{EQE} = \frac{\text{photogenerated electrons/s}}{\text{incident photons/s}} \tag{2.1a}$$

$$\mathrm{IQE} = \frac{\text{photogenerated electrons/s}}{\text{absorbed photons/s}} \tag{2.1b}$$

EQE is the ratio of photogenerated electrons to *incident* photons. In PEC, typical EQE values are greater than 10% and can approach 100% for wavelengths above the bandgap.[49] In contrast, PEEC systems without semiconductor or molecular co-absorbers typically have EQE values below 1% at the plasmon resonance wavelength.[50,51] For example, if we compare PEC

to PEEC for CO_2 reduction at -0.9 V_{RHE} in neutral electrolyte under 360 nm illumination, a zinc telluride (ZnTe) photocathode has an EQE of 80%[52] while a plasmonic silver cathode has an EQE of 0.45%.[51]

IQE is the ratio of photogenerated electrons to *absorbed* photons. IQE is generally higher than EQE for both PEC and PEEC materials due to the exclusion of losses from photons that are transmitted or reflected. However, the difference in order of magnitude between PEC and PEEC electrodes found in EQE still exists for IQE. From the previous CO_2 reduction example, the semiconductor IQE is 100%[52] while the plasmonic metal IQE is 1.2%.[51]

One key difference for the disparity in PEC and PEEC efficiencies is carrier lifetime. Photoexcited electrons and holes in semiconductors can have lifetimes on the order of nanoseconds[53] while excited carriers in plasmonic metals exist for less than a picosecond[54] due to the high density of electronic states in metals and other conductive media (Figure 2.1). Due to their brief existence, plasmonically-generated excited carriers must be co-located with the charge-accepting species in order for charge transfer to occur. In contrast, photoexcited carriers in semiconducting materials have time to diffuse to the solid-liquid interface and can have diffusion lengths on the order of tens of nanometers.[53] These differences in carrier lifetime and diffusion length help explain why the EQE and IQE of plasmonic metals used in PEEC is much lower than that of semiconducting materials used in PEC.

Just as in PEC, reporting the EQE and IQE in PEEC will deconvolute a material's ability to separate and collect photoexcited electrons and holes from its optical absorption. This provides insight for further optimization of the material's optical absorption or extraction of charge carriers.

Calculating EQE and IQE requires measuring the incident light intensity. It is important to measure the light *at the electrode surface*, especially in studies that focus on catalyst performance and mechanism rather than overall device efficiency. Glass, quartz, water, common electrolytes, and gas bubbles can all have significant reflection or absorption, making the light intensity incident on the photoelectrode significantly less than the light intensity incident on the cell (Figure 2.3). For example, Figure 2.3 shows that the transmission of light through glass is reduced by 50% at a wavelength of 350 nm and is completely blocked for wavelengths below 300 nm. This means that if the light intensity were measured before the light passed through the glass, the reported EQE and IQE values for the photoelectrode would be half of the actual values at 350 nm.

Researchers should also bear in mind that the optical properties of all materials are temperature-dependent.[42] While full device research, common in PEC, incorporates short path lengths through electrolyte and anti-reflective coatings on cell windows,[42] most laboratory-scale PEEC cells are not designed with maximum light transmission to the plasmonic electrode in mind. Thus, the light attenuation may be significant. Low light intensity may impact the signal to noise ratio between the photocurrent and background "dark" current as plasmonic photoactivity increases with light intensity. Additionally, it may be difficult to control the temperature of electrochemical cells that are not designed for high light transmission due to the high light intensity needed to achieve a measurable photocurrent.

The light attenuation through the electrochemical cell walls and electrolyte becomes especially

important with broad-spectrum illumination because the light transmission of cell components is wavelength dependent and often has especially low transmission in the UV or IR regions of the spectrum (Figure 2.3B). While glass is often replaced with quartz for UV transmission, the effect of the absorption of water or the electrolyte salt is not commonly accounted for.[41]

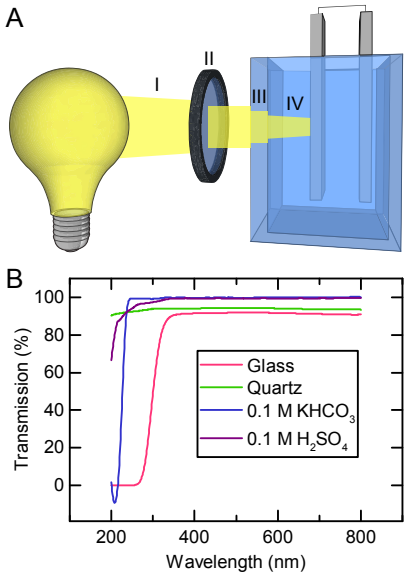

Figure 2.3: Light intensity attenuation from the light source to the plasmonic electrode surface. (A) Light intensity per unit area decreases (I) as a function of distance from a non-collimated source, (II) when passing through optical lenses or filters, (III) when passing through electrochemical cell walls, and (IV) when passing through electrolyte. (B) Transmission spectra of a 1 mm thick glass slide, 2 mm thick quartz window, 1 cm path length through 0.1 M potassium bicarbonate ($KHCO_3$), and 1 cm path length of 0.1 M sulfuric acid (H_2SO_4). Transmission spectra of glass and quartz are measured relative to air. Transmission spectra of salt solutions are measured in a quartz cuvette relative to a quartz cuvette filled with ultrapure water.

Additionally, both PEC and PEEC researchers should confirm that the cell components intended to define the illumination and active area of a photoelectrode (e.g., epoxy or o-rings) are opaque for all of the light spectrum (not just the visible) that will be used for illumination. A UV-transmissive epoxy or o-ring, for example, could result in the photoactive area of an electrode being much larger than the electrochemically active area.[41] For example, in a cell with an electrochemically active area of 1.0 cm^2 and an o-ring outer diameter (OD) of 1.4 cm, a UV-transmissive o-ring would result in an actual illumination area of 1.6 cm^2, an increase of 60%.

Light power incident on the cell can be measured with a power meter, thermopile, or photodiode and then corrected to find the light power incident on the plasmonic electrode using the transmission of the cell components. For broad-spectrum illumination most common in PEC, it is important to measure the light spectrum rather than just the light intensity because of the wavelength dependence of the photoactivity and the wavelength dependence of the optical properties of the cell components.[55] The method for correcting spectral mismatch

between a lamp and solar irradiance is also suitable for correcting for decreased transmission of cell components.[41]

Standards for calibrating light sources to closely match the AM 1.5 G spectrum have been well-defined within the field of PEC.[40,56–58] While these standards can be directly applied to PEEC systems for broad-spectrum illumination studies, they are not relevant for single-wavelength light experiments that are commonly used in the field of PEEC. High-intensity single-wavelength illumination at the plasmon resonance wavelength can help increase the photocurrent for PEEC systems, improving the signal-to-noise ratio and enhancing the difference in product distribution between light and dark conditions. Varying the light intensity at a single wavelength is also prevalent in PEEC studies. A linear relationship between photocurrent and light intensity demonstrates that the mechanism is photonic, as a thermal process would result in an exponential relationship.[59] Probing behavior at different wavelengths can lead to a fundamental understanding of the mechanism of plasmon-enhanced charge transfer.[54] To accurately compare different PEEC electrodes it is important that researchers measure and report the light spectrum and intensity at the electrode surface for any illuminated experiments.

2.5 Surface Changes Under Reaction Conditions

The activity and performance of all photoelectrocatalysts depends on the specific surface morphologies and structural features (e.g., high index planes, step edges). Both PEC and PEEC photoelectrode behavior can be extremely sensitive to nanoscale morphology. In PEC, nanofeatures can influence charge separation and transport, scattering rate, and the size of the band gap.[60] For example, Wu et al.[61] showed that increasing the length of silicon nanowires by 700 nm decreased the photocurrent by 40% at 1.0 V while the minority carrier lifetime decreased by just 2% during PEC bromide reduction. They related these effects to changes in light adsorption and photogenerated carrier collection caused by the increased length. In PEEC, the size, shape, and proximity of nanostructures can change the peak plasmon resonance wavelength, energy distribution and number of hot carriers, and intensity of the local electric field.[9,62,63] Shi et al.[13] demonstrated that changing from silver nanowires to nanotriangles caused the plasmon resonance to red-shift by 50%, the maximum electric field enhancement to triple, and the photocurrent to increase by 33% at 0.65 V_{RHE} during O_2 reduction. These changes were attributed to enhanced light adsorption and a higher rate of hot electron production. It is clear that changes to the surface morphology of PEC and PEEC photoelectrodes on the scale of nanometers can significantly impact their performance, but the underlying physical reason for this change is inherently different between the two fields due to the distinct mechanisms of photoexcitation of charge carriers. Therefore, changes in nanofeatures that benefit one system may be detrimental to the other.

Active catalysts can delaminate from the electrode surface or undergo dramatic morphological, composition, phase, and activity changes under reaction conditions[64,65] or when exposed to voltage.[36] All of these changes can impact not only the catalytic performance but also the optical properties of the PEC or PEEC photoelectrode. Thus, it is critical to characterize microscopic catalyst evolution and any differences in optical properties in order to understand and control or prevent morphological changes induced by reaction conditions.

Researchers often use the stability of the current over time in long-term constant voltage experiments as a measure of electrode stability, but this method gives no insight into the mechanism for activity degradation. It is well known that successive oxidation and reduction cycles can degrade catalysts, but constant-voltage experiments also induce catalyst dissolution, corrosion, and restructuring. Our recent PEEC study of a plasmonic silver thin film cathode showed decreased electrochemical surface area (ECSA), increased broad-spectrum absorption, and a broader grain size distribution after performing CO_2 electrolysis without illumination (Figure 2.4). We found that the changes in optical properties and electrochemical surface area changed quickly in the first few minutes of applied potential but reached a steady state between 30 and 60 minutes of electrolysis. In this case, we were able to "electrochemically condition" the plasmonic silver cathode for 45 minutes to achieve stable performance over hours. After 45 minutes, the absorption at the plasmon resonance was 37% higher and the relative surface area was 50% lower than the as-prepared electrode (Figure 2.4).[36]

An analogous example from PEC is the anodic photocorrosion of gallium nitride (GaN).[66] The researchers observed that the photocurrent decreased over time during H_2 evolution in aqueous 1.0 M sodium hydroxide (NaOH). A surface morphology study by atomic force microscopy (AFM) revealed that the root mean square (RMS) roughness continued to increase throughout the 22-hour photoelectrochemical experiment. In contrast to the previous PEEC example, this electrochemically-induced surface morphology change never stabilized and was detrimental to the photoelectrode performance.

Measuring the changes in morphology during any electrochemical reaction is critical when attempting to understand the structure-function relationships of an electrode. It is especially important for PEEC researchers to check for reaction-induced morphology changes because small structural changes may modify the optical properties of the plasmonic electrode significantly (Figure 2.4).[9,62,63] Changes to the absorption of the electrode will alter the IQE as well as the photoactivity. Both PEC and PEEC researchers should, at a minimum, compare the morphology and optical changes before and after photoelectrochemistry using scanning electron microscopy (SEM), transmission electron microscopy (TEM), atomic force microscopy (AFM), UV-visible spectroscopy, or other readily available techniques.[40]

2.6 Conclusion

We have shown that standards developed in the established field of PEC can be used to build best practices for PEEC. The key distinctions and similarities between PEC and PEEC presented in this chapter are summarized in Table 2.1. Cell temperature control is still critical for PEEC, especially when comparing light and dark performance. While not all efficiency measures from PEC are relevant to PEEC, EQE and IQE are valid and useful for characterizing plasmonic electrodes. However, it is important to recognize that fundamental differences between semiconductors and plasmonic metals result in EQE and IQE values for PEEC systems that are often two orders of magnitude lower than PEC systems. Surface morphology can affect the catalytic and optical properties of semiconductors and plasmonic metals. Changes to the surface induced by reaction conditions should be monitored and controlled for repeatable results. By learning from the 50-year history of PEC water splitting we can ensure that PEEC research is comparable and reproducible.

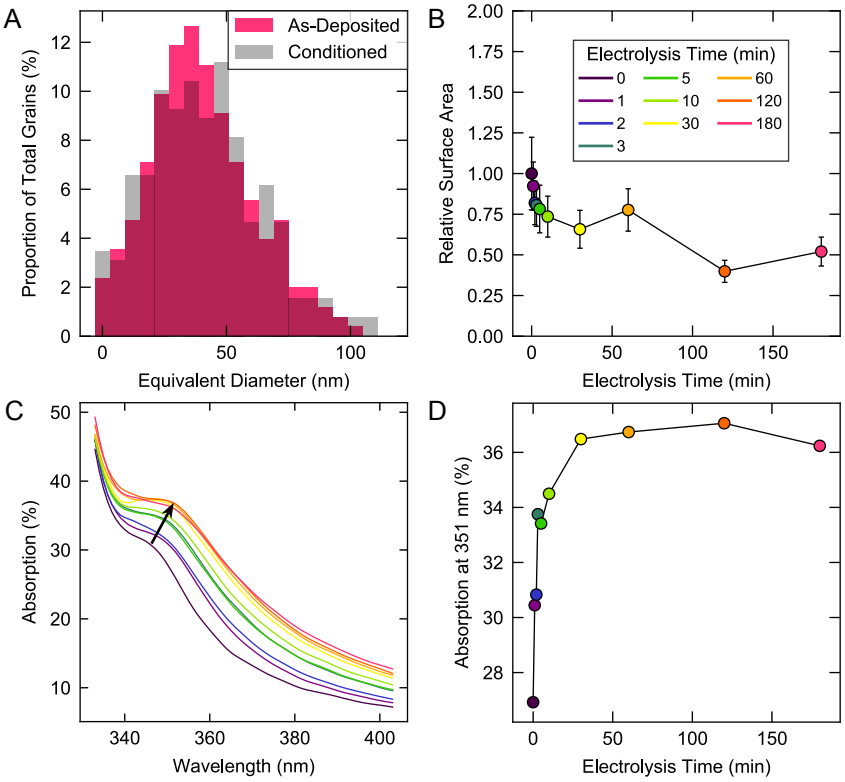

Figure 2.4: Changes in morphology and optical properties of a silver thin film cathode after carbon dioxide (CO_2) electrolysis without illumination in 0.5 M potassium carbonate (K_2CO_3) at -1.1 V versus the reversible hydrogen electrode (V_{RHE}). The electrode was made by electron-beam (e-beam) depositing 200 nm of silver over a glass slide with 5 nm of titanium used as an adhesion layer. (A) Comparison of the silver grain size distribution on the cathode in terms of equivalent diameter—the diameter of a circle with the same projected area as the projected area of the grain—as measured by atomic force microscopy (AFM). "As-Deposited" indicates a silver film that has not been used as an electrode, and "Conditioned" indicates that the silver thin film has undergone 45 minutes of CO_2 electrolysis. (B) Evolution of the electrochemical surface area (ECSA) of the cathode relative to the as-deposited silver film after various CO_2 electrolysis times. Legend for parts B–D where electrolysis time is the time that the silver electrode was used as a CO_2 electrolysis cathode. Error bars represent one standard deviation. (C) Evolution of the UV-visible absorption spectra of the cathode after various CO_2 electrolysis times. (D) Evolution of the absorption of the electrode at 351 nm after various CO_2 electrolysis times. Absorption is calculated as 100% − %R where %R is the total reflection measured by an integrating sphere. Figures adapted from Creel et al.[36]

Table 2.1: Comparison of PEC and PEEC

	PEC	PEEC
Experimental		
Photoelectrode	Semiconductor	Metal or other conductive material
Mechanism	Band gap excitation	Plasmon excitation
Applied Potential	Optional	Always
Temperature Increase		
Reaction Kinetics	↑ Reaction rate constants	↑ Reaction rate constants
Solubility	↓ Gaseous reactants	↓ Gaseous reactants
Electron Excitation	↓ Photovoltage	↑ Hot carrier generation rate
Light Flux		
Efficiency	IQE and EQE > 10 %	IQE and EQE < 1 %
Typical Light Source	Broadband	Monochromatic
Surface Morphology		
Nanoscale Changes	Can impact charge carrier dynamics and band edge positions	Can impact plasmon resonance wavelength, hot carrier distribution, and local electric field intensity

Chapter 3
A Temperature-Controlled Photoelectrochemical Cell for Quantitative Product Analysis[†]

3.1 Abstract

In this chapter, we describe the design and operation of a temperature-controlled photoelectrochemical cell for analysis of gaseous and liquid products formed at an illuminated working electrode. This cell is specifically designed to quantitatively analyze photoelectrochemical processes that yield multiple gas and liquid products at low current densities and exhibit limiting reactant concentrations that prevent these processes from being studied in traditional single chamber electrolytic cells. The geometry of the cell presented in this chapter enables front illumination of the photoelectrode and maximizes the electrode surface area to electrolyte volume ratio to increase liquid product concentration and hence enhances ex situ spectroscopic sensitivity toward them. Gas is bubbled through the electrolyte in the working electrode chamber during operation to maintain a saturated reactant concentration and to continuously mix the electrolyte. Gaseous products are detected by an in-line gas chromatograph, and liquid products are analyzed ex situ by nuclear magnetic resonance. Cell performance was validated by examining carbon dioxide reduction on a silver foil electrode, showing comparable results both to those reported in the literature and identical experiments performed in a standard parallel-electrode electrochemical cell. To demonstrate a photoelectrochemical application of the cell, carbon dioxide reduction experiments were carried out on a plasmonic nanostructured silver photocathode and showed different product distributions under dark and illuminated conditions.

3.2 Introduction

Photocatalytic reactions have been widely studied for both semiconducting and plasmonic systems as a means of overcoming high activation barriers and storing solar energy.[9,67] The less-explored field of photoelectrocatalysis (PEC) uses light to excite carriers and enhance the applied electric field to drive the excited carriers to the catalytically active surface. Reaction pathways can be selective to the light intensity, light wavelength, electrochemical potential, or a combination of these factors, all of which can be tuned independently in PEC. Investigating photoelectrochemical reactions requires a vessel that contains electrolyte and permits illumination of the photoelectrode that is immersed in the electrolyte. While a simple single chamber electrolytic cell with a transparent window may be appropriate for the study of well-characterized reactions with a single product, a new photoelectrochemical cell design is needed for more complicated reactions where quantification of multiple gaseous and/or liquid products is required, as in the case of carbon dioxide (CO_2) reduction.

PEC CO_2 reduction can be used for the storage of solar energy by converting CO_2 into

[†]This chapter was originally published in *Review of Scientific Instruments* and is adapted with permission from co-authors E. B. Creel, Y. Kim, J. J. Urban, R. Kostecki, and B. D. McCloskey and with the permission of AIP Publishing.[43]

renewable fuels such as methane (CH_4) or ethanol (C_2H_4OH). Electrochemical CO_2 reduction suffers from high overpotentials and low selectivity, producing a mixture of gaseous and liquid products.[68,69] Plasmonic hot-carriers and the strong local electric fields produced by plasmon excitation may open new mechanistic pathways for electrochemical reactions.[9,18,70,71] A PEC cell that allows one to measure how light changes the product distribution is critical to understanding the mechanism of plasmon-enhanced photoelectrochemistry.

To accurately measure these products, the photoelectrochemical cell must be leak tight, have a small electrolyte volume while maximizing the electrode surface area, maintain CO_2 saturation of the electrolyte, and have a membrane separating the anode and cathode to prevent product transfer between chambers. In addition, the cell must be able to operate isothermally under dark and illuminated conditions, have parallel electrodes to ensure even current distribution, and be constructed from electrochemically-stable materials that resist contamination. While we will test the PEC cell presented here for CO_2 reduction, these design considerations apply to any PEC system with multiple products, low current densities, and limiting reactant concentration. Examples include nitrogen reduction to ammonia and CH_4 oxidation to methanol (CH_3OH), ethane (C_2H_6), or ethylene (C_2H_4).

Our unique PEC cell satisfies these design criteria while simultaneously achieving front illumination of the photoelectrode. Front illumination of the electrode's active surface is desired over back illumination—in which the electrode is illuminated through the inactive but ideally transparent back side of the electrode—to remove the need for electrode optical transparency and to maximize the light intensity on the active surface of the electrode. To validate the cell and demonstrate its effectiveness, we present three sets of CO_2 reduction experiments and their corresponding product analyses. First, we compare the product distribution during the reduction of CO_2 on a silver (Ag) foil electrode in the photoelectrochemical cell to the same reaction performed in a common CO_2 reduction electrochemical cell, showing no significant difference in the results. Second, to demonstrate the temperature control of the cell, we reduced CO_2 on Ag foil at four different temperatures ranging from 8 to 45°C. Finally, we performed PEC CO_2 reduction on a nanostructured Ag electrode and compare the product distribution under light and dark conditions. We show that irradiation of the plasmonic Ag electrode results in the selective promotion of CO_2 reduction to carbon monoxide (CO) over the reduction of water to hydrogen (H_2). The PEC cell and methods presented here provide precise and accurate measurement of multiple gaseous and liquid products while illuminating the active surface of one of the electrodes.

3.3 Photoelectrochemical Cell Design

PEC CO_2 reduction is challenging to study due to the low solubility of CO_2 in water and generally low current density which yields a mixture of gaseous and liquid products at low concentrations.[51] Researchers studying electrochemical CO_2 reduction have addressed these issues with CO_2-flow cells that maximize the electrode surface area to electrolyte volume ratio, generally by minimizing the cell volume.[2,72] As a result of the low electrolyte and cell mass in such configurations, these cells are especially susceptible to heating under illumination, making temperature control requisite when studying photoelectrochemical processes. While these cell configurations are effective for dark electrochemistry, no comparable cell exists

that allows for front illumination of the working electrode while still providing all the useful characteristics of the small volume, parallel-electrode cell configurations.[2,72] In particular, the desired design features of a PEC cell include separation of the working and counter chambers for liquid and gaseous product segregation, in situ gaseous product sampling for analysis, maximizing the electrode surface area to electrolyte volume ratio to increase liquid product concentration, establishing isothermal conditions during illumination, preventing contamination, maintaining a high concentration of CO_2 in the electrolyte, and ensuring that the working electrode chamber is well mixed.

Our front-illumination photoelectrochemical cell (PEC cell) was designed based on the dark compression cells reported in the literature.[2,72] These dark compression cells meet several, but not all, of the design criteria for a PEC cell, failing to allow for electrode illumination and temperature control. We modified the aligned parallel plate design to allow front illumination through a quartz window by offsetting the parallel working and counter electrodes as seen in Figure 3.1. The PEC cell is leak tight and incorporates a membrane to separate the working and counter chambers. CO_2 flows continuously through a glass frit at the bottom of the cell to maintain CO_2 saturation of the electrolyte and to carry the evolved gaseous products to a gas chromatograph (GC) for analysis. The PEC cell is milled from polyether ether ketone (PEEK), a chemically inert hard polymer, and has a 0.43 cm^2 mL^{-1} surface area to volume ratio (S/V) that allows for high sensitivity in ex situ liquid product analysis. For comparison, the cell used by Kuhl et al. had a S/V of 0.56 cm^2 mL^{-1},[2] and Lobaccaro et al. reported a S/V of 0.67 cm^2 mL^{-1}.[72] Both the working and counter electrodes of our PEC cell have a surface area of 1 cm^2. The cell is sealed around five o-rings and compressed by tightening four screws with wing nuts. A complete list of cell parts is provided in Table 3.8 and Table 3.9.

The reference electrode and thermistor are located in close proximity to the working electrode without blocking the light, as shown in the wireframe view of the working electrode chamber (Figure 3.2). As described in more detail later, the temperature can be monitored continuously and controlled within ±0.1°C during an electrochemical experiment using an external proportional-integral-derivative (PID) controller coupled to a Peltier element located directly behind the working electrode (part 2 in Figure 3.1). It typically takes 10 to 20 minutes to reach a steady state temperature. In this chapter we demonstrate the cell operating from 8 to 45°C. However, the true operating range is much larger. When using aqueous electrolyte, the cell temperature is limited primarily by the phase transitions of water.

3.4 Experimental Methods

A 0.5 M solution of potassium carbonate (K_2CO_3) (Alfa Aesar, 99.997% metals basis) was prepared with 18.2 MΩ deionized water from a Millipore system, which became 1 M potassium bicarbonate ($KHCO_3$) when saturated with CO_2 (Praxair, 99.999%). The pH of the saturated electrolyte was 7.57 (Hanna Instruments, pH meter 9124). In the PEC cell, the working chamber was filled with 2.3 mL of electrolyte and the counter chamber with 0.8 mL. Both chambers of the standard, dark electrochemical cell (EC cell), designed by Lobaccaro et al. and used here as a comparison to the PEC cell,[72] were filled with 1.9 mL of electrolyte (Figure 3.13). The materials of construction and principles of operation of the EC cell are the same as the PEC cell, except the EC cell does not have temperature control. The geometries

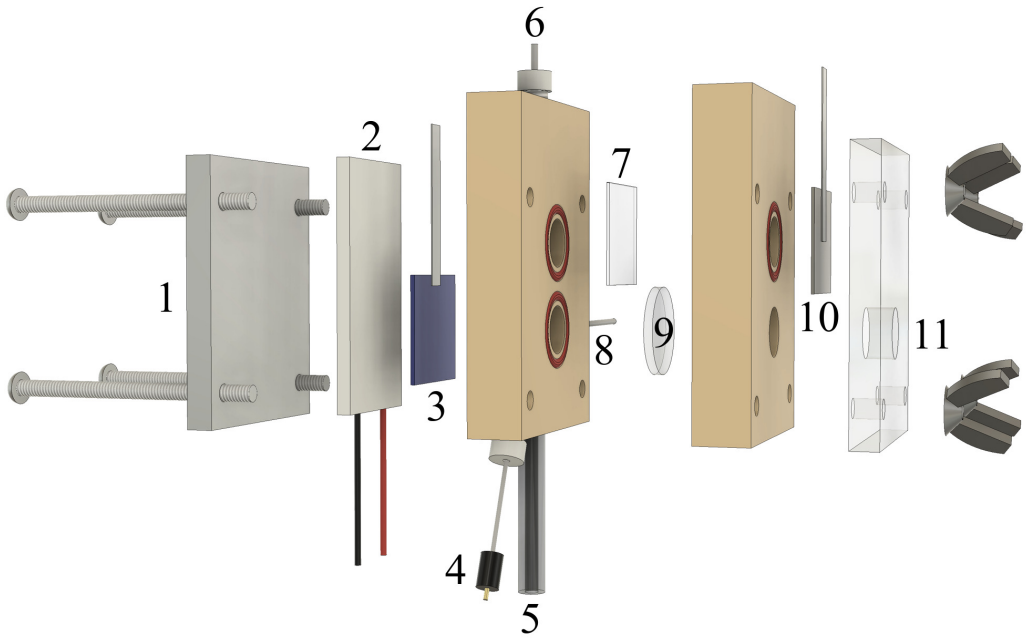

Figure 3.1: Schematic of the photoelectrochemical (PEC) cell. The copper and aluminum heat sink (not shown) is secured against the aluminum back plate (1) that transfers heat from the Peltier element (2). The working photoelectrode (3) is in close proximity to the reference electrode (4) and thermistor (8) and is separated from the counter electrode (10) by a membrane (7). Gas enters through the glass frit at the bottom (5) and flows through tubing at the top (6) to the gas chromatograph (GC) for product analysis. A hole in the front plate (11) allows light to shine through the quartz window (9) onto the photoelectrode (3). The total volume of electrolyte used in the working electrode chamber is 2.3 mL, and the electrode surface areas are 1 cm^2 (1.1 cm diameter).

of the cells are very similar, with the largest variation resulting from the aligned parallel electrode configuration of the EC cell versus the offset parallel electrodes of the PEC cell.

The Ag foil cathode (thickness 0.1 mm, Alfa Aesar, 99.998% metals basis) was mechanically polished (Norton T401, 2000 grit) before each use. The nanostructured Ag cathodes were created using nanosphere lithography to form Ag pyramids regularly spaced across a substrate in a hexagonal pattern. A schematic of this method used by Kim et al. is shown in Figure 3.12.[51] To improve adhesion of Ag, the glass slides were first cleaned with air plasma for 4 minutes; then a 5 nm layer of titanium (Ti) was deposited via an electron-beam (e-beam) evaporator followed by a 120 nm layer of Ag. A solution was prepared by mixing 60 mL of an aqueous 1.7 v/v% 310 nm polystyrene sphere solution (Thermo-Scientific 5031A) with 100μL of 10 v/v% Triton X-100 in water. The glass slide was then submerged in this solution and slowly withdrawn at a rate of 5 μm min^{-1}, depositing a monolayer of hexagonally arrayed spheres.[68] Oxygen (O_2) plasma etching was performed for 210 seconds at 150 W to open small triangular spaces between the spheres.[69] Finally, an e-beam deposition of 75 nm of Ag was performed to fill in the spaces between the spheres and the electrode was sonicated in tetrahydrofuran (THF) to remove the polystyrene spheres.[73] The counter electrode was a

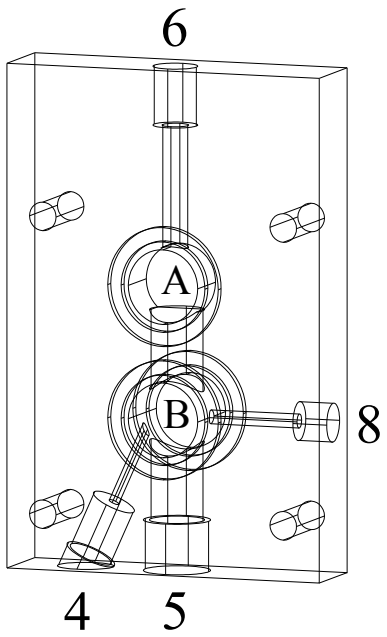

Figure 3.2: Wireframe view of the photoelectrode chamber of the PEC cell. As shown in Figure 3.1, the gas enters a port at the bottom of the cell (5) and exits through a port at the top of the cell (6). The reference electrode port (4) and the thermistor port (8) enter the bottom chamber (B) near the photoelectrode. The photoelectrode covers the back of the bottom chamber, and the working-chamber electrolyte is connected to the counter-chamber electrolyte through a membrane covering the top chamber (A). A cylindrical bore connects the top and bottom chambers. 2.3 mL of electrolyte is added to the sealed chamber and entirely fills both the bottom and top chambers.

platinum (Pt) foil and the reference electrode was a leak-free Ag/AgCl electrode (Innovative Instruments, LF-1, 3.4 M KCl). The working and counter chambers were separated by an anion-exchange membrane (AGC Engineering, Selemion AMV).

The cell was sonicated in 20 v/v% nitric acid and deionized water after fabrication and sonicated in deionized water before each use. The chambers of the cell were rinsed with 0.05 M K_2CO_3 before adding new electrolyte between consecutive electrolysis measurements on the same cathode. The assembled cell was connected to a gas manifold with leak-tight fittings (IDEX, P-210). A mass flow controller (Alicat, MC-10SCCM-D) set the gas flow rate into the cell. A mass flow meter (Alicat, M-50SCCM-D) placed in line before the gas entered the GC gas-switching valve verified the flow of the controller and was used as a check to ensure the system was leak free. A CO_2 flow rate of 5.0 sccm was used for all experiments reported in this chapter. The CO_2 is bubbled into the electrolyte through a glass frit (Ace Glass, Porosity E).

Temperature Control

A planar Peltier element (Ferro Tec, 72008/131/150B) was compressed between the aluminum back plate and the cathode. The back plate was attached to a heat sink with a mounted fan (Deep Cool, GAMMAXX 400). The interfaces between the heat sink, back plate, and Peltier

element were coated with thermal paste (Chemtronics, CW7250). A thermistor (Microlab, Model 103) covered with a heat-shrink fluorinated ethylene propylene (FEP) probe cover (Tef-Cap Industries) monitored the temperature of the catholyte through the cell side port. A PID temperature controller (Accuthermo Technology, ATEC302) was used to maintain the catholyte at a constant temperature set point throughout electrolysis. If temperature control is not needed, the Peltier element and heat sink can be removed. In this case, the back plate can be fabricated from a variety of materials including aluminum and polycarbonate.

Product Analysis

A GC (SRI Instruments, Multiple Gas Analyzer 5) with a 12' HayeSep D column, argon (Ar) carrier gas, and a gas-switching valve with a 1 mL sample loop was used for gaseous product analysis. Products separated by the column flow through a Thermal Conductivity Detector (TCD) that detects H_2 followed by a methanizer that converts CO and CO_2 to CH_4 and a Flame Ionization Detector (FID) that detects CH_4, C_2H_4, and C_2H_6 (Figure 3.9). An 11-minute GC method was developed to minimize analysis time while separating all products of interest. During CO_2 elution a solenoid vent valve diverts gas from the FID to prevent overloading of the detector signal. At the end of the run the column is backflushed with Ar; if multiple runs are to be performed the column is backflushed for 1 minute before the next injection. Ar was selected as the carrier gas because the thermal conductivity of helium (He, 190.6 mW m^{-1} K^{-1}), the most popular carrier gas, is too close to that of H_2 (230.4 m^{-1} K^{-1}) for meaningful discrimination in the TCD, and H_2 cannot be detected by the FID. However, the thermal conductivity of Ar (22.6 m^{-1} K^{-1}) is very similar to that of the CO_2 reduction products (32.3 to 49.1 m^{-1} K^{-1}). While Ar allows for the detection of H_2 in the TCD, a FID is required for the detection of the carbon-containing products.

The GC was calibrated with a set of three calibration gases containing a known mixture of H_2, CO, CH_4, C_2H_4, and C_2H_6 in a balance of CO_2 (Airgas) at concentrations between 100 and 8,000 ppm (Table 3.1). A linear calibration curve for each product was calculated from points representing the average of runs repeated multiple times across several days, with the intercept set at zero and R^2 values of 99.89% to 99.99% (Table 3.2, Figure 3.8).

Proton nuclear magnetic resonance (^{1}H NMR) spectroscopy (500 MHz Bruker Avance III) was performed for liquid product analysis. 400 μL of an electrolyte sample collected at the end of an experiment was combined with 50 μL of deuterium oxide (D_2O) (Sigma Aldrich, 151882) as the internal solvent lock and 50 μL of an internal standard comprised of 1 mM phenol in H_2O. A proton water suppression method with a 60 second acquisition time was averaged 16 times. Formate was quantified by comparing the integrated area of the product peak to that of phenol (Table 3.3, Figure 3.10, Figure 3.11).[2]

Electrochemical Measurements

Electrochemical measurements were controlled with a Bio-Logic SP-300 potentiostat. Impedance spectroscopy was used before each experiment to determine the uncompensated electrolyte resistance (R_u). R_u was found to be 6–9 Ω at 22°C in the PEC cell and EC cell and decreased with increasing temperature as expected. The potentiostat compensated for 85% of R_u during electrolysis, where the set potential was applied for 16 minutes with a GC injection occurring

after 15 minutes. Reported potentials have been converted to a reversible hydrogen electrode (RHE) scale (Equation 3.1) and adjusted for the final 15% of R_u (Equation 3.2). Equation 3.1 shows the Nernst conversion from the 85% compensated $V_{Ag/AgCl}$ (3.4 M KCl) to the RHE scale, where $pH_{electrolyte}$ is the pH of the electrolyte. The potential difference between the Ag/AgCl reference and the standard hydrogen electrode (SHE) is 0.205. The factor 0.059 is (RT/F)·(1/log(e)) where R is the ideal gas constant, T is room temperature in K, F is Faraday's constant, and e is Euler's number.

$$V_{85\%\text{ IR corrected vs. RHE}} = V_{85\%\text{ IR corrected vs. Ag/AgCl}} + 0.205 + 0.059 \cdot \text{pH}_{\text{electrolyte}} \tag{3.1}$$

Equation 3.2 shows the post-experiment calculation from 85% to 100% IR corrected potential, where $I_{average}$ is the average current in the five minutes leading up to the GC injection.

$$V_{100\%\text{ IR corrected vs. RHE}} = V_{85\%\text{ IR corrected vs. RHE}} - 0.15 \cdot R_u \cdot I_{average} \tag{3.2}$$

Each electrochemical experiment was repeated at least three times; reported results are the average of all runs with error bars showing one standard deviation.

Photoelectrochemical Measurements

The Ag photoelectrode was illuminated by a collimated array of three light-emitting diodes (LED) (Mightex) with a combined power of 3 W cm^{-2} at wavelengths of 385, 405, and 470 nm, which were selected due to their proximity to the reported surface plasmon resonance of Ag.[9] Electrolysis with product analysis was performed as described above under continuous illumination.

To measure the photocurrent, a mechanical shutter (ThorLabs, SHB1) was operated at 3 Hz and controlled by a lock-in amplifier (Stanford Research Systems, SR850) to lock-in the square wave of photocurrent generated by the chopped light. The photocurrent is the difference between the current when the light is on and the current when the light is off. The lock-in amplifier was also linked with the potentiostat to record the photocurrent. Linear sweep voltammetry (LSV) was performed from the open circuit potential to -1.4 V_{RHE} at a rate of 5 mV s^{-1} while chopping the light from the LED array (Figure 3.14). The measured power of each LED is reported in Table 3.4.

3.5 Dark CO_2 Reduction on a Ag Foil Electrode

Offset parallel electrodes represent the most straightforward geometry for front illumination of the electrode. However, they also introduce the possibility of non-uniform current distributions across the surface of the electrode. In fact, during initial trials current instabilities were observed during constant voltage measurements below -0.7 V_{RHE} in 0.1 M $KHCO_3$. Current gradients can be suppressed by increasing electrolyte conductivity, and thus concentration.[74] We observed a substantial reduction of current instabilities by increasing the concentration of the electrolyte to 1 M $KHCO_3$. To determine the impact of offset parallel electrodes at this higher electrolyte concentration, the product distribution and current densities on Ag foil at four different potentials at ambient temperature were measured in the PEC cell as

well as the EC cell with aligned parallel electrodes fabricated based on a previously reported design by Lobaccaro et al. (Figure 3.13).[72] Faradaic efficiencies for each product are plotted in Figure 3.3, with equations for calculating Faradaic efficiencies for gaseous and liquid products provided in the Faradaic Efficiency section of the Supplementary Information. The observed products were CO, H_2, and formate with an average total Faradaic efficiency of 99.9% across both cells (Figure 3.17). The results in the PEC cell were remarkably similar to those measured in the EC cell; using a two-sample t-test assuming unequal variances with a significance level $\alpha = 0.05$, there was no statistical difference between the PEC cell and EC cell performance (Table 3.5). In addition, there was no statistical difference between the average current densities at each potential between the PEC cell and the EC cell, which ranged from -0.9 mA cm^{-2} to -15 mA cm^{-2} (Figure 3.15). These results indicate that any current distribution due to the offset parallel electrode design of our cell does not impact the product current efficiencies or the overall current density.

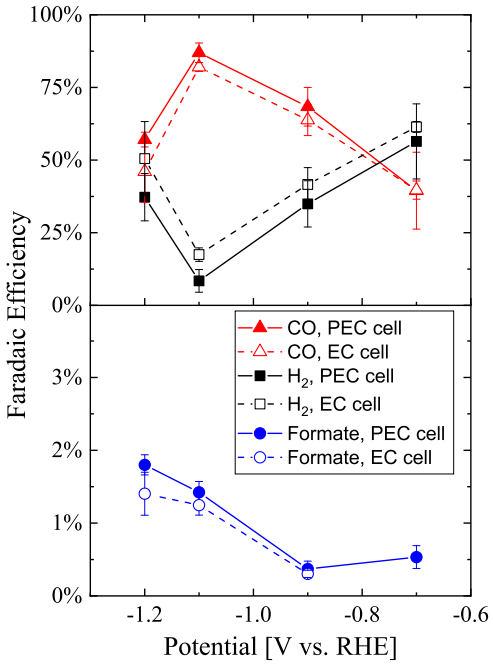

Figure 3.3: Faradaic efficiency results after 15 minutes of electrolysis without illumination at various potentials on Ag Foil in 1 M $KHCO_3$ with continuous CO_2 flow at 22°C. The PEC cell results are connected with solid lines and the EC cell results are connected with dashed lines to guide the eye. No formate was detected in the EC cell at -0.7 V_{RHE}.

Not only are the results in the PEC cell and EC cell nearly identical, they also agree with similar studies reported in literature.[17] Although minor differences in exact product distributions between prior reports and ours are observed, the trend of CO production going through a maximum at -1.1 V_{RHE}, with H_2 production going through a minimum, is in excellent agreement with prior work.[17] Similarly, the continually increasing trend of formate production with more cathodic potentials also matches those results. Variations in operating conditions may explain the differences between our studies and those previously published; Hatsukade et al. used 0.1 M $KHCO_3$, flowed CO_2 through tubing at 20 sccm, and operated

for one hour prior to product analysis.[17]

3.6 Temperature Variation During CO_2 Reduction

Like all gases, CO_2 solubility in aqueous electrolytes at moderate temperatures (0 to 50°C) decreases with increasing temperature, which in turn can have a profound effect on the product distribution during electrolysis of CO_2-saturated solutions. Nevertheless, only a few studies have been published on the influence of temperature on CO_2 reduction.[69,75–81] To demonstrate the temperature control capabilities of our PEC cell, we studied constant potential (-1.1 V_{RHE}) electrolysis of CO_2-saturated 1 M $KHCO_3$ at a smooth Ag foil electrode at 8, 22, 35, and 45°C. Figure 3.4 shows the temperature in the cell over time during a representative 8°C run; the PID controller brings the cell temperature to the set point without overshooting and stabilizes in 10 minutes. Over the course of the electrochemical run, the temperature is maintained between 7.9 and 8.1°C. Fluctuations in the current density are attributed to the high rate of CO_2 bubbling between the working electrode and the reference electrode.

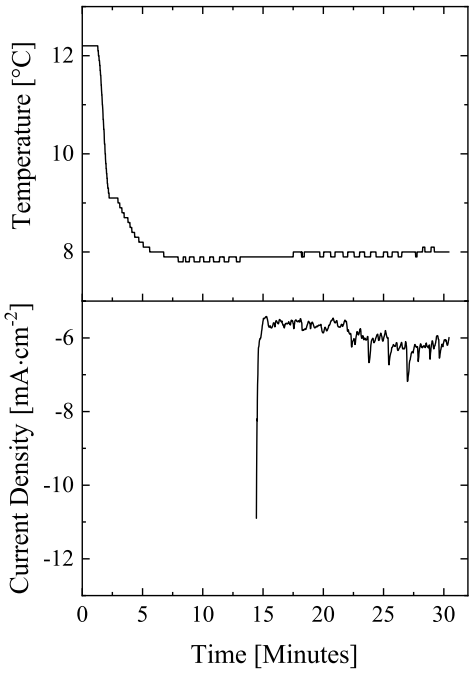

Figure 3.4: Electrolysis without illumination of CO_2-saturated electrolyte at a smooth Ag foil electrode at 8°C. Cell temperature was maintained using a PID-controlled Peltier element as shown in Figure 3.1. In this measurement, the control feedback was started after one minute of temperature recording with a set point of 8°C. Electrolysis started at 14 minutes at -1.1 V_{RHE} on Ag foil in 1 M $KHCO_3$ with continuous CO_2 flow in the photoelectrochemical cell.

Faradaic efficiencies of CO_2, H_2, and formate at 8, 22, 35, and 45°C are presented in Figure 3.5 and indicate that the selectivity towards CO production is the highest at 8°C and decreases as the cell temperature is increased with a concomitant increase in H_2 selectivity. Current

density, as well as the partial current densities of CO, H_2, and formate, was observed to increase with increasing temperature (Figure 3.16). In particular, H_2 partial current density, which increased by more than an order of magnitude from 8 to 45°C, was influenced to a much greater extent than CO formation with increasing temperature. These trends are likely a result of diminished CO_2 solubility in the electrolyte, which decreases exponentially with temperature.[72] The lower CO_2 concentration in the electrolyte at higher temperature allows more active sites to reduce water to H_2. However, it is worth noting that the Faradaic efficiency of formate remained constant with varying temperature. Azuma et al. similarly saw CO decrease and H_2 increase from 2°C to room temperature on a Ag electrode in 0.05 M $KHCO_3$, although they observed formate decrease with increasing temperature.[75] Hori et al. reported increasing H_2 production on Cu in 0.5 M $KHCO_3$ with increasing temperature (0 to 40°C), and while the total current efficiency of CO_2 reduction products decreased with increasing temperature, CO and C_2H_4 increased, formate remained constant, and CH_4 decreased with increasing temperature.[69] Clearly temperature can affect factors beyond solubility, such as reaction rates, coverage of adsorbed species, and reaction pathways, making it a vital parameter for understanding the fundamental mechanisms of CO_2 reduction.[69,75,82]

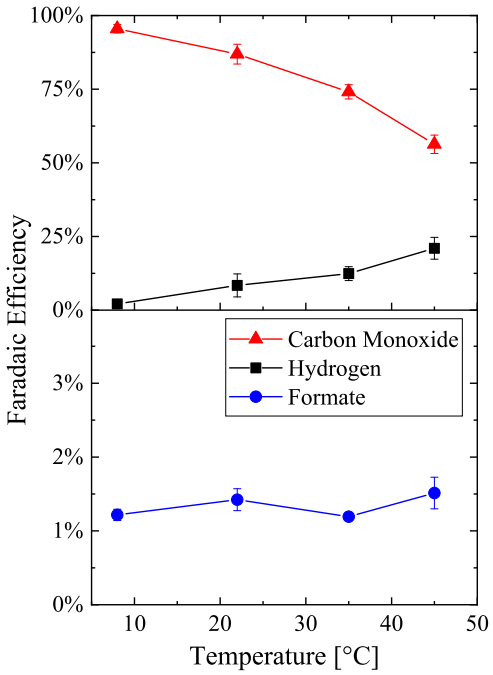

Figure 3.5: Faradaic efficiency results after 15 minutes of electrolysis without illumination at -1.1 V_{RHE} on Ag foil in 1 M $KHCO_3$ with continuous CO_2 flow in the photoelectrochemical cell at 8, 22, 35, and 45°C.

3.7 Photoelectrochemical CO_2 Reduction on a Ag Electrode

When studying photoelectrodes, it is critical to separate temperature effects from light effects, particularly because light absorption can cause fast temperature rise in low-volume electrolyte cells. For example, in our small-volume cell, the temperature increased 10°C in the first ten minutes of illumination without temperature control (Figure 2.2);[21] as seen in the previous section, such a temperature difference can drastically change the product distribution. Without temperature control it would be impossible to draw meaningful conclusions between results with and without illumination. To demonstrate the isothermal operation of the PEC cell under illumination, we used plasmonic nanostructured Ag electrodes.[51] Figure 3.6 shows the temperature of the cell over time during a typical experiment with continuous illumination of the photoelectrode. After one minute of temperature recording, the LED array is turned on and the temperature control is started with a set point of 22°C. The LED illumination initially causes the temperature to rise by 0.3°C before the temperature controller cools the cell to the set point temperature within 20 minutes. Once the set point is achieved, the system is held within 0.1°C of the desired temperature for the duration of the electrochemical experiment. PID tuning was important to ensure that temperature set point overshoot was not observed (Table 3.7).

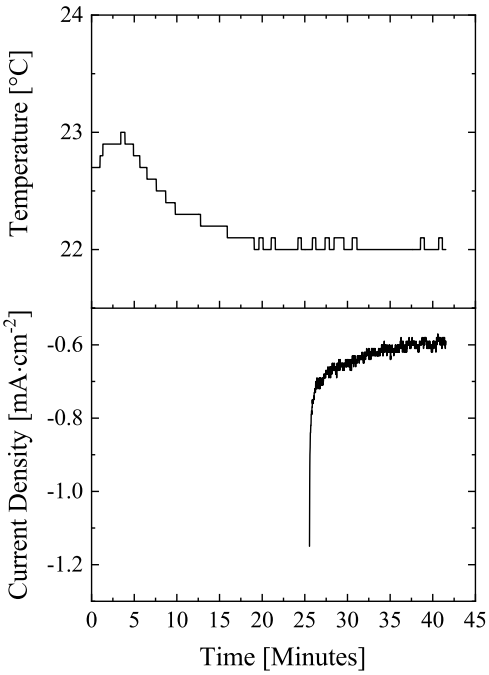

Figure 3.6: Temperature control during electrolysis at a front-illuminated photoelectrode using an LED array (385, 405, and 470 nm). Illumination and cell temperature control started after one minute of temperature recording with a set point of 22°C. Continuous illumination and temperature control were maintained when electrolysis started at 26 minutes; -0.8 V_{RHE} on a nanostructured Ag electrode in 1 M $KHCO_3$ with continuous CO_2 flow through the cell.

The product distribution from electrolysis at the nanostructured Ag electrodes in the dark and under continuous illumination at an applied potential of -0.8 V_{RHE} is shown in Figure 3.7.

Interestingly, under the same applied potential and temperature, the product distribution changes when the surface of the plasmonic electrode is illuminated. CO production increases from 55% to 68% in the light and formate generation increases from 0.3% to 1.0%. This difference in product distribution is statistically significant, as determined by a two-sample t-test assuming unequal variances with $\alpha = 0.05$ (Table 3.6). At this potential the photocurrent was 0.14 mA cm^{-2}, which is 10% of the total current density (Figure 3.14). The 13% increase in CO_2 reduction products over H_2 evolution correlates with the magnitude of the photocurrent at the applied voltage.

As further evidence of effective temperature control, the results in the previous sectionindicate that if the difference in product distribution between dark and light conditions were due to heating, we would expect to see an increase in H_2 evolution rather than CO. In previous studies, plasmon-enhanced CO production was hypothesized when a large photocurrent was observed on nanostructured Ag electrodes in CO_2-saturated electrolyte, but a negligible photocurrent was observed in Ar-saturated electrolyte.[4,5,51,83] While some groups have shown photocatalytic CO_2 reduction on plasmonic electrodes,[84–88] this is the first demonstration of a change in the product distribution driven by plasmon-enhanced photoelectrochemical CO_2 reduction. Further investigation using our PEC cell will shed light on the mechanism of plasmonic CO_2 electrochemical reduction, which is not yet known. The selectivity change under illumination highlights the need to understand the role of light in CO_2 reduction at plasmonically active electrodes, which requires the careful measurement of products as this cell allows.

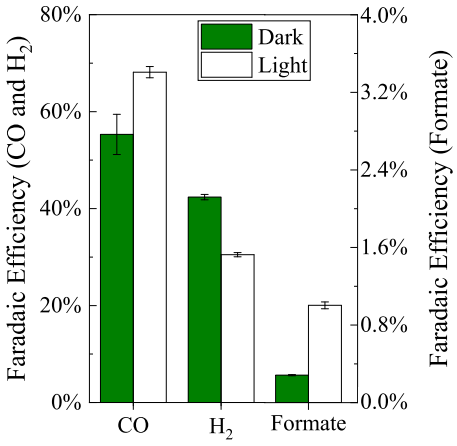

Figure 3.7: Faradaic efficiency results after 15 minutes of electrolysis at -0.8 V_{RHE} on nanostructured Ag electrodes in 1 M $KHCO_3$ with continuous CO_2 flow in the photoelectrochemical cell at 22°C. Dark indicates no illumination, and Light indicates continuous illumination by the LED array (385, 405, and 470 nm).

3.8 Conclusions

We have designed a photoelectrochemical cell for studying challenging systems which evolve multiple gaseous and/or liquid products, and possess low current densities and limiting reactant concentrations. While the cell can be adapted to many reactions, we demonstrate its efficacy for the CO_2 reduction reaction in this chapter. We show our cell is effective for studying photoelectrochemical CO_2 reduction and the influence of illumination on photoactive electrodes. We have shown that our PEC cell can match the results of a standard electrochemical cell while incorporating the additional features of temperature control and allowing front illumination of the working electrode. The plasmonic nanostructured Ag electrode was shown to selectively promote CO_2 reduction to CO over H_2 evolution upon illumination. In future work, we will use this cell to fully characterize nanostructured plasmonic electrodes to understand the mechanism of plasmon-enhanced CO_2 reduction.

3.9 Supplementary Information

Gas Chromatography (GC) Calibration

The concentrations of the GC calibration gases are shown in Table 3.1. The gradients of the forced-zero-intercept linear calibration curves and the R^2 values are shown in Table 3.2.

Table 3.1: Calibration gas concentrations.

Component	**Low [ppm]**	**Medium [ppm]**	**High [ppm]**
Carbon Dioxide	*Balance*	*Balance*	*Balance*
Hydrogen	101.5	3049	8149
Carbon Monoxide	99.9	2993	7946
Methane	100.4	3068	6256
Ethylene	101.5	518.3	3107
Ethane	101.5	511.8	2060

Table 3.2: Calibration curve gradients and R^2 values.

Component	**Gradient**	**R^2**
Hydrogen	0.2249	99.89%
Carbon Monoxide	0.3414	99.99%
Methane	0.3326	99.96%
Ethylene	0.5938	99.99%
Ethane	0.5935	99.98%

The calibration curves are plotted in Figure 3.8, showing the area under the detector response peak (y-axis) versus the gas concentration (x-axis). The points represent the average of 15 runs repeated multiple times across several days. Error bars of one standard deviation are graphed but barely visible, due to the high level of precision. A typical chromatogram showing the TCD and FID response to the "high" calibration gas is shown in Figure 3.9.

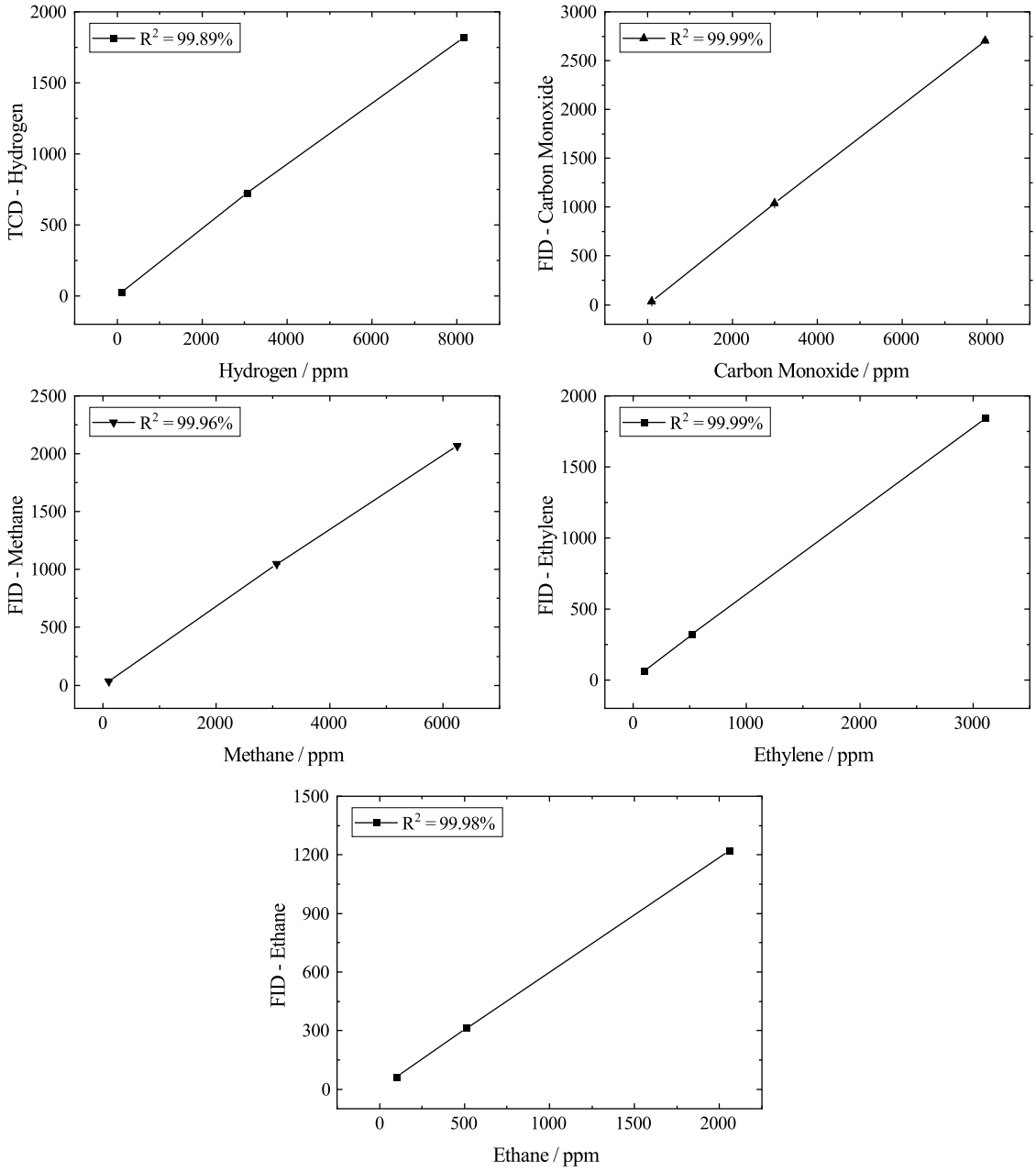

Figure 3.8: Calibration curves for the TCD (H_2) and the FID (CO, CH_4, C_2H_4, and C_2H_6).

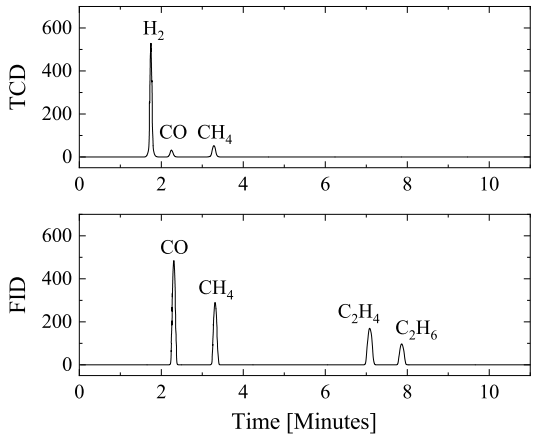

Figure 3.9: A typical chromatogram showing the TCD and FID response to the "high" calibration gas. CO and CH_4 are detected by the TCD but the stronger response in the FID is used for quantification.

Nuclear Magnetic Resonance (NMR) Spectroscopy

The chemical shifts of formate and phenol (the internal standard) are shown in Table 3.3. The area of the phenol triplet appearing at 7.2 ppm that corresponds to protons H3 and H5 (Figure 3.10) is used to determine the formate concentration from its singlet at 8.33 ppm. This water suppression method was used by Kuhl et al. to quantify 13 different liquid products formed during CO_2 reduction on copper foil.[2] A typical NMR spectrum is shown in Figure 3.11.

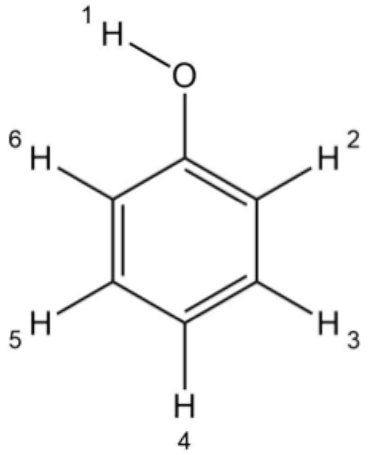

Figure 3.10: Chemical structure of phenol. The peak corresponding to protons H3 and H5 is used for quantification.

Table 3.3: NMR peak identification. The peak used for quantification is highlighted in grey.

Component	Probed Nucleus	^{1}H Splitting	Chemical Shift
Formate	$HCOO^-$	Singlet	8.33
Phenol *(Internal Standard)*	H3 and H5	Triplet	7.2
Phenol *(Internal Standard)*	H4	Triplet	6.86
Phenol *(Internal Standard)*	H_2 and H6	Doublet	6.8

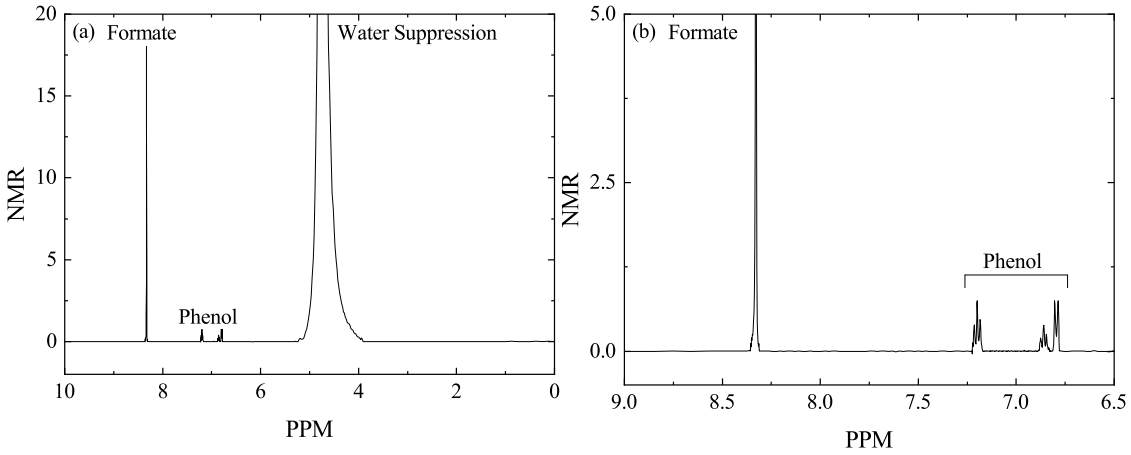

Figure 3.11: A typical NMR spectrum showing formate produced after 16 minutes of electrolysis at -1.2 V_{RHE} on Ag foil in 1 M $KHCO_3$ with continuous CO_2 flow at 22°C in the PEC cell. The entire spectrum is shown in (a) and a close view of formate and phenol from the same spectrum is shown in (b).

Nanopyramid Electrode Fabrication

A schematic of the nanosphere lithography method used by Kim et al. to form Ag nanopyramids is shown in Figure 3.12.[51]

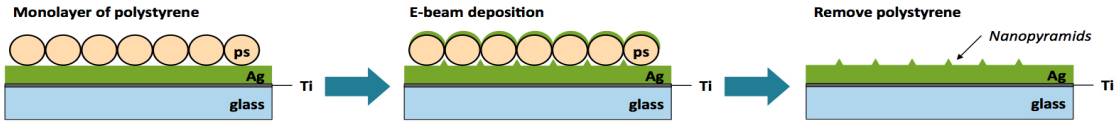

Figure 3.12: Schematic of the nanosphere lithography technique use to create the Ag nanopyramid electrodes.[51]

Electrochemical Cell

The standard electrochemical cell (EC cell) used to validate the performance of the photoelectrochemical cell (PEC cell) is shown in Figure 3.13.

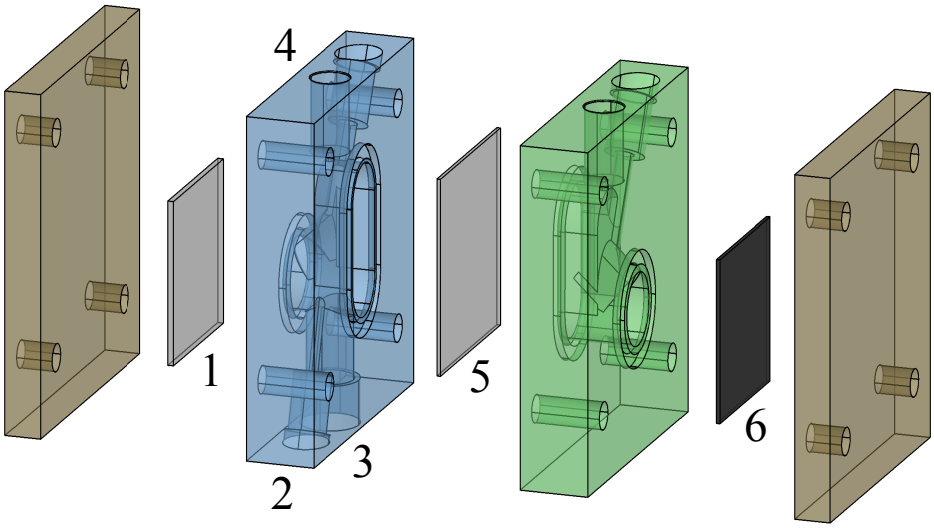

Figure 3.13: Schematic of the electrochemical cell (EC cell).[72] The working electrode (1) is in close proximity to the reference electrode (2) and is separated from the counter electrode (6) by a membrane (5). Gas enters through the glass frit at the bottom (3) and flows through tubing at the top (4) to the GC for product analysis.

Photocurrent Measurements

The measured power of each LED is reported in Table 3.4.

Table 3.4: LED power.

Wavelength (nm)	Power (W cm^{-2})
385	0.1
405	0.2
470	2.7

The effect of bubbles in the electrolyte on the light intensity reaching the photoelectrode surface was measured by comparing the light power passing through the electrolyte with and without gas bubbling. The cell was assembled with a transparent polycarbonate backplate and no electrodes. Thus, there was a direct path for light entering through the quartz window to pass through the electrolyte and the polycarbonate back of the cell. A solar cell (Oriel Instruments, 91150V) was used to measure the light intensity 5 inches from the back

of the cell. This distance was selected so the entire solar cell surface (2 cm x 2 cm) was illuminated. The light intensity measured with the cell filled with CO_2-saturated 1 M $KHCO_3$ was normalized to 100%. Then CO_2 was bubbled through the cell at 5 sccm and the light intensity measured was 73% of the light intensity through electrolyte without bubbles. These results represent the average of 10 measurements.

The total current and photocurrent densities were calculated with regard to the electrode geometric surface area (1 cm^2), which is identical to the cross section of light incident on the surface. Figure 3.14 shows the total current density and the photocurrent density measured during LSV. At -0.8 V_{RHE} the total current was -1.4 mA cm^{-2} and the photocurrent was -0.14 mA cm^{-2}. At -0.9 V_{RHE} the total current was -4.4 mA cm^{-2} and the photocurrent was at its maximum of -0.18 mA cm^{-2}.

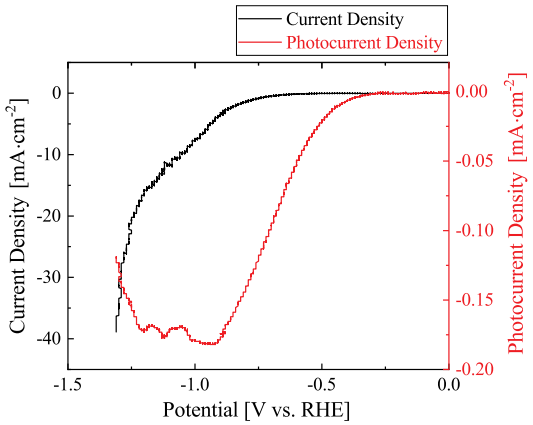

Figure 3.14: Linear sweep voltammetry on the Ag nanopyramid electrode illuminated by the LED array (385, 405, and 470 nm) with the mechanical shutter operated at 3 Hz. Performed in 1 M $KHCO_3$ with continuous CO_2 flow in the photoelectrochemical cell at 22°C. The total current is shown in black (left axis) and the photocurrent is shown in red (right axis).

Current Density

Figure 3.15 shows current densities at 22°C from representative runs in the PEC cell and EC cell at four different potentials during 16 minutes of electrolysis on Ag foil in 1 M $KHCO_3$ with continuous CO_2 flow. The PEC cell experiences slightly more noise in the current than the EC cell, likely due to the elongated bubble path. These results are very similar in magnitude to the current densities reported by Hatsukade et al. when studying CO_2 reduction on Ag foil in a different EC cell.[17] Figure 3.16 shows current densities at -1.1 V_{RHE} at 8, 22, 35, and 45°C from representative runs in the PEC cell during 16 minutes of electrolysis on Ag foil in 1 M $KHCO_3$ with continuous CO_2 flow.

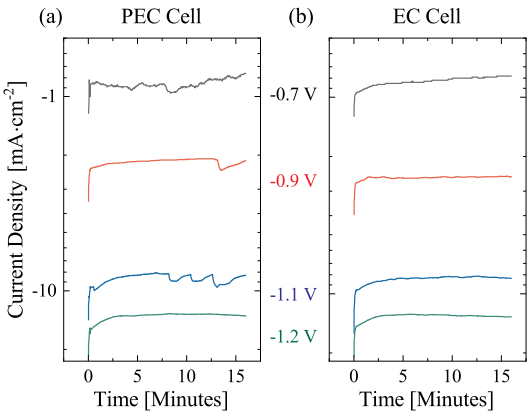

Figure 3.15: Current densities during electrolysis at -0.7 V_{RHE} (black), -0.9 V_{RHE} (red), -1.1 V_{RHE} (blue), and -1.2 V_{RHE} (green) on Ag foil in 1 M $KHCO_3$ with continuous CO_2 flow at 22°C in the (a) PEC cell and in the (b) EC cell.

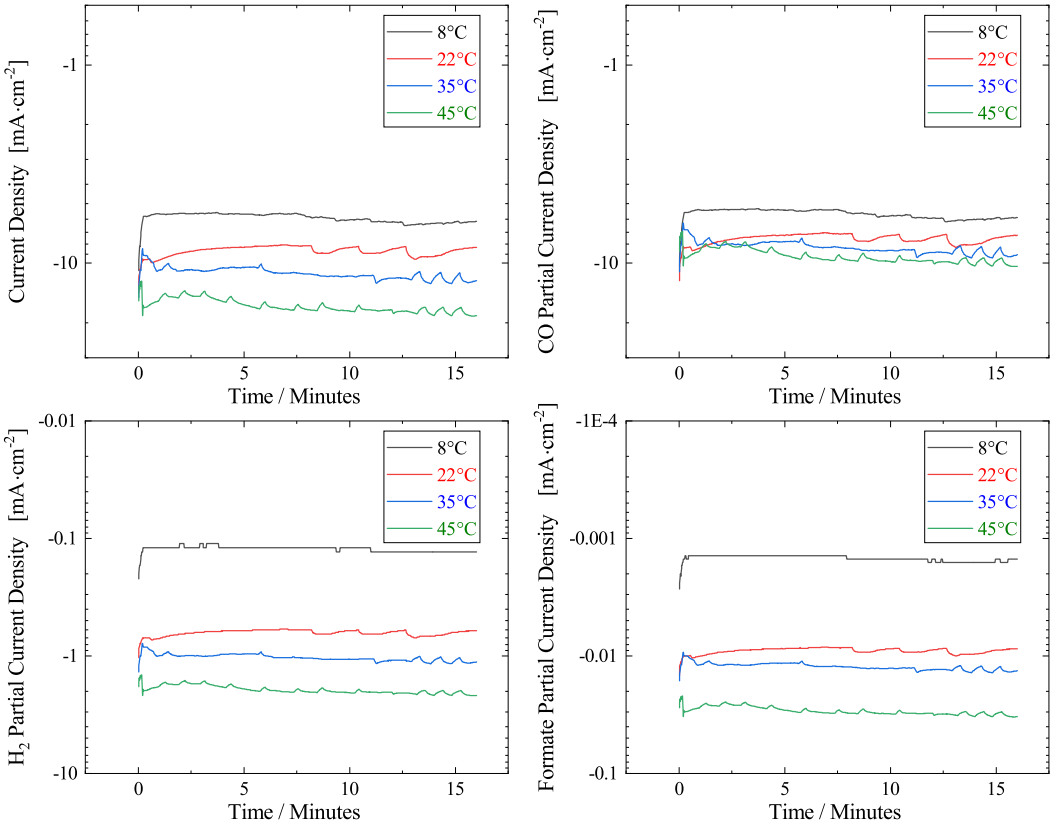

Figure 3.16: Current densities during electrolysis at -1.1 V_{RHE} at 8°C (black), 22°C (red), 35°C (blue), and 45°C (green) on Ag foil in 1 M $KHCO_3$ with continuous CO_2 flow in the PEC cell.

Faradaic Efficiency

Faradaic efficiency for liquid products (FE_{liquid}) was calculated by Equation 3.3, where M is the product molarity as measured by NMR, V is the volume of the electrolyte in the working electrode chamber, N is the number of moles of electrons to produce 1 mole of product, F is Faraday's constant, and Q is the total charge delivered during electrolysis.

$$FE_{\text{liquid}} = 100\% \cdot (M \cdot V \cdot N \cdot F)/Q \tag{3.3}$$

Faradaic efficiency for gaseous products (FE_{gas}) was calculated by Equation 3.4, where x is the product mole fraction as measured by the GC, V is the volumetric flow rate of CO_2, V_m is the molar volume of CO_2 at room temperature and atmospheric pressure, and $I_{average}$ is the average current in the five minutes leading up to the GC injection.

$$FE_{\text{gas}} = 100\% \cdot (x \cdot N \cdot F \cdot \dot{V})/(V_m \cdot I_{\text{average}}) \tag{3.4}$$

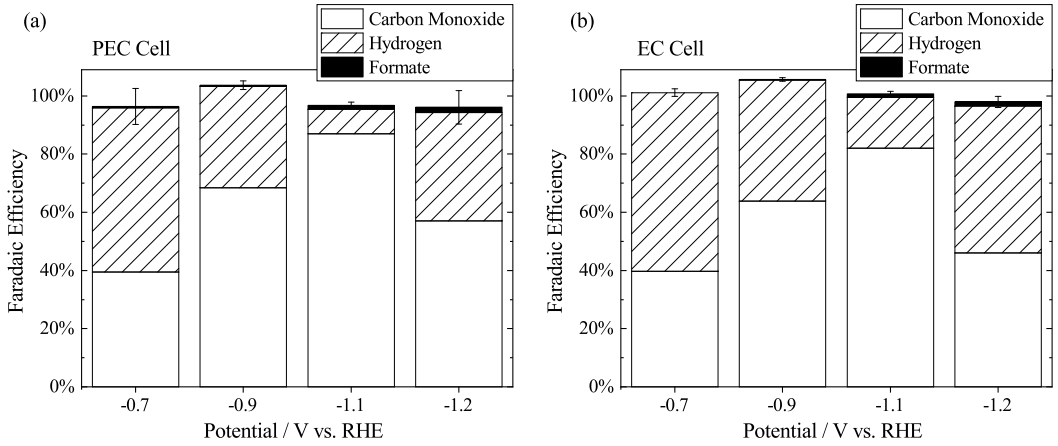

Figure 3.17: Total Faradaic efficiency results after 15 minutes of electrolysis at the specified potential on Ag foil in 1 M $KHCO_3$ with continuous CO_2 flow at 22°C in (a) the PEC cell and (b) the EC cell. Error bars represent one standard deviation for the total faradaic efficiency after three repetitions.

The total Faradaic efficiencies were close to 100%, as shown in Figure 3.17. The sole exception was the total Faradaic efficiencies at elevated temperatures, which repeatably decreased from 88% at 35°C to 79% at 45°C (Figure 3.5). The cause of this trend is strongly suspected to be enhanced diffusion of products through the membrane separating the electrode chambers at elevated temperatures, thereby reducing the product collection efficiency. When the CO_2 flow rate was increased to 10 sccm (rather than 5 sccm, as is used in Figure 3.5) during CO_2 reduction on Ag foil at 45°C, the total Faradaic efficiency increased from 79% to 89% (we note that 10 sccm is the highest flow rate we can reproducibly achieve with our flow meter). The improved product collection efficiency with increased CO_2 sparging rate very likely results from reduced total diffusion of CO and H_2 through the membrane with increased convective gas transport through the working electrode chamber. Of note, the anion-exchange membrane,

Selemion AMV, has a manufacturer-recommended operating range of 5 to 40°C with an optimal range of 20 to 30°C, such that membrane degradation at elevated temperatures could be problematic. A different membrane with a wider temperature operating range should be selected for future experiments above 30°C.

Statistical Analysis

A two-sample t-test assuming unequal variances was used to compare the means of two sets of data. The null hypothesis was that the means were identical. If the two-tail P-value was greater than the significance level $\alpha = 0.05$, we failed to reject the null hypothesis, concluding that the difference between the means was not statistically significant. The P-values presented in Table 3.5 compare the Faradaic efficiency results and the average current measured in the PEC cell and the EC cell at four different potentials using Ag foil. The average current is calculated from the five minutes before the GC injection. As all of the P-values are greater than α we conclude that there is no statistically significant difference between the means. Therefore, the performance in the PEC cell is identical to the performance in the EC cell.

Table 3.5: P-values for two-sample t-test assuming unequal variances with $\alpha = 0.05$ comparing Faradaic efficiencies and average currents in the PEC cell to the EC cell after 15 minutes of electrolysis at the specified potential on Ag foil in 1 M $KHCO_3$ with continuous CO_2 flow at 22°C.

Applied Potential	**P-value**			
(V_{RHE})	**Hydrogen**	**Carbon Monoxide**	**Formate**	**Average Current**
-0.7	0.58	0.98	*N/A*	0.72
-0.9	0.32	0.42	0.43	0.05
-1.1	0.09	0.20	0.29	0.35
-1.2	0.23	0.22	0.17	0.32

The P-values in Table 3.6 compare the Faradaic efficiency results measured in the PEC cell under dark and light conditions at the same applied potential. As all of the P-values were less than α, we rejected the null hypothesis and concluded that the difference between the means was statistically significant. Therefore, the product distribution on Ag pyramid electrodes changes upon illumination.

Table 3.6: P-values for two-sample t-test assuming unequal variances with $\alpha = 0.05$ comparing Faradaic efficiencies in the Dark and Light on Ag pyramid electrodes. Faradaic efficiency results were measured after 15 minutes of electrolysis at -0.8 V_{RHE} in 1 M $KHCO_3$ with continuous CO_2 flow in the photoelectrochemical cell at 22°C. Dark indicates no illumination, and Light indicates continuous illumination by the LED array (385, 405, and 470 nm).

Applied Potential	**P-value**		
(V_{RHE})	**Hydrogen**	**Carbon Monoxide**	**Formate**
-0.8	8.6 x 10^{-5}	0.036	8.1 x 10^{-4}

PID Tuning

The PEC cell was assembled normally with the temperature controlled to a set point of 22°C during continuous CO_2 flow using some initial values of controller gain (K_c), integral time (τ_I), and derivative time (τ_D). Once steady state was achieved the integral control was eliminated by maximizing τ_I, the derivative control was eliminated by minimizing τ_D, and K_c was set to a low value. Small temperature perturbations were introduced with a heat gun and the response was recorded. K_c was gradually increased until a sustained oscillation with a constant amplitude (continuous cycling) was observed. The ultimate gain, K_{cu}, and the ultimate period, P_u, were recorded from the oscillating temperature response. Appropriate values for K_c, τ_I, and τ_D were calculated using the Tyreus-Luyben method as shown in Table 3.7.[89]

Table 3.7: Tyreus-Luyben method for calculating PID controller parameters.[89]

	$\mathbf{K_c}$	$\boldsymbol{\tau_I}$	$\boldsymbol{\tau_D}$
Tyreus-Luyben PID	$\frac{K_{cu}}{2.2}$	$2.2P_u$	$\frac{P_u}{6.3}$

PEC Cell Parts List

Table 3.8 and Table 3.9 list all of the parts needed to assemble one complete PEC cell with temperature control. Parts for electrolytic control, illumination, gas flow, and product analysis are not included.

Table 3.8: Parts list for the PEC cell temperature control apparatus. All quantities needed are 1.

Purpose	**Part Description**	**Supplier**	**Part No.**
Temp Control	Peltier Element PID Panel Controller	Accuthermo Technology	ATEC302
Amplifier	Peltier Element H-Bridge Amplifier	Accuthermo Technology	FTX700D
Probe Fitting	M6 Flat Bottom PEEK Nut for 2 mm OD	IDEX	P-357
	1/4-28 Flat-Bottom ETFE Flangeless Ferrule for 2 mm OD	IDEX	P-314N
Temp Power	150 W, 12 V, 12.5 A Switching Power Supply	Mean Well	RS-150-12
Heat/Cool	30 mm × 60 mm, 131-couple, 15 A Peltier Cooler	Ferro Tec	72008/131/150B
Thermal Conductivity	Boron Nitride Thermal Grease	Chemtronics	CW7250-ND
Temp Sensor	5” × 1/16” Stainless Steel NTC Thermistor	Micro Lab	103
Sensor Cover	4.5” × 1/16” ID FEP Heat Shrink Caps	Tef-Cap	Custom

Table 3.9: PEC cell parts list to make one complete device. All quantities needed are 1 unless indicated by * (quantity: 6) or † (quantity: 4).

Purpose	**Part Description**	**Supplier**	**Part No.**
Cell Body	2" × 1' × 1/2" Bar, PEEK	McMaster	9089K126
Cell Front Plate	12" × 12" × 1/4" Sheet, Polycarbonate	McMaster	8707K173
Cell Back Plate	6" × 6" × 1/4" Sheet, Aluminum	McMaster	86825K721
Tubing to Frit	1/16" Tube to 1/4" Tube Reducing Union	Swagelok	NY-400-6-1
Frit to Cell	1/4" Tube to 1/8" NPT PTFE Connector	Swagelok	T-400-1-2
Glass Frit	1/4" OD × 135 mm Porosity E Filter Stick	Ace Glass	Custom
Reference Electrode	1 mm OD leak-free Ag/AgCl, 3.4 M KCL	Innovative Instruments	LF-1
Reference Fitting	1/4-28 Blue ETFE Flangeless Nut for 1/16" OD	IDEX	P-210
	1/4-28 Flat-Bottom ETFE Flangeless Ferrule for 1/16" OD	IDEX	P-200x
Reference Sleeve	1/16" OD × 0.042" ID × 1.6" NanoTight Sleeve Purple	IDEX	F-252
Gas Out Fitting	1/4-28 Blue ETFE Flangeless Nut for 1/16" OD	IDEX	P-210
	1/4-28 Flat-Bottom ETFE Flangeless Ferrule for 1/16" OD	IDEX	P-200x
O-rings*	15/16" OD × 13/16" ID × 1/16" Buna-N O-ring	Apple Rubber	AS-568-019 70 hardness
In/Out Tubing	1/16" OD × 0.02" ID FEP Tubing, 5 m	Valco	TFEP120-5M
Window	20 mm × 2 mm Quartz Disk	Aireka Cells	QD10008
Compression†	2.2" Stainless Steel Screws		
	Stainless Steel Wing nuts		

Chapter 4
Effects of Illumination, Pressure, and Temperature on Carbon Dioxide Reduction at a Plasmonically Active Silver Cathode[‡]

4.1 Abstract

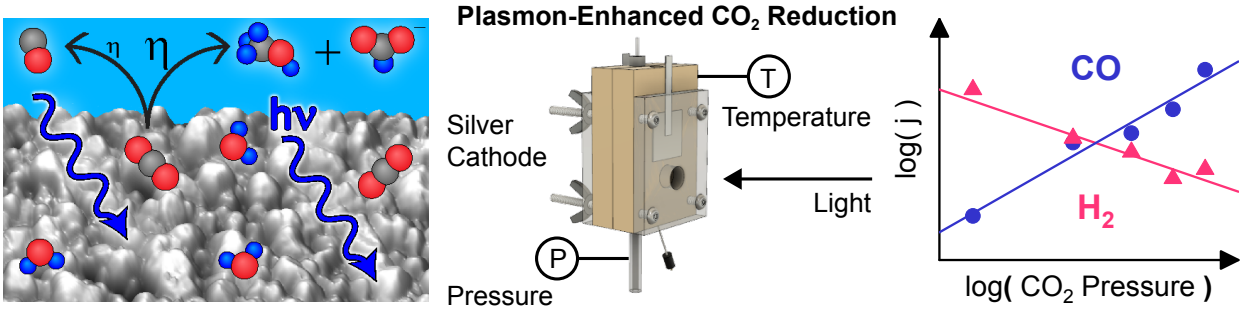

Catalysts for electrochemical carbon dioxide reduction in aqueous electrolytes suffer from high energy input requirements, competition with hydrogen evolution from water reduction, and low product selectivity. Theory suggests that plasmonic catalysts can be tuned to selectively lower the energy barrier for a specific reaction in a set of competitive reactions, but there has been little experimental evidence demonstrating plasmon-driven selectivity in complicated multielectron electrochemical processes. Here, the photoactivity at a plasmonically active silver thin film cathode at small cathodic potentials selectively generates carbon monoxide while simultaneously suppressing hydrogen production. At larger cathodic potentials, the photoactivity promotes production of methanol and formate. Methanol production is observed only under illumination, not in dark conditions. The preference of the plasmonic activity for carbon dioxide reduction over hydrogen evolution and the ability to tune plasmonic activity with voltage demonstrates that plasmonics provide a promising approach to promote complex electrochemical reactions over other competing reactions.

To understand the mechanism of the selectivity changes, the pressure and temperature are varied at multiple applied potentials under both dark and illuminated conditions. At a given applied overpotential the total current density increased with increasing P_{CO_2} in both the dark and the light, but there were significant differences in the Tafel behavior between dark and illuminated conditions. The formation of carbon monoxide is found to have first-order behavior with respect to carbon dioxide partial pressure at all applied potentials in both the dark and the light, likely indicating no change in the rate-determining step upon illumination. Activity for the hydrogen evolution reaction decreases with increasing carbon dioxide partial

[‡]Portions of this chapter were originally published in *ACS Energy Letters* and are adapted with permission from co-authors E. B. Creel, J. Eichhorn, R. Kostecki, J. J. Urban, and B. D. McCloskey.[36] Copyright 2019 American Chemical Society. Portions of this chapter were submitted to *Electrochimica Acta* and are adapted with permission from co-authors E. B. Creel, R. Kostecki, J. J. Urban, and B. D. McCloskey.[90]

pressure at slightly different rates in the dark and the light at each applied potential, making it unclear if light is influencing the carbon monoxide or hydrogen intermediate adsorbate coverage. Both formate and methanol production show no dependence on carbon dioxide partial pressure under any conditions, but the true reaction orders may be masked by the much higher activity for carbon monoxide and hydrogen at the silver cathode. The investigation of product distribution with temperature in both the dark and the light demonstrates that the selectivity changes observed upon illumination are not caused by local heating of the cathode surface.

4.2 Introduction

The rapid increase in atmospheric carbon dioxide (CO_2) concentration due to the burning of fossil fuels is the primary cause of atmospheric and oceanic warming, decreasing snow and ice cover, and rising sea levels over the last three decades.[91] The need to lessen the impacts of climate change is driving the need to mitigate CO_2 levels and find an alternative fuel source. One possible component of this approach, electrochemical reduction of CO_2, converts water and waste CO_2 into a variety of value-added chemicals such as carbon monoxide (CO), methanol, and ethylene. However, CO_2 reduction suffers from the high overpotentials needed to overcome sluggish kinetics, low selectivity for desired products, and unfavorable competition with water reduction (the hydrogen evolution reaction (HER)).[92,93] Challenges limiting energy efficiency and selective product formation must be addressed to make CO_2 reduction a viable energy storage solution.

Plasmonic catalysis may bypass the shortcomings in traditional "dark" catalysis for multi-electron reductions because of its ability to couple light energy into surface chemistry.[94] Surface plasmon resonance (SPR) in nanostructured metals has been shown to increase reaction rates in a variety of reactions,[70,95–97] including gas-phase CO_2 reduction.[84,98] However, the effect of SPR on the Coulombic efficiency and selectivity of electrochemical CO_2 reduction product(s) has not been extensively explored despite the promising improvements in selectivity seen in purely plasmonic photocatalytic (without voltage bias) CO_2 reduction.[99]

SPR is the incident-light-stimulated collective oscillation of conduction electrons at the interface between a material with positive permittivity such as water or air and a material with negative permittivity such as a metal. This phenomenon is induced by strong, resonant light absorption at a wavelength of light dictated by the size, shape, dielectric environment, and composition of the nanostructure. The plasmon resonance produces a dramatic enhancement of the local electric field on the nanostructure surface and excites "hot" electrons and holes as the initial plasmon oscillation decays. Plasmonic catalysis theory has predicted that plasmonic catalysts can be tuned such that hot carriers can be selectively injected into specific adsorbates to promote a desired reaction over other competing reactions.[9,59,100,101] However, experimental evidence of plasmon-induced product selectivity changes in electrochemical systems is limited.[88,102,103] Furthermore, the role of using an applied voltage in photoelectrochemical plasmonic catalysis has received little attention as a strategy for altering product selectivity and reactivity. While some research on plasmonic photoelectrochemical CO_2 reduction at a single potential has shown plasmonic enhancement of CO production,[35,43,104] there have been no studies characterizing plasmonic photoelectrochemical CO_2 reduction at

a range of voltages.

We use a silver cathode without a supporting absorber to probe the effect of plasmonic excitation on CO_2 reduction at several potentials. Silver is an ideal heterogeneous catalyst for plasmonic electrochemical reduction of CO_2 because of its well-understood "dark" CO_2 electrocatalytic performance,[17,92] and the resonant excitation of silver surface plasmons occurs upon illumination with near-UV-visible light irradiation at 340–400 nm (3.1–3.6 eV).[105] Moreover, due to the electronic band structure of silver, SPR is predicted to generate high-energy hot electrons,[18] making this metal appropriate for a reduction reaction study. Many transition metals are poor CO_2 reduction catalysts because they produce primarily hydrogen, but silver cathodes promote CO production at ambient temperature and pressure with reasonable CO formation selectivity over hydrogen evolution, albeit at large overpotentials (approximately 1 V) in near-neutral-pH aqueous electrolyte.[17,92] Silver cathodes also produce small amounts of formate at potentials more cathodic than -0.6 V versus the reversible hydrogen electrode (V_{RHE}) and exceedingly small amounts of methanol, ethanol, and methane at highly cathodic potentials (more cathodic than -1.3 V_{RHE}).[17]

Here, we show that the plasmonic activity over a polycrystalline silver thin film cathode is significant and selective for CO_2 reduction while suppressing hydrogen evolution at low applied cathodic potentials. Hydrogen production is also suppressed under illumination of a silver cathode in CO_2-free (Ar-saturated) electrolyte, resulting in a decrease in activity. An illuminated silver cathode generates CO at >90% Faradaic efficiency at much lower overpotentials than an unilluminated silver cathode. Methanol production is not observed without illumination at cathodic potentials down to -1.2 V_{RHE}, but methanol production under illumination is produced at 0.1–2% Faradaic efficiency between -0.8 and -1.1 V_{RHE}, which is an unprecedented methanol Faradaic efficiency for silver cathodes. Interestingly, the enhancement in CO production is observed only at -0.8 V_{RHE} and potentials more anodic, while the methanol production occurs only at -0.8 V_{RHE} and potentials more cathodic. This is the first known example of using applied voltage to control the product selectivity of plasmon-driven reactions, indicating that voltage bias is an important variable in tuning and understanding plasmonic selectivity in complex electrochemical reactions. Additionally, the combined enhancement of CO_2 reduction and suppression of hydrogen evolution via plasmonic catalysis may be an important breakthrough in directing selective aqueous electrochemical CO_2 reduction.

To shed light on the plasmonic mechanisms causing these selectivity changes we further study CO_2 reduction in the dark and the light at partial pressures of CO_2 (P_{CO_2}) from 0.2–1 atm and at electrolyte temperatures from 14–32°C across a range of applied potentials (-0.7, -0.9, and -1.1 V_{RHE}). We select these three potentials to focus on the key selectivity findings: CO enhancement and hydrogen suppression is highest at -0.7 V_{RHE}, formate enhancement in the light compared to the dark is maximized at -0.9 V_{RHE}, and methanol formation is greatest at -1.1 V_{RHE}.

CO_2 partial pressure studies during dark electrochemistry along with Tafel analysis have previously been used to reveal the rate-determining step and reaction pathway at different metallic cathodes in aqueous electrolyte.[82,106–122] CO_2 partial pressure studies have also been extensively explored during photocatalytic CO_2 reduction at semiconductor electrodes,[30,123,124]

which have a different physical response to light than plasmonically active electrodes.[21] There are some examples of studies investigating how partial pressure influences reactions at plasmonically active electrodes. Zhang et al. studied plasmon-enhanced CO_2 hydrogenation at rhodium (Rh) nanoparticles supported on titanium dioxide (TiO_2) and found differences in the thermal reaction order with hydrogen partial pressure when compared to the reaction order under illuminated conditions.[38] Zhou et al. investigated ammonia (NH_3) decomposition on Cu nanoparticles on a Cu-Ru (ruthenium) surface and discovered that the plasmonic photocatalytic reaction was first-order with NH_3 pressure but the thermocatalytic reaction was zeroth-order.[125] Here we present the first report investigating how P_{CO_2} influences CO_2 reduction at a plasmonically active electrode in the dark and the light, with the goal of understanding the plasmonic mechanisms behind the light-driven selectivity and efficiency changes.

4.3 Synthesis and Structural Characterization of Silver Thin Films

We fabricated the silver photocathodes by electron-beam (e-beam) evaporating silver onto a glass slide substrate using titanium as an adhesion layer (Figure 4.1A) followed by electrochemical conditioning of the surface at -1.1 V_{RHE} in aqueous CO_2-saturated potassium bicarbonate ($KHCO_3$) electrolyte. Electrochemical conditioning of the cathode was necessary due to the evolution of the cathode's optical properties and morphology with CO_2 electrolysis. The as-deposited silver film exhibited a weak absorption peak at 346 nm (Figure 4.1B) that corresponds to the silver SPR.[105] After only 1 min of CO_2 electrolysis, the absorption of the rinsed and dried cathode increased across the spectrum, with the plasmonic peak broadening and red-shifting. The plasmonic absorption peak continued to widen and move toward larger wavelengths with further CO_2 electrolysis until it reached a steady state between 30 and 60 min of electrolysis with an absorption maximum at 351 nm (Figure 4.1B–C). No change in the plasmonic absorption occurred when the cathode was immersed in electrolyte without applied bias. We hypothesized that the large applied voltage caused the silver nanostructures on the rough evaporator-deposited surface to ripen into larger, more stable nanostructures.[126,127]

To test this hypothesis, we measured the electrochemical double layer capacitance as a proxy for electrochemical surface area (ECSA) at various intervals over the electrolysis time (Figure 4.21). The ECSA decreases then stabilizes over electrolysis time (Figure 4.1D), consistent with the coarsening hypothesis from absorption measurements.

Scanning electron microscopy (SEM) images and atomic force microscopy (AFM) topographic images (Figures 4.1E–F, 4.13, and 4.14) show nodule-like features of 10–100 nm on the cathode surface both before and after 45 min of electrolysis even though the cathode surfaces appear mirror-like to the naked eye. AFM root mean squared (RMS) surface roughness measurements before and after electrochemical conditioning—6.0 nm and 4.4 nm, respectively—indicate a slight decrease in surface roughness, matching the ECSA measurements. The AFM topographic images indicate that the grain size distribution broadens slightly, increasing the population of both large and small features, after electrochemical conditioning (Figure 4.14E). However, this difference is difficult to observe when comparing the SEM and AFM images, indicating that the morphology differences that result in the plasmonic activity are likely too subtle to be detected by examination of these images.

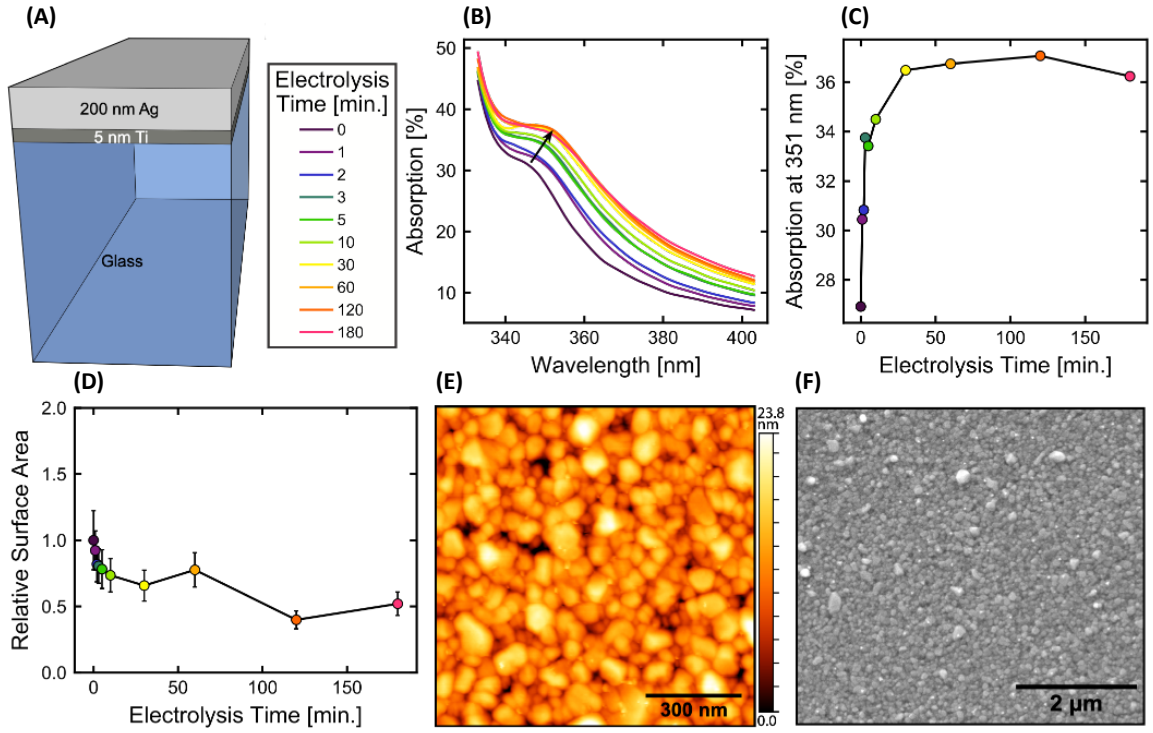

Figure 4.1: Silver thin film cathode characterization. (A) Diagram of a silver cathode showing e-beam-deposited 200 nm silver on 5 nm titanium on a glass slide (B) Evolution of the UV-visible absorption spectra of a cathode after CO_2 reduction at -1.1 V_{RHE} for various times. (C) Evolution of the absorption of a cathode at 351 nm after biasing at -1.1 V_{RHE} in CO_2-saturated 1 M $KHCO_3$ for various times. (D) Evolution of the electrochemical surface area measured by double-layer capacitance normalized to the as-deposited cathode after biasing at -1.1 V_{RHE} for various times. (E) AFM topographic image of the cathode surface after biasing at -1.1 V_{RHE} for 45 min. (F) SEM image of the cathode surface after biasing at -1.1 V_{RHE} for 45 min.

4.4 Product Distribution Trends with Illumination

The gaseous products of CO_2 reduction over the silver cathode were measured by an in-line gas chromatograph (GC) while applying a constant voltage.[43] The liquid products were measured by proton nuclear magnetic resonance (^{1}H NMR) of the electrolyte after the electrochemical measurement was complete. The cathode was continuously illuminated from the front with 170 mW cm^{-2} incident light intensity from a 365 nm light emitting diode (LED), which was selected given its proximity in energy to the plasmon resonance peak (351 nm, Figure 4.1B) of our conditioned silver cathodes, or left unilluminated for the "dark" control. No high-power LEDs (2–3 W cm^{-2}) are available below 365 nm, limiting the range of photon energies studied here to the visible spectrum, which is interesting for solar-driven processes. Our electrolysis cell was specifically designed to ensure precise temperature control, and all measurements reported in this section, both illuminated and in the dark, were performed at 22 ± 0.1°C.[43]

The difference in product distributions between the illuminated and dark conditions is dramatic and dictated by the applied potential. At potentials more anodic than -0.9 V_{RHE},

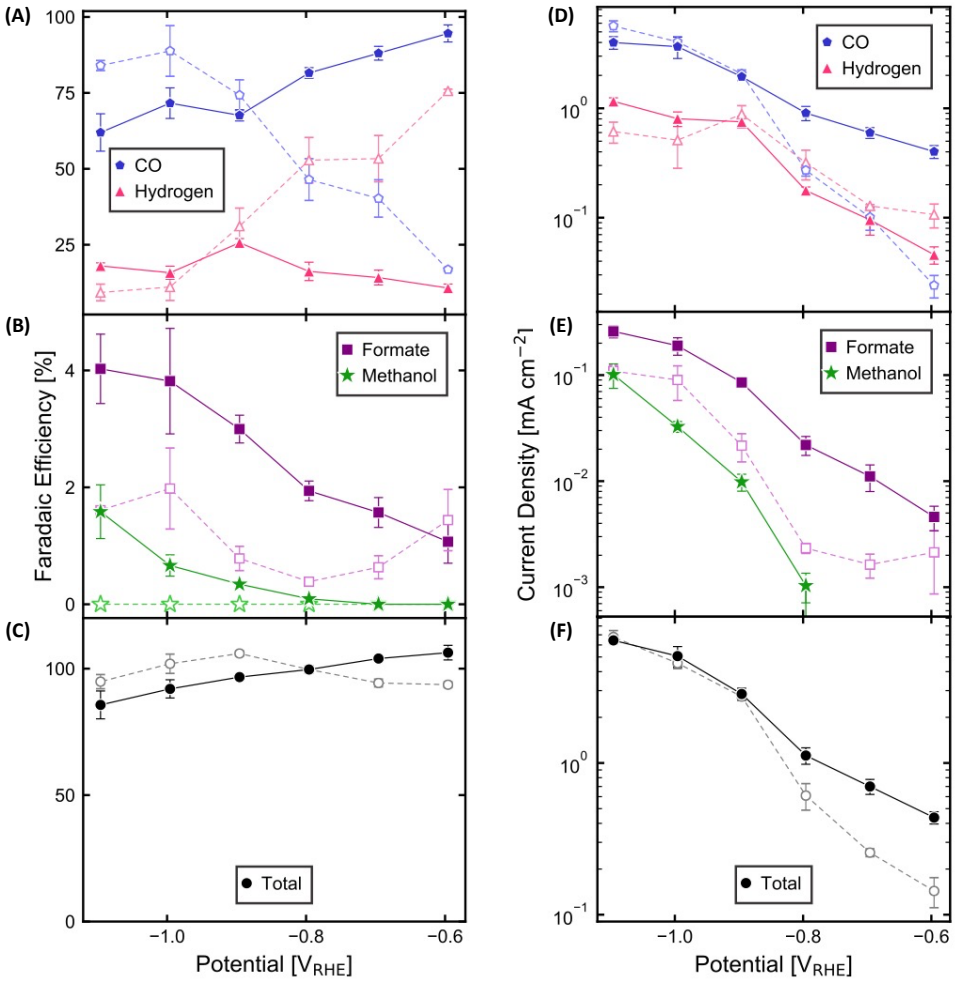

Figure 4.2: (A–C) Faradaic efficiency and (D–F) partial current density for each product over an illuminated and dark silver cathode at 22°C and 100% CO_2 mol fraction. Filled symbols with solid lines represent data collected under 365 nm LED illumination at 170 mW cm^{-2}. Open symbols with dashed lines represent data collected without illumination. (A) Faradaic efficiencies and (D) partial current densities of CO and hydrogen at a range of applied potentials. (B) Faradaic efficiencies and (E) partial current densities of formate and methanol at a range of applied potentials. No methanol was detected in the dark. (C) Total Faradaic efficiencies and (F) total current densities at a range of applied potentials. Error bars represent the standard deviation of experiments performed in triplicate on three different cathodes.

the Faradaic efficiency and production rate of CO are significantly enhanced when the silver plasmonic catalyst is illuminated (Figure 4.2A and D). The most dramatic enhancement of CO occurs at the lowest potential used in this study, -0.6 V_{RHE}, where the Faradaic efficiency of carbon monoxide increases from 17% in the dark to 95% when the cathode is illuminated. The increase in CO Faradaic efficiency reflects a 3, 5, and 16-fold increase in the CO production rate in the light versus that in the dark at -0.8, -0.7, and -0.6 V_{RHE}, respectively (Figure 4.2D). The decrease in hydrogen Faradaic efficiency when the silver

cathode is illuminated at these small cathodic potentials (Figure 4.2A) stems not only from the increase in CO production but also a notably lower rate of hydrogen generation in the light at these potentials (Figure 4.2D).

The cathodic sweep of a cyclic voltammogram (CV) in CO_2-saturated 1 M $KHCO_3$ predictably shows increased cathodic current and a decreased onset potential when the silver cathode is illuminated (Figure 4.3A). CO is the only product detected over the illuminated silver cathode at -0.37 V_{RHE} while no products were detected at the same potential without illumination. CVs in Ar-saturated 0.5 M potassium carbonate (K_2CO_3) show the opposite trend—the cathodic current decreases under illumination relative to the unilluminated cathode (Figure 4.3B). Though the same starting electrolyte was used in both the Ar- and CO_2-saturated CVs, the presence of CO_2 lowers the pH, as noted in the legends of Figure 4.3. Similar results are observed in CO_2- and Ar-saturated 0.5 M sodium perchlorate ($NaClO_4$) (Figure 4.15), indicating that a plasmon interaction with adsorbed bicarbonate (which could plausibly be adsorbed to, and therefore blocking, active sites) is likely not impacting these results. Therefore, hydrogen production is suppressed on a plasmonic silver cathode regardless of the presence of CO_2 or specific electrolyte anions.

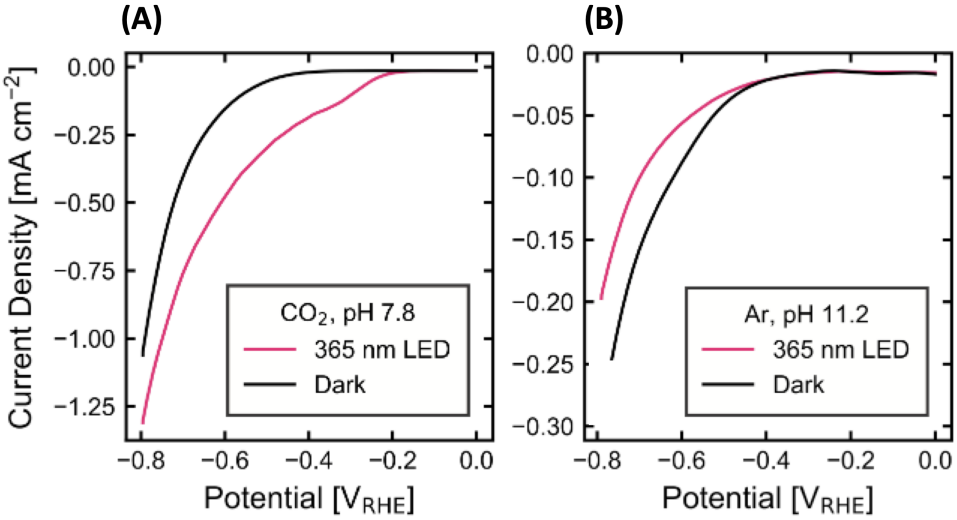

Figure 4.3: Cathodic voltage sweep at 100 mV s^{-1} at an illuminated and dark silver cathode in (A) 100% CO_2- and (B) 100% Ar-saturated 0.5 M K_2CO_3 under 365 nm LED light at 170 mW cm^{-2} at 22°C. The voltage ranges were selected to ensure that no silver oxidation occurred at the anodic limit and to include all potentials where a photoeffect is observed for CO and hydrogen in CO_2-saturated electrolyte at the cathodic limit.

A plausible explanation for this CO formation selectivity over hydrogen evolution is that the plasmonically generated hot electrons are selectively, rather than indiscriminately, transferred to molecules adsorbed on the metal surface. In the case of plasmonic electrochemical CO_2 reduction, there are several leading theories for the mechanism of plasmonic hot-electron-driven photocatalysis that may be valid in this photoelectrochemical system.[9,59,100,101,128,129] In an indirect charge transfer mechanism, SPR excites a hot electron in the silver catalyst; subsequently, that hot electron is transferred to unoccupied molecular orbitals of an adsorbate. In a direct charge transfer mechanism, SPR induces direct charge transfer in the metal-

adsorbate complex from an electronic state with primarily silver character to a hybridized orbital with primarily CO_2 reduction intermediate character.[128,129] In a transient negative ion (TNI) mechanism, plasmonic hot electrons are generated on the silver, populate unoccupied adsorbate states for a short time, and then return to the metal, leaving the adsorbate molecule in a vibrationally excited state with increased reactivity.[9,59,100,101] These three mechanisms are all consistent with the transfer of electron density to adsorbed CO_2 or an intermediate in the pathway to selectively form CO, formate, or methanol, as is observed in this study.

The plasmonic suppression of hydrogen evolution superficially appears to be a completely different process than the promotion of CO_2 reduction. However, it is possible that hydrogen is suppressed because protons (or hydroxide ions) or water molecules are selectively purged from the surface of the silver cathode through desorption induced by electronic transitions (DIET), the basis for the TNI mechanism discussed above.[9,130] In the DIET mechanism, the hydrogen precursor is excited electronically through the transient population of unoccupied adsorbate orbitals. The DIET mechanism diverges from the TNI mechanism in the result of the vibrational excitation. In DIET, the adsorbate overcomes the surface binding energy and desorbs rather than overcoming a reaction barrier. Another possible explanation for hydrogen suppression is that the plasmonic hot electron populates a hybridized antibonding orbital in the metal-adsorbate complex. These mechanisms share the common theme of inhibition of a critical intermediate in hydrogen generation.

In the case of CO_2, the interaction with a plasmonic catalyst spurs reaction, while the interaction of hydrogen precursors leads to a reversion to the initial state. Further studies are needed to distinguish among the proposed mechanisms, but the observation of differing interactions among adsorbates in the same catalytic system is unprecedented. Thus, plasmonic catalysis may allow the tuning of selectivity in complex reactions by promoting the surface reaction of some species and the depopulation of others.

At more cathodic potentials (-0.9 V_{RHE} and below), the differences in partial current density between light and dark conditions for hydrogen and carbon monoxide formation are small (Figure 4.2D). However, starting at -0.8 V_{RHE} and continuing to more cathodic potentials, the silver catalyst produces methanol when illuminated but no detectable methanol in the dark up to -1.1 V_{RHE} (Figure 4.2B and C). The initial detection of methanol in illuminated conditions at -0.8 V_{RHE} represents a 550 mV decrease in the required overpotential to produce methanol compared to a previous report of methanol production on unilluminated polycrystalline silver.[17] The rate of methanol production continues to increase at more cathodic potentials (Figure 4.2E), and the maximum methanol Faradaic efficiency achieved in this study is 1.4% when the cathode is illuminated and biased at -1.1 V_{RHE}, which is more than 130 times greater than the methanol production efficiencies reported at 250 mV higher overpotential on polycrystalline silver in dark conditions.[17] Given that methanol is the sole product that is only produced under illumination, we compare its partial current density at various wavelengths of constant photon flux (Figure 4.4). Partial current densities for other products at the same wavelengths show no obvious trends (Figure 4.16) likely due to the difficulty in deconvoluting dark and light currents. The methanol production rate at -1.1 V_{RHE} is proportional to the absorption of the conditioned silver cathode at the wavelength of illumination. The correlation between absorption and methanol production is a strong indication that methanol

is generated via photonic effects. We present further evidence of photonic effects in later sections.

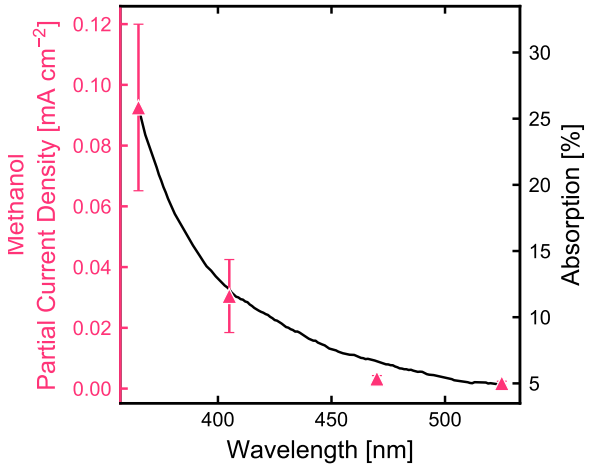

Figure 4.4: Methanol production rate under equal LED photon fluxes (3×10^17 photons cm^{-2} s^{-1}) of different wavelengths at 22°C and 100% CO_2 partial pressure (P_{CO_2}) (left ordinate). Absorption of the cathode (right ordinate) after performing CO_2 reduction at -1.1 V_{RHE} for 45 min. Absorption is calculated as 100% - %R, where %R is the total reflection measured by an integrating sphere.

The formate production rate and Faradaic efficiency increase in the light relative to those in the dark from -1.1 to -0.7 V_{RHE} (Figure 4.2B and E). For example, in the potential window of -1.1 to -0.9 V_{RHE}, formate is produced under illumination at 2–4 times the rate of formate production at the same potential in the dark. The Faradaic efficiencies for all products reported for dark conditions here are in very good agreement with similar measurements reported by Hatsukade et al. on a polycrystalline silver foil cathode.[17]

4.5 Product Distribution Trends with CO_2 Partial Pressure

Total Current Density

LSV experiments were performed at 5 mV s^{-1} at 20, 40, 60, 80, and 100% CO_2 mol fraction (0.2–1 atm) in the dark and during continuous illumination at 22°C. As shown in the Tafel plots in Figure 4.5 and LSV curves in Figure 4.18, at a given applied overpotential, the total current increased with increasing P_{CO_2} in both the dark and the light. This trend was also observed in the dark at polycrystalline silver in 0.1 M $KHCO_3$.[17,109] The shift from a non-Faradaic to a Faradaic regime in the light occurred at a lower overpotential than in the dark at all P_{CO_2}. In the light the average onset potential was -0.19 V_{RHE} and in the dark the average onset potential was -0.40 V_{RHE}. Onset potentials at each P_{CO_2} in the dark and the light are tabulated in Table 4.1. This approximately 200 mV difference in onset potential between the light and the dark can be seen clearly by overlaying the dark and light Tafel curves at 100% CO_2 mol fraction in Figure 4.6 and at all CO_2 mol fractions in Figure 4.22.

There was a strong inflection point in all of the light Tafel curves at an average value of -0.3 V_{RHE} that was never observed in the dark. Inflection points at each P_{CO_2} in the light are

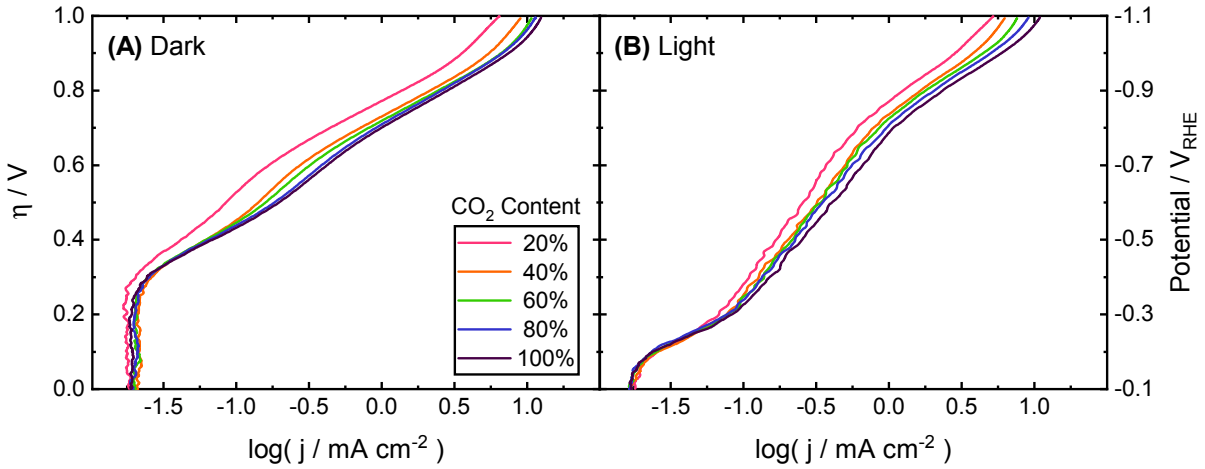

Figure 4.5: Tafel plots of the total current density at various CO_2 mol fractions during linear sweep voltammetry at 5 mV s^{-1} at a silver cathode in CO_2-saturated 1.0 M $KHCO_3$ at 22°C (A) in the dark and (B) while illuminated with a 365 nm LED at 170 mW cm^{-2}. The legend in (A) applies to both (A) and (B). The overpotential (η) is shown for the CO evolution reaction. Corresponding total current density vs. potential plots are shown in Figure 4.18. Overlays of light and dark Tafel plots at 100% CO_2 mol fraction are shown in Figure 4.6 and at all CO_2 mol fractions are shown in Figure 4.22.

tabulated in Table 4.1. Indeed, the total current trends in the light were different from those in the dark, especially at low overpotentials, and those trends were consistent across all P_{CO_2}. This indicates that the light does not merely shift the dark activity to a lower overpotential but fundamentally changes the electrochemical processes occurring at the cathode, as shown by changes in product selectivity in the light. The previous section showed that from -0.6 to -0.8 V_{RHE} the light enhances the production of CO and suppresses hydrogen evolution when compared to the dark. This result is also shown at -0.7 V_{RHE} for all P_{CO_2} (Figures 4.7A, 4.8A, 4.23A, and 4.24A).

As shown in Figure 4.6 and Figure 4.22, the difference in dark and light activity continues from around -0.2 V_{RHE} until approximately -0.8 V_{RHE}, where the dark and light total current densities cross and the activity in the dark is now higher than that in the light at all P_{CO_2}. The only exception to this is at 20% CO_2 mol fraction, where the dark and light curves cross at -0.88 V_{RHE}. This shift in the total current density trends corresponds to the product analysis trends where, at potentials more negative than -0.8 V_{RHE}, there is no longer an enhancement of CO production or suppression of hydrogen formation in the light when compared to the dark (Figure 4.2A and D).

Although Figure 4.5 and Figure 4.6 are represented as Tafel plots, we do not use the Tafel slopes (Table 4.3) to identify reaction mechanisms for two key reasons. First, Dunwell et al.[131] have shown that the Tafel region for CO_2 reduction, where the overpotential is sufficiently low so that the reaction rate is kinetically controlled, occurs only at very low overpotentials (less negative than -0.4 V_{RHE}). However, in this region the product concentration is too low for reliable gaseous product quantification in our constant gas flow cell. As both hydrogen and CO may form in the Tafel region in the dark we cannot reliably extract the CO partial

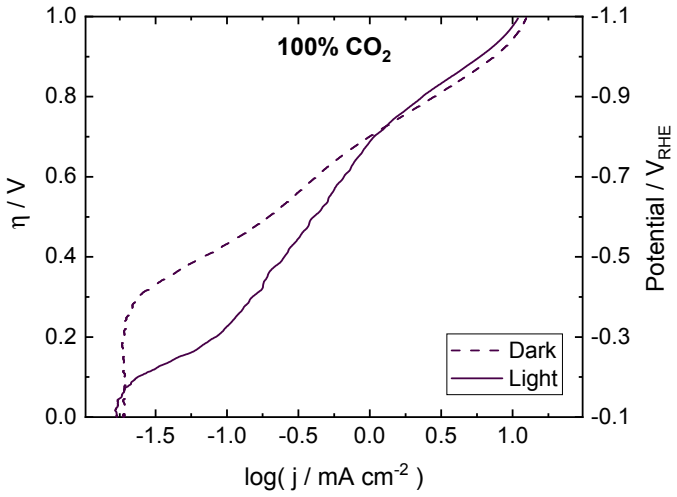

Figure 4.6: Tafel plot of the total current density at 100% CO_2 mol fraction during linear sweep voltammetry at 5 mV s^{-1} at a silver cathode in CO_2-saturated 1.0 M $KHCO_3$ at 22°C in the dark (dashed line) and while illuminated with a 365 nm LED at 170 mW cm^{-2} (solid line). The overpotential (η) is shown for the CO evolution reaction. Similar overlays of light and dark Tafel plots at all CO_2 mol fractions are shown in Figure 4.22. Separate light and dark Tafel plots are shown in Figure 4.5 and corresponding total current density vs. potential plots are shown in Figure 4.18.

current density.

AS only CO is formed in the light at potentials less negative than -0.37 V_{RHE}, we can conclude that the linear region in the light before the inflection point at -0.3 V_{RHE} is related solely to CO production. In Table 4.3 the Tafel slopes for CO formation in the light are calculated from -0.20 to -0.26 V_{RHE} (η = 100 to 160 mV) and range from 169 to 201 mV dec^{-1}. However, the expected Tafel slopes range from 30–118 mV dec^{-1} at a symmetry factor (β) of 0.5, depending on the reaction mechanism.[122] β is the fraction of the applied potential that promotes the cathodic reaction. It is only possible to achieve such high Tafel slopes if β is much lower than 0.5, indicating that only a small fraction of the total energy change is impacting the activation energy for the cathodic reaction. This brings us to our second reason for not using these Tafel slopes to identify a reaction mechanism: it is not clear that Butler-Volmer kinetics are applicable to electrochemical reactions that are influenced by a plasmonic mechanism. The Butler-Volmer equation was derived for an elementary reaction involving the transfer of a single electron from the electrode to the reactant where the energy level of the electron is defined by the applied potential. In contrast, at an illuminated plasmonically active electrode, the excited electron energy is defined by the applied potential, the incident light wavelength, and the band structure of the metal. Butler-Volmer kinetics have been applied to plasmon-enhanced electrochemical hydrogen evolution at Au nanoparticles to compare Tafel slopes and exchange current densities (j_0) in the dark and under illumination.[14,38,39] Wilson et al. proposed adding a plasmon-excitation-generated cathodic potential ($E_{h\nu}$) to the applied potential which would change j_0 but cannot account for the high Tafel slopes we observe in the light.[14] Thus, while comparing the light and dark current densities at low overpotentials is valuable for demonstrating the markedly different behavior, we cannot

confidently use the Tafel slopes to identify the reaction pathway.

Carbon Monoxide

Product analysis was performed at -0.7, -0.9, and -1.1 V_{RHE} at various P_{CO_2} in both dark and light conditions. At -0.9 V_{RHE} the entire range from 20 to 100% CO_2 mol fraction could be investigated, but at -0.7 and -1.1 V_{RHE} the current was unstable at lower P_{CO_2}. The product distribution at -0.7 V_{RHE} could only be investigated from 40–100% and -1.1 V_{RHE} was only stable from 60–100%.

The logarithm of the CO partial current density (j_{CO}) is plotted against the logarithm of P_{CO_2} in Figure 4.7 and the Faradaic efficiency plots are shown in Figure 4.23. The slopes of the best-fit linear regression curves are shown in Figure 4.7 and the slopes and R^2 values are also tabulated in Table 4.4. The linear regression curves in the dark and the light at -0.9 and -1.1 V_{RHE} have R^2 values greater than 0.9, indicating that the linear fit can account for greater than 90% of the variability in the data.

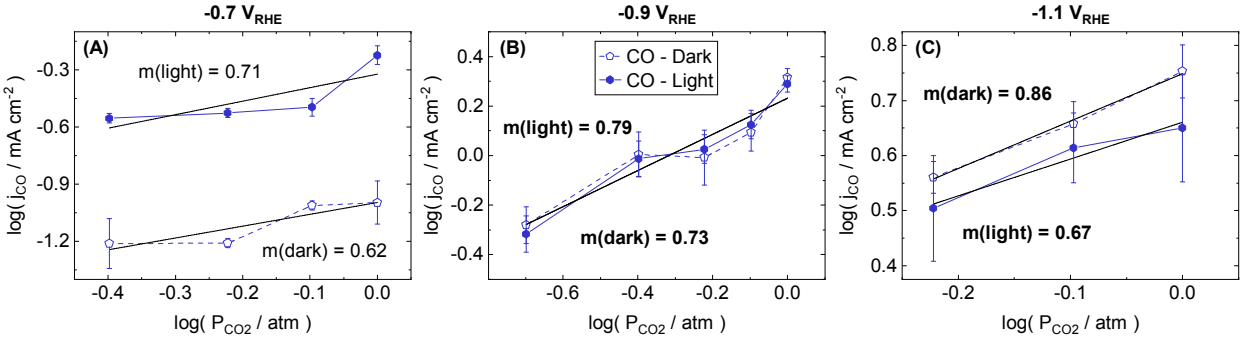

Figure 4.7: Logarithm of carbon monoxide partial current density (j_{CO}) vs. logarithm of CO_2 partial pressure (P_{CO_2}) at (A) -0.7, (B) -0.9, and (C) -1.1 V_{RHE} at a silver cathode in CO_2-saturated 1.0 M $KHCO_3$ at 22°C in the dark (dashed lines) and while illuminated with a 365 nm LED at 170 mW cm^{-2} (solid lines). Error bars represent one standard deviation of experiments performed in triplicate. Black lines represent best-fit linear regression curves. Slopes in the light are shown on the graph as m(light) and slopes in the dark are shown on the graph as m(dark). Slopes in bold have R^2 values greater than 0.9. Slopes and R^2 values are also tabulated in Table 4.4. Corresponding Faradaic efficiencies are plotted in Figure 4.23.

We expect the reaction rate, and thus j_{CO}, to depend on P_{CO_2} with some reaction order, m (Equation 4.1).

$$j_{CO} \propto P_{CO_2}^{m} \tag{4.1}$$

By taking the logarithm of both sides we find

$$\log(j_{CO}) = m \log(P_{CO_2}) \tag{4.2}$$

Thus the slope of $\log(j_{CO})$ vs. $\log(P_{CO_2})$ will give the CO reaction order m with respect to P_{CO_2} (Equation 4.2)..

There are some reports of CO formation on silver cathodes at varying P_{CO_2}. A slope of 0.94 was reported for a cathode of nanoporous silver at -0.35 V_{RHE} in 0.5 M $KHCO_3$.[116,117] Quan et al. found a slope of 1.14 at a silver foil at -0.90 V_{RHE} in 0.5 M $NaHCO_3$ with 20 mM of ionic liquid.[120] All of these studies concluded that CO formation at silver cathodes has a first-order dependence on P_{CO_2}. In contrast, Singh et al. investigated a silver foil in 0.1 M $KHCO_3$ and used a power law fit to find the intrinsic reaction order with respect to P_{CO_2} to be 1.49 at -0.9 V_{RHE}, 1.63 at -1.0 V_{RHE}, and 1.83 at -1.1 V_{RHE}, and concluded that the intrinsic reaction order is greater than one.[121]

In this study we find the average value of slopes in the dark and light are statistically similar and roughly 0.7 at all potentials studied (Figure 4.7), although in the dark a slight increase in slope is observed with increasing overpotential (from 0.62 at -0.7 V_{RHE} to 0.86 at -1.1 V_{RHE}). From this we conclude that the reaction order of CO with respect to P_{CO_2} is likely first order in both the dark and the light; the experimentally measured slopes may be less than one due to the influence of mass transfer.[121] Indeed, in prior studies, the slopes closest to one on silver cathodes were performed at low overpotentials where mass transfer effects are minimal, ca. -0.35 V_{RHE}.[116,117]

As mentioned earlier, we find that the slope in the dark increases slightly with more negative applied potentials: 0.62 at -0.7 V_{RHE}, 0.73 at -0.9 V_{RHE}, and 0.86 at -1.1 V_{RHE}. However, this trend is broken in the light with a smaller slope at -1.1 V_{RHE} than at -0.7 or -0.9 V_{RHE}. While our results show linear, first-order trends at these potentials, it is interesting to find the same trend of increasing reaction order with more negative potentials in the study by Singh et al. They concluded that the reaction order increases because the adsorption free energy of CO_2 on silver increases with more negative potentials due to stronger π back-bonding.[121] It is possible for the local electric fields that can be generated at an illuminated plasmonically active cathode to influence the adsorption energy of species, which could account for the different slope trend in the light. No other silver study has reported P_{CO_2} at more than one applied potential. Given the statistical similarity in the P_{CO_2} reaction orders among all measurements described in Figure 4.7, at this time there is not enough evidence on silver to conclude whether or not the dark reaction order with P_{CO_2} truly increases with more negative potentials and if there is a change in this trend upon illumination.

The possible reaction mechanisms for CO formation and their reaction order with P_{CO_2} are nicely summarized by Williams et al.[122] The majority are first order with P_{CO_2}, but some reaction mechanisms would result in second order behavior. From our results in Figure 4.7 we can conclude that the light does not cause the reaction mechanism to change from a mechanism that is first order with P_{CO_2} to one that is second order with P_{CO_2}. We can also state that the reaction order of CO with respect to P_{CO_2} is first order in both the dark and the light, likely indicating that the rate-determining step does not change upon illumination. However, this data alone cannot conclusively identify the reaction pathway nor discount that the reaction mechanism in the light may be a different first-order pathway than that in the dark.

Hydrogen

The logarithm of the hydrogen partial current density (j_{H_2}) is plotted against the logarithm of P_{CO_2} in Figure 4.8 and the Faradaic efficiency plots are shown in Figure 4.24. The slopes of the best-fit linear regression curves are shown in Figure 4.8 and the slopes and R^2 values are also tabulated in Table 4.4. Only half of the linear regression curves have R^2 values greater than 0.9, indicating that the logarithm of j_{H_2} is only approximately linear with the logarithm of P_{CO_2} in both the dark and the light.

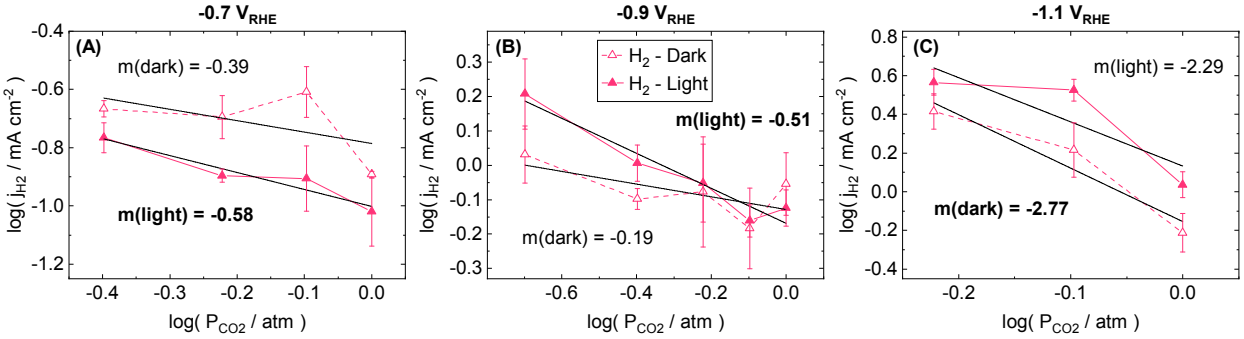

Figure 4.8: Logarithm of hydrogen partial current density (j_{H_2}) vs. logarithm of CO_2 partial pressure (P_{CO_2}) at (A) -0.7, (B) -0.9, and (C) -1.1 V_{RHE} at a silver cathode in CO_2-saturated 1.0 M $KHCO_3$ at 22°C in the dark (dashed lines) and while illuminated with a 365 nm LED at 170 mW cm^{-2} (solid lines). Error bars represent one standard deviation of experiments performed in triplicate. Black lines represent best-fit linear regression curves. Slopes in the light are shown on the graph as m(light) and slopes in the dark are shown on the graph as m(dark). Slopes in bold have R^2 values greater than 0.9. Slopes and R^2 values are also tabulated in Table 4.4. Corresponding Faradaic efficiencies are plotted in Figure 4.24.

As CO_2 does not participate in the hydrogen evolution reaction, the reaction rate expression does not depend on P_{CO_2}. However, we find that j_{H_2} decreases with increasing P_{CO_2} at all applied potentials in both the dark and the light. This trend has also been theoretically predicted[82] and experimentally observed on Cu[107,108] and indium (In).[111] While one study on Cu was also performed at CO_2 pressures at and below 1 atm,[107] the second report on Cu[108] and the study on In[111] investigated CO_2 pressures of 1 to 60 atm and both found hydrogen production continued to decrease throughout this range.

This decrease in hydrogen evolution with increasing P_{CO_2} indicates a competition in adsorption between the hydrogen and CO reactants, as shown in Figure 4.9. Chaplin et al. predicted that increasing P_{CO_2} would promote the retention of CO_x^{y-} species and suppress H(ads) coverage.[82] At illuminated plasmonically active electrodes it is possible for local electric fields or hot electrons to influence the binding energy, and thus coverage, of adsorbates. There are differences in the hydrogen slopes with P_{CO_2} between the light and the dark at each applied potential but the difference is not sufficiently significant to determine if the light is affecting the CO_x^{y-} or H(ads) adsorbate coverage on this cathode.

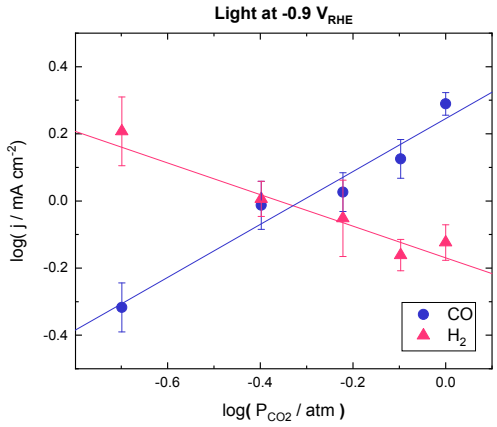

Figure 4.9: Logarithm of carbon monoxide and hydrogen partial current densities (j) vs. logarithm of CO_2 partial pressure (P_{CO_2}) at -0.9 V_{RHE} at a silver cathode in CO_2-saturated 1.0 M $KHCO_3$ at 22°C while illuminated with a 365 nm LED at 170 mW cm^{-2}. Error bars represent one standard deviation of experiments performed in triplicate. Lines represent best-fit linear regression curves. Slopes and R^2 values are tabulated in Table 4.4. Partial current densities at other potentials and light conditions are plotted in Figures 4.7 and 4.8 and corresponding Faradaic efficiencies are plotted in Figures 4.23 and 4.24.

Liquid Products

There were two liquid products formed in this study, formate and methanol. The logarithm of the formate partial current density (j_{HCOO^-}) is plotted against the logarithm of P_{CO_2} in Figure 4.10 and the Faradaic efficiency plots are shown in Figure 4.25. The slopes of the best-fit linear regression curves are shown in Figure 4.10 and the slopes and R^2 values are also tabulated in Table 4.4. All of the linear regression curves have R^2 values much lower than 0.9, indicating that the linear fit cannot account for most of the variability in the data.

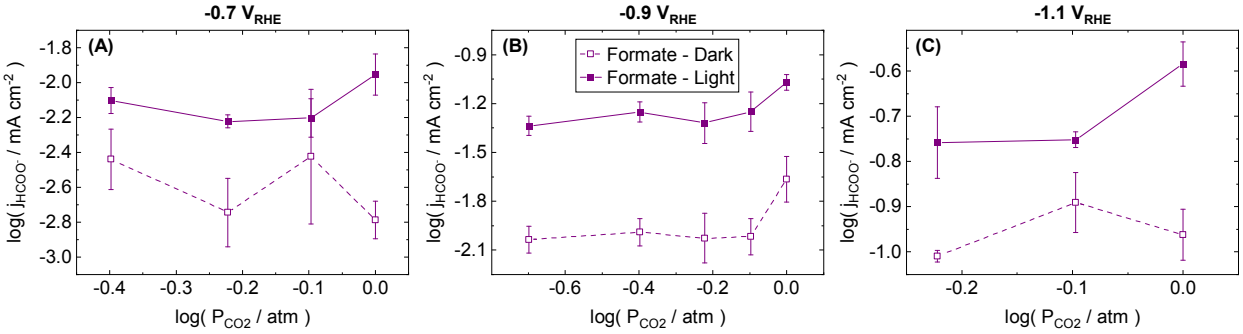

Figure 4.10: Logarithm of formate partial current density (j_{HCOO^-}) vs. logarithm of CO_2 partial pressure (P_{CO_2}) at (A) -0.7, (B) -0.9, and (C) -1.1 V_{RHE} at a silver cathode in CO_2-saturated 1.0 M $KHCO_3$ at 22°C in the dark (dashed lines) and while illuminated with a 365 nm LED at 170 mW cm^{-2} (solid lines). Slopes and R^2 values are tabulated in Table 4.4. All R^2 values are much lower than 0.9. Corresponding Faradaic efficiencies are plotted in Figure 4.25.

As the slopes and R^2 values are quite low, it appears that the production of formate has very

little dependence on P_{CO_2} in the pressure range of 0.2 to 1 atm at this silver cathode. When studying much higher P_{CO_2}, Hara et al. found that the formate Faradaic efficiency increased from 0.8% at 1 atm to 17% at 30 atm at a silver wire in 0.1 M $KHCO_3$ at -0.9 V_{RHE}.[109] Todoroki also found that formate formation increased with P_{CO_2} from 1 to 60 atm at an In electrode in 0.5 M $KHCO_3$ under galvanostatic conditions, reaching nearly 100% Faradaic efficiency by 20 atm.[111] Kyriacou et al. found that the formate Faradaic efficiency increased from 5 to 20% with P_{CO_2} from 0.15 to 1 atm over a Cu foil electrode in 0.5 M $KHCO_3$ at -1.0 V_{RHE}[107] and Hara et al. similarly found that the formate Faradaic efficiency increased from 0.8 to 13.7% from 10 to 60 atm over a Cu wire electrode in 0.1 M $KHCO_3$ at -1.0 V_{RHE}.[108] Chaplin et al. reviewed and tabulated experimental results of CO_2 reduction at 25 different metallic electrodes, summarizing that high CO_2 pressure especially favors formate production and suppresses hydrogen evolution at *sp* metals such as In or tin (Sn).[82] It appears that a formate dependence on P_{CO_2} is observed only at much higher pressures for cathodes with low selectivity towards formate, or at pressures less that 1 atm for catalysts with higher selectivity.

There is no significant difference between the formate trends in the dark and the light at any applied potential; both exhibit what is statistically a zeroth order dependence on P_{CO_2}, which is likely not the true reaction order. However, of the proposed mechanisms for CO_2 reduction to formate, most would result in a reaction order of one with respect to P_{CO_2}[132–134] with one proposed mechanism resulting in second order dependence.[79] In some reaction pathways, CO and formate share the same reaction intermediate[132,134] and in others the pathways are completely distinct,[79,133,134] but both CO and formate are competing for CO_2. As CO production changes significantly with P_{CO_2} and has partial current densities 1–2 orders of magnitude larger than those of formate, it may obscure the actual dependence of formate on P_{CO_2}.

The second liquid product, methanol, was only detected in the light at -0.9 and -1.1 V_{RHE}. The logarithm of the methanol partial current density (j_{CH_3OH}), is plotted against the logarithm of P_{CO_2} in Figure 4.11 and the Faradaic efficiency plots are shown in Figure 4.26. The slopes of the best-fit linear regression curves are shown in Figure 4.11 and the slopes and R^2 values are also tabulated in Table 4.4. The two linear regression curves have R^2 values much lower than 0.9, indicating that the linear fit cannot account for most of the variability in the data.

There are no prior studies of CO_2 reduction at metal electrodes in aqueous electrolyte that explore the dependence of methanol formation on P_{CO_2}. Lais et al. reviewed the research on the photoreduction of CO_2 at TiO_2 and found that methanol formation beginning at 1 atm initially increased with increasing P_{CO_2}, reached an optimal pressure for peak methanol formation (1.2, 1.3, or 10 atm), then decreased at higher pressures.[124] Li et al. studied methanol formation at a Cu disk in an ethanol-water solution of 0.1 M lithium chloride and found that the current increased with increasing P_{CO_2} from 14–54 atm and was independent of P_{CO_2} up to 95 atm.[112] In the pyridine-catalyzed reduction of CO_2 to methanol at a Pt foil in 0.5 M potassium chloride (KCl) both Morris et al. and Rybchenko et al. found that the current increased with increasing P_{CO_2} (1–6 atm and 1–50 atm, respectively).[113,119] While Morris et al. concluded that the rate-determining step for methanol formation was first order with P_{CO_2},[113] Rybchenko et al. determined that the increase in current was not related to

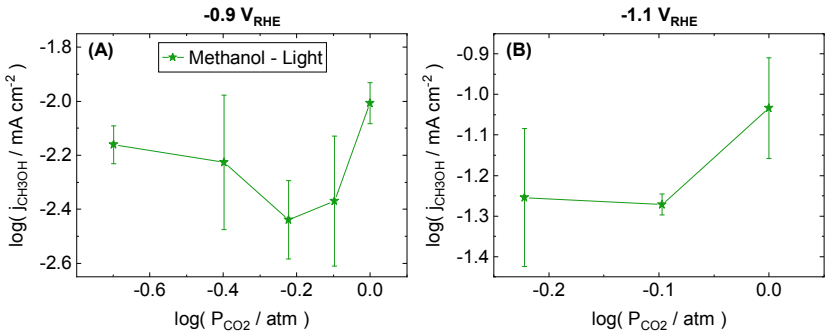

Figure 4.11: Logarithm of methanol partial current density (j_{CH_3OH}) vs. logarithm of CO_2 partial pressure (P_{CO_2}) at (A) -0.9 and (B) -1.1 V_{RHE} at a silver cathode in CO_2-saturated 1.0 M $KHCO_3$ at 22°C while illuminated with a 365 nm LED at 170 mW cm^{-2}. No methanol was measured in the dark at any applied potential and no methanol was measured under illuminated conditions at -0.7 V_{RHE}. Slopes and R^2 values are tabulated in Table 4.4. All R^2 values are less than 0.9. Corresponding Faradaic efficiencies are plotted in Figure 4.26.

methanol formation.[119]

In this study we find no significant dependence of methanol formation in the light with 0.2–1 atm P_{CO_2}. This difference from the previous studies may be due to the lower pressure or because the cathode material and operating conditions are significantly different. While the exact mechanism of CO_2 reduction to methanol on silver is unknown, the reaction pathway is thought to involve either CO or formate as an intermediate.[135] As there are variations in both CO and formate production with P_{CO_2} in the light at -0.9 and -1.1 V_{RHE} and the methanol partial current density is one order of magnitude lower than that of formate and two orders of magnitude lower than that of CO, the true dependence of methanol on P_{CO_2} may be masked.

4.6 Product Distribution Trends with Temperature

Product variations with temperature were studied at 14, 22, and 32°C at 1 atm P_{CO_2} in the dark and the light at -0.7, -0.9, and -1.1 V_{RHE}. Partial current density variations with temperature and applied potential are shown for CO (Figure 4.27), hydrogen (Figure 4.28), formate (Figure 4.29), and methanol (Figure 4.30). These plots correspond with the Faradaic efficiency plots for CO (Figure 4.31), hydrogen (Figure 4.32), formate (Figure 4.33), and methanol (Figure 4.34).

Overall, very little variation was observed between 14 and 22°C for all products, likely reflecting the opposing influences of a decrease in reaction rate with an increase in CO_2 solubility at 14°C. From 22 to 32°C the general trend was a decrease in CO_2 reduction product formation and an increase in hydrogen evolution. This cannot solely be explained by a decrease in CO_2 solubility at 32°C because the selectivity does not match that at 0.8 atm P_{CO_2} where the CO_2 concentration is expected to be similar (Figure 4.35). While there are some differences in temperature trends between the dark and the light, they are difficult to interpret in terms of reaction kinetics due to the changes in selectivity caused by the light

and differences in CO_2 concentration.

If plasmonically generated hot carriers are not extracted from the electrode, their excess energy is transferred to heating of other electrons, the lattice, and eventually the surroundings. SPR can be used to promote reactions by local heating, but the change in selectivity observed in this study cannot be explained by an increase in the local temperature at the cathode surface or heating from the LED. Where CO production was enhanced and hydrogen evolution was suppressed in the light when compared to the dark from -0.6 to -0.8 V_{RHE} (Figure 4.2A and D), the temperature variation results show that at -0.7 V_{RHE} an increase in temperature causes a decrease in CO formation (Figure 4.31) and an increase in hydrogen production (Figure 4.32). While formate was enhanced in the light at most potentials with a maximum difference at -0.9 V_{RHE} (Figure 4.2B and E), we see that formate decreases at elevated temperatures at -0.9 V_{RHE} (Figure 4.33). Finally, where methanol is only produced in the light beginning at -0.8 V_{RHE} (Figure 4.2B and E), we find that an increase in temperature causes methanol production to decrease at both -0.9 and -1.1 V_{RHE} (Figure 4.34). This strongly suggests that localized plasmonic heating is not the source of the observed selectivity changes.

4.7 Photocurrent Measurements

The photocurrent magnitude measured at constant voltage with 3 Hz light modulation (Figure 4.12A) grows with the magnitude of applied cathodic potential (Figure 4.12B), in agreement with previous studies.[51] The maximum photocurrent of 0.62 mA cm^{-2} at -1.1 V_{RHE} represents an internal quantum efficiency of 4% for conversion of 170 mW cm^{-2} of 365 nm light. The difference in photocurrent at -1.1 V_{RHE} reported in Figure 4.12B and the photocurrent observed in Figure 4.12A results from the difference in CO_2 flow between the two measurements, resulting in different mass transport effects; CO_2 is sparged through the cell before the measurement in Figure 4.12A but stopped during data collection to reduce signal noise, whereas CO_2 is bubbled vigorously throughout in Figure 4.12B.

In the potential window of -0.8 to -0.6 V_{RHE} where CO production is plasmonically enhanced, the increase in CO partial current density at each potential (Figure 4.2D) is greater than the photocurrent density at the corresponding potential (Figure 4.12B). The decrease in hydrogen evolution (Figure 4.2D) at these potentials counteracts the promotion of CO, leading to a smaller than expected photocurrent. The rise in soluble product (formate and methanol) formation under illumination accounts for 14–41% of the photocurrent at potentials from -1.1 to -0.9 V_{RHE}. The remainder of the photocurrent likely modifies the production of CO and hydrogen slightly, although this production formation difference is not significant compared to statistical variation between trials. Notably, the difference between the total current density with and without illumination is also only statistically significant from -0.8 to -0.6 V_{RHE} (Figure 4.2F) where the photocurrent represents a relatively large proportion of the total current.

The photocurrent on the silver cathode depends linearly on the incident 365 nm LED illumination intensities (Figure 4.12C), consistent with both an athermal mechanism for the photoactivity and the results shown in Figure 4.4.[70,136] No apparent trends are observed

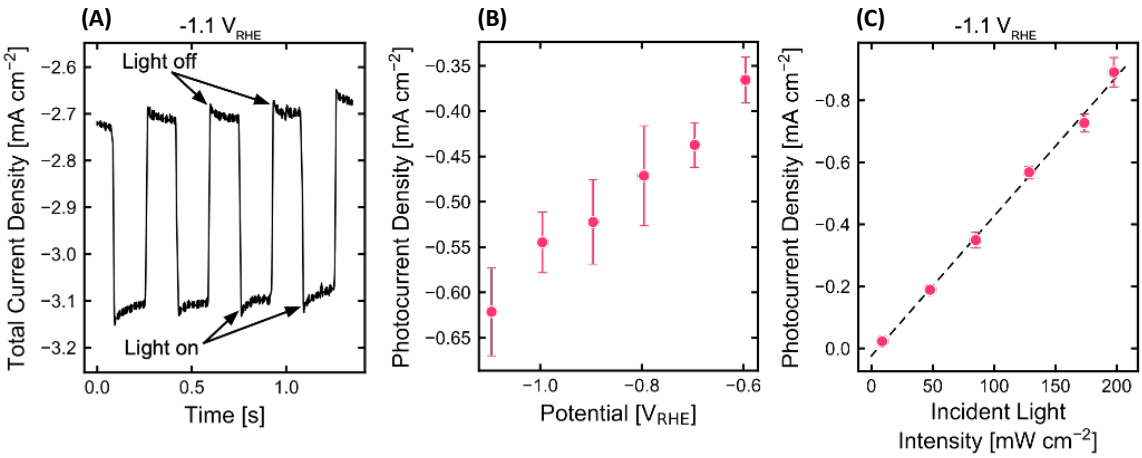

Figure 4.12: Photocurrent on silver cathodes under 170 mW cm^{-2} incident light intensity from a 365 nm LED at 22°C and 100% CO_2 mol fraction. (A) Chopped-light chronoamperometry at -1.1 V_{RHE} over a silver cathode without CO_2 bubbling to decrease the noise in the signal. (B) Photocurrent density at various potentials. (C) Photocurrent density at various light intensities incident on the silver cathode at -1.1 V_{RHE}. The dotted line represents the least-squares regression line. Error bars in each figure represent the standard deviation of experiments performed in triplicate.

in light-intensity-dependent product analysis (Figure 4.20). The difference between the photocurrent reported for 170 mW cm^{-2} illumination with a 365 nm LED in Figure 4.12B and Figure 4.12C is a result of slight experimental variations. The trends shown here are repeatable across all trials.

4.8 Conclusions

In this study, we find that a simple electrochemically conditioned polycrystalline silver thin film exhibits strong plasmonic activity that is selective for three different CO_2 reduction products, depending on the applied potential. The same cathode simultaneously suppresses hydrogen evolution. These combined effects indicate that plasmonics can be used to achieve selectivity in aqueous electrochemical CO_2 reduction. The silver nanostructures that give rise to these effects are not intentionally structured but formed electrochemically under highly cathodic conditions, meaning that the heterogeneous nanostructures are stable for hours at those conditions for product evolution.

We observe that the CO reaction order with P_{CO_2} is first order in both the dark and the light, likely indicating that the rate-determining step is not changed upon illumination. We find that increasing the electrolyte temperature decreases the selectivity for CO_2 reduction products and increases the formation of hydrogen. As these trends are exactly the opposite of what we observe upon illumination, we conclude that the plasmon-induced selectivity changes are not caused by local heating of the cathode surface.

While we continue to search for the plasmonic mechanisms that drive the enhancement of CO_2 reduction to CO, formate, and methanol while suppressing hydrogen evolution at an

illuminated silver cathode, this study has helped to eliminate several possible pathways. Further spectroscopic and computational research is needed to determine the role of the local electric field and the mechanism for hot electron transfer into acceptor molecules. A different nanostructure size or shape distribution to alter the SPR absorption or hot carrier generation could change the CO_2 reduction selectivity or make the plasmonic nanostructure selective for a different reaction altogether. Plasmonic nanostructures likely exhibit potential-dependent activity and selectivity for other electrochemical redox reactions, but we do not know whether all reactions can be catalyzed plasmonically. We will gain further insight into these mechanisms with the development of plasmonic catalysts with improved photon-to-current efficiencies and enhanced selectivities for other complex electrochemical reactions.

4.9 Supplementary Information

Synthesis of Silver Cathodes

3 in. × 1 in. × 1.2 mm glass microscope slides were cleaned by sonication in acetone for 10 minutes followed by oxygen plasma cleaning for 4 min. The catalyst was fabricated by e-beam evaporation of 5 nm of titanium (99.999%) as an adhesion layer on the clean glass slide and 200 nm of silver (99.97%) over the titanium. Silver cathodes were stored in a vacuum chamber after fabrication until use. Except where noted, all silver cathodes were electrochemically conditioned at -1.1 V_{RHE} for 45 min in CO_2-saturated aqueous 1 M $KHCO_3$ before use.

X-Ray Photoelectron Spectroscopy

X-Ray photoelectron spectroscopy (XPS) spectra were collected using a Thermo Scientific K-Alpha XPS System with a monochromated aluminum Kα source. A pass energy of 100 eV was used for survey scans and 20 eV for high resolution scans with an energy resolution of 0.1 eV. Thin film surfaces were cleaned using an argon cluster gun (6000 eV, 150 atoms per cluster) for 60 s before all XPS measurements. XPS spectra show the characteristic silver 3d3/2 and 3d5/2 peaks but do not show any sign of the underlying titanium glass adhesion layer after electrochemical conditioning.

Absorption Measurements

UV-visible total reflection, R, measurements of dry silver cathodes were collected on a Shimadzu SolidSpec-3700 UV-vis-NIR spectrophotometer equipped with an integrating sphere after various electrolysis times in a beaker with CO_2-saturated aqueous 1 M $KHCO_3$ with a platinum wire counter electrode and a Basi MF-2052 silver/silver chloride (Ag/AgCl) reference electrode. Spectra were referenced to a NIST-calibrated mirror, and the calibration was used to find the absolute reflection values. Absorption values reported here are 100% - %R.

Cathode Surface Imaging

SEM images were acquired using a Thermo Scientific Quanta FEG 250 SEM and a 10 kV accelerating voltage.

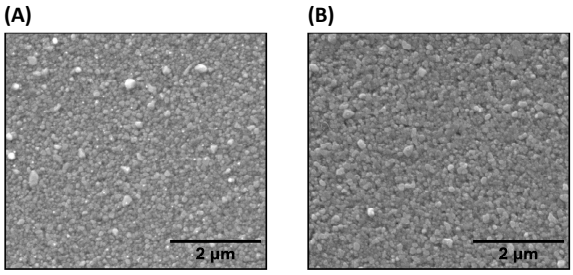

Figure 4.13: Scanning electron micrographs of the thin film silver cathode (A) as-deposited and (B) after biasing at -1.1 V_{RHE} for 45 minutes.

AFM measurements were acquired with a Bruker Dimension Icon commercial AFM system using the PeakForce Quantitative Nanoscale Mechanical tapping mode under ambient conditions. For all topography measurements, uncoated silicon probes (SCANASYST-AIR) with spring constants of 0.4 N m^{-1} were used. Grain size analysis was performed using the watershed algorithm in the Gwyddion software package. The grain location was determined with 100 steps, a drop size of 0.10%, and a threshold of 150 nm^2. Segmentation was determined with 20 steps and a drop size of 15.00%. No additional preparation for AFM was performed on the as-deposited silver cathodes, but cathodes were rinsed profusely in ultrapure water (Millipore, 18 MΩ) and dried with a nitrogen stream after electrochemical conditioning in preparation for AFM measurements.

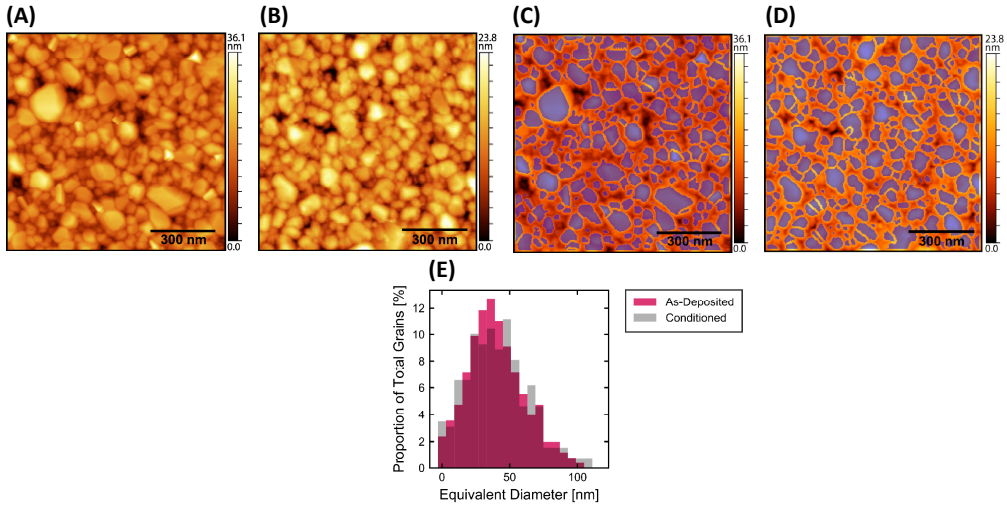

Figure 4.14: Atomic force microscopy (AFM) topographic images of the thin film silver cathode (A) as-deposited and (B) after biasing at -1.1 V_{RHE} for 45 minutes (conditioned). Grains detected by the watershed algorithm (purple) in the AFM image of the cathode (C) as-deposited and (D) conditioned. (E) Comparison of the as-deposited and conditioned grain size distribution on the cathode in terms of equivalent disc diameter, the diameter of the disc with the same projected area as the grain.

Photoelectrochemical Measurements

The electrolyte used in this study was CO_2-saturated aqueous 1 M $KHCO_3$ made by saturating 0.5 M K_2CO_3 (Alfa Aesar, 99.997% metals basis) prepared with ultrapure water (Millipore, 18 MΩ). The electrolyte was sparged with CO_2 for 10 minutes prior to electrolysis. For partial pressure experiments, CO_2 was mixed with argon (Ar) using two mass flow controllers (Alicat, MC-10SCCM-D) to achieve the desired P_{CO_2} at a total flow rate of 5 sccm and total pressure of 1 atm. See Table 4.2 for the electrolyte pH at each P_{CO_2}.

85%-IR-corrected measurements were performed with a Biologic SP-300 potentiostat in a gas-tight polyether ether ketone (PEEK) electrochemical compression cell[43] with Ace Seal 2-015 Kalrez 6375 o-rings exposing 1 cm^2 geometric surface area of the cathode and anode. Impedance spectroscopy from 100 to 1 kHz with 10 mV amplitude at open circuit voltage was used to calculate the IR correction for each measurement. Typical resistances

measured between the working and reference electrodes in our cell fell between 5 and 10 Ω. A temperature control system comprising a Ferrotec 72008/131/150B peltier cooler mounted flush with the backside of the cathode, CPU heat sink with fan, and proportional integral derivative (PID) controller held the catholyte at a constant 22.0 ± 0.1°C. For temperature experiments the catholyte was held at 14.0 ± 0.1°C or 32.0 ± 0.1°C at 1 atm P_{CO_2}.

A Selemion AMV anion exchange membrane separated the catholyte and anolyte. CO_2 was continuously bubbled at 5 sccm through a glass frit at the bottom of the cell unless otherwise noted. Platinum foil was used as the water oxidation anode, and no platinum dissolution or deposition was observed on the silver cathode, as our product Faradaic efficiencies matched those in a previous study.[17] An Innovative Instruments, Inc., LF-1 leak-free Ag/AgCl electrode was used as the potential reference, but all potentials were converted to and reported versus the reversible hydrogen electrode. The overpotential (η) for the CO evolution reaction was calculated using the theoretical potential (E_T = -0.10 V)[2] and the applied potential (E), where $\eta = E_T - E$. Cyclic voltammograms were performed in Ar- or CO_2-saturated 0.5 M K_2CO_3 or 0.5 M $NaClO_4$ at a sweep rate of 100 mV s^{-1}. The cathodic sweep of the 10th cycle, representative of any cycle, is plotted in Figure 4.3 and Figure 4.15.

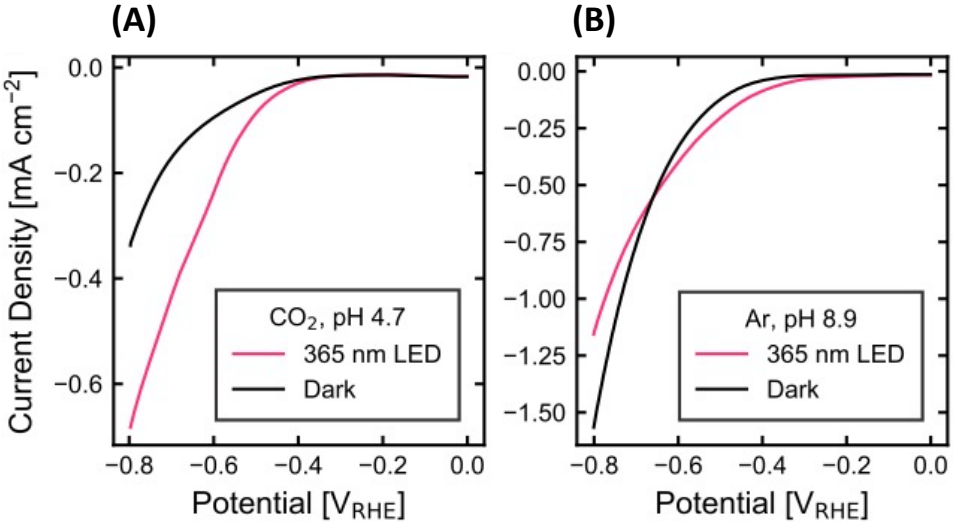

Figure 4.15: Cathodic voltage sweep at 100 mV s^{-1} over an illuminated and dark silver cathode in (A) 100% CO_2- and (B) 100% Ar-saturated 0.5 M $NaClO_4$ under 365 nm LED light at 170 mW cm^{-2} at 22°C. The voltage ranges were selected to ensure no silver oxidation occurred at the anodic limit and to include all potentials where a photoeffect is observed for CO and hydrogen in CO_2-saturated K_2CO_3 at the cathodic limit.

The cathode was illuminated from the front using a LCS-0365-48-22 Mightex Systems 365 nm ultra-high-power LED. While the output power of the LED was 2.5 W, only 170 mW reached the surface of the cathode due to the size of the cell window, absorption of the electrolyte, and scattering by the CO_2 bubbles. The light intensity incident on the cathode was determined by measuring the transmission of light through the photoelectrochemical cell with electrolyte, CO_2 bubbles, and a glass slide in place of the thin film silver cathode then corrected for the 91.1% transmission of 365 nm light through the glass slide. The electrolyte was saturated, but the CO_2 bubbling was turned off for the example chopped-light chronoamperometry

plot (Figure 4.12A) to minimize noise in the signal. The output light intensity for only that measurement was decreased to maintain an incident light intensity of 170 mW cm^{-2}. Wavelength-dependent measurements were performed at equal incident photon flux (3.2 × 10^{17} photons cm^{-2} s^{-1}) to the 365 nm LED using Mightex Systems LCS-0405-50-22, LCS-0470-50-22, and LCS-0525-60-22 LEDs at 405, 470, and 525 nm, respectively. The emission spectra of the LEDs provided by the manufacturer are included as Figure 4.17. The output and incident power were measured with a Coherent PowerMax PM10 power meter connected to a Coherent LabMax-TOP power meter console. Photocurrent was extracted from 3 Hz chopped-light chronoamperometry measurements using a SRI SR850 lock-in amplifier and a ThorLabs SHB1 shutter system.

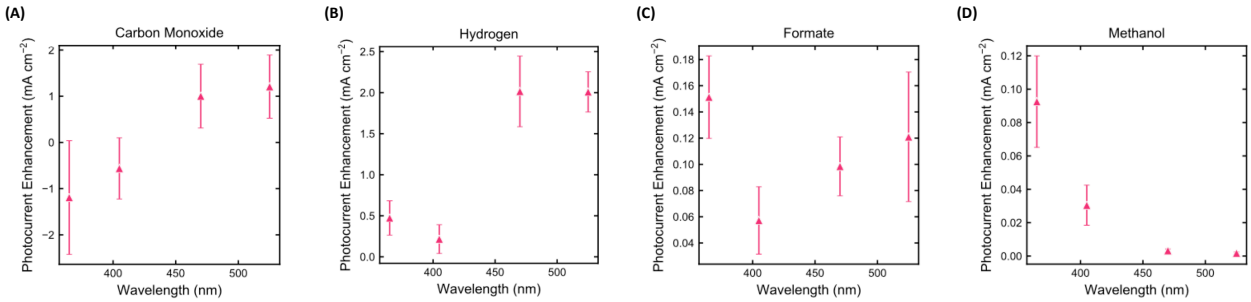

Figure 4.16: Difference between the partial current density of each product under 3.2 × 10^{17} photons cm^{-2} s^{-1} illumination of various wavelengths and in dark conditions at -1.1 V_{RHE} at 22°C and 100% CO_2 mol fraction. (A) Carbon monoxide, (B) hydrogen, (C) formate, and (D) methanol.

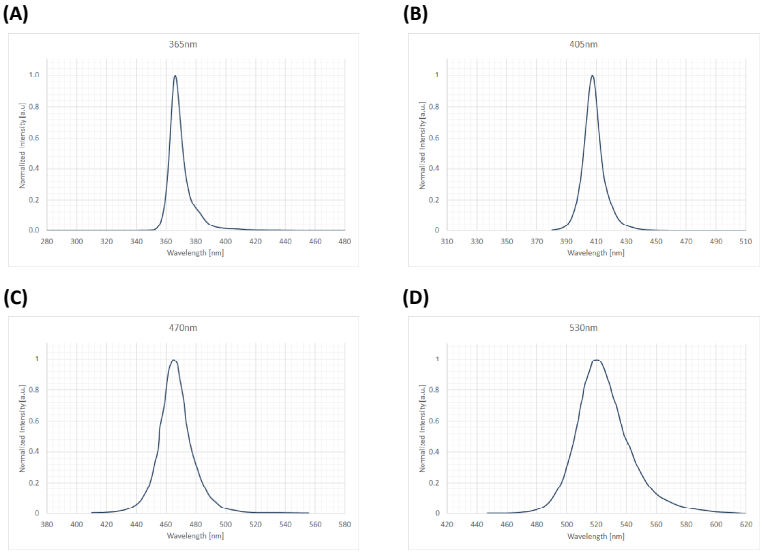

Figure 4.17: Emission spectra of the ultra-high-power Mightex Systems LEDs used in this study provided by Mightex. (A) 365 nm LED (LCS-0365-48)-22, (B) 405 nm LED (LCS-0405-50-22), (C) 470 nm LED (LCS-0470-50-22), and (D) 525 nm LED (LCS-0525-60-22).

Linear Sweep Voltammetry

Linear sweep voltammetry (LSV) was performed at 5 mV s^{-1} from the open circuit potential (OCV) to -1.1 V_{RHE}. Figure 4.18 shows the LSV results in the dark and the light across the range of CO_2 mol fractions used in this study. Corresponding Tafel plots are shown in Figure 4.5. Overlays of dark and light Tafel plots at 100% CO_2 mol fraction are shown in Figure 4.6 and at all CO_2 mol fractions are shown in Figure 4.22.

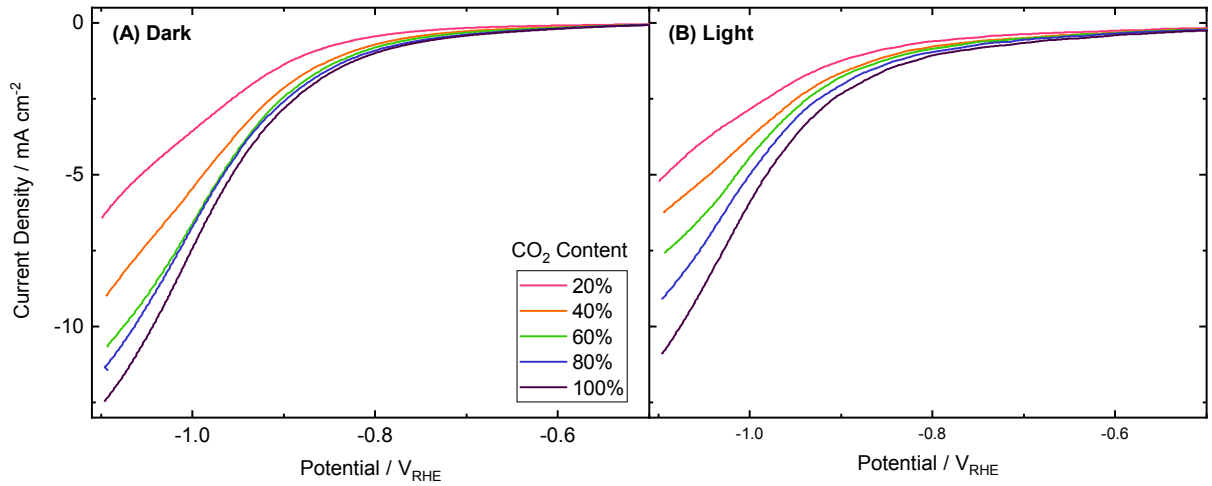

Figure 4.18: Total current density vs. potential at various CO_2 mol fractions during linear sweep voltammetry at 5 mV s^{-1} at a silver electrode in CO_2-saturated 1.0 M $KHCO_3$ at 22°C (A) in the dark and (B) while illuminated with a 365 nm LED at 170 mW cm^{-2}. The legend in (A) applies to both (A) and (B). Corresponding Tafel plots are shown in Figure 4.5. Overlays of dark and light Tafel plots at 100% CO_2 mol fraction are shown in Figure 4.6 and at all CO_2 mol fractions are shown in Figure 4.22.

The onset potentials and inflection points were determined from a second derivative analysis of the total current density. The total current density at each P_{CO_2} in the dark and the light was smoothed with a Butterworth filter and the second derivative was calculated numerically. The onset potentials in the dark and the onset potentials and inflection points in the light were found from the most prominent peak(s) in the second derivative and are tabulated in Table 4.1. Examples of this analysis are plotted in Figure 4.19.

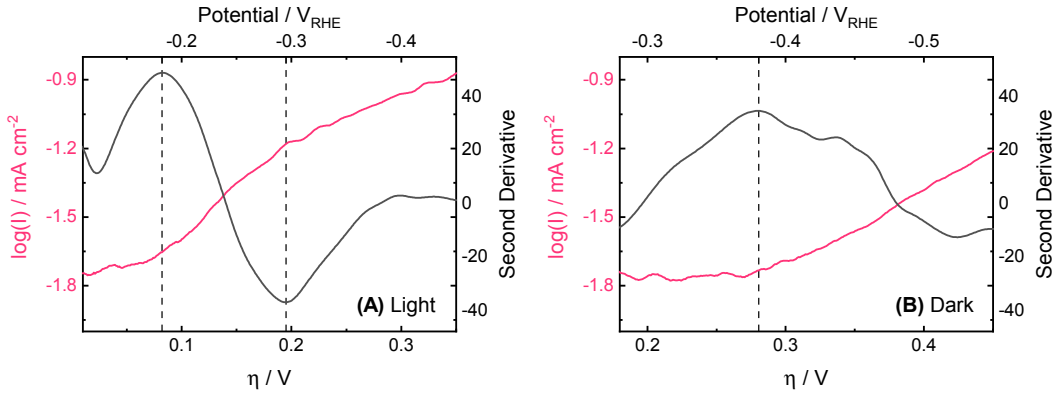

Figure 4.19: Total current density (pink, left ordinate) vs. overpotential (η, bottom axis) and potential (top axis) at 20% CO_2 mol fraction during linear sweep voltammetry at 5 mV s^{-1} at a silver electrode in CO_2-saturated 1.0 M $KHCO_3$ at 22°C (A) while illuminated with a 365 nm LED at 170 mW cm^{-2} and (B) in the dark. The onset potentials and inflection point are indicated with black dashed lines, as determined from the second derivative of the total current density (black, right ordinate). Corresponding total current density vs. potential plots are shown in Figure 4.18. Corresponding Tafel plots are shown in Figure 4.5. Overlays of dark and light Tafel plots at 100% CO_2 mol fraction are shown in Figure 4.6 and at all CO_2 mol fractions are shown in Figure 4.22.

Table 4.1: Onset potentials and inflection points found from the second derivative of the total current density at each P_{CO_2}.

	Dark	Light	
P_{CO_2} [atm]	Onset Potential, V_{RHE}	Onset Potential, V_{RHE}	Inflection Point, V_{RHE}
1	-0.406	-0.186	-0.296
0.8	-0.397	-0.189	-0.303
0.6	-0.398	-0.196	-0.303
0.4	-0.402	-0.182	-0.296
0.2	-0.380	-0.182	-0.295
Average	**-0.40 ± 0.010**	**-0.19 ± 0.006**	**-0.30 ± 0.004**

CO_2 Reduction Product Measurements

Gaseous products of the electrochemical reactions were analyzed by an in-line SRI Instruments Multiple Gas Analyzer #5 GC equipped with a 12 ft HayeSep D (divinylbenzene) column, thermal conductivity detector (TCD), flame ionization detector (FID) with methanizer, and argon carrier gas. The detection limit of the GC is 1 ppm. For a single product analysis run, a constant potential was applied for 64 min with GC injections at 3, 15, 27, 39, 51, and 63 minutes. Gas in the headspace and gas line to the GC does not equilibrate by the three minute injection, so the average concentration from only the last five cycles was used in calculations of product generation. The concentration of the gas in each injection was computed from calibration curves with at least three points for each gas type. The partial current density, j_x, for each gaseous product, x, in each GC injection is given by

$$j_x = \frac{\mathrm{F} c_x n f}{m a} \tag{4.3}$$

where F is Faraday's constant (96485 C mol^{-1} of electrons), c_x is the concentration of product x as a molecular fraction of the total injected gas, n is the number of electrons needed to produce product x (2 mol of electrons per mol of hydrogen or carbon monoxide), f is the flow rate of CO_2 into the electrochemical cell (5 cm^3 min^{-1} or 8.333×10^{-5} L s^{-1} in this study), m is the the molar volume of CO_2 at 21°C (24.01 L mol^{-1} from the National Institute of Standards and Technology (NIST) WebBook), and a is the geometric surface area of the cathode (1 cm^2 in this study). We assume that the evolved gases have similar molar volumes as CO_2. The Faradaic efficiency (FE) of a product is given by

$$\mathrm{FE} = \frac{j_x}{j} \tag{4.4}$$

where j is the average total current density measured by the potentiostat over the five minutes before the GC injection. The average values for current density and faradaic efficiency over the last five injections are reported here.

Liquid products in the catholyte and anolyte were quantified after the electrolysis was complete by ^{1}H NMR spectroscopy on a Bruker Avance III 500 MHz magnet using phenol and dimethylsulfoxide (DMSO) as internal standards and a water suppression method with 60 s between pulses to allow for complete proton relaxation.[2,43] The detection limit of the NMR is 1 ppb. Each product analysis experiment was performed three times on different days with a new electrode used each day. Error bars represent one standard deviation of experiments performed in triplicate.

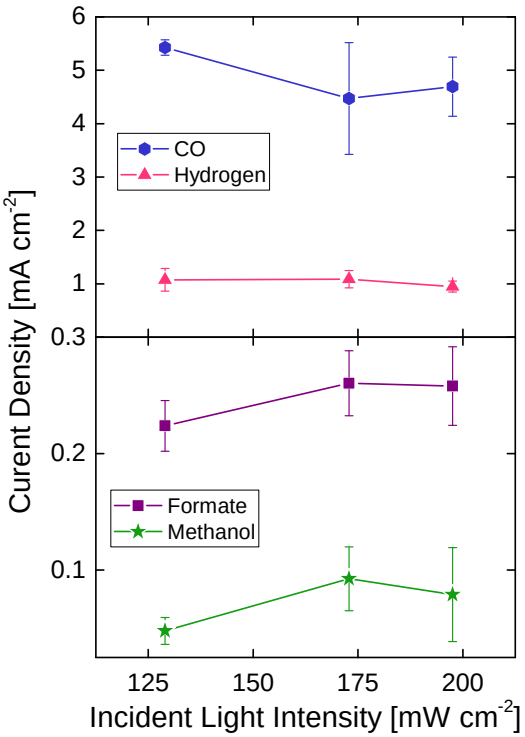

Figure 4.20: Partial current density for each product at -1.1 V_{RHE} under 365 nm LED illumination of various incident light intensities at 22°C and 100%
chCO2 mol fraction. Error bars represent the standard deviation of experiments performed in triplicate.

Electrochemical Surface Area Measurements

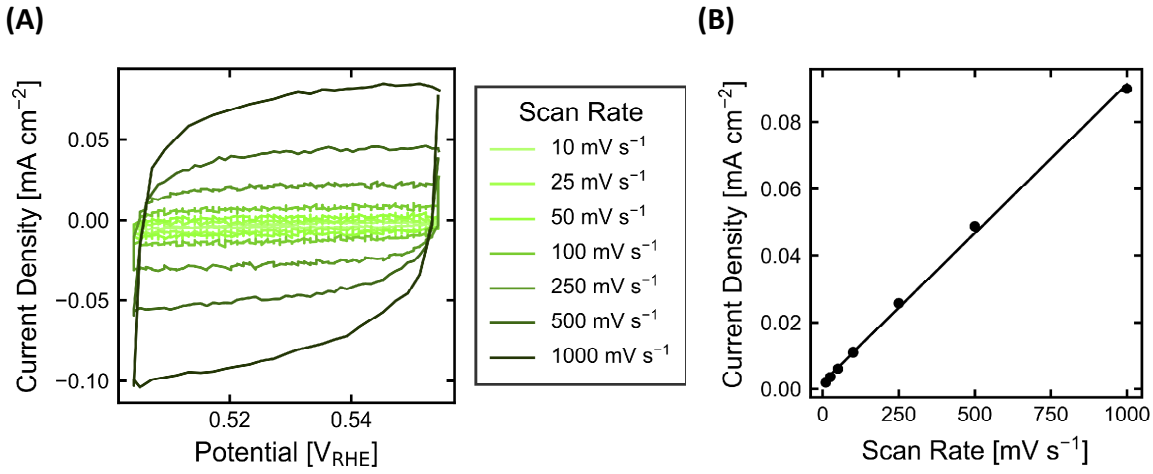

Figure 4.21: Relative electrochemical surface area (ECSA) measurement by capacitive cycling measurements on a silver cathode. (A) Capacitive cycles over a 50 mV non-Faradaic region at a series of rapid scan rates after 0 minutes of electrolysis. Only the third cycle for each scan rate is shown here. (B) Capacitive current for a series of scan rates after 0 minutes of electrolysis where the slope of the best-fit line gives the capacitance.

The ECSA of electrochemically conditioned cathodes was determined relative to the as-e-beam-evaporated cathode by taking the ratio of their double layer capacitances as measured by the cyclic linear potential sweep method.[137] First, the non-Faradaic charging current in CVs was measured at a series of increasingly rapid scan rates (Figure 4.21A). A Savitzky-Golay filter was used to smooth the CV data in Figure 4.21A, but the raw data was used in the determination of the charging current. The charging current was taken as half of the difference between the average current between 0.544 and 0.549 V_{RHE} in the anodic direction and the average current between 0.509 and 0.514 V_{RHE} in the cathodic direction on the third CV cycle. The capacitance is the slope of the best-fit line of the charging current versus scan rate (Figure 4.21B). The capacitance was measured for the same cathode after various electrolysis times. Each measured capacitance was normalized to the capacitance of the as-deposited cathode for the relative ECSA (Figure 4.1D).

Electrolyte pH

The electrolyte pH varies with the partial pressure of CO_2 (P_{CO_2}). Table 4.2 shows the pH as measured at each P_{CO_2} used in this study.

Table 4.2: The pH of CO_2-saturated 1.0 M $KHCO_3$ at various CO_2 partial pressures (P_{CO_2}).

P_{CO_2} [atm]	CO_2 mol fraction [%]	pH
1	100	7.75
0.8	80	7.75
0.6	60	7.96
0.4	40	8.29
0.2	20	8.54

Tafel Slopes

Table 4.3 shows Tafel slopes at various P_{CO_2} in the dark and the light. Tafel slopes are calculated from an overpotential of 280 to 450 mV (-0.38 to -0.55 V_{RHE}) in the dark using the total current densities. In this region the product concentration is too low for reliable gaseous product quantification in our constant gas flow cell. As both hydrogen and CO may form in the Tafel region in the dark we cannot reliably extract the CO partial current density.

Tafel slopes are calculated from an overpotential of 100 to 160 mV (-0.20 to -0.26 V_{RHE}) in the light using the total current densities. From previous work[36] we can conclude that the linear region in the light before the inflection point at -0.3 V_{RHE} is related solely to CO production. The overpotential referenced is for the CO evolution reaction. These slopes correspond to the Tafel plots of the total current density shown in Figure 4.5, Figure 4.6, and Figure 4.22.

Table 4.3: Tafel slopes calculated from an overpotential of 280 to 450 mV (-0.38 to -0.55 V_{RHE}) in the dark and from an overpotential of 100 to 160 mV (-0.20 to -0.26 V_{RHE}) in the light at various P_{CO_2}. Tafel plots of the total current density are shown in Figure 4.5, Figure 4.6, and Figure 4.22.

	Dark		Light	
P_{CO_2} [atm]	Slope, mV dec^{-1}	R^2	Slope, mV dec^{-1}	R^2
1	215	*0.993*	169	*0.998*
0.8	230	*0.991*	178	*0.994*
0.6	241	*0.992*	183	*0.995*
0.4	258	*0.993*	197	*0.995*
0.2	307	*0.993*	201	*0.996*

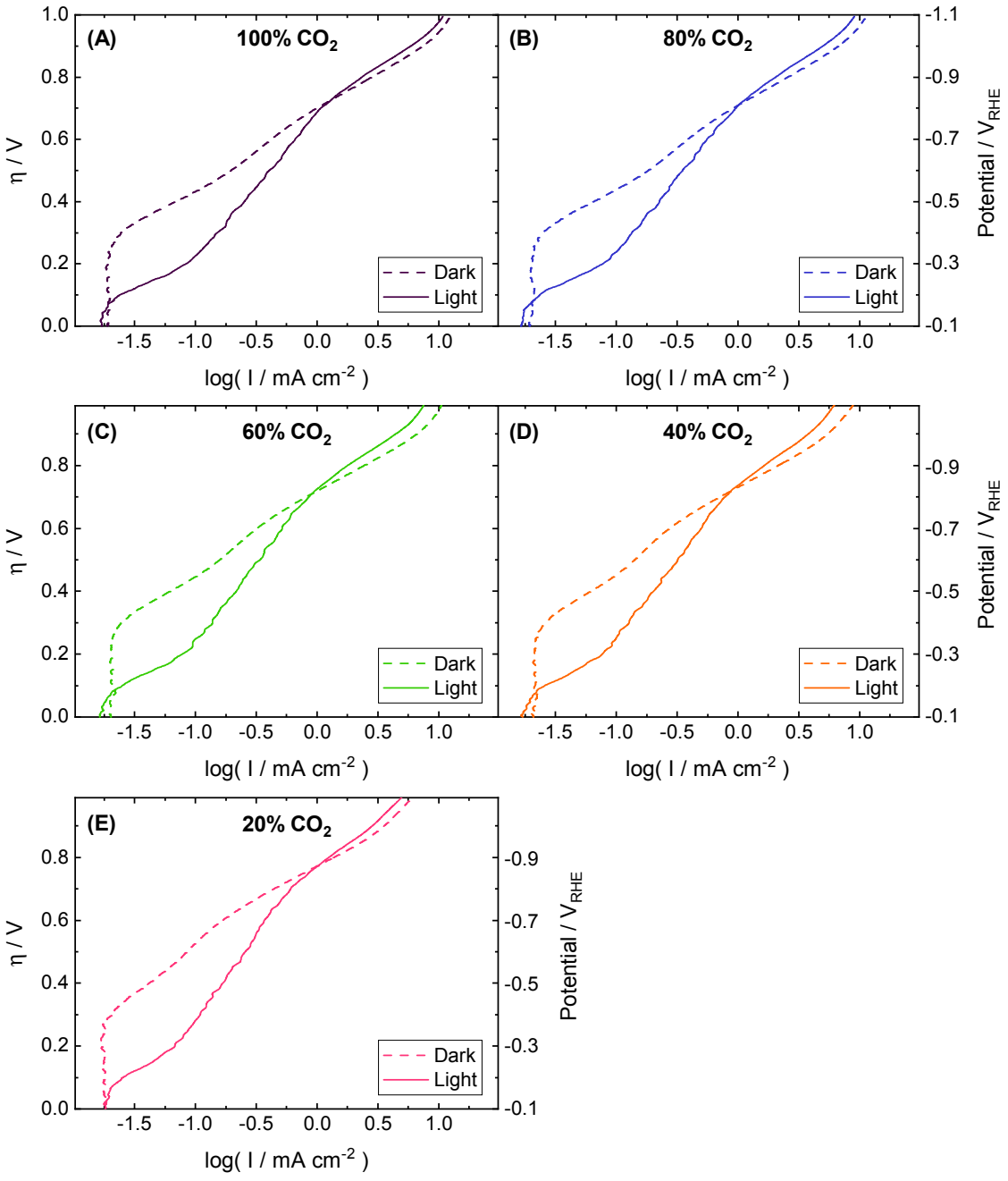

Figure 4.22: Tafel plots of the total current density at (A) 100%, (B) 80%, (C) 60%, (D) 40%, and (E) 20% CO_2 mol fraction during linear sweep voltammetry at 5 mV s^{-1} at a silver electrode in CO_2-saturated 1.0 M $KHCO_3$ at 22°C in the dark (dashed lines) and while illuminated with a 365 nm LED at 170 mW cm^{-2} (solid lines). The overpotential (η) is shown for the CO evolution reaction. The 100% CO_2 mol fraction Tafel plot is also shown in Figure 4.6. Separate dark and light Tafel plots are shown in Figure 4.5 and corresponding total current density vs. potential plots are shown in Figure 4.18.

P_{CO_2} Reaction Order

Table 4.4 shows the slopes and R^2 values of the best-fit linear regression curves of the logarithm of the partial current density vs. logarithm of CO_2 partial pressure (P_{CO_2}) plots of carbon monoxide (CO) (Figure 4.7), hydrogen (H_2) (Figure 4.8), formate (Figure 4.10), and methanol (Figure 4.11). These slopes correspond to the reaction order of the given product with respect to P_{CO_2}.

Table 4.4: Slopes and R^2 values of the best-fit linear regression curves of the logarithm of the partial current density vs. logarithm of CO_2 partial pressure (P_{CO_2}) plots of carbon monoxide (Figure 4.7), hydrogen (Figure 4.8), formate (Figure 4.10), and methanol (Figure 4.11). No methanol was measured in the dark at any applied potential and no methanol was measured under illuminated conditions at -0.7 V_{RHE}.

	-0.7 V_{RHE}		-0.9 V_{RHE}		-1.1 V_{RHE}	
	Dark	Light	Dark	Light	Dark	Light
Carbon Monoxide						
Slope	0.62	0.71	0.73	0.79	0.86	0.67
R^2	*0.80*	*0.64*	*0.88*	*0.96*	*0.99*	*0.96*
Hydrogen						
Slope	-0.39	-0.58	-0.19	-0.51	-2.77	-2.29
R^2	*0.30*	*0.93*	*0.43*	*0.94*	*0.92*	*0.75*
Formate						
Slope	-0.54	0.26	0.34	0.27	0.25	0.75
R^2	*0.23*	*0.14*	*0.35*	*0.51*	*0.21*	*0.71*
Methanol						
Slope	–	–	–	-0.02	–	0.94
R^2	–	–	–	*0.00*	–	*0.62*

Faradaic Efficiency

Faradaic efficiency variations with P_{CO_2} and applied potential are shown for CO (Figure 4.23), hydrogen (Figure 4.24), formate (Figure 4.25), and methanol (Figure 4.26). These plots correspond with the partial current density plots for CO (Figure 4.7), hydrogen (Figure 4.8), formate (Figure 4.10), and methanol (Figure 4.11).

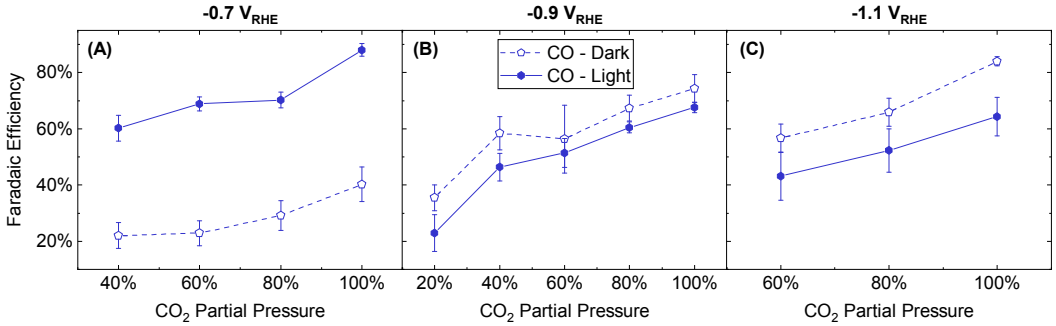

Figure 4.23: Carbon monoxide Faradaic efficiency vs. CO_2 partial pressure (P_{CO_2}) at (A) -0.7, (B) -0.9, and (C) -1.1 V_{RHE} in CO_2-saturated 1.0 M $KHCO_3$ at 22°C in the dark (dashed lines) and while illuminated with a 365 nm LED at 170 mW cm^{-2} (solid lines). Error bars represent one standard deviation of experiments performed in triplicate. Corresponding partial current densities are plotted in Figure 4.7.

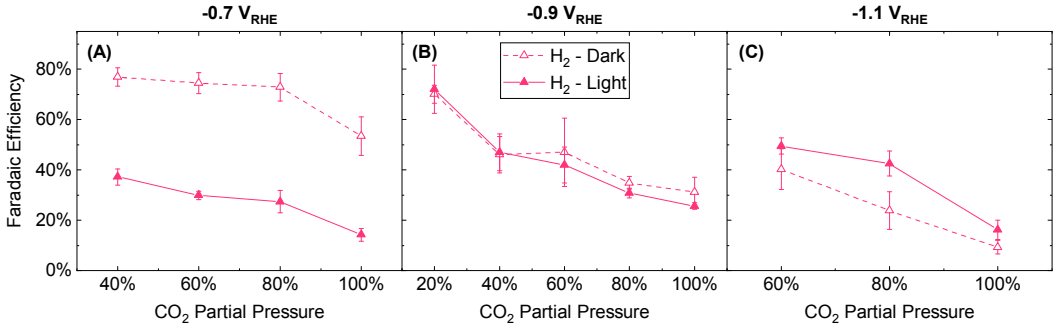

Figure 4.24: Hydrogen Faradaic efficiency vs. CO_2 partial pressure (P_{CO_2}) at (A) -0.7, (B) -0.9, and (C) -1.1 V_{RHE} in CO_2-saturated 1.0 M $KHCO_3$ at 22°C in the dark (dashed lines) and while illuminated with a 365 nm LED at 170 mW cm^{-2} (solid lines). Error bars represent one standard deviation of experiments performed in triplicate. Corresponding partial current densities are plotted in Figure 4.8.

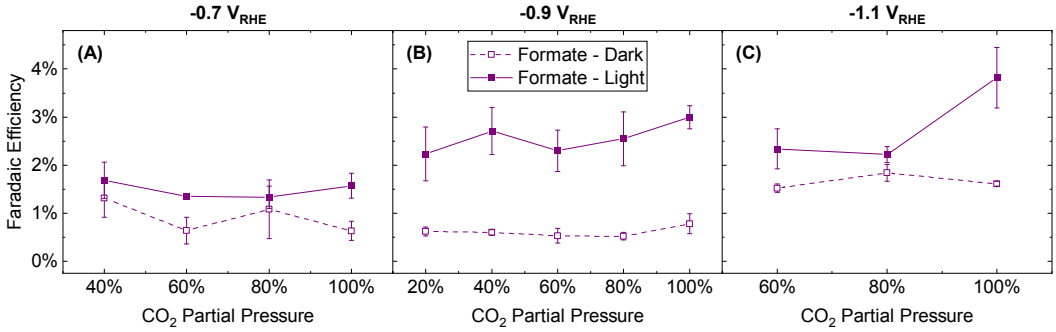

Figure 4.25: Formate Faradaic efficiency vs. CO_2 partial pressure (P_{CO_2}) at (A) -0.7, (B) -0.9, and (C) -1.1 V_{RHE} in CO_2-saturated 1.0 M $KHCO_3$ at 22°C in the dark (dashed lines) and while illuminated with a 365 nm LED at 170 mW cm^{-2} (solid lines). Error bars represent one standard deviation of experiments performed in triplicate. Corresponding partial current densities are plotted in Figure 4.10.

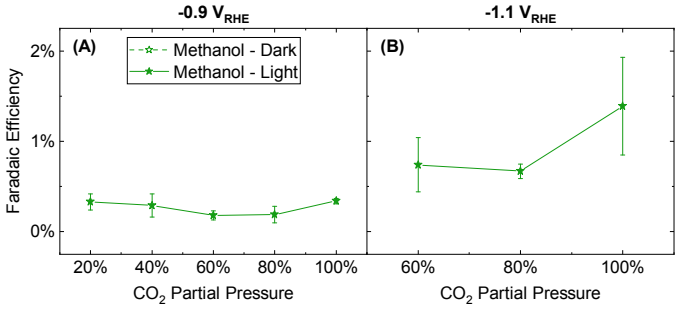

Figure 4.26: Methanol Faradaic efficiency vs. CO_2 partial pressure (P_{CO_2}) at (A) -0.9 and (B) -1.1 V_{RHE} in CO_2-saturated 1.0 M $KHCO_3$ at 22°C while illuminated with a 365 nm LED at 170 mW cm^{-2}. No methanol was measured in the dark at any applied potential and no methanol was measured under illuminated conditions at -0.7 V_{RHE}. Error bars represent one standard deviation of experiments performed in triplicate. Corresponding partial current densities are plotted in Figure 4.11.

Temperature Trends

Temperature-dependent product analysis experiments were performed at 100% CO_2 mol fraction at 14, 22, and 32°C at -0.7, -0.9, and -1.1 V_{RHE}. The partial current density and Faradaic efficiency trends for CO with temperature are shown in Figure 4.27 and Figure 4.31. At -0.7 V_{RHE}, j_{CO} and the CO Faradaic efficiency in the dark did not change with temperature, but in the light the j_{CO} and Faradaic efficiency went through a maximum at 22°C. At -0.9 and -1.1 V_{RHE} there was no significant change in the j_{CO} with temperature. However, at -0.9 V_{RHE} the CO Faradaic efficiency decreased at 32°C in the light but did not change in the dark, and at -1.1 V_{RHE} the CO Faradaic efficiency at 32°C decreased in the both the dark and the light.

Plots of the partial current density and Faradaic efficiency vs. temperature for hydrogen are shown in Figure 4.28 and Figure 4.32. j_{H_2} increased at 32°C at all applied potentials in both the dark and the light. The Faradaic efficiency of hydrogen increased at 32°C in the light at -0.7 V_{RHE} but showed no change in the dark while at -0.9 V_{RHE} the Faradaic efficiency increased at 32°C in the dark but showed no change in the light. At -1.1 V_{RHE} the Faradaic efficiency increased at 32°C in both the dark and the light.

The partial current density and Faradaic efficiency trends for formate with temperature are shown in Figure 4.29 and Figure 4.33. The j_{HCOO^-} at -0.7 V_{RHE} increased slightly at 32°C in the dark with no significant change in the Faradaic efficiency, but the j_{HCOO^-} and Faradaic efficiency decreased slightly at 32°C in the light. At -0.9 V_{RHE} there was no significant change in the j_{HCOO^-} or Faradaic efficiency with temperature in the dark, but in the light there was a slight decrease in both at 32°C. At -1.1 V_{RHE} the j_{HCOO^-} increased at 32°C in both the dark and the light while no change was observed in the Faradaic efficiency.

Methanol partial current density and Faradaic efficiency plots vs. temperature in the light are shown in Figure 4.30 and Figure 4.34. At -0.9 V_{RHE} there was no change in j_{CH3OHO} with temperature but the Faradaic efficiency went through a maximum at 22°C. At -1.1 V_{RHE} the j_{CH3OHO} and Faradaic efficiency decreased at 32°C.

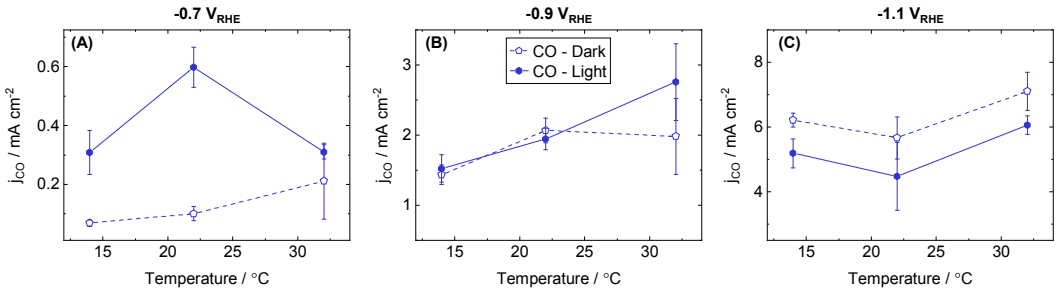

Figure 4.27: Carbon monoxide partial current density (j_{CO}) vs. temperature at 100% CO_2 mol fraction at (A) -0.7, (B) -0.9, and (C) -1.1 V_{RHE} in CO_2-saturated 1.0 M $KHCO_3$ in the dark (dashed lines) and while illuminated with a 365 nm LED at 170 mW cm^{-2} (solid lines). Error bars represent one standard deviation of experiments performed in triplicate. Corresponding Faradaic efficiencies are plotted in Figure 4.31.

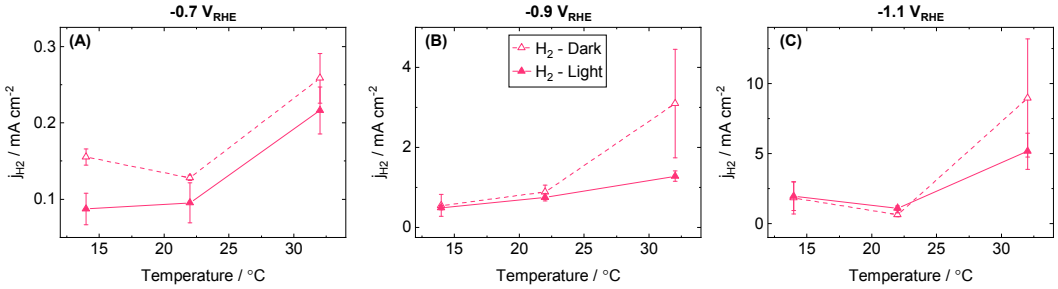

Figure 4.28: Hydrogen partial current density (j_{H_2}) vs. temperature at 100% CO_2 mol fraction at (A) -0.7, (B) -0.9, and (C) -1.1 V_{RHE} in CO_2-saturated 1.0 M $KHCO_3$ in the dark (dashed lines) and while illuminated with a 365 nm LED at 170 mW cm^{-2} (solid lines). Error bars represent one standard deviation of experiments performed in triplicate. Corresponding Faradaic efficiencies are plotted in Figure 4.32.

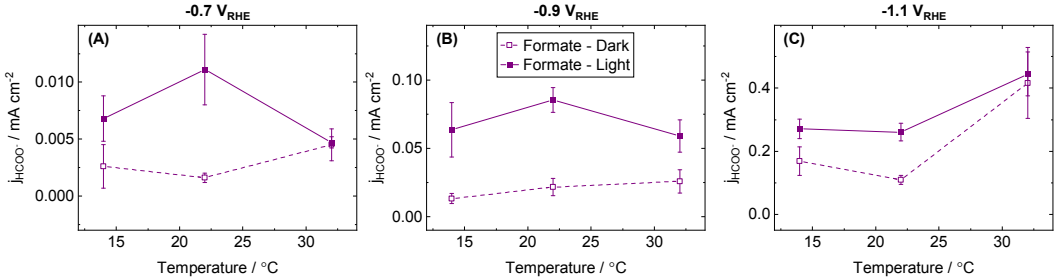

Figure 4.29: Formate partial current density (j_{HCOO^-}) vs. temperature at 100% CO_2 mol fraction at (A) -0.7, (B) -0.9, and (C) -1.1 V_{RHE} in CO_2-saturated 1.0 M $KHCO_3$ in the dark (dashed lines) and while illuminated with a 365 nm LED at 170 mW cm^{-2} (solid lines). Error bars represent one standard deviation of experiments performed in triplicate. Corresponding Faradaic efficiencies are plotted in Figure 4.33.

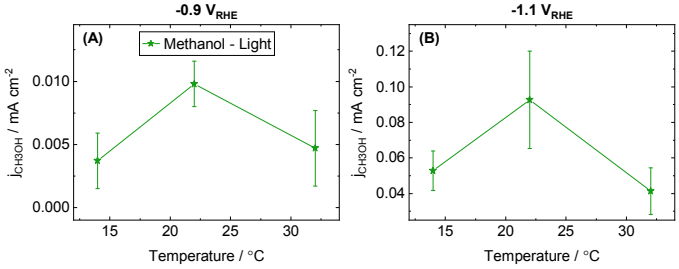

Figure 4.30: Methanol partial current density vs. temperature at 100% CO_2 mol fraction at (A) -0.9 and (B) -1.1 V_{RHE} in CO_2-saturated 1.0 M $KHCO_3$ while illuminated with a 365 nm LED at 170 mW cm^{-2}. No methanol was measured in the dark at any applied potential and no methanol was measured under illuminated conditions at -0.7 V_{RHE}. Error bars represent one standard deviation of experiments performed in triplicate. Corresponding Faradaic efficiencies are plotted in Figure 4.34.

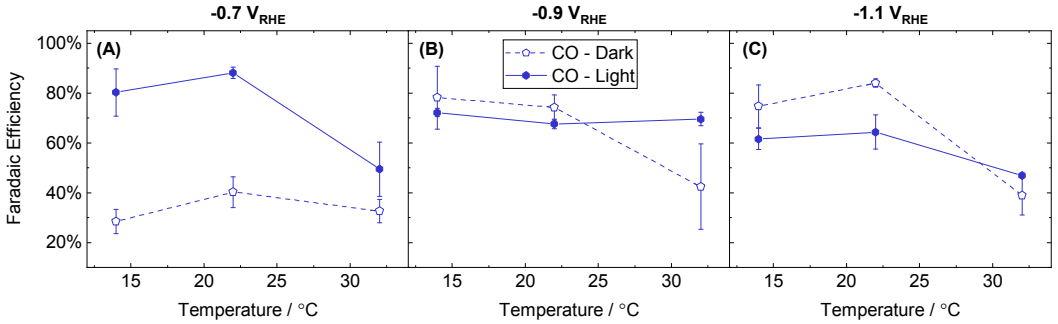

Figure 4.31: Carbon monoxide Faradaic efficiency vs. temperature at 100% CO_2 mol fraction at (A) -0.7, (B) -0.9, and (C) -1.1 V_{RHE} in CO_2-saturated 1.0 M $KHCO_3$ in the dark (dashed lines) and while illuminated with a 365 nm LED at 170 mW cm^{-2} (solid lines). Error bars represent one standard deviation of experiments performed in triplicate. Corresponding partial current densities are plotted in Figure 4.27.

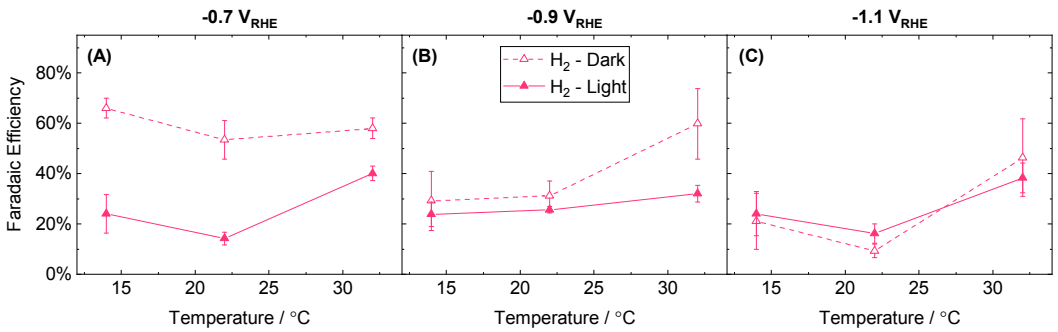

Figure 4.32: Hydrogen Faradaic efficiency vs. temperature at 100% CO_2 mol fraction at (A) -0.7, (B) -0.9, and (C) -1.1 V_{RHE} in CO_2-saturated 1.0 M $KHCO_3$ in the dark (dashed lines) and while illuminated with a 365 nm LED at 170 mW cm^{-2} (solid lines). Error bars represent one standard deviation of experiments performed in triplicate. Corresponding partial current densities are plotted in Figure 4.28.

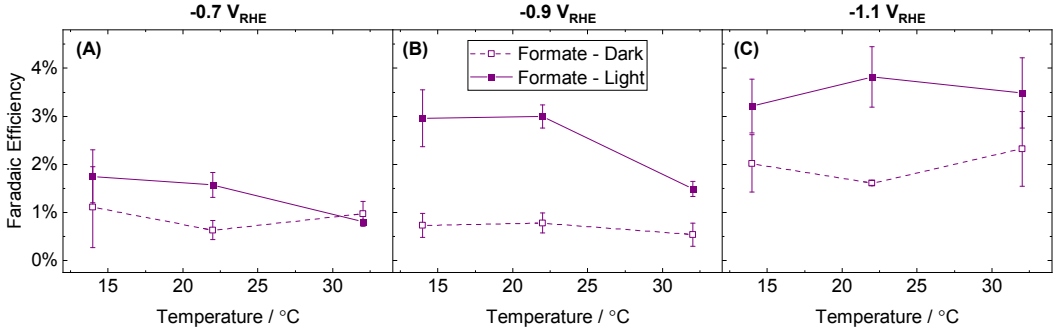

Figure 4.33: Formate Faradaic efficiency vs. temperature at 100% CO_2 mol fraction at (A) -0.7, (B) -0.9, and (C) -1.1 V_{RHE} in CO_2-saturated 1.0 M $KHCO_3$ in the dark (dashed lines) and while illuminated with a 365 nm LED at 170 mW cm^{-2} (solid lines). Error bars represent one standard deviation of experiments performed in triplicate. Corresponding partial current densities are plotted in Figure 4.29.

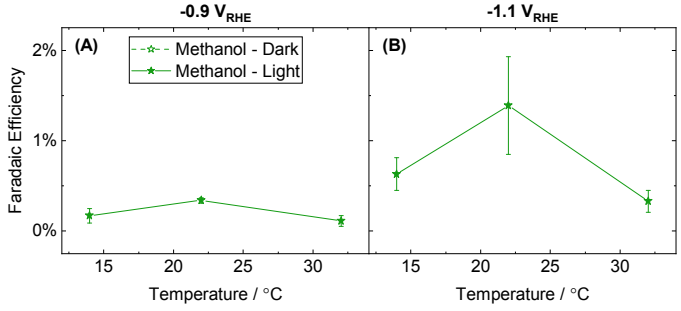

Figure 4.34: Methanol Faradaic efficiency vs. temperature at 100% CO_2 mol fraction at (A) -0.9 and (B) -1.1 V_{RHE} in CO_2-saturated 1.0 M $KHCO_3$ while illuminated with a 365 nm LED at 170 mW cm^{-2}. No methanol was measured in the dark at any applied potential and no methanol was measured under illuminated conditions at -0.7 V_{RHE}. Error bars represent one standard deviation of experiments performed in triplicate. Corresponding partial current densities are plotted in Figure 4.30.

Electrolyte CO_2 Concentration

The CO_2 concentration in the electrolyte varies with P_{CO_2} and with temperature. The approximate CO_2 concentration was calculated at a given temperature and pressure using Henry's law and parameters from the NIST Chemistry WebBook for CO_2 solubility in water. Figure 4.35 shows the approximate CO_2 concentration calculated at each P_{CO_2} and temperature used in this study.

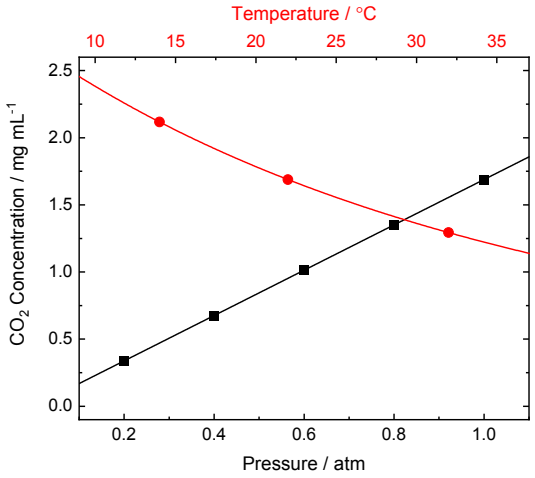

Figure 4.35: Calculated CO_2 concentration in water with CO_2 partial pressure (P_{CO_2}, black, bottom axis) and with temperature (red, top axis). Pressure values were calculated at 22°C and temperature values were calculated at 1 atm P_{CO_2}. Black data points indicate the P_{CO_2} used in this study and red data points indicate the electrolyte temperatures used in this study.

Chapter 5
In Situ ATR–SEIRAS of Carbon Dioxide Reduction at a Plasmonic Silver Cathode[§]

5.1 Abstract

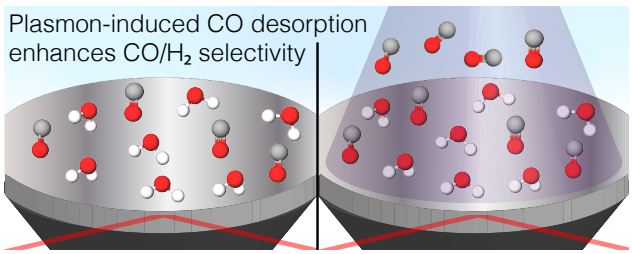

Illumination of a voltage-biased plasmonic Ag cathode during CO_2 reduction results in a suppression of the H_2 evolution reaction while enhancing CO_2 reduction. This effect has been shown to be photonic rather than thermal, but the exact plasmonic mechanism is unknown. Here, we conduct an in situ ATR–SEIRAS study of a sputtered thin film Ag cathode on a Ge ATR crystal in CO_2-saturated 0.1 M $KHCO_3$ over a range of potentials in both dark and illuminated (365 nm, 125 mW cm^{-2}) conditions to elucidate the nature of this plasmonic enhancement. We find that the onset potential of CO_2 reduction to adsorbed CO on the Ag surface is -0.25 V_{RHE} and is identical in the light and the dark. As the production of gaseous CO is detected in the light near this onset potential but is not observed in the dark until -0.5 V_{RHE}, we conclude that the light must be assisting the desorption of CO from the surface. Furthermore, the HCO_3^- wavenumber and peak area increase immediately upon illumination, precluding a thermal effect. We propose that the enhanced local electric field that results from the localized surface plasmon resonance (LSPR) is strengthening the HCO_3^- bond, further increasing the local pH. This would account for the decrease of H_2 formation and increase of CO_2 reduction products in the light.

5.2 Introduction

Electrochemical carbon dioxide (CO_2) reduction creates chemicals and fuels from electricity, water, and CO_2 that would have otherwise been released to the atmosphere. By using renewable electricity, the process can be carbon-neutral, replacing thermochemical methods that consume fossil fuels. To be cost-competitive, we need CO_2 electrocatalysts that can operate at low overpotentials and have high selectivity.[3] We have approached this challenge through plasmon-enhanced electrochemical conversion (PEEC).

PEEC is the application of potential to a plasmonically active electrode while illuminating the surface to impact the electrocatalytic performance. PEEC has been shown to impact

[§]This chapter was originally published in the *Journal of the American Chemical Society* and is adapted with permission from co-authors R. Kas, R. Kostecki, J. J. Urban, W. A. Smith, B. D. McCloskey, and R. Kortlever.[138] Copyright 2020 American Chemical Society.

the product distribution and decrease overpotentials for CO_2 reduction,[36,51] oxygen (O_2) reduction,[13,37] and hydrogen (H_2) evolution.[14,38,39] While these effects have been shown to be photonic in nature, it is difficult to pinpoint the exact plasmonic mechanism.

In this study, we use in situ ATR–SEIRAS (attenuated total reflectance–surface-enhanced infrared absorption spectroscopy) to understand how the electric double layer (EDL) structure changes with applied potential, time, and illumination and how this impacts CO_2 reduction at a plasmonic Ag cathode. In previous work, we demonstrated that a plasmonic Ag cathode showed significant differences in the product distribution and overpotential during CO_2 reduction in the dark and under 365 nm LED illumination, which was near the plasmon resonance peak for the Ag electrode (351 nm).[36] At low overpotentials, carbon monoxide (CO) production was enhanced and H_2 evolution was suppressed upon illumination. In addition, the onset potential for CO production appeared to be reduced by 300 mV in the light compared to the dark. Formate production was enhanced in the light at potentials more cathodic than –0.7 V_{RHE}, and methanol was formed only under illuminated conditions at potentials more cathodic than –0.8 V_{RHE}, reaching a maximum Faradaic efficiency (FE) of nearly 2% at -1.1 V_{RHE}.[36] This represents a 550 mV decrease in the overpotential and a 100-fold increase in selectivity for methanol production when compared to the CO_2 reduction results reported by Hatsukade et al. on a polycrystalline Ag foil in the dark.[17]

Studies have been published on infrared (IR) spectroscopy during electrochemical CO_2 reduction in aqueous electrolytes on cathodes such as Ag[139,140], Au[141], and Cu[139,142–144] with a review of recent work presented by Kas et al.,[145] although none have explored PEEC combined with in situ IR spectroscopy measurements. In fact, only a handful of studies have used IR spectroscopy to study photocatalytic reactions at illuminated catalysts, including aqueous photoreduction of O_2,[146] the photooxidation of water,[147,148] and the photooxidation of glyoxylic acid.[149] Here, we use ATR–SEIRAS to provide new insights into the potential-dependent structure of the EDL at a negatively biased Ag cathode in an aqueous electrolyte and present further clues into the possible mechanism of plasmon-enhanced electrochemical CO_2 reduction.

5.3 Experimental Methods

Cathode Fabrication

To prepare the cathode, a 60° Ge ATR crystal (Pike Technologies, 013-3132) was polished three times with subsequently smaller-diameter alumina suspensions of 1.0, 0.3, and 0.05 μm (Buehler, 40-10081, 40-10082, and 40-10083) using microcloth pads (BASi, MF-1040). The crystal surface was cleaned with water and acetone using lint-free wipes and dried with compressed nitrogen. The crystal was placed in a Faraday cage and subjected to air plasma for 8 minutes on high power (Harrick Plasma, PDC-002-CE). A 40 nm film of Ag was deposited on the crystal surface in a custom-built sputtering tool with an argon (Ar) pressure of 50 μbar, deposition rate of 0.01455 nm s^{-1}, and a substrate rotation of 15° s^{-1}. After deposition, the resistance across the surface of the cathode was typically 4–8 Ω, as measured by a multimeter. A schematic of the cathode is shown in Figure 5.8.

Cathode Surface Imaging and Profiling

Scanning electron microscopy (SEM) images were taken with a Thermo Scientific Quanta FEG 250 SEM. Atomic force microscopy (AFM) measurements were performed with a commercial AFM system (Bruker Dimension Icon) using the PeakForce quantitative nanoscale mechanical tapping mode under ambient conditions. X-ray photoelectron spectroscopy (XPS) measurements were acquired with a Thermo Scientific K-Alpha XPS.

In Situ ATR–SEIRAS Measurements

SEIRAS experiments were performed in a custom single-chamber electrochemical cell (Figure 5.7).[145] A 0.05 M solution of potassium carbonate (K_2CO_3) (Alfa Aesar, 10838, 99.997% metals basis) was prepared with 18.2 MΩ deionized water from a Millipore system, which became 0.1 M potassium bicarbonate ($KHCO_3$) when saturated with CO_2. The anode was a graphite rod (Alfa Aesar, 40766, 99.9995% metals basis), and the reference electrode was Ag/AgCl with 3 M NaCl (BASI, MF-2052). All potentials were converted to and reported versus the reversible hydrogen electrode (RHE). All electrochemical measurements were IR- corrected and performed with a Biologic SP-200 potentiostat. CO_2 flowed through the electrolyte for 30 minutes before the start of an experiment and continued flowing throughout the experiment. Additionally, the ATR attachment and the chamber surrounding it were purged with nitrogen (N_2) for 30 minutes before the start of an experiment. Before use, the cathode surface was activated by three cyclic voltammetry (CV) scans at 50 mV s^{-1} (Figure 5.9) from –0.50 to approximately 0.70 V_{RHE}. The anodic potential was adjusted to keep the current density below 0.80 mA cm^{-2} to prevent film degradation.

SEIRAS spectra reported during CV were an average of 32 spectra taken at a resolution of 8 cm^{-1}. A new background spectrum (Figure 5.16) was taken for each experiment during chronoamperometry (CA) at 0.2 V_{RHE} before continuing to the CV from 0.2 to –0.9 V_{RHE} at 2 mV s^{-1}. The negative logarithm of the ratio between the single-beam sample spectrum (R) and the single-beam background spectrum (R_0) gives the absorbance (A) spectrum of the sample in absorbance units (a.u.): $A = -\log(R/R_0)$. The return scan continued to potentials more anodic than 0.2 V_{RHE} and was stopped when the SEIRAS spectrum was as close to the baseline as possible. See Figure 5.17 for representative SEIRAS spectra from 0.2 to 0.6 V_{RHE}.

SEIRAS spectra reported during CA were an average of 32 spectra taken at a resolution of 8 cm^{-1} or, if designated as "high-resolution", an average of 72 spectra taken at a resolution of 4 cm^{-1}. A new background spectrum was taken for each experiment during CA at 0.2 V_{RHE} before continuing to the applied potential of the CA experiment. After 90 seconds of CA, a linear voltammetry sweep (LSV) was performed at 5 mV s^{-1} to an anodic potential where the SEIRAS spectrum was as close to the baseline as possible.

Photoelectrochemical Measurements

The electrode was illuminated through the center port of the cell using a Mightex Systems LCS-0365-48-22 365 nm ultra-high-power LED. During illuminated SEIRAS experiments, the light intensity at the surface of the cathode was 125 mW cm^{-2}. During illuminated product analysis experiments, the light intensity at the surface of the cathode was 170 mW cm^{-2}.

The incident power was measured with a Coherent PowerMax PM10 power meter connected to a Coherent LabMax-TOP power meter console.

Product Measurements

Experiments for product analysis were performed in a custom cell described by Corson et al.[43] Gaseous products were analyzed by an in-line Multiple Gas Analyzer #5 SRI Instruments GC with a 12 ft HayeSep D (divinylbenzene) column, thermal conductivity detector (TCD), flame ionization detector (FID) preceded by a methanizer, and Ar carrier gas. For a single product analysis run, a constant potential was applied for 16 minutes with GC injections at 3 and 15 minutes. The results from the 15 minute injection are reported here. Gaseous product concentrations were calculated from a calibration curve of at least three different concentrations for each gas type. Liquid products in the catholyte and anolyte were quantified after the electrolysis was complete by ^{1}H NMR spectroscopy on a Bruker Avance III 500 MHz magnet. Liquid product concentrations were determined by using phenol and DMSO as internal standards.[2] Complete details on the GC and NMR calibration and quantification methods are reported in Corson et al.[43]

5.4 Cathode Fabrication

The cathode fabrication method was optimized to synthesize a Ag thin film that both enhanced the SEIRAS signal while remaining stable and intact during (photo)electrochemical experiments. The preparation of Ag films for ATR–SEIRAS using vacuum evaporation, chemical deposition, and Ar sputtering has previously been reported.[150,151] Our cathode fabrication method was guided by prior studies that showed how the sputtered Ag thin film morphology was influenced by changes in the deposition rate, sputtering pressure, substrate temperature, sputtering gas, and film thickness.[151–153]

Sputtering thin films of Ag at 3 μbar of Ar pressure on bare Ge or Si ATR crystals resulted in films with limited SEIRAS signal that delaminated quickly. A thin (0.5–3 nm) Ti adhesion layer deposited on the Ge or Si crystal before depositing the Ag layer produced extremely stable cathodes; however, these displayed no SEIRAS signal. To improve adhesion via an alternate route, the crystal was cleaned with air plasma before deposition. To enhance the SEIRAS signal, the sputtering pressure was increased to 50 μbar, which decreases the mean-free path length of the sputtered atoms. This results in collisions and agglomeration of the Ag atoms before deposition, producing a rougher surface.[152] This technique created a Ag film on a Ge crystal that was both stable and SEIRAS-active, but the Ag film on a Si crystal remained unstable.

However, the SEIRAS activity of the Ag film on a Ge crystal was still not sufficient. Figure 5.10 shows an example of SEIRAS spectra collected during a CV scan on an as-deposited Ag cathode prepared using the optimized deposition method. Spectroscopic peaks are observed, but they are small and deformed. To further enhance the SEIRAS signal, the surface was activated by three CV scans. A representative CV curve is shown in Figure 5.9. SEM and AFM images (Figure 5.11 and Figure 5.12) before and after activation show that the surface is further roughened by this CV cycling. Larger grains (75–150 nm) are formed on the

surface, and the grain size distribution of the Ag film increases after activation, expanding the population of both small and large features. The AFM root-mean-square (RMS) roughness increases from 3.7 nm on the as-deposited film to 5.6 nm on the activated film.

XPS measurements taken on the as-deposited cathode (after sputtering) show Ag to be the predominant component (Figure 5.13). There are small peaks for Ge and the environmental contaminants of O and C. Extremely small Cu peaks were resolved only by focusing on the region for Cu $2p_{1/2}$ and Cu $2p_{3/2}$ and increasing the acquisition time. XPS measurements of the same cathode after activation by CV cycling show an increase in the Ge peaks and a reduction in the Cu peaks to a signal that is barely distinguishable from the noise. The source of this trace Cu contamination is believed to be from the sputtering chamber. Complete removal of the Cu was verified by gaseous and liquid product analysis at –0.60, –0.75, and –0.80 V_{RHE} for Ag cathodes sputtered under the same conditions on glass slides with a 3 nm Ti adhesion layer. The FE and partial current densities shown in Figure 5.14 and Figure 5.15 for H_2, CO, and formate under dark and illuminated conditions closely match the results we reported for an e-beam-deposited Ag cathode.[36] If any Cu were present, then we would expect to detect methane, ethylene, and ethanol in this potential range.[2] Any Ge on the surface is not expected to influence the SEIRAS results because Ge is not an active catalyst for CO_2 reduction, a bare Ge crystal showed no peaks during a CV scan under otherwise identical electrochemical conditions, and it has been shown that CO does not adsorb to a Ge ATR crystal.[154]

SEIRAS spectra from an activated Ag cathode (Figure 5.1) show multiple distinct peaks. The SEIRAS signal could be further enhanced by more aggressive CV cycling, but the film stability would be greatly diminished. The activation method described above resulted in a Ag film that could withstand hours of successive (photo)electrochemical experiments at modest applied potentials. CV scans could be performed up to –0.9 V_{RHE}, and CA experiments could be run up to –0.7 V_{RHE} without film delamination. The cathode was visually inspected after each experiment to confirm that the film was intact. A new cathode was prepared each day.

5.5 Peak Assignment

In Figure 5.1A the system is first held at 0.2 V_{RHE}, close to the open circuit voltage (OCV), to measure the background spectrum (Figure 5.16). At OCV, we expect that there are no CO_2 reduction products adsorbed on the Ag surface because no CO_2 reduction has occurred. Because the OCV is approximately 300 mV above the potential of zero charge (pzc) for Ag, we expect the surface to have a slightly positive charge that will influence the orientation of the water molecules.[155,156] The concentration of components in the bulk electrolyte is $[H_2O] \gg [K^+] > [HCO_3^-] > [CO_2] > [CO_3^{2-}] > [H^+] > [OH^-]$. The concentration of components in the EDL at OCV is expected to be similar to that of the bulk, but with a somewhat higher representation of negatively charged species due to the slightly positive surface charge of the electrode. The potential is scanned cathodically at 2 mV s^{-1} to -0.9 V_{RHE} with a new SEIRAS spectrum taken every 10 seconds. Peaks that appear in the spectra represent changes in the concentration or orientation of surface and near-surface species with respect to the OCV baseline. "Near-surface" species are those in the 5–10 nm region that can be detected by ATR–SEIRAS, with stronger signals coming from molecules closest to the

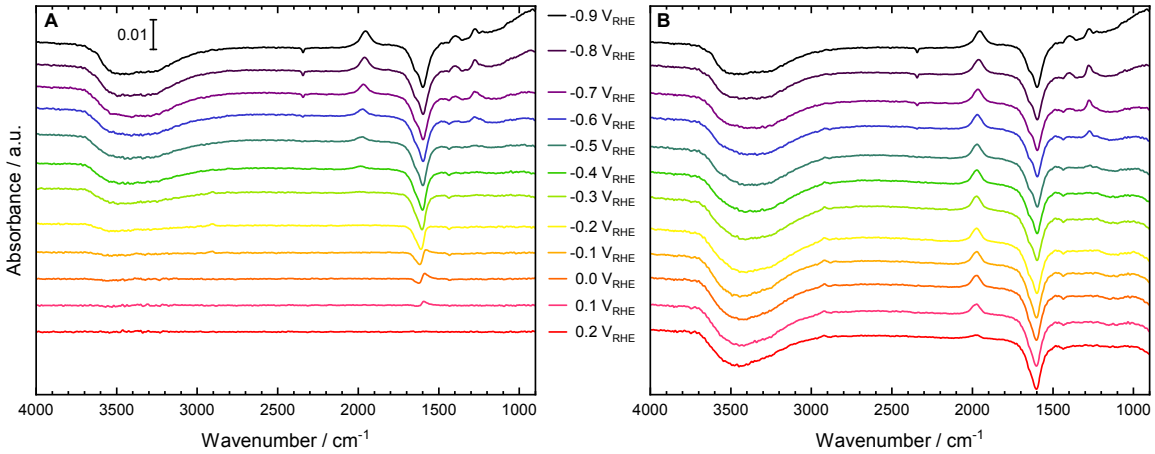

Figure 5.1: SEIRAS spectra taken during a CV scan at 2 mV s^{-1}. (A) shows the cathodic scan from 0.2 to -0.9 V_{RHE} and (B) shows the anodic scan from -0.9 to 0.2 V_{RHE}. The activated Ag cathode on a Ge ATR crystal was in a 0.1 M $KHCO_3$ electrolyte with a continuous CO_2 purge through the electrolyte. The background spectrum was taken at 0.2 V_{RHE}. The scale bar in (A) gives the y-axis scale in absorbance units (a.u.) and applies to both (A) and (B). The peaks are HCO_3^- (1278 cm^{-1}), CO_3^{2-} (1395 cm^{-1}), δ^{HOH} (1600 cm^{-1}), CO (1970 cm^{-1}), CO_2 (2342 cm^{-1}), and ν^{OH} (3402 cm^{-1}).

surface due to the strength of the evanescent IR wave.[141] Water peaks signify changes in the orientation of water molecules, which will be discussed more extensively in the Water Bend and Stretch section.[155,157] Positive peaks corresponding to other species represent an increase in concentration at or near the surface, and negative peaks indicate a decrease in concentration at or near the surface.

At 0.1 V_{RHE}, a peak appears at 1597–1623 cm^{-1} that is attributed to the HOH bend vibration (δ^{HOH}).[139,140,157,158] From 0.1 to -0.1 V_{RHE} the δ^{HOH} feature comprises a positive and negative component, with the positive part disappearing at -0.2 V_{RHE}. At this same time, a broad negative peak is observed at 3351–3520 cm^{-1} that is assigned to the O−H stretch absorption (ν^{OH}).[139,156–158] By -0.4 V_{RHE}, we observe a single positive peak at 1962–1981 cm^{-1} which is attributed to CO that has formed from the reduction of CO_2 and is adsorbed on the surface.[139,159] Finally, by -0.7 V_{RHE} we see the three remaining peaks observed in this study: a positive HCO_3^- peak at 1276–1279 cm^{-1}, a positive CO_3^{2-} peak at 1393–1401 cm^{-1}, and a negative CO_2 peak at 2342 cm^{-1}.[140,141,158] The average position of each peak and the corresponding standard deviation are listed in Table 2.1; they are calculated from five CV scans performed during different experiments with newly prepared cathodes.

The anodic scan from -0.9 to 0.2 V_{RHE} is shown in Figure 5.1B. The peaks for HCO_3^-, CO_3^{2-}, and CO_2 disappear near the same potential of their appearance. The remaining peaks, however, display extreme hysteresis in the anodic scan; the peaks for CO, δ^{HOH}, and ν^{OH} remain at 0.2 V_{RHE}. The average values of the potential when each peak appears and disappears are shown in Figure 5.2 along with the cyclic voltammogram corresponding to Figure 5.1. The tabulated values and standard deviations are shown in Table 5.2.

We will discuss what these trends imply for the behavior of each species in the following

Table 5.1: Average SEIRAS peak positions. Average values and standard deviations are calculated from five CV experiments performed on different days with a new cathode prepared each day.

Peak	**Average Position** (cm^{-1})
Bicarbonate (HCO_3^-)	1278 ± 1.9
Carbonate (CO_3^{2-})	1395 ± 3.8
Water Bend (δ^{HOH})	1600 ± 1.1
CO	1970 ± 2.7
CO_2	2342 ± 0.0
Water Stretch (ν^{OH})	3402 ± 22.6

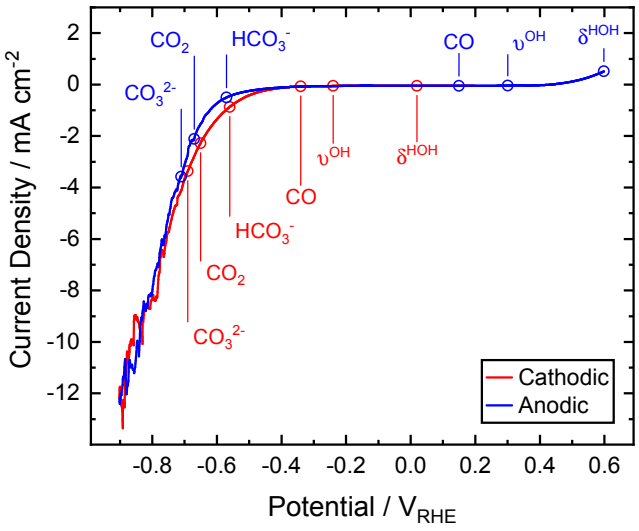

Figure 5.2: Cyclic voltammogram (CV) of a Ag cathode in a 0.1 M $KHCO_3$ electrolyte recorded at a scan rate of 2 mV s^{-1} corresponding to the spectra displayed in Figure 5.1. The average potential of the appearance of each SEIRAS peak is marked (red circles) as the potential is scanned from 0.2 to −0.9 V_{RHE} (cathodic scan). The average potential of the disappearance of each SEIRAS peak is marked (blue circles) as the potential is scanned from −0.9 to 0.6 V_{RHE} (anodic scan). Average values are calculated from five CV experiments performed on different days with a new cathode prepared each day.

sections, but it is apparent that scanning the potential back to the OCV is not sufficient for returning the cathode surface and the EDL to their initial states. If, after an electrochemical experiment, the system is simply returned to OCV before beginning the next experiment, the SEIRAS peak trends may appear to be quite different. This is a result of the adsorbates formed during the previous experiment remaining on the surface and the different EDL structure. In this study, the surface was "reset" back to the initial conditions after every experiment by continuing to scan to more anodic potentials. Figure 5.17 shows the SEIRAS spectra from 0.2 to 0.6 V_{RHE}. Adsorbed CO is completely removed from the surface by 0.3

V_{RHE}, and the δ^{HOH} and ν^{OH} peaks cross the baseline and become positive around 0.4 V_{RHE}. The δ^{HOH} peak goes from a negative peak, to overlapping positive and negative peaks, to a positive peak during this anodic scan, similar to the behavior observed at the beginning of the cathodic scan from 0.1 to −0.1 V_{RHE}. As these two water-related peaks flip from positive to negative at different potentials, there is no potential where the original baseline is achieved. For every experiment presented in this study, the anodic scan was stopped when the SEIRAS spectrum was as close to the baseline as possible.

The cathode surface can also be reset by letting the system equilibrate at OCV. Figure 5.20 shows the SEIRAS spectra during 30 minutes of OCV, and Figure 5.4 shows the corresponding normalized peak areas. While CO desorbs from the surface after 10 minutes, the δ^{HOH} and ν^{OH} peaks continue to change. Eventually, these peaks will become positive and reach a steady state that is distinct from the initial baseline recorded under OCV conditions, but it could take as long as two hours in this particular electrochemical cell with a continuous purge of CO_2 through the electrolyte for convection. The time for stabilization during OCV is likely highly dependent on the geometry of the cell and the degree of electrolyte mixing. That the final steady-state EDL structure is different from the initial conditions may reflect subtle changes in the cathode surface resulting from the electrochemical experiment.

In the next sections, we will discuss the significance of the trends presented here as well as the differences observed during measurements in the dark and in the light. A more detailed analysis of the trends during cathodic and anodic CV scans is shown in Figure 5.3, where the average peak positions and normalized areas for the CO, δ^{HOH}, and ν^{OH} peaks are plotted. Similar plots for HCO_3^-, CO_3^{2-}, and CO_2 peaks are shown in Figure 5.19.

5.6 Carbon Monoxide

In this study, the CO signal appears as a single positive peak whose position ranges from 1962 to 1981 cm^{-1} with an average value of 1970 cm^{-1} (Table 2.1). This position and peak shape matches closely with other reports of CO adsorbed linearly (atop) on Ag under electrochemical conditions: 1990 cm^{-1} in 0.1 M $NaClO_4$ at −0.15 V_{RHE}[159] on polycrystalline Ag and 1980 cm^{-1} in 0.05 M Na_2SO_4 at −0.2 V_{RHE} for seven monolayers of Ag over platinum (Pt).[139] In contrast, two peaks for linearly adsorbed CO are reported for Cu electrodes: 1983 and 2103 cm^{-1} in 0.05 M Na_2SO_4 at −0.2 V_{RHE} for six monolayers of Cu over Pt[139] and 2050 and 2080 cm^{-1} in 0.1 M $KHCO_3$ at −0.4 V_{RHE} at a Cu thin film.[143] The fact that we observe a single CO peak at a much lower wavenumber provides further evidence that no Cu is present on the cathode surface, corroborating our XPS (Figure 5.13) and product analysis (Figure 5.14 and Figure 5.15) results. Furthermore, bridged CO, where the C is bonded to two metal atoms, is commonly reported on Pt surfaces in the 1750–1850 cm^{-1} range[158,160,161] but has not been reported for Ag surfaces. We do not observe any peaks at 1750–1850 cm^{-1}, providing further confirmation of a Ag surface that is not contaminated with other metals.[131]

The CO peak experiences a shift in position from 1981 to 1962 cm^{-1} on the cathodic scan that is largely reversible on the anodic scan, only deviating at −0.4 V_{RHE} to stabilize around 1974 cm^{-1} until it desorbs (Figure 5.3A). The general trend in the CO peak position decreasing with more cathodic potentials was also observed on other Ag electrodes.[139,159] This shift may

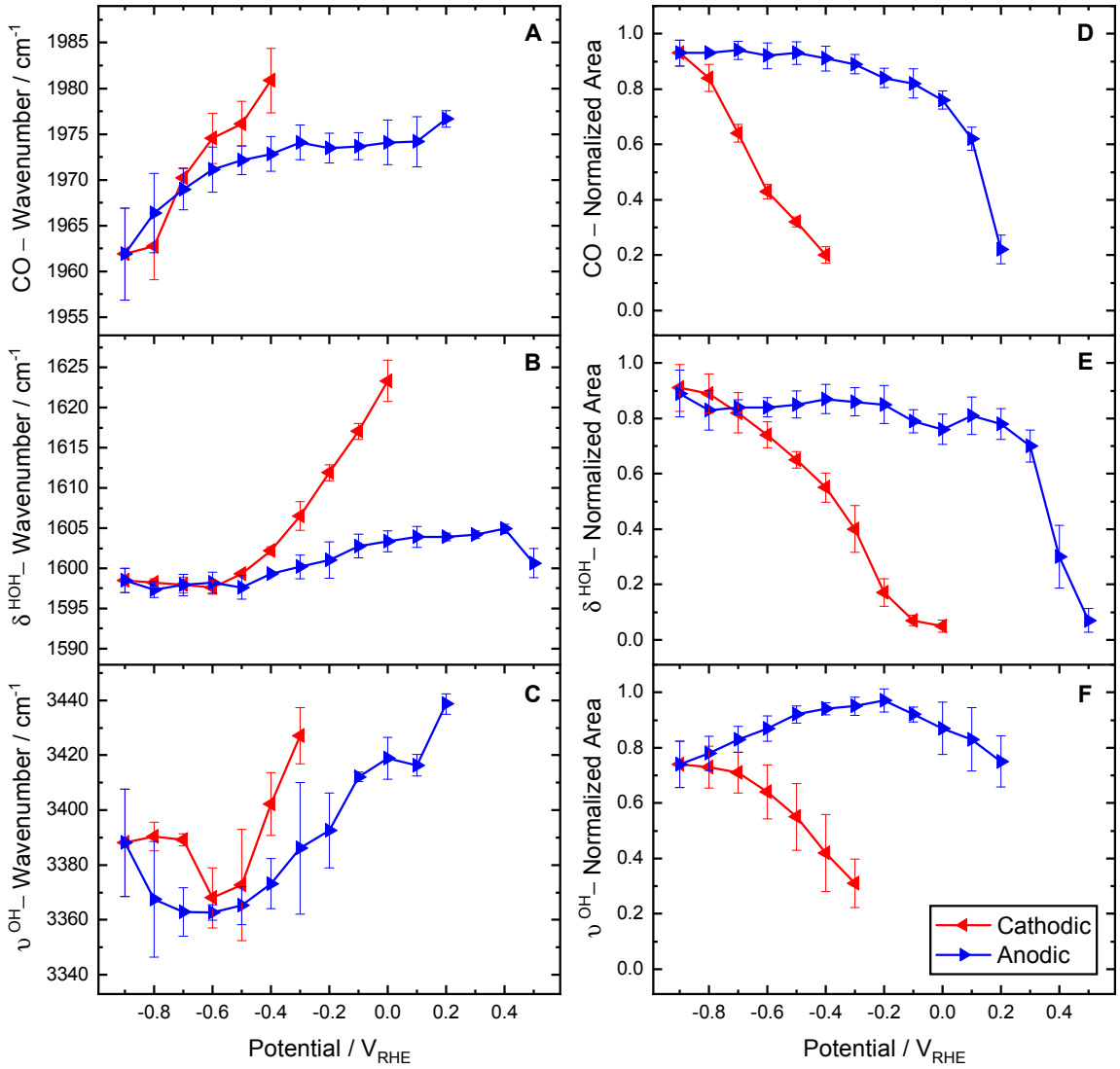

Figure 5.3: Average position (A–C) and normalized area (D–F) of three SEIRAS peaks during CV: CO (A and D), δ^{HOH} (B and E), and ν^{OH} (C and F). Average values and standard deviations are calculated from five CV experiments performed at 2 mV s^{-1} on different days, with a new cathode prepared each day. The area is normalized by the largest area in each individual data set. Error bars represent one standard deviation. Red lines show the cathodic scan from 0.2 to −0.9 V_{RHE} and blue lines show the anodic scan from −0.9 to 0.6 V_{RHE}. The activated Ag cathode on a Ge ATR crystal was in 0.1 M $KHCO_3$ with continuous CO_2 flow through the electrolyte.

be a result of the Stark effect and/or chemical bonding effects due to orbital interactions (donation, back donation, and steric repulsion). Multiple effects may contribute to the field-dependent shift, and it is difficult to distinguish the dominant effect.[162] The Stark effect is an interaction of the molecule's dipole with the electric field at the interface, resulting in a change in the vibrational frequency. Chemical bonding effects can influence surface-adsorbed species by altering the charge donation between the metal and the molecular orbitals of the

adsorbate as the applied potential is changed.[159,160] A possible explanation for the observed decrease in the CO wavenumber with more negative applied potentials is an increase in the occupancy of the CO antibonding $2\pi^*$ molecular orbital, a chemical bonding effect which would decrease the bond strength.[163] While the mechanism cannot be determined conclusively, we hypothesize that the chemical bonding effect is dominant because CO is expected to be bound to the surface as a reduction product, and density function theory (DFT) has shown this to be the dominant effect at other metal surfaces.[162]

The CO coverage has been quantitatively measured on other metallic electrodes, such as Pt, through electrooxidative stripping, where CO is oxidized to CO_2 at around 0.80 V_{RHE}.[158] However, we were unable to quantify the CO coverage in this study because, as described in the In Situ ATR–SEIRAS Measurements section and shown in Figure 5.9, the greatest anodic potential we could achieve was 0.70 V_{RHE} before the film began to degrade. No CO oxidation peak was ever observed on the anodic scan up to 0.70 V_{RHE} under any conditions. However, the intensity and area of the CO peak do indicate the relative concentration of CO bound to the surface of the Ag cathode. The concentration is relative because in SEIRAS only the sites that experience the surface enhancement result in a strong infrared absorption. The SEIRAS intensity greatly depends on the size, shape, and interparticle spacing of the nanofeatures of the thin film.[164] The nanoparticles must be smaller than the wavelength of visible light, and the largest enhancement is obtained when they are aggregated very densely with small gaps in between.[150] Interestingly, plasmonic properties also depend on the size, shape, and density of nanofeatures.[9] While there is no guarantee that the SEIRAS active sites are also the plasmonically active sites, this similarity in enhancement related to nanofeatures increases the likelihood. It is also possible that the sites that exhibit SEIRAS enhancement are not the electrochemically active sites. However, as we are detecting CO, a CO_2 reduction product, it is clear that we are probing at least one electrochemically relevant active site.

The positive direction of the peak signifies that the CO concentration at the surface is greater than the concentration during the background scan at 0.2 V_{RHE} (which is expected to be zero). The CO peak area increases rapidly during the cathodic scan but is fairly constant on the anodic scan, only beginning to decrease after -0.3 V_{RHE} before being completely removed at around 0.20 V_{RHE} (Figure 5.3D). This trend of CO remaining adsorbed on the surface is somewhat unexpected for Ag, which is generally described as having a low affinity for CO.[16] However, a recent theoretical prediction of CO binding strength on Ag clusters found the adsorption energy to be much higher, close to that of Cu surfaces.[165] In this study, CO is even shown to remain on the surface after the applied potential is removed. After CA at -0.6 V_{RHE} for 90 seconds, the applied potential was stopped, and the system was monitored during OCV. The normalized surface area of the CO peak during OCV decreased for 10 minutes before all of the CO was fully desorbed (Figure 5.4A). The open circuit potential started at 0.22 V_{RHE} and stabilized at 0.245 V_{RHE} after 10 minutes, corresponding to the complete desorption of CO (Figure 5.20B).

Performing these same CV scans under constant illumination was possible but resulted in a 10 °C increase in the temperature of the electrolyte during the 20 minute experiment. Increasing the electrolyte temperature decreases the solubility of CO_2 and can change the product distribution as each reaction rate constant will change according to the Arrhenius

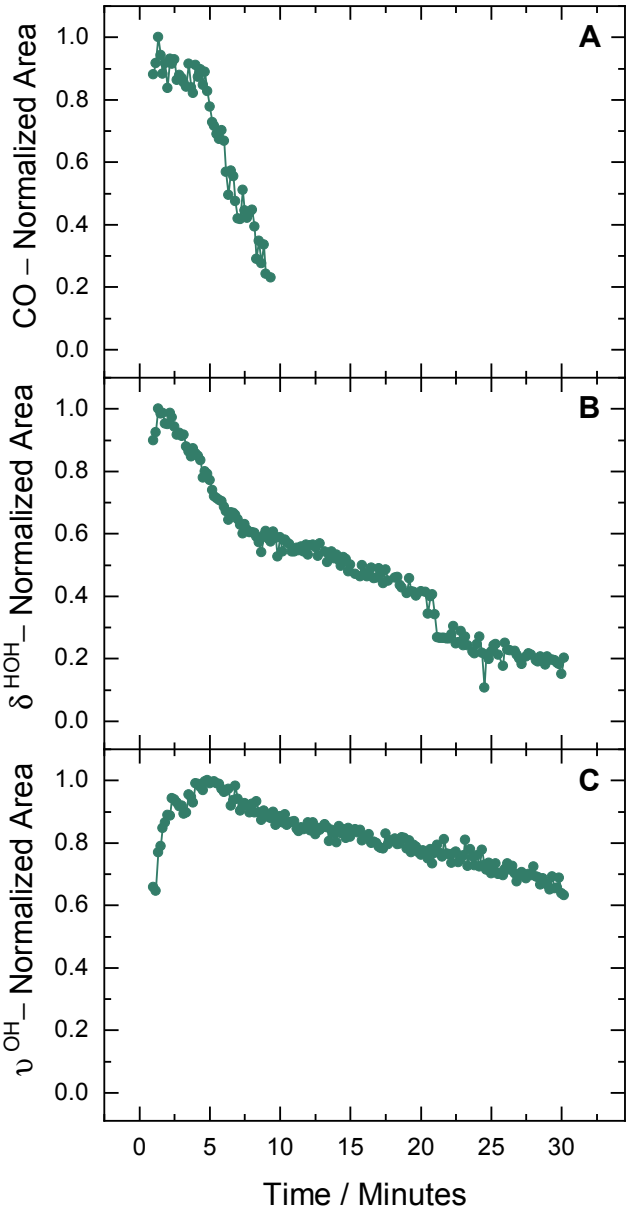

Figure 5.4: Normalized area of three SEIRAS peaks during open circuit relaxation: (A) CO, (B) δ^{HOH}, and (C) ν^{OH}. The area is normalized by the largest area of each peak. The system was allowed to relax at open circuit after CA at -0.6 $\mathrm{V_{RHE}}$ for 90 seconds. The activated Ag cathode on a Ge ATR crystal was in 0.1 M $\mathrm{KHCO_3}$ with continuous $\mathrm{CO_2}$ flow through the electrolyte. Figure 5.20 shows the SEIRAS scans and open circuit potential corresponding to these plots.

equation. Therefore, it is important to perform dark and illuminated experiments at the same temperature. CA experiments were conducted for 90 seconds in the dark and under constant illumination from the 365 nm LED light source (125 mW $\mathrm{cm^{-2}}$) at -0.2, -0.3, -0.4, -0.5, -0.6, and -0.7 $\mathrm{V_{RHE}}$ (Figure 5.18 and Figure 5.6). While no area trends can be discerned from this technique, the peak positions can be compared. The CO peak position

shifted from 1983 to 1964 cm^{-1} as the potential increased cathodically from −0.4 to −0.7 V_{RHE} in both the dark and the light (Figure 5.18A). The overlapping error bars show there is no statistical difference between the CO peak positions under dark or illuminated conditions. This indicates that the plasmonic effect is not influencing the strength of the CO bond by changing its binding orientation or by changing the electronic coupling with Ag.

In prior work, we observed that the apparent onset potential for CO_2 reduction to CO was reduced by 300 mV in the light compared to the dark.[36] The total current density in the light begins to increase at −0.2 V_{RHE}, while the total current density in the dark begins to increase only at −0.5 V_{RHE}. Product analysis at −0.37 V_{RHE} confirmed that the only product being produced in the light was CO, and no products were detected in the dark. To confirm this observation, CA was performed at −0.2, −0.25, and −0.3 V_{RHE} with SEIRAS spectra taken at a higher resolution to pinpoint the onset of CO adsorption in the light and in the dark. Figure 5.5A shows the SEIRAS spectra during constant illumination; no CO peak is observed at −0.2 V_{RHE}, a small CO peak begins to appear at −0.25 V_{RHE}, and a CO peak is clearly visible at −0.3 V_{RHE}. The appearance of the CO peak exactly coincides with the onset of Faradaic cathodic current under 365 nm illumination, implying that, under illuminated conditions, CO is able to desorb at potentials close to where it initially forms on the Ag surface, hence resulting in a measured Faradaic current.

Figure 5.5B shows the high-resolution SEIRAS spectra in the dark during CA with the same range of applied potentials. Surprisingly, the results in the dark are identical to those in the light, indicating that the onset potential of CO_2 reduction to CO in the dark is also −0.25 V_{RHE}, although the desorption of CO (and resulting measured current) in the dark is not observed until potentials are more cathodic than −0.5 V_{RHE}. This finding reveals that the plasmonic effect induced by the light enables the desorption of CO from the surface, making more active sites available for the further reduction of CO_2 to CO. This explains why we observe CO production and a higher current density at these low overpotentials in the light and not the dark.

A possible explanation for the plasmonic mechanism enhancing CO desorption is that energy from plasmonically excited charge carriers could be dissipating into the lattice, resulting in localized heating of the cathode surface.[166] This increase in temperature could enable the desorption of CO from the Ag surface, which has been shown to occur at around 40 °C under gas-phase conditions.[167] However, in our previous studies we showed that plasmonic heating was not the cause of enhanced CO_2 reduction at the Ag cathode because the photocurrent increases linearly with light intensity[36] and increasing the electrolyte temperature from 22 to 35 °C results in a decrease in CO production.[43]

Another explanation for plasmon-enhanced CO desorption is, broadly, the transfer of energized charge carriers from the Ag to the surface-adsorbed CO. The localized surface plasmon resonance (LSPR) can relax through nonradiative excitation of energetic charge carriers, resulting in the formation of energetic electron–hole pairs at the cathode surface. The strong local electric fields generated during LSPR also promote higher rates of this process.[6] While the enhanced electric field can also affect the bond strength and orientation of adsorbed molecules, we see no change in the CO peak position upon illumination at any applied potential (Figure 5.18C).

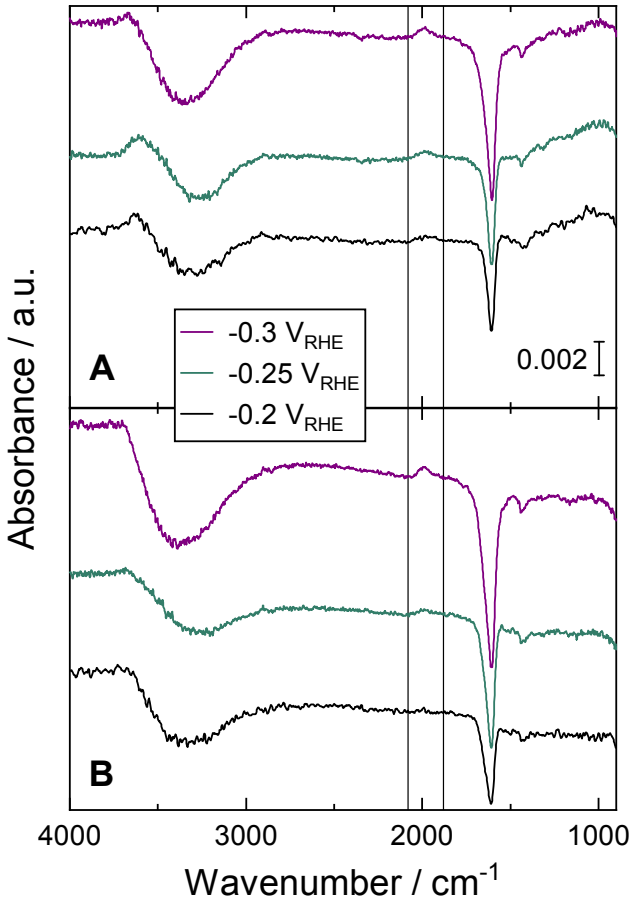

Figure 5.5: SEIRAS spectra taken during CA at −0.2, −0.25, and −0.3 V_{RHE}. (A) Spectra taken under 365 nm LED illumination (125 mW cm^{-2}) and (B) spectra taken in the dark. The two vertical lines frame the CO peak position. The activated Ag cathode on a Ge ATR crystal was in 0.1 M $KHCO_3$ with continuous CO_2 flow through the electrolyte. The background spectrum was taken at 0.2 V_{RHE}. The scale bar in (A) gives the y-axis scale in absorbance units (a.u.) and applies to both (A) and (B).

In the desorption induced by electronic transitions (DIET) mechanism, the excited electron at the Ag surface can temporarily transfer to partially occupied or unoccupied molecular orbitals of an adsorbed species, forming an excited metal–adsorbate complex with a different potential energy surface (PES). On this new PES, the energy of the donated charge carrier is converted to the kinetic energy of the metal–adsorbate complex. After a few femtoseconds, the donated electron decays back to the metal Fermi level and the adsorbate returns to the ground state PES. If the energy transfer exceeds the activation barrier for desorption, the adsorbate will leave the surface.[9] This mechanism has been invoked for NO[168], CO[169,170], and H_2[171] desorption from metal surfaces under vacuum. The DIET mechanism can also be reframed as a *reaction* induced by electronic transitions, where a reaction intermediate adsorbed on the surface overcomes the activation barrier for the reaction to occur. Reports of this mechanism include H_2 dissociation[11], O_2 dissociation[12], and C–O bond dissociation.[172]

5.7 Water Bend and Stretch

We observe the water bending, δ^{HOH}, signal in the range of 1597–1623 cm^{-1} with an average value of 1600 cm^{-1} (Table 2.1). This matches well with other reports of the HOH stretch on Ag in electrochemical conditions: 1608 cm^{-1} in 0.05 M Na_2SO_4 at −0.2 V_{RHE} for seven monolayers of Ag over Pt[139] and 1635 cm^{-1} in 0.1 M KCl at −0.85 V_{RHE} on a sputtered Ag thin film.[140] The other water peak observed in this study, the water stretching peak, ν^{OH}, appears in the range of 3351–3520 cm^{-1} with an average value of 3402 cm^{-1} (Table 2.1). A broad peak centered at 3300 cm^{-1} and spanning this range was also reported for Ag(100) at −0.2 V_{RHE} in 0.1 M NaF.[156] In fact, the regions observed for both the δ^{HOH} and ν^{OH} peaks on Ag are also the typical ranges for those peaks on other metals, such at Pt,[158] Cu,[139] and Au.[157]

In acidic media it is possible to see a hydronium cation (H_3O^+) bending peak at a higher wavenumber than the δ^{HOH} peak. For example, H_3O^+ peaks were reported at 1758 cm^{-1} at 0.4 V_{RHE} in 0.5 M H_2SO_4 for Pt(111)[173] and at 1730 cm^{-1} at 0.2 V_{RHE} in 5 M H_2SO_4 for Au(111).[157] However, in this study no peaks were observed in the H_3O^+ bending region, which is unsurprising as the electrolyte solution was at a pH of 6.8. In basic electrolyte a broad hydroxide anion (OH^-) stretching peak may be observed as a higher-frequency shoulder or component of the ν^{OH} peak. A hydroxide peak was reported at 3480 cm^{-1} as a feature in the high-frequency range of the broad water peak from 3100–3500 cm^{-1} (0.2 V_{RHE} in 0.1 M NaOH on a Au film).[174] In this study, the ν^{OH} peak is broad and asymmetrical, but no clear features emerge that could be attributed to hydroxide. This is expected in nearly neutral electrolyte, although the local pH is expected to increase at the surface of a cathode where CO_2 reduction is occurring as a result of proton consumption.[142]

The δ^{HOH} peak position begins at 1623 cm^{-1} and shifts rapidly to 1599 cm^{-1} during the cathodic scan from 0 to −0.5 V_{RHE} (Figure 5.3B). For the remainder of the cathodic scan, the peak position is constant at 1598 cm^{-1}. On the anodic scan, the peak position is identical to the cathodic scan from −0.9 to −0.5 V_{RHE}. Then the peak position begins to increase, but only incrementally, reaching a maximum of 1605 cm^{-1} at 0.4 V_{RHE}. A small positive shoulder at around 1630 cm^{-1} in the negative-going δ^{HOH} peak that appears and disappears near −0.6 V_{RHE} is attributed to HCO_3^- and will be discussed in the Carbonate, Bicarbonate, and CO_2 section.

The ν^{OH} peak position shifts quickly from 3427 to 3373 cm^{-1} on the cathodic scan from −0.3 to −0.5 V_{RHE} and essentially stabilizes for the remainder of the cathodic scan at 3375 cm^{-1} (Figure 5.3C). On the anodic scan, the peak positions are identical from −0.9 to −0.5 V_{RHE}. Then the peak position begins to increase again for potentials more anodic than −0.5 V_{RHE}, with values similar to the cathodic scan, reaching 3439 cm^{-1} at 0.2 V_{RHE}.

The wide range of peak positions, large error bars, and broad peak shape of the ν^{OH} feature reflect the many different types and orientations of water and hydroxide that contribute to this peak. The different types of contributing molecules include surface-bound water and OH^-, free water and OH^-, and water associated with anions.[156] All of these contributors have both symmetric and asymmetric stretching vibrations as well as different degrees of hydrogen bonding, both of which can shift the peak position. For example, the asymmetric

stretch of nonbonded water has a higher frequency than the symmetric stretch. A higher degree of hydrogen bonding lowers the wavenumber of the OH stretch, but less hydrogen bonding raises it. In addition, species may experience a Stark effect or chemical bonding effect shift with changes in applied potential. For this reason, we will not interpret the peak shifts described above as resulting from any one phenomena because they likely represent a complicated array of changes from each of the different types of molecules present at the surface.

However, we can use the area trends of the ν^{OH} and δ^{HOH} peaks to understand how the EDL structure is changing under conditions relevant to CO_2 reduction. The intensity of the δ^{HOH} and ν^{OH} water peaks is an indication of the average orientation of the first layer of water molecules at the electrode surface. At the potentials more negative than the pzc, the water molecules are oriented H-down.[155] As they pass through the pzc, the water molecules become oriented with H parallel to the electrode surface, and just above the pzc, they form an ice-like structure by hydrogen bonding with water molecules in the second layer.[175] At potentials more positive than the pzc, the water molecules are oriented O-down. The density of water at the surface is at a minimum near the pzc and increases with the magnitude of the applied voltage.[155] We can now use this understanding of water reorientation in the EDL to interpret the peak area trends for the δ^{HOH} and ν^{OH} water peaks.

In CO_2 reduction, the relevant region of interest is at potentials more negative than the pzc. The pzc for Ag(100) was -0.2 V_{RHE} in 0.1 M NaF and 0.1 M KF,[156] and the pzc for Ag(111) was -0.07 V_{RHE} in 0.1 M NaF.[155] In this region for both δ^{HOH} and ν^{OH}, we see that the peak area increases with more cathodic potentials until it stabilizes at -0.8 V_{RHE} (Figure 5.3E and F). This indicates that the water molecules at the surface are reorienting to be more H-down, perhaps reaching the maximum orientation at -0.8 V_{RHE}. On the anodic scan, the peak area is constant (δ^{HOH}) or even increasing slightly (ν^{OH}) until 0.3 V_{RHE}.

As clearly seen on the anodic scan, the EDL structure is not the same as it was on the cathodic scan. It seems once the water molecules are oriented H-down they stay in that position, beyond where we might expect the pzc to be. This resistance to change in the average water molecule orientation can also be seen in the OCV behavior (Figure 5.4B and C). After 90 seconds of CA at -0.6 V_{RHE}, the δ^{HOH} and ν^{OH} peak areas decrease slowly over the course of 30 minutes. While the open circuit potential changes from 0.22 to 0.245 V_{RHE} within the first 10 minutes, the potential is stable for the remaining 20 minutes (Figure 5.20B). As described above, these peaks, and thus the EDL structure, will eventually reach a steady state over the course of one to two hours. We also observe during longer CA experiments that the EDL structure changes rapidly during the first 5–10 minutes, with the δ^{HOH} and ν^{OH} peak areas increasing sharply (Figure 5.21). After this initial region, the rate of peak area change slows down considerably, although it still continues to increase. This implies that CO_2 reduction experiments performed in the first 5–10 minutes of applied potential may have different results than longer experiments due to differences in the EDL structure. The dense, close-packed layer of water that eventually forms at the surface of a charged electrode is thought to be favorable for rapid proton transfer,[176] which would impact the partial current densities towards H_2 production and all CO_2 reduction products.

Above 0.3 V_{RHE}, the peak area of δ^{HOH} drops suddenly during anodic scanning. As described

previously and shown in Figure 5.1, there are potential regions where the δ^{HOH} peak has a positive and negative component. δ^{HOH} peaks with this same shape have been reported during potential scans at Pt[158] and Au[157,175] surfaces. This rapid peak area decrease corresponds to the region in the anodic scan where the peak again has a positive and negative component before finally becoming a positive peak at around 0.6 V_{RHE} (Figure 5.17). Near this same potential on the anodic scan, the ν^{OH} peak flips from negative to positive. This behavior is interpreted as the shift from H-down to O-down water orientation at the surface, where the positive and negative δ^{HOH} peak components likely result from this reorientation. Similarly, the initial region where the δ^{HOH} peak has both a positive and negative component and where the peak position decreases rapidly reflects the reorientation of water to the H-down position.

5.8 Carbonate, Bicarbonate, and CO_2

Although there are no reports of HCO_3^- or CO_3^{2-} species at biased Ag electrodes in aqueous electrolytes, there are several IR spectroscopy reports of these species in aqueous solutions.[177–180] There are many IR-active modes of both HCO_3^- and CO_3^{2-}, with several appearing in the fingerprint region.[179] Here we will focus on the HCO_3^- and CO_3^{2-} peaks that may appear above 1100 cm^{-1}. For HCO_3^-, these modes are the COH bend (δ^{COH}) near 1300–1320 cm^{-1};[177,179,180] the symmetric CO_2 stretch ($\nu_s^{CO_2}$) at around 1355–1364 cm^{-1}, which is commonly seen as the most intense peak;[177,179,180] and the asymmetric CO_2 stretch ($\nu_{as}^{CO_2}$) near 1620–1634 cm^{-1}, which in this study would overlap with δ^{HOH}.[177,179] There is one IR-active mode for CO_3^{2-} above 1100 cm^{-1}: the asymmetric stretch ($\nu_{as}^{CO_3^{2-}}$) at around 1374–1396 cm^{-1}, which is typically the most intense peak.[177–180] While these studies report a single average peak position for each mode, they acknowledge that the assignments are approximate because there can be coupling between the modes, and the peak positions vary with the solution composition and concentration.[179]

In addition to these reports of HCO_3^- and CO_3^{2-} in aqueous solutions, there is also an IR spectroscopy study of gas-phase $HCO_3^-(H_2O)_{1-10}$ clusters.[181] The study found that the HCO_3^- peak positions increased with increasing water coordination, except for the peak which overlaps with δ^{HOH}.[181] They reported the δ^{COH} mode from 1177–1205 cm^{-1}, the $\nu_s^{CO_2}$ mode from 1288–1353 cm^{-1}, and the $\nu_{as}^{CO_2}$ mode from 1653–1706 cm^{-1}.[181] Finally, there are two IR spectroscopy studies of HCO_3^- and CO_3^{2-} species at biased metallic electrodes in aqueous electrolyte.[141,158] Iwasita et al. reported adsorbed HCO_3^- at 1330 cm^{-1} and adsorbed CO_3^{2-} at 1400 cm^{-1} at a positively biased (0.6–0.9 V_{RHE}) Pt(111) electrode in CO_2-saturated 0.1 M $HClO_4$.[158] Dunwell et al. observed a HCO_3^- peak at 1362 cm^{-1} and a CO_3^{2-} peak at 1402 cm^{-1} at a negatively biased (-0.9 V_{RHE}) Au film in 1.0 M $NaHCO_3$.[141]

In this study, we observe two peaks in the 1100–1500 cm^{-1} region: a peak from 1276–1279 cm^{-1} with an average value of 1278 cm^{-1} and a peak from 1393–1401 cm^{-1} with an average value of 1395 cm^{-1}. We attribute the peak at 1395 cm^{-1} to the $\nu_{as}^{CO_3^{2-}}$ mode because the position is consistent with reports of CO_3^{2-} in aqueous solutions[177–180] and at biased metallic electrodes in aqueous electrolyte.[141,158] The peak at 1278 cm^{-1} is a little lower than expected for the dominant HCO_3^- $\nu_s^{CO_2}$ mode[141,158,177,179,180] or the δ^{COH} mode.[177,179,180] However, in all of these reports the HCO_3^- modes always appear at a lower wavenumber than the $\nu_{as}^{CO_3^{2-}}$

mode.[141,158,177–181] In addition, the HCO_3^- $\nu_s^{CO_2}$ in the hydrated gas phase was reported from 1288–1353 cm^{-1},[181] very close to our observed peak at 1276–1279 cm^{-1}. The explanation for the lower wavenumber was less water coordination,[181] which could certainly occur close to the negatively biased Ag cathode where water is highly oriented.[155] While two peaks are expected for formate at 1350 and 1383 cm^{-1}, the dominant peak should appear at 1580 cm^{-1}.[182] However, no peak is observed near 1580 cm^{-1}, and the concentration of formate, with a Faradaic efficiency of just 2% at -0.7 V_{RHE},[36] would be five orders of magnitude less than the concentration of HCO_3^-. Finally, a small positive shoulder at around 1630 cm^{-1} in the negative-going δ^{HOH} peak appears and disappears at the same potentials as the peak at 1278 cm^{-1} (Figure 5.1), consistent with the HCO_3^- $\nu_{as}^{CO_2}$ mode.[177,179] Thus, we conclude that the peak we observe at 1278 cm^{-1} is most likely the HCO_3^- $\nu_s^{CO_2}$ mode. Additionally, because we do not expect anions to adsorb to an electrode that is biased to potentials negative of the pzc, we interpret these HCO_3^- and CO_3^{2-} peaks as near-surface species, within 10 nm of the cathode surface.[141,183]

In this study, we observed CO_2 as a single peak at 2342 cm^{-1} for all potentials where it appears. The assignment of the CO_2 peak is consistent with several literature reports of CO_2 at biased metallic electrodes in aqueous electrolyte. CO_2 has been observed at 2343 cm^{-1} at a positively biased (0.6–0.9 V_{RHE}) Pt(111) electrode in CO_2-saturated 0.1 M $HClO_4$,[158] at 2340 cm^{-1} at a negatively biased (-0.9 V_{RHE}) Au film in 1.0 M $NaHCO_3$,[174] and at 2345 cm^{-1} in CO_2-saturated 0.1 M KCl at -0.9 V_{RHE} on a sputtered Ag thin film.[140]

The average peak positions and normalized areas during cathodic and anodic CV scans for HCO_3^-, CO_3^{2-}, and CO_2 peaks are shown in Figure 5.19. The trends are remarkably similar; all three peaks appear and disappear at around -0.6 V_{RHE} (Table 5.2). The peak areas increase with more cathodic potentials and decrease on the anodic scan with only slightly larger peak areas than on the cathodic scan. The CO_2 position never deviates, and the CO_3^{2-} position varies slightly but the generally overlapping error bars show no trend with potential. Only the HCO_3^- peak position changes, increasing with more cathodic potentials with no hysteresis on the anodic scan (Figure 5.19A and Figure 5.6). Accordingly, no shift in peak position for HCO_3^-, CO_3^{2-}, or CO_2 was reported from 0.1 to -0.9 V_{RHE} for a polycrystalline Au film.[141] On Pt(111), the HCO_3^- peak position was independent of potential while the CO_3^{2-} peak position increased with more anodic potentials from 0.6 to 0.95 V_{RHE}, but as discussed above, the the orientation and structure of water at the surface of a positively charged electrode is quite different from that of a negatively charged electrode and the changes in peak position were attributed to shifts in the water orientation.[158]

We consider these three species together because their concentrations are linked by the following reactions (Equation 5.1 and Equation 5.2).

$$CO_2 + OH^- \rightleftharpoons HCO_3^- \tag{5.1}$$

$$HCO_3^- + OH^- \rightleftharpoons H_2O + CO_3^{2-} \tag{5.2}$$

The peak area trends can be understood through the equilibrium among HCO_3^-, CO_3^{2-}, and CO_2. As the applied cathodic potential increases in magnitude, the current density increases

due to increasing CO_2 reduction and H_2 formation rates (Figure 5.15) and equations 5.1 and 5.2 shift to the right, converting CO_2 at the surface into HCO_3^- and CO_3^{2-}. This results first in an increase in the concentration of HCO_3^- beginning at -0.56 V_{RHE} followed by an increase in the concentration of CO_3^{2-} starting at -0.69 V_{RHE}, as seen through the positive peaks that increase in area (Figure 5.1 and Figure 5.19). This also results in a decrease in the concentration of CO_2, which we observe as a negative peak with an increasing area beginning at -0.65 V_{RHE} (Figure 5.1 and Figure 5.3). Additionally, the CO_2 concentration will decrease near the surface as it is reduced to form CO and formate, especially as the current density increases and exceeds the mass-transfer rate of CO_2 to the surface. The OH^- concentration will also increase at the cathode surface, resulting in an increase in the local pH.[144,184]

When comparing dark and 365 nm illuminated conditions, the IR spectra are very similar for nearly all species discussed in this article, with the lone difference being a shift in the HCO_3^- peak position. As presented in the introduction, our prior study of a plasmonic Ag cathode showed significant differences in the product distribution in the dark and under 365 nm LED illumination.[36] CO production was enhanced and H_2 evolution was suppressed at low overpotentials upon illumination, formate production was enhanced at all overpotentials in the light, and methanol was formed only under illuminated conditions at potentials more cathodic than -0.8 V_{RHE}.[36] In this study, we performed both CV and CA experiments under 365 nm LED illumination, but we observed very few differences between SEIRAS spectra in the light and the dark. No methanol (1470 and 2970 cm^{-1})[185] or formate (1350, 1383, and 1581 cm^{-1})[182] peaks were observed in the light or the dark at any potential. Because the expected methanol Faradaic efficiency at -0.8 and -0.9 V_{RHE} is 0.1 and 0.4%, respectively,[36] it is possible that the methanol concentration at the surface was below the detection limit of the IR spectrometer. Due to stability issues with the Ag thin film at potentials more cathodic than -0.9 V_{RHE}, we were unable to study the potential regions with higher methanol Faradaic efficiencies.

As previously discussed, the onset of CO formation in the light and the dark was -0.25 V_{RHE} (Figure 5.5). Figure 5.18 shows there is no difference between the light and dark average peak positions for CO_2, CO, ν^{OH}, or δ^{HOH} during 90 seconds of CA at any potential from -0.2 to -0.7 V_{RHE}. CO_3^{2-} is not plotted because there is insufficient data for this peak in this potential range. Surprisingly, the only measureable difference between the illuminated and dark cathode is the HCO_3^- peak position, which increases by approximately 6 cm^{-1} under illumination at -0.5, -0.6, and -0.7 V_{RHE} (Figure 5.6). This 6 cm^{-1} increase in position can also be observed when the system is allowed to stabilize in the dark at -0.5 V_{RHE} for 20 minutes before rapidly turning on the light source. The change was observed in the first spectrum taken in the light (10 seconds) before any heating could occur. This peak shift was also accompanied by an immediate increase in the peak area.

An increase in the HCO_3^- peak position signifies an increase in the strength of the bond. Because no other immediate changes are apparent between the dark and light spectra, we can conclude that this increase in the HCO_3^- bond strength is not caused by changes in the other species we observe at the surface. In the potential range of -0.5 to -0.7 V_{RHE} where this change occurs, we know that CO production will be enhanced and H_2 evolution will be suppressed, and at -0.7 V_{RHE}, formate production will be enhanced in the light (Figure 5.14

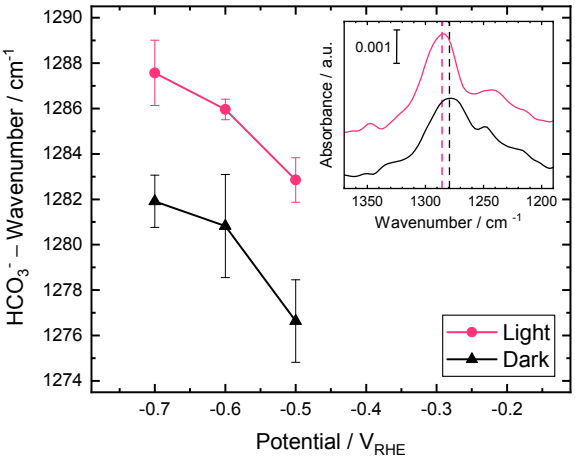

Figure 5.6: Average position of the HCO_3^- peak during CA for 90 seconds at -0.5, -0.6, and -0.7 V_{RHE} in the dark (black) and under 365 nm LED illumination (125 mW cm^{-2}) (pink). Average values and standard deviations are calculated from two to five CA experiments at each applied potential. Experiments were performed on different days with a new cathode prepared each day. Error bars represent one standard deviation. The inset shows two representative spectra in the dark and light at -0.6 V_{RHE}. The activated Ag cathode on a Ge ATR crystal was in 0.1 M $KHCO_3$ with continuous CO_2 flow through the electrolyte. The background spectrum was taken at 0.2 V_{RHE}. The inset scale bar gives the y-axis scale in absorbance units (a.u.).

and Figure 5.15).[36] An increase in the concentration of HCO_3^- near the surface would increase the local pH, which would lead to enhancement in CO_2 reduction and diminished H_2 evolution.[186]

The Raman shift of a probe molecule (4-methoxyphenyl isocyanide) on Au core Pt shell nanoparticles upon illumination at the plasmon resonance frequency (530 nm) was used by Yang et al. to determine the surface temperature. They found that the peak position decreased linearly with increasing temperature, which they attributed to a weakening of the interaction between the molecule and the substrate, allowing the molecules to reorient. Similarly, we find that the HCO_3^- peak position continues to increase linearly over time under constant illumination, which corresponds to a linear increase in temperature. However, they showed that the peak position did not change upon illumination until 50 seconds had elapsed.[187] Therefore we conclude that the immediate HCO_3^- peak shift we observe within the first 10 seconds of illumination is not caused by a temperature rise at the surface. We hypothesize that the observed increase in the peak position upon illumination is due to interactions of HCO_3^- molecules with the enhanced local electric field generated by the plasmon resonance, similar to the observed increase in peak position in the dark due to the electric field generated by the applied voltage (Stark effect).

Although CO also experiences a shift in peak position in the dark, there is no change in the wavenumber upon illumination (Figure 5.18C). We would expect a shift in the CO peak position in the light similar to that of HCO_3^- if the change in the dark was due to the Stark effect. However, if the CO shift in the dark is due to the chemical bonding effect, then we

would not expect an additional shift with a plasmonically enhanced local electric field.

5.9 Conclusions

We used in situ ATR–SEIRAS to probe the species at the surface of a plasmonic Ag cathode during CO_2 reduction in both the dark and under illumination. The SEIRAS signal can be enhanced while still maintaining cathode stability by optimizing the deposition conditions and through electrochemical CV cycling. We observe peaks for HCO_3^- (1278 cm^{-1}), CO_3^{2-} (1395 cm^{-1}), δ^{HOH} (1600 cm^{-1}), CO (1970 cm^{-1}), CO_2 (2342 cm^{-1}), and ν^{OH} (3402 cm^{-1}) under a range of applied potentials relevant to CO_2 reduction. Trends in the water δ^{HOH} and ν^{OH} peaks show that the water reorientation at the charged electrode surface can be slow to stabilize and slow to return to the original orientation. It is therefore important to "reset" the EDL by an anodic scan during SEIRAS to ensure that experimental results are repeatable. In addition, experiments considering product distribution should wait until the EDL has stabilized (approximately 5–10 minutes) before conducting product analysis.

We find that CO remains on the Ag surface until an anodic potential of 0.20 V_{RHE} is reached or after 10 minutes during OCV relaxation. Despite current density trends showing a decrease in the overpotential for CO formation upon illumination, we find that the onset of CO_2 reduction to CO is identical in the light and the dark (-0.25 V_{RHE}). We conclude that the light must be assisting the desorption of CO from the surface, possibly through a DIET mechanism induced by excited electrons generated through LSPR relaxation.

Finally, we confirm the expected increase in local pH at higher current densities through the changing concentrations of HCO_3^-, CO_3^{2-}, and CO_2 near the surface. The only change between spectra in the light and the dark is the immediate increase in the HCO_3^- wavenumber and peak area upon illumination. We propose that the enhanced local electric field that results from the LSPR is strengthening the HCO_3^- bond, further increasing the local pH. While the exact mechanism of plasmon-enhanced CO_2 reduction at a Ag surface is still uncertain, this in situ ATR–SEIRAS study sheds some light on how H_2 evolution is suppressed while CO_2 reduction is promoted at an illuminated Ag cathode.

5.10 Supplementary Information

Schematics

Figure 5.7 shows the electrochemical cell that was used for SEIRAS measurements in the dark and the light. Figure 5.8 represents the working electrode, a 60° Ge ATR crystal with 40 nm of Ag sputtered on the top.

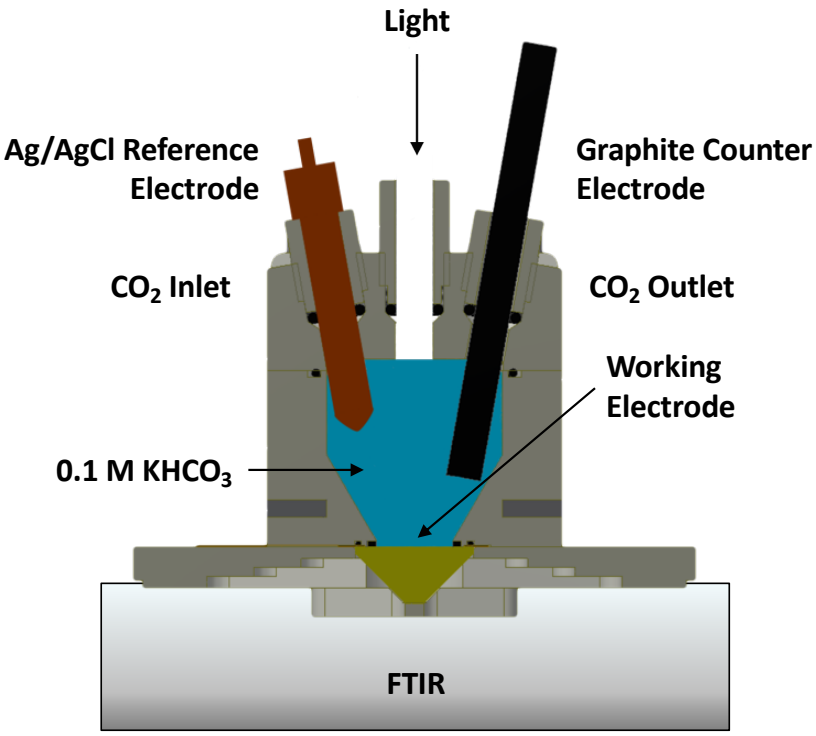

Figure 5.7: Electrochemical cell used for in situ ATR–SEIRAS experiments.[145]

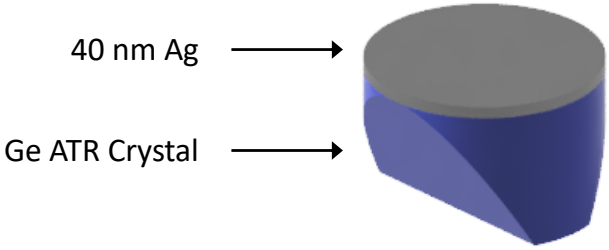

Figure 5.8: Schematic of 40 nm of Ag sputtered on a Ge ATR crystal.

Cathode Activation

Figure 5.9 shows the current density during CV activation of the Ag thin film electrode. Figure 5.10 shows SEIRAS spectra during a cathodic scan at a Ag thin film electrode that did not undergo the activation process shown in Figure 5.9.

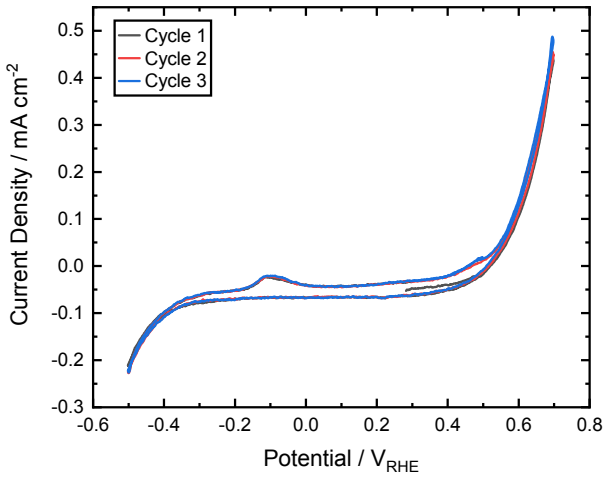

Figure 5.9: A representative run of three cyclic voltammograms (CV) performed at 50 mV s^{-1} from -0.3 to 0.7 V_{RHE} on a pristine Ag cathode for activation. The anodic potential was adjusted to keep the current density below approximately 0.80 mA cm^{-2} to prevent film degradation. The electrolyte is 0.1 M $KHCO_3$ with continuous CO_2 flow through the electrolyte.

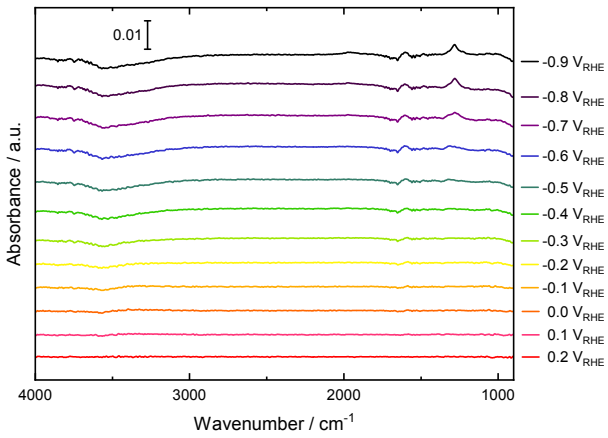

Figure 5.10: A cathodic scan at 2 mV s^{-1} from 0.20 to -0.90 V_{RHE} using a non-activated Ag cathode. The electrolyte is 0.1 M $KHCO_3$ with continuous CO_2 flow through the electrolyte. The background spectrum was taken at 0.2 V_{RHE}. The scale bar gives the y-axis scale in absorbance units (a.u.).

Cathode Characterization

Scanning electron microscopy (SEM) images were acquired using a Thermo Scientific Quanta FEG 250 SEM and a 10 kV accelerating voltage (Figure 5.11).

Atomic force microscopy (AFM) measurements were acquired with a Bruker Dimension Icon AFM system using the PeakForce Quantitative Nanoscale Mechanical tapping mode under ambient conditions (Figure 5.12). For all topography measurements, uncoated silicon (Si) probes (SCANASYST-AIR) with spring constants of 0.4 N m^{-1} were used. Grain size analysis was performed using the watershed algorithm in the Gwyddion software package. The grain location was determined with 100 steps, a drop size of 0.20%, and a threshold of 140 nm^2. Segmentation was determined with 20 steps and a drop size of 15.00%.

XPS spectra were obtained using a Thermo Scientific K-Alpha apparatus with an Al K-Alpha X-ray source (Figure 5.13). Parameters used for the survey measurements were: spot size, 400 μm; pass energy, 50 eV; energy step size, 0.1 eV; dwell time, 10 ms; 10 scans. In the vicinity of Cu2p1/2 and Cu2p3/2 the following parameters were changed: dwell time, 50 ms; 20 scans.

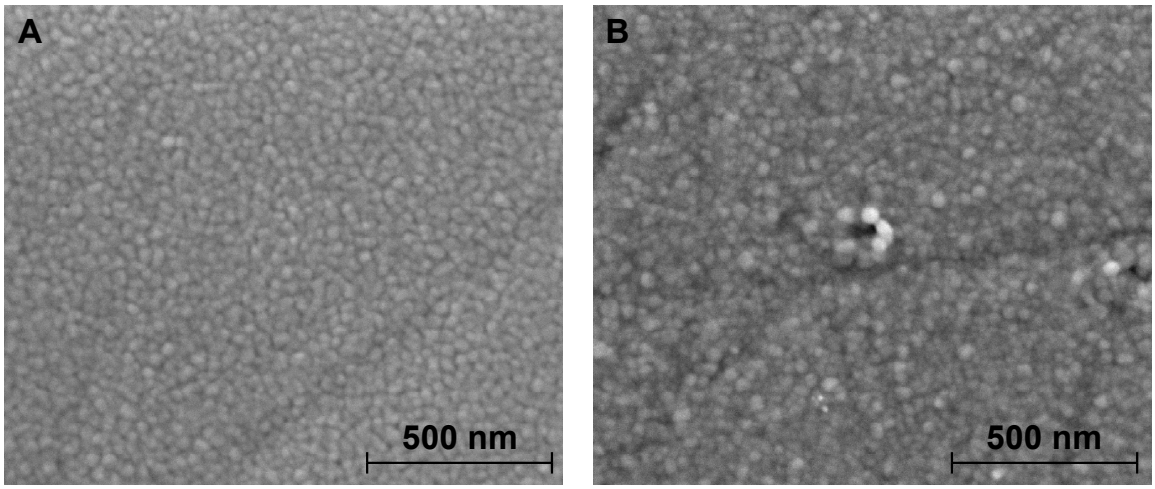

Figure 5.11: SEM images of a sputtered Ag cathode on a Ge ATR crystal before (A) and after (B) activation by CV cycling.

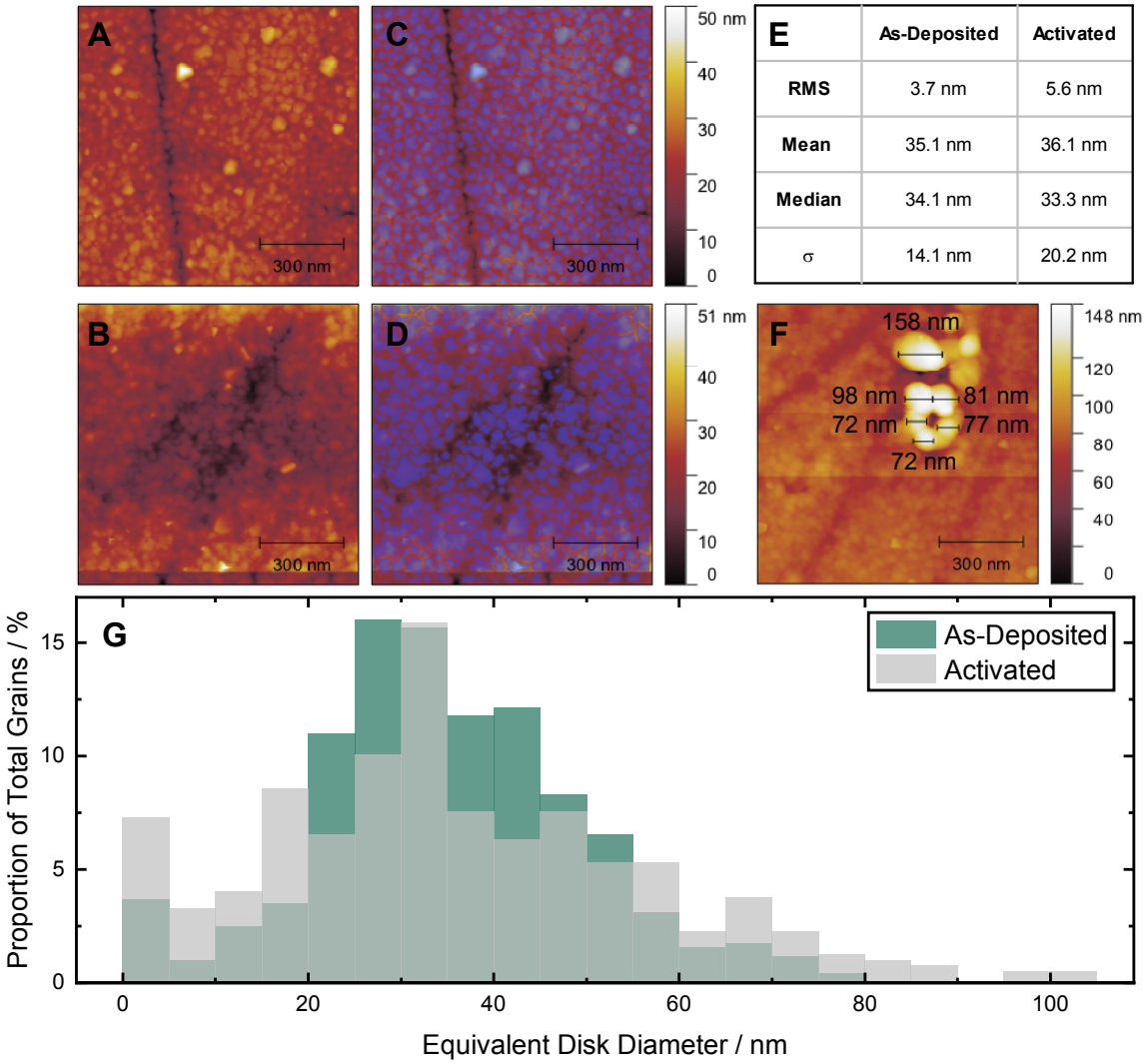

E	As-Deposited	Activated
RMS	3.7 nm	5.6 nm
Mean	35.1 nm	36.1 nm
Median	34.1 nm	33.3 nm
σ	14.1 nm	20.2 nm

Figure 5.12: AFM topographic images of a sputtered Ag cathode on a Ge ATR crystal before (A) and after (B and F) activation by CV cycling. Grains detected by the watershed algorithm are shown in purple over the AFM images before (C) and after (D) activation by CV cycling. (E) Table shows the root mean square (RMS) roughness and the mean, median, and standard deviation (σ) of the equivalent diameter. (G) Comparison of the grain size distribution on the "As-Deposited" and "Activated" cathode in terms of equivalent disc diameter, the diameter of the disc with the same projected area as the grain.

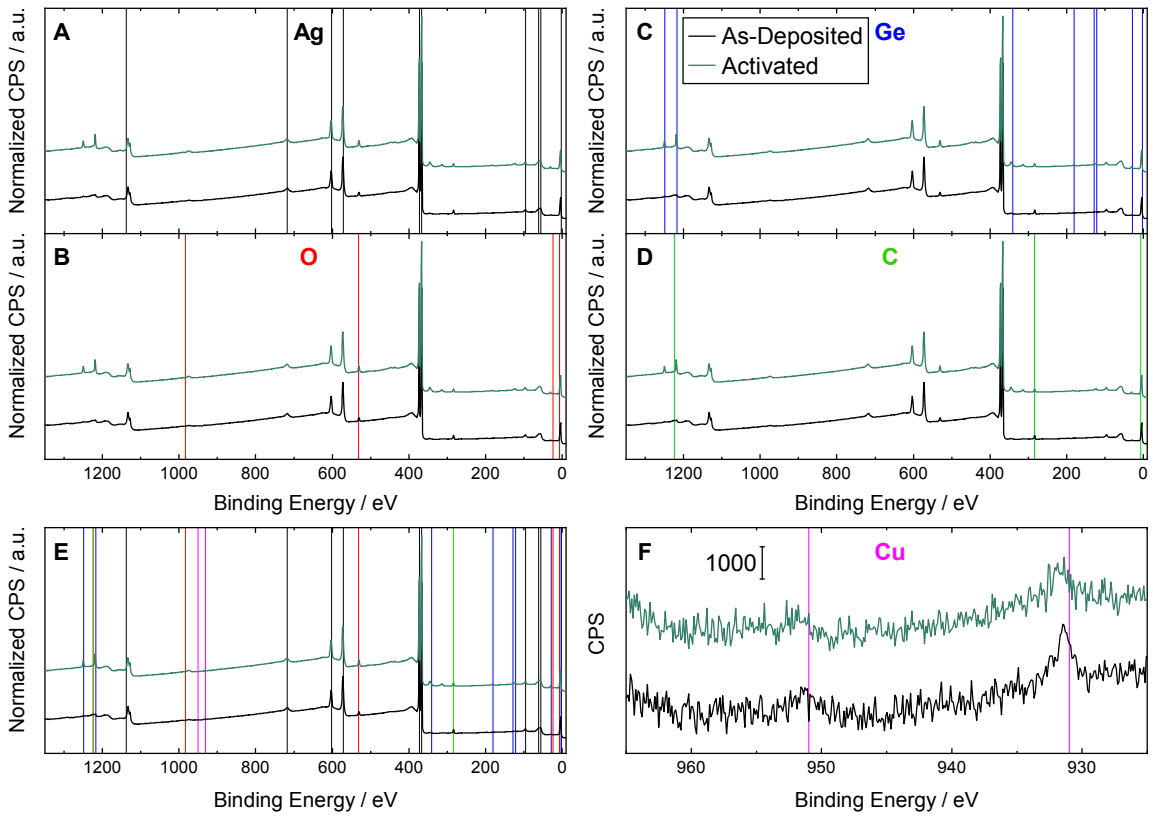

Figure 5.13: XPS spectra of a sputtered Ag cathode on a Ge ATR crystal before (black) and after (teal) activation by CV cycling. Separately, vertical lines are shown of the binding energies for Ag (A), oxygen (B), germanium (C), and carbon (D). (E) Together, vertical lines are shown of the binding energies for Ag, O, Ge, C, and the two most prominent binding energies for Cu (2p1/2 and 2p3/2). (F) Very small peaks corresponding to Cu $2p_{1/2}$ and Cu $2p_{3/2}$ are observed on the cathode before activation and are essentially removed after activation.

Product Analysis

Experiments for product analysis were performed in a custom cell described by Corson et al[43] with a catholyte volume of 2.3 mL, active electrode surface area of 1 cm^2, and continuous CO_2 gas flow of 5 sccm. Gaseous products were analyzed by an in-line Multiple Gas Analyzer #5 SRI Instruments GC with a 12 ft HayeSep D (divinylbenzene) column, thermal conductivity detector (TCD), flame ionization detector (FID) preceded by a methanizer, and Ar carrier gas. For a single product analysis run, a constant potential was applied for 16 minutes with GC injections at 3 and 15 minutes. The results from the 15 minute injection are reported here. Gaseous product concentrations were calculated from a calibration curve of at least three different concentrations for each gas type. Liquid products in the catholyte and anolyte were quantified after the electrolysis was complete by ^{1}H NMR spectroscopy on a Bruker Avance III 500 MHz magnet. Liquid product concentrations were determined by using phenol and DMSO as internal standards.[2] Complete details on the GC and NMR calibration and quantification methods are reported in Corson et al.[43] Faradaic efficiencies are reported in Figure 5.14 and partial current densities are reported in Figure 5.15.

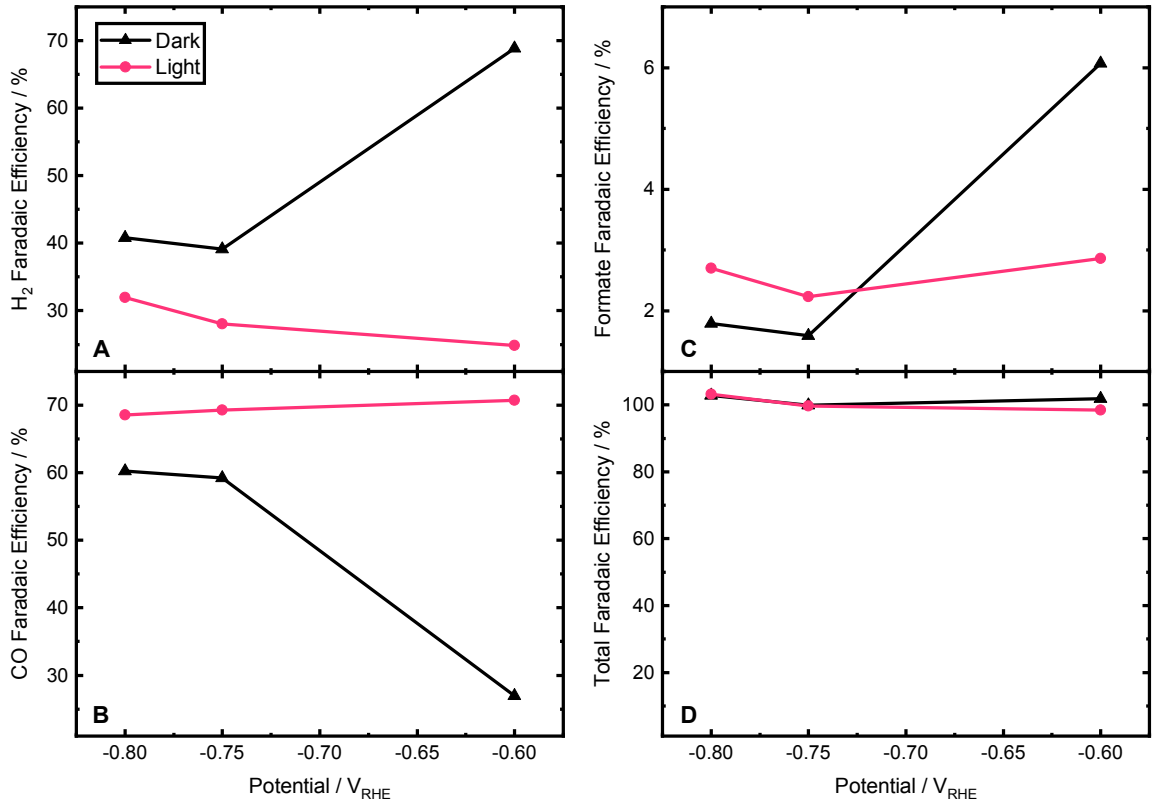

Figure 5.14: Faradaic efficiencies for H_2 (A), CO (B), Formate (C), and the total faradaic efficiency (D) at various potentials under 365 nm LED illumination (125 mW cm^{-2}) (pink lines) and in the dark (black lines). The sputtered Ag cathode on a glass slide was in 1.0 M $KHCO_3$ with continuous CO_2 flow through the electrolyte.

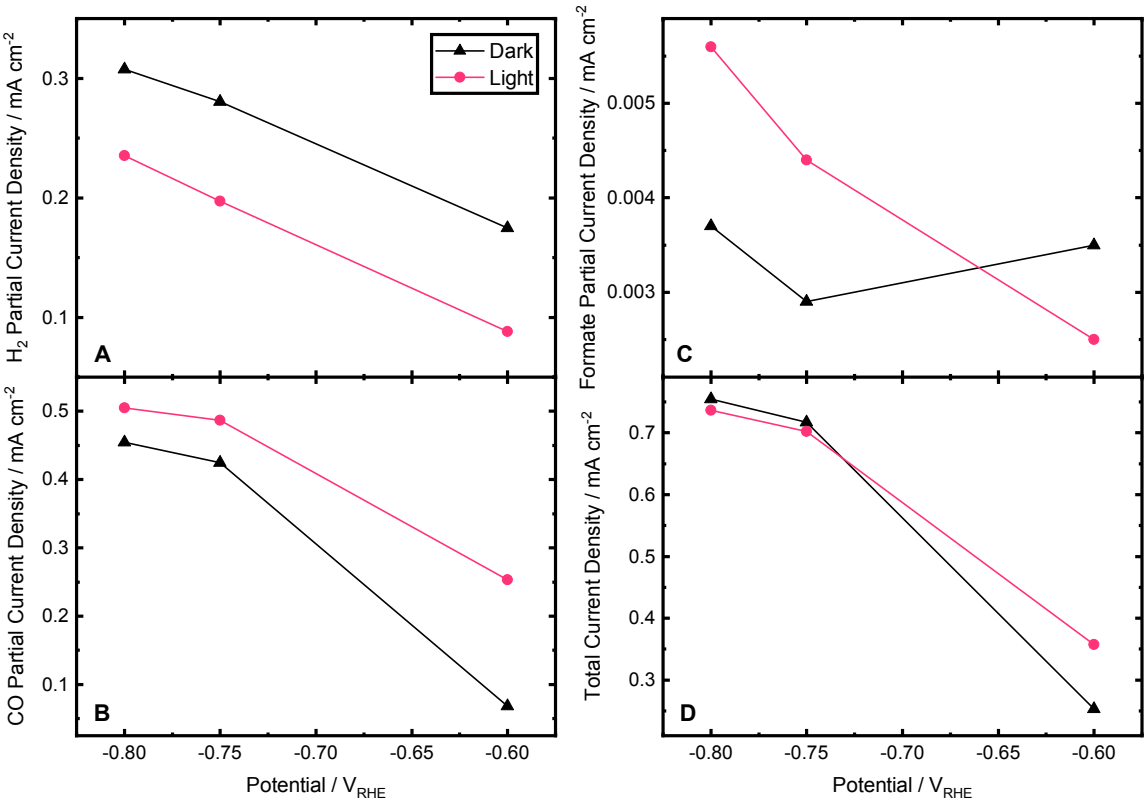

Figure 5.15: Partial current densities for H_2 (A), CO (B), Formate (C), and the total current density (D) at various potentials under 365 nm LED illumination (125 mW cm^{-2}) (pink lines) and in the dark (black lines). The sputtered Ag cathode on a glass slide was in 1.0 M $KHCO_3$ with continuous CO_2 flow through the electrolyte.

Surface-Enhanced Infrared Absorption Spectroscopy

Figure 5.16 shows a representative SEIRAS single-beam background spectrum taken at 0.2 V_{RHE}. Figure 5.17 shows SEIRAS spectra during an anodic CV scan. Table 5.2 shows the average values and standard deviations of the potential when each peak appears and disappears, calculated from five CV scans performed on different days with different cathodes. The disappearance potential of the δ^{HOH} peak does not have a standard deviation because only one CV scan showed the disappearance of that peak.

Figure 5.19 shows the average position and normalized area of the HCO_3^-, CO_3^{2-}, and CO_2 peaks during cathodic and anodic CV scans. The corresponding plots for the CO, δ^{HOH}, and ν^{OH} peaks are shown in Figure 5.3. Figure 5.18 represents the average positions of δ^{HOH}, ν^{OH}, CO, and CO_2 peaks during CA in the dark and in the light. The corresponding plot for HCO_3^- is shown in Figure 5.6. CO_3^{2-} is not plotted because there is insufficient data for this peak in this potential range.

Figure 5.20A shows SEIRAS spectra over 30 minutes during open circuit relaxation after CA at -0.6 V_{RHE} for 90 seconds. The open circuit potential during this time is shown in Figure 5.20B, also corresponding to the data plotted in Figure 5.4. Figure 5.21 represents

the normalized peak area of δ^{HOH} and ν^{OH} over time during CA at -0.4 V_{RHE}.

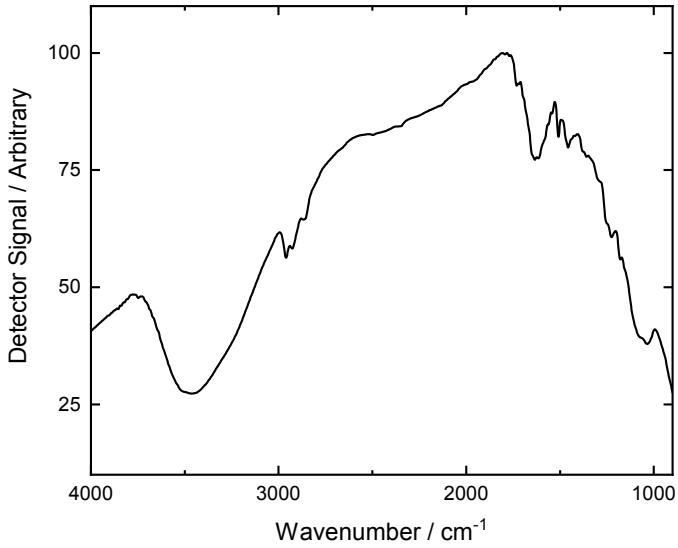

Figure 5.16: Representative single-beam background SEIRAS spectrum taken at 0.2 V_{RHE}. The activated Ag cathode on a Ge ATR crystal was in 0.1 M $KHCO_3$ with continuous CO_2 flow through the electrolyte.

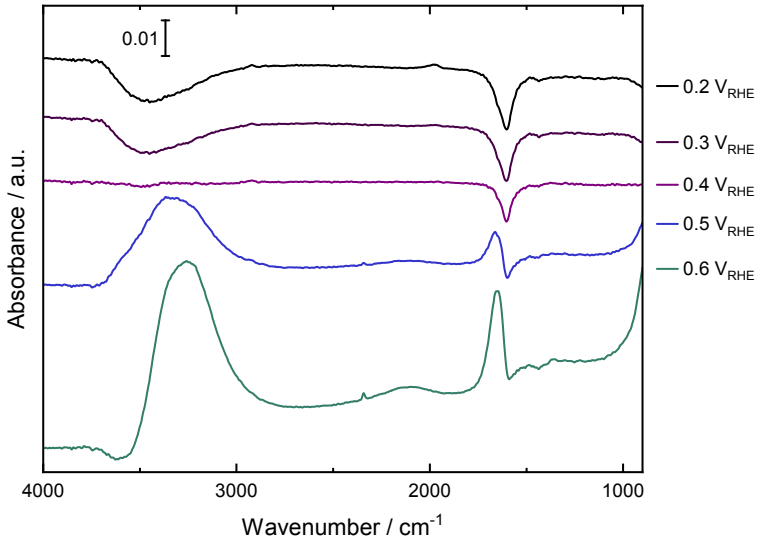

Figure 5.17: SEIRAS spectra taken during a CV scan at 2 mV s^{-1}. The cathodic scan went from 0.2 to -0.9 V_{RHE} and the anodic scan went from -0.9 to 0.6 V_{RHE}. The activated Ag cathode on a Ge ATR crystal was in 0.1 M $KHCO_3$ with continuous CO_2 flow through the electrolyte. The background spectrum was taken at 0.2 V_{RHE}. The scale bar gives the y-axis scale in absorbance units (a.u.).

Table 5.2: Average potential of the appearance and disappearance of ATR–SEIRAS peaks. Average values and standard deviations are calculated from five CV experiments performed on different days with a new cathode prepared each day.

Peak	**Appearance** (V_{RHE})	**Disappearance** (V_{RHE})
Water Bend (δ^{HOH})	0.02 ± 0.07	0.60
Water Stretch (ν^{OH})	-0.24 ± 0.15	0.30 ± 0.09
CO	-0.34 ± 0.06	0.20 ± 0.03
Bicarbonate	-0.56 ± 0.03	-0.57 ± 0.12
CO_2	-0.65 ± 0.03	-0.67 ± 0.06
Carbonate	-0.69 ± 0.03	-0.71 ± 0.01

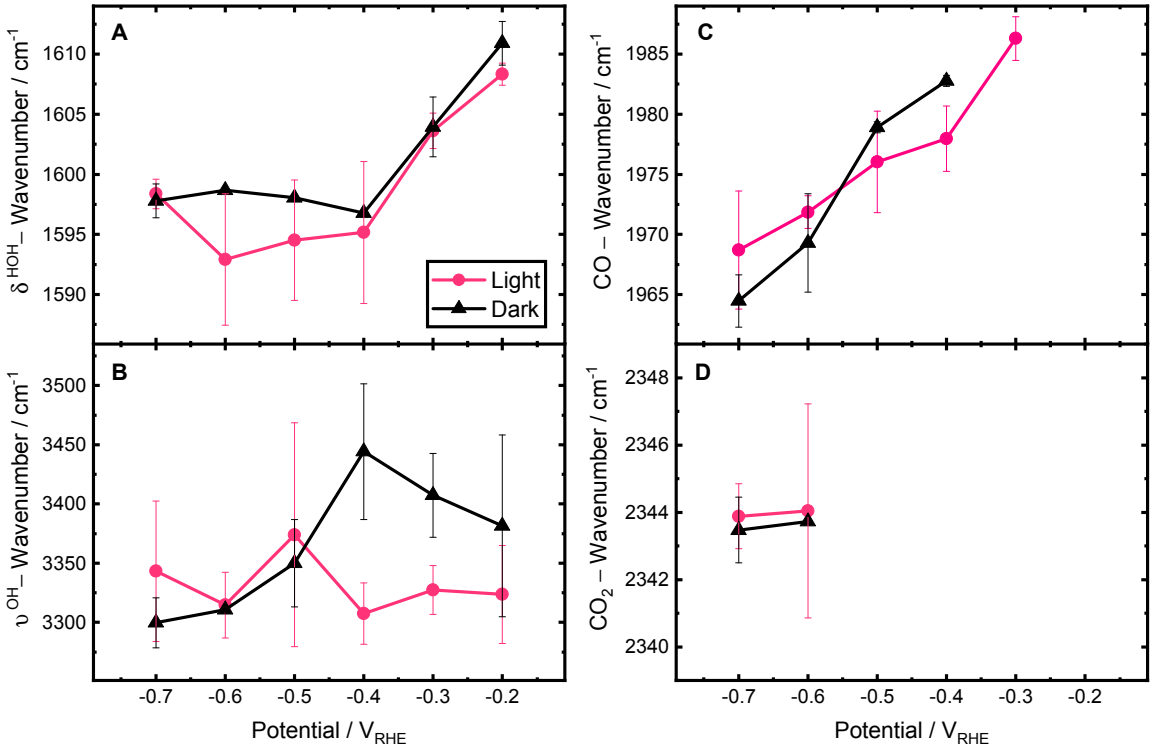

Figure 5.18: Average position of four SEIRAS peaks during CA for 90 seconds under 365 nm illumination (125 mW cm^{-2}) (pink) and in the dark (black): (A) δ^{HOH}, (B) ν^{OH}, (C) CO, and (D) CO_2. Average values and standard deviations are calculated from 2–5 CA experiments at each applied potential. Experiments were performed on different days with a new cathode prepared each day. Error bars represent one standard deviation. The activated Ag cathode on a Ge ATR crystal was in 0.1 M $KHCO_3$ with continuous CO_2 flow through the electrolyte.

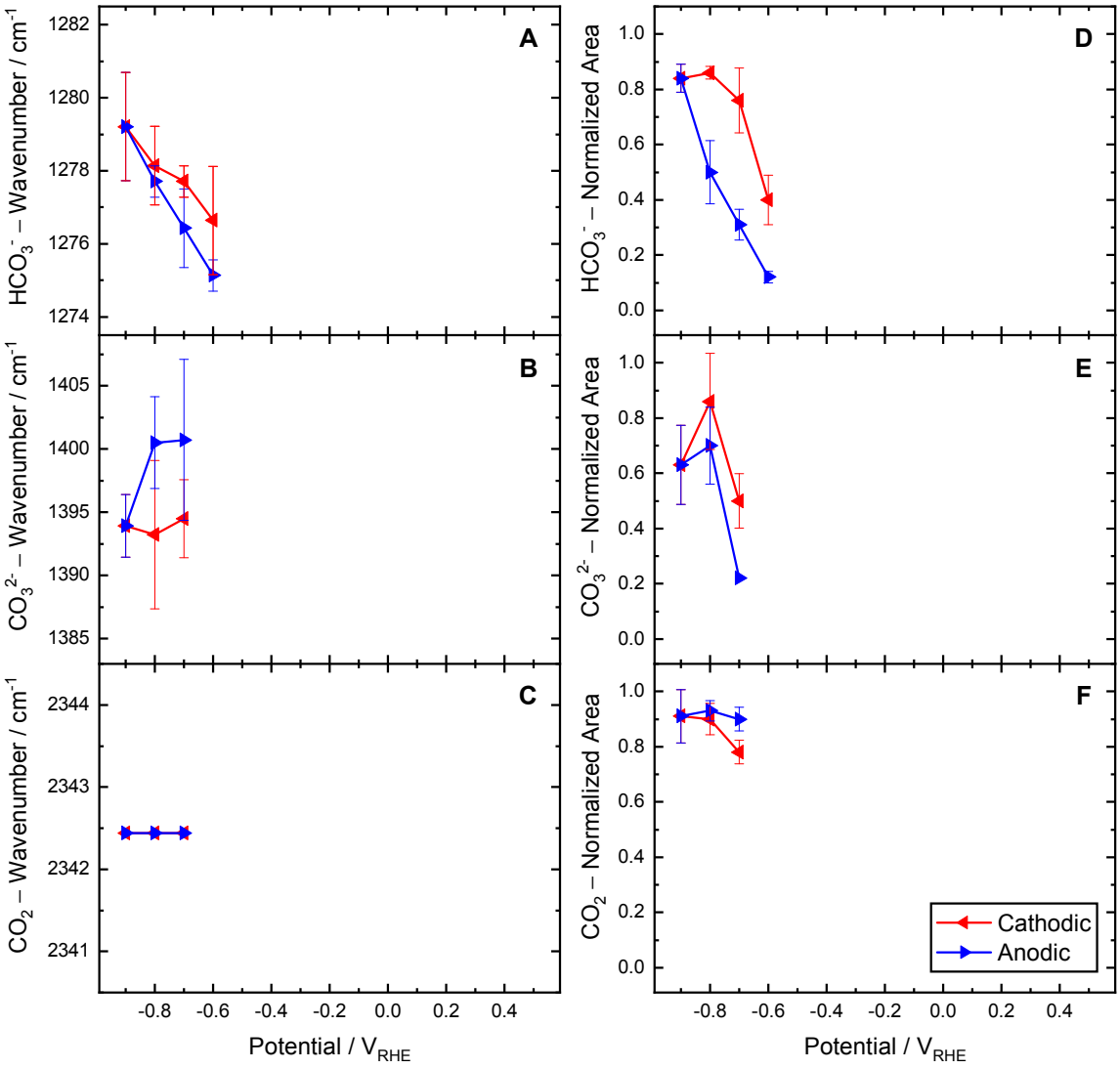

Figure 5.19: Average position (A–C) and normalized area (D–F) of three SEIRAS peaks during CV: HCO_3^- (A and D), CO_3^{2-} (B and E), and CO_2 (C and F). Average values and standard deviations are calculated from five CV experiments performed at 2 mV s^{-1} on different days with a new cathode prepared each day. The area is normalized by the largest area in each individual data set. Error bars represent one standard deviation. Red lines show the cathodic scan from 0.2 to -0.9 V_{RHE} and blue lines show the anodic scan from -0.9 to 0.6 V_{RHE}. The activated Ag cathode on a Ge ATR crystal was in 0.1 M $KHCO_3$ with continuous CO_2 flow through the electrolyte.

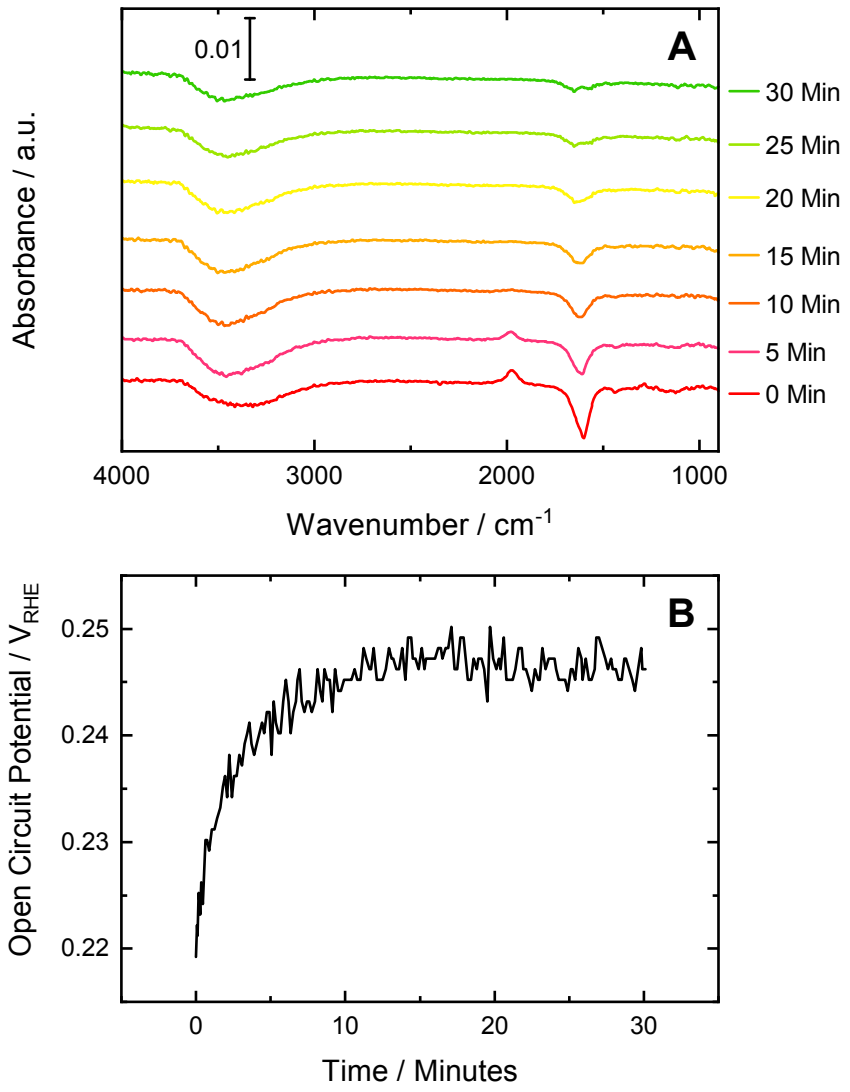

Figure 5.20: SEIRAS spectra (A) and the corresponding open circuit potential (B) recorded during open circuit relaxation. The system was allowed to relax at open circuit after CA at -0.6 V_{RHE} for 90 seconds. The activated Ag cathode on a Ge ATR crystal was in 0.1 M $KHCO_3$ with continuous CO_2 flow through the electrolyte. The background spectrum was taken at 0.2 V_{RHE}. The scale bar in (A) gives the y-axis scale in absorbance units (a.u.).

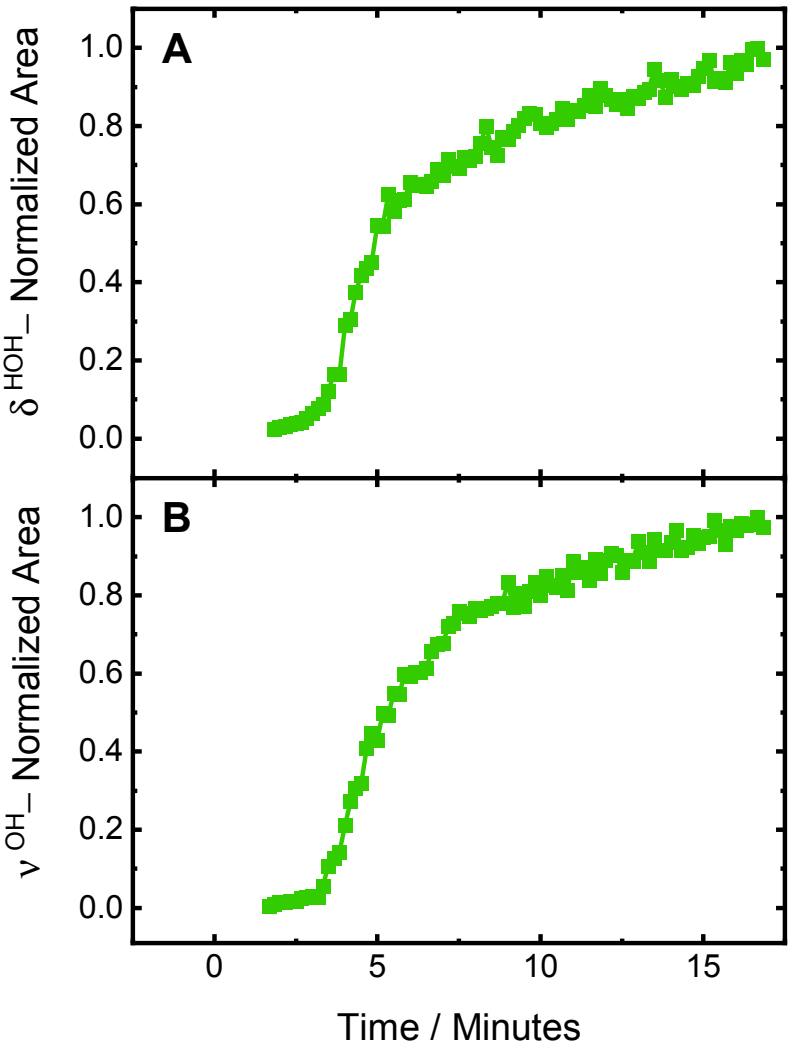

Figure 5.21: Normalized area of two SEIRAS peaks over time during CA at -0.4 V_{RHE}: δ^{HOH} (A) and ν^{OH} (B). The area is normalized by the largest area of each peak. The activated Ag cathode on a Ge ATR crystal was in 0.1 M $KHCO_3$ with continuous CO_2 flow through the electrolyte.

Chapter 6
Reduction of Carbon Dioxide at a Plasmonically Active Copper–Silver Cathode[¶]

6.1 Abstract

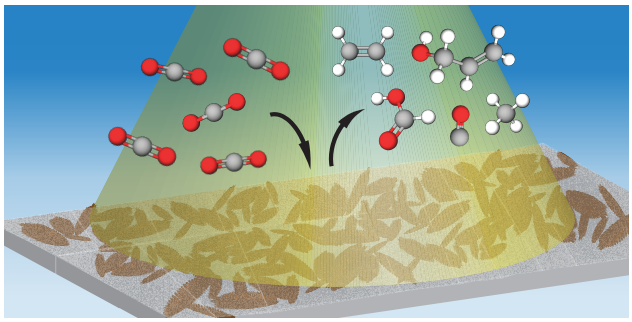

Electrochemically deposited copper nanostructures were coated with silver to create a plasmonically active cathode for carbon dioxide (CO_2) reduction. Illumination with 365 nm light, close to the peak plasmon resonance of silver, selectively enhanced 5 of the 14 typically observed copper CO_2 reduction products while simultaneously suppressing hydrogen evolution. At low overpotentials, carbon monoxide was promoted in the light and at high overpotentials ethylene, methane, formate, and allyl alcohol were enhanced upon illumination; generally C_1 products and C_2/C_3 products containing a double carbon bond were selectively promoted under illumination. Temperature-dependent product analysis in the dark showed that local heating is not the cause of these selectivity changes. While the exact plasmonic mechanism is still unknown, these results demonstrate the potential for enhancing CO_2 reduction selectivity at copper electrodes using plasmonics.

6.2 Introduction

Carbon dioxide (CO_2) reduction can prevent emission of CO_2 into the atmosphere while simultaneously generating valuable products to be used as renewable fuels and chemical precursors. The key challenge in CO_2 reduction is selectively producing multiple-carbon-containing compounds that have higher energy density or higher value than single carbon (C_1) products like methane or carbon monoxide (CO). Copper (Cu) catalysts are well known for their ability to form many two- and three-carbon products (C_2 and C_3), but these products are formed concurrently and often with low Faradaic efficiencies (FE).[2]

Recently we have explored the use of localized surface plasmon resonance (LSPR) in roughened or nanostructured silver (Ag) electrodes to address poor CO_2 reduction selectivity.[36,51] Nanostructured plasmonic metals exhibit peak plasmon resonance at a specific wavelength of light that can be tuned by changing the size, shape, and composition of the nanostructures.[9]

[¶]This chapter was originally published in *Chemical Communications* and is adapted with permission from co-authors A. Subramani, J. K. Cooper, R. Kostecki, J. J. Urban, and B. D. McCloskey and with permission from The Royal Society of Chemistry.[188]

The LSPR can decay to form energetic electron–hole pairs and can generate strong local electric fields, both of which can interact with adsorbates at the cathode surface and influence electrochemical reactions.[6,9] We have shown that an illuminated, plasmonically active Ag cathode enhances all CO_2 reduction products, increasing the formation of CO, formate, and methanol while simultaneously suppressing undesired hydrogen (H_2) evolution.[36,51] Here we investigate a plasmonically active Cu–Ag cathode, combing nanostructured Cu, that has catalytic activity for multi-carbon-containing CO_2 reduction products, with highly plasmonic Ag in an effort to create a more selective catalyst. We explore the changes in product distribution in the light and the dark and with temperature in a custom temperature-controlled photoelectrochemical cell[43] to determine if the plasmonic activity of Ag combined with the catalytic properties of Cu can direct CO_2 reduction towards the formation of select valuable products.

6.3 Electrode Characterization

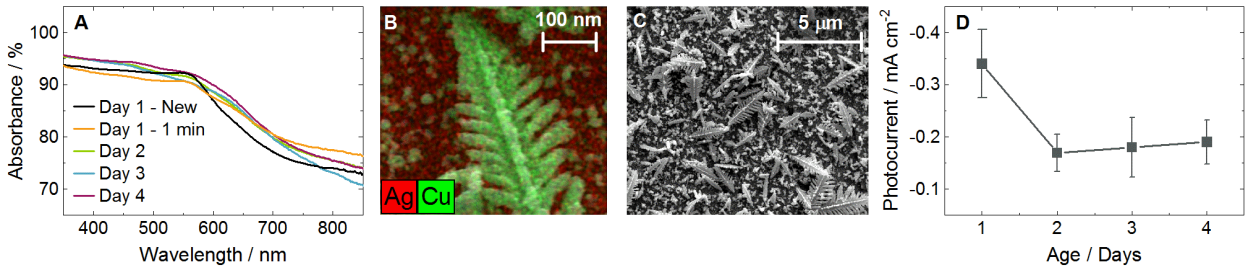

Figure 6.1: Characterization of the cathode stability. (A) UV-visible (UV-vis) absorbance of plasmonically active cathodes as-prepared, after 1 minute of chronoamperometry (CA) at -1.0 V_{RHE}, and after 2, 3, and 4 days of electrochemical experiments. Different cathodes were measured for each day. (B) Energy-dispersive X-ray spectroscopy (EDS) of a nanocoral feature on the surface of the cathode after 3 days of electrochemical experiments. (C) Scanning electron microscopy (SEM) of the cathode surface after 4 days of electrochemical experiments. (D) Photocurrent over time during CA at -0.78 V_{RHE} with 365 nm LED illumination at 170 mW cm^{-2}. Error bars represent one standard deviation of experiments performed in triplicate. See Fig. 6.4–6.6 for further UV-vis plots, Fig. 6.7 for more photocurrent plots, and Fig. 6.9 and 6.10 for additional SEM and EDS images.

Cu nanocorals were electrochemically formed on the surface of a Ag foil following the procedure reported by Gurudayal et al., where a high current density results in the formation of H_2 bubbles that define the nanofeature morphology.[189,190] We selected the nanocoral morphology to study here given their sharp features that should serve to enhance the LSPR (Fig. 6.1B). Despite the bare Cu nanocorals having high optical absorbance across the visible spectrum (Fig. 6.4), the photocurrent density was small (Fig. 6.7C). To enhance the plasmonic photocurrent, 10 nm of Ag was deposited by electron-beam (e-beam) evaporation, forming the "cathode" (Fig. 6.8). This was expected to improve the cathodic photocurrent because Ag has been theoretically shown to produce a bimodal distribution of high-energy electrons and holes, whereas Cu photoexcitation results in a hole-dominant energy distribution.[18] Scanning electron microscopy (SEM) images show a heterogeneous coverage of Cu features ranging

from 10 nm to 2 μm in size with no apparent change observed by SEM in the Cu features after 1 to 4 days of electrochemical experiments (Fig. 6.1C and 6.9). The energy-dispersive X-ray spectroscopy (EDS) image in Fig. 6.1B shows the dominant Cu composition of the nanocorals and the tilted EDS image in Fig. 6.10E more clearly shows the 10 nm Ag layer. X-ray diffraction (XRD) indicates that both Ag and Cu are polycrystalline (Fig. 6.11). X-ray photoelectron spectroscopy (XPS) shows a decrease in the ratio of Ag to Cu after 180 minutes of chronoamperometry (CA) at -1.0 V_{RHE} (V vs. the reversible hydrogen electrode) (Fig. 6.12).

The absorbance measured by UV-visible spectroscopy (UV-vis) showed a flattening of the observable plasmonic peak at 560 nm after just 1 minute of CA at -1.0 V_{RHE}, but thereafter remained relatively constant over 4 days of electrolysis (Fig. 6.1A and 6.5). While the peak at 560 nm matches the plasmon resonance of Cu, it was found that photocurrent measurements were maximized under 365 nm illumination, close to the plasmon resonance of Ag (Fig. 6.6). Fig. 6.7D shows that the decreasing photocurrent density from 365 to 525 nm followed the absorbance trend measured by UV-vis, but where the absorbance only dropped by 2% in this range the photocurrent was diminished by 90%. Thus, all experiments in this study performed in the "light" were conducted with a 365 nm light-emitting diode (LED) at 170 mW cm^{-2}. The peak photocurrent of a new cathode, -0.34 mA cm^{-2}, decreased after exposure to electrolysis but stabilized over 4 days of use at -0.18 mA cm^{-2}, nearly twice the peak photocurrent of bare Cu nanocorals, -0.10 mA cm^{-2} (Fig. 6.1D and 6.7C). We observed that the gaseous product distribution at -0.8 V_{RHE} in the dark and the light was constant over 3 days of electrolysis (Fig. 6.13). From the XPS, photocurrent, UV-vis, and product distribution trends over time we conclude that the e-beam deposited Ag does initially reorganize during electrolysis but stabilizes in a structure that is distinct from, and more plasmonically active than, bare Cu nanocorals.

6.4 Product Analysis Trends with Illumination

The product distribution was investigated from -0.6 to -1.0 V_{RHE} under dark and light conditions at 22°C in 0.1 M potassium bicarbonate ($KHCO_3$) continuously sparged by CO_2. 15 products were detected, but only 5 were selectively enhanced upon illumination. The FE of majority species (>1%) is shown in Fig. 6.2 with the corresponding partial current densities shown in Fig. 6.14. The FE and partial current densities of minority species can be found in Fig. 6.16 and 6.17. All detected products are listed in Table 6.1. Of the 14 products reported by Gurudayal et al. on bare Cu nanocorals,[189] only ethylene glycol was not detected in this study. We measured two additional products, gycolaldehyde and acetone, which have previously been reported as CO_2 reduction products on Cu foil.[2] While there are variations in the dark product distribution between our study and that of Gurudayal et al.,[189] the most notable difference is an increase in CO production, as expected from the addition of Ag.

At low overpotentials (-0.6 and -0.7 V_{RHE}) CO production was enhanced in the light and H_2 was suppressed. While there was no difference in H_2 production in the dark and light at high overpotentials (-0.8, -0.9, and -1.0 V_{RHE}), a *suppression* of CO FE and partial current density was observed in the light at -0.9 and -1.0 V_{RHE}. At these same potentials we find an enhancement of ethylene, methane, formate, and allyl alcohol. These CO, H_2, and formate

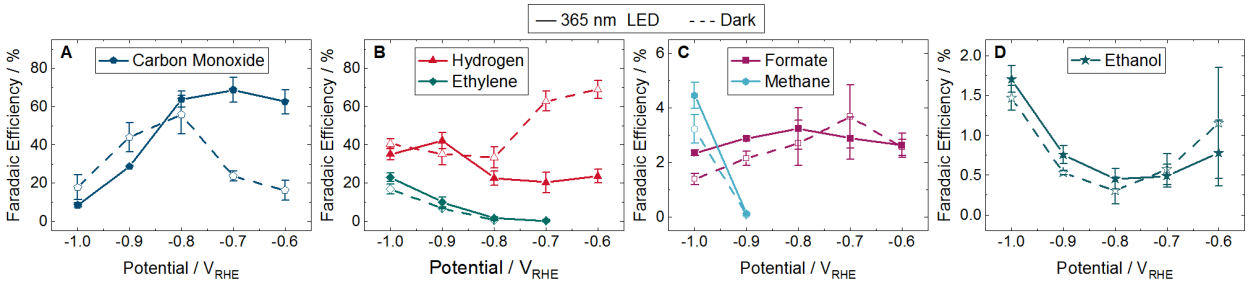

Figure 6.2: Faradaic efficiency (FE) of major products from -0.6 to -1.0 V_{RHE} at 22°C. Dashed lines with unfilled symbols show results performed in the dark and solid lines with filled symbols show results performed under continuous illumination using a 365 nm LED with an intensity of 170 mW cm^{-2}. No points are plotted if the product was not detected. Products shown are (A) carbon monoxide, (B) hydrogen and ethylene, (C) formate and methane, and (D) ethanol. Fig. 6.14 shows the partial current densities for these major products. The FE and partial current densities of the minority products methanol, glycolaldehyde, acetaldehyde, ethane, hydroxyacetone, acetone, allyl alcohol, propionaldehyde, and n-propanol are shown in Fig. 6.16 and 6.17, respectively. Error bars represent one standard deviation of experiments performed in triplicate.

trends in the light are similar to those reported on a plasmonically active Ag cathode.[36] However, where Creel et al.[36] found that all CO_2 reduction products were enhanced in the light, we find that the illuminated Cu–Ag cathode is only selective to 5 of the 14 CO_2 reduction products.

CO is widely cited as an intermediate in the reaction pathway to ethylene and methane.[19] While the exact reaction pathways of C_3 products are unknown,[2] it has been shown that CO can be reduced to propionaldehyde, n-propanol, and allyl alcohol.[191,192] This consumption of CO to create further reduced products may account for the decrease in CO production in the light at these high overpotentials.

While 4 of the 5 major CO_2 reduction species were influenced by the light, ethanol showed no difference between the light and the dark at any applied potential (Fig. 6.2D and 6.14D). Many of the minority products were only produced at potentials cathodic to -1.0 V_{RHE} and all but allyl alcohol have overlapping error bars, indicating no distinction between the light and the dark (Fig. 6.16 and 6.17). Of the minority products, only methanol was detected at every applied potential investigated. There was no difference between methanol results in the light and the dark, and the FE remained below 0.15%. This is in contrast to the results on a plasmonically active Ag cathode, where methanol was only formed in the light at up to 2% FE.[36]

Chemical groupings reveal some trends in the selectivity of CO_2 reduction products. C_1 products (CO, formate, and methane) are generally enhanced in the light, with the exception of methanol. Of C_2 products, only ethylene production is promoted in the light while no significant change is observed in ethanol, glycolaldehyde, acetaldehyde, or ethane. Of C_3 products, only allyl alcohol showed a significant increase in the light, with no difference measured between the light and the dark for propionaldehyde, acetone, n-propanol, or hydroxyacetone.

We also look for trends by functional groups. Alkanes show mixed results with methane enhanced in the light but no change for ethane. The only alkene, ethylene, is promoted in the light. The primary alcohols—methanol, ethanol, and n-propanol—showed no difference between light and dark, but allyl alcohol, which has a double carbon bond like ethylene, was enhanced in the light. No aldehydes were influenced by the light (glycolaldehyde, acetaldehyde, and propionaldehyde). Finally, ketones experienced no difference between the light and the dark, namely acetone and hydroxyacetone, which also have a hydroxyl functional group like the alcohols.

6.5 Product Analysis Trends with Temperature

It is possible for plasmons to decay into phonons, resulting in localized heating that can influence product selectivity.[6] To determine if localized heating was a contributing factor, we measured the product distribution at -0.6 and -1.0 V_{RHE} in the dark at 14, 22, and 35°C in otherwise identical conditions. The FE of majority species are shown in Fig. 6.3 with the corresponding partial current densities shown in Fig. 6.15. The FE and partial current densities of minority species can be found in Fig. 6.18 and 6.19. At -0.6 V_{RHE} CO production in dark conditions showed no trends with temperature (Fig. 6.3A), as opposed to the increase in CO FE in the light (Fig. 6.2A). H_2 formation at -0.6 V_{RHE} increased with increasing temperature (Fig. 6.3B), opposite of the decrease in H_2 production observed in the light (Fig. 6.2B). At -1.0 V_{RHE} CO production increased with increasing temperature (Fig. 6.3A), in direct contrast with the decrease in CO observed in the light (Fig. 6.2A). Similarly, the production of ethylene, methane, formate, and allyl alcohol decreased with increasing temperature at -1.0 V_{RHE} (Fig. 6.3B, 6.3C, and 6.18G), the opposite trend observed in the light (Fig. 6.2B, 6.2C, and 6.16G). Because the product distribution changes caused by the light do not match the product selectivity at elevated temperatures, we conclude

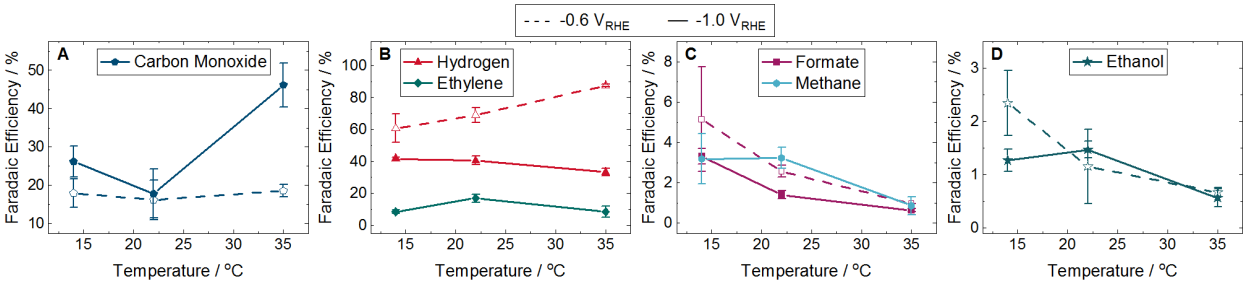

Figure 6.3: Faradaic efficiency (FE) of major products at 14, 22, and 35°C in the dark. Dashed lines with unfilled symbols show results performed at -0.6 V_{RHE} and solid lines with filled symbols show results performed at -1.0 V_{RHE}. Products shown are (A) carbon monoxide, (B) hydrogen and ethylene, (C) formate and methane, and (D) ethanol. Fig. 6.15 shows the partial current densities for these major products. Ethylene and methane were not detected at any temperature at -0.6 V_{RHE}. The FE and partial current densities of the minority products methanol, glycolaldehyde, acetaldehyde, ethane, hydroxyacetone, acetone, allyl alcohol, propionaldehyde, and n-propanol are shown in Fig. 6.18 and 6.19, respectively. Error bars represent one standard deviation of experiments performed in triplicate.

that localized heating from plasmon decay is not contributing to the enhancement of CO_2 reduction in the light.

In addition, we measured the photocurrent at different intensities of 365 nm LED illumination while applying -0.78 V_{RHE} during normal CO_2 reduction conditions (Fig. 6.7E). The photocurrent increased linearly with increasing light intensity which, because we would expect an exponential dependence in the case of heating, further demonstrates an athermal plasmonic mechanism.[70]

6.6 Plasmonic Mechanisms

Other possible plasmonic mechanisms include a permanent or temporary hot electron transfer to an unoccupied molecular orbital (MO) of an adsorbate, or an enhancement of the local electric field (Fig. 6.21).[6,9] In prior work using in situ infrared spectroscopy at a plasmonically active Ag cathode we showed that the increase in CO production at low overpotentials was likely due to an enhanced desorption of CO in the light.[?] This can be understood through a desorption induced by electronic transitions (DIET) mechanism, where an excited metal–CO complex gains enough energy to overcome the activation barrier for desorption before the hot electron decays back to the metal.[9] Because the CO selectivity trends in the light are very similar on this Cu–Ag cathode, it is possible that this DIET mechanism also explains the enhanced CO production in the light at -0.6 and -0.7 V_{RHE}. In the same study we found that light increased the bond strength of bicarbonate (HCO_3^-) at the surface, likely as a result of the enhanced local electric field.[?] This would cause an increase in the local pH, depleting the concentration of protons at the surface and thus suppressing H_2 evolution.[193] Again, because H_2 evolution is also suppressed in the light on this Cu–Ag cathode, the same local electric field mechanism may account for this behavior. However, there is not enough experimental evidence at this time to conclusively determine the plasmonic mechanism influencing CO or H_2 selectivity.

This additional increase in the local pH in the light may explain the results observed at low overpotentials, but it cannot account for the behavior at high overpotentials. Hori et al. showed that in higher pH environments methane formation is suppressed and ethylene production is enhanced.[194] However, we find that both ethylene and methane are enhanced in the light at -1.0 V_{RHE}. Because formate, methane, and ethylene represent branching pathways in the CO_2 reduction reaction, it is likewise difficult to pinpoint a common reaction intermediate that may be selectively accepting a hot electron.[19,194]

6.7 Conclusion

In conclusion, we combined nanostructured Cu with Ag to create a plasmonically active cathode that was stable over multiple days of use. Where a Ag cathode enhanced all CO_2 reduction products in the light,[36] this Cu–Ag cathode is selective to 5 of 14 CO_2 reduction products upon illumination while simultaneously suppressing H_2 evolution, compared to similar results in the dark. At higher overpotentials this Cu–Ag catalyst enhances ethylene, methane, formate, and allyl alcohol in the light; generally C_1 products and C_2/C_3 species with a double carbon bond. A temperature-dependent study showed that product selectivity trends at elevated temperatures are exactly opposite of the behavior we observe upon illumination. In addition, the photocurrent was found to increase linearly with increasing light intensity. From these results we can conclusively state that local heating is not the cause of the selectivity changes in the light, although the exact plasmonic mechanism is still unknown.

This enhancement of select CO_2 reduction products on Cu is a promising demonstration of the potential for plasmon-enhanced electrochemical conversion. With more investigation into the plasmonic mechanisms that influence product selectivity, we can begin to tune plasmonic properties through nanostructure size, shape, and composition to develop a highly selective, plasmonically active catalyst for CO_2 reduction.

6.8 Supplementary Information

Absorption Measurements

UV-vis total reflection measurements of dry cathodes were measured with a Shimadzu SolidSpec-3700 UV-vis-NIR spectrophotometer with an integrating sphere. A NIST-calibrated mirror was used as a reference to find the absolute reflection values, and absorption values were calculated as 100 - % reflectance (Fig. 6.1A and 6.4–6.6).

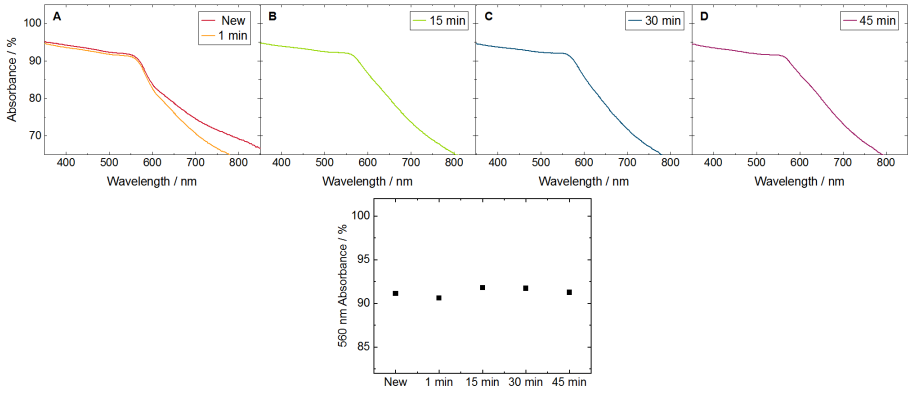

Figure 6.4: UV-visible (UV-vis) absorbance of bare Cu nanocorals (A) as-prepared and after 1 minute of chronoamperometry (CA) at -1.0 V_{RHE} and after (B) 15, (C) 30, and (D) 45 minutes of electrochemical experiments. (E) UV-vis absorbance at 560 nm over time extracted from (A–D). All measurements were performed on the same cathode.

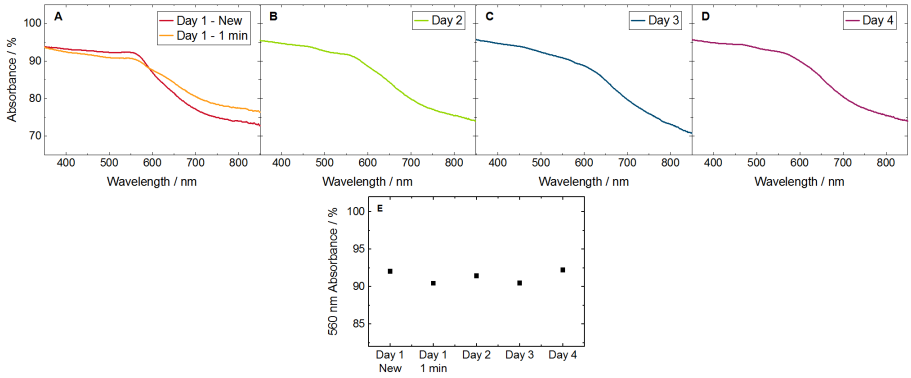

Figure 6.5: UV-visible (UV-vis) absorbance of the plasmonically active cathode (10 nm of Ag on Cu nanocorals) (A) as-prepared and after 1 minute of chronoamperometry (CA) at -1.0 V_{RHE} and after (B) 2, (C) 3, and (D) 4 days of electrochemical experiments. (E) UV-vis absorbance at 560 nm over time extracted from (A–D). The same cathode was used for the measurements performed on Day 1. Different cathodes were used for the measurements performed after 2, 3, and 4 days.

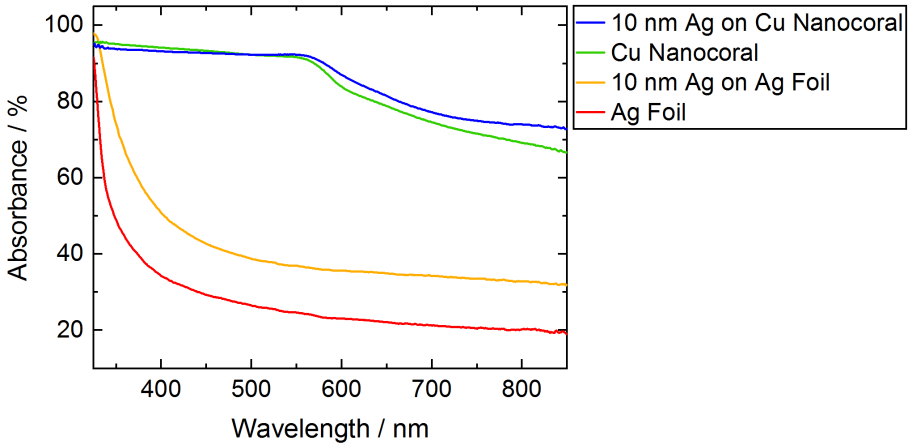

Figure 6.6: UV-visible (UV-vis) absorbance of Ag foil (red), 10 nm of Ag on Ag foil (orange), bare Cu nanocorals (green), and 10 nm of Ag on Cu nanocorals (blue). Different Ag foil substrates were used for each measurement. All samples were as-prepared, no electrochemistry was performed prior to the UV-vis measurement. For the 10 nm Ag on Ag foil, a 3 nm Ti layer was first deposited by electron-beam (e-beam) evaporation for adhesion.

Photocurrent Measurements

Photocurrent measurements were performed by chopping the light at 3 Hz using a Stanford Research Systems SR850 lock-in amplifier to control a ThorLabs SHB1 shutter. A square wave is produced (Fig. 6.7A) and the photocurrent is calculated as the difference between the current when the light is incident on the cathode and the current when the cathode is in the dark. A photocurrent is only produced through a plasmonic mechanism when an electron has sufficiently high energy to transfer to an adsorbate, and if that transfer occurs.

Linear sweep voltammetry (LSV) was performed at 5 mV s^{-1} while chopping the light to identify the peak photocurrent voltage, -0.78 V_{RHE} (Fig. 6.7B). Reported photocurrent values were collected while chopping the light during chronoamperometry (CA) at -0.78 V_{RHE} for 4 minutes and averaging the photocurrent over the last 2 minutes. Depositing Ag on the Cu nanocorals more than tripled the photocurrent (Fig. 6.7C). The photocurrent decreased with increasing wavelength of incident light at equal photon flux (3.2 x 10^{17} photons cm^{-2} s^{-1}), following the light absorbance trend measured by UV-visible spectroscopy (UV-vis) (Fig. 6.1A, 6.5, and 6.7D). The photocurrent increased linearly with increasing light intensity during 365 nm LED illumination at -0.78 V_{RHE} (Fig. 6.7E).

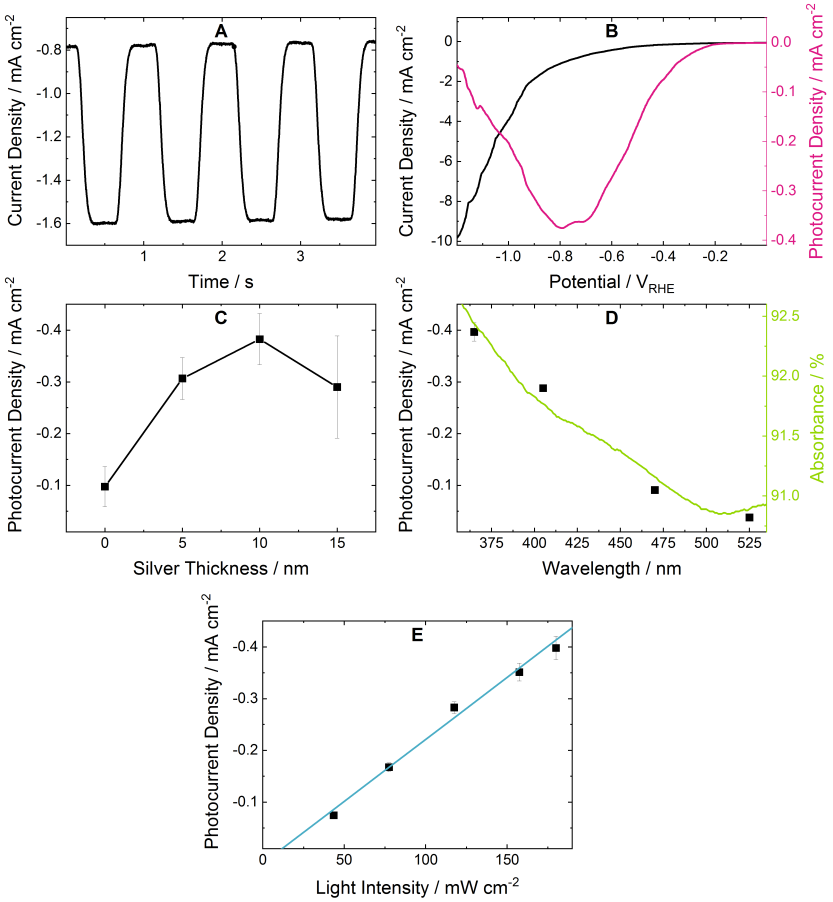

Figure 6.7: Photocurrent measurements. (A) Example of the square wave produced during chopped light experiments using the 365 nm LED. The carbon dioxide (CO_2) bubbles were stopped and the frequency set at 1 Hz to reduce the noise, resulting in a higher photocurrent. (B) Representative linear sweep voltammetry (LSV) at 5 mV s^{-1} during 3 Hz chopping of the 365 nm LED (170 mW cm^{-2}) with continuous CO_2 flow. The total current density is shown in black (left axis) and the extracted photocurrent density is shown in pink (right axis), both filtered with exponential smoothing for clarity. The peak photocurrent voltage occurred at -0.78 V_{RHE}. The cathode had previously experienced 45 minutes of chronoamperometry (CA) at -1.0 V_{RHE}. (C) Photocurrent densities measured at -0.78 V_{RHE} using cathodes of bare Cu nanocorals and Cu nanocorals with 5, 10, and 15 nm of Ag deposited on top by electron-beam (e-beam) evaporation. Error bars represent one standard deviation of experiments performed in triplicate. (D) Photocurrent densities measured at different wavelengths of light with equal photon fluxes of 3.2 x 10^{17} photons cm^{-2} s^{-1} (black, left axis). The cathode had previously experienced 45 minutes of CA at -1.0 V_{RHE}. Error bars represent one standard deviation of experiments performed in triplicate. Absorbance measured by UV-visible spectroscopy (UV-vis) was averaged over measurements performed after 0 to 120 minutes of CA at -1.0 V_{RHE} (green, right axis). (E) Photocurrent densities during 365 nm LED illumination across a range of light intensities at -0.78 V_{RHE}. The line represents the least-squares regression line. Error bars represent one standard deviation of experiments performed in triplicate.

Cathode Fabrication

Silver (Ag) foil (Alfa Aesar 12126, 0.1 mm thick, hard, Premion 99.998%) was cut into a square with a side length of approximately 2.5 cm. The Ag foil was then wet sanded (Norton T401, 2000 grit) and polished with alumina nanoparticles (TED Pella Inc. 895-55, 0.3 µm). Subsequently, the Ag foil was rinsed with 18.2 MΩ deionized water from a Millipore system in between polishing steps. The Ag foil was then sonicated for 15 minutes in each of the following solutions: acetone, isopropanol, and Millipore water. Then the Ag foil was sonicated for 5 minutes in 0.1 M hydrochloric acid (HCl) followed by another 15 minutes of sonication in Millipore water. A 2:1 solution of 0.1 M copper(II) sulfate hydrate ($CuSO_4$) (Alfa Aesar 10701, Puratronic 99.999%) and 0.1 M sulfuric acid (H_2SO_4) was created with a pH of 1 to be used as the electrolyte in the electrodeposition of the Cu nanocorals.[189] A beaker cell setup was used to deposit the nanocorals with the cleaned Ag foil as the working electrode and platinum mesh (approximately 1 cm^2) as both the counter and reference electrode. In order to deposit the nanocorals, -400 mA was applied to the Ag foil for 10 seconds; this high current density results in the formation of H_2 bubbles that define the nanofeature morphology.[189] The electrode was then rinsed in Millipore water and dried with compressed nitrogen. Unless otherwise noted, all cathodes in this study then had 10 nm of Ag deposited on the Cu nanocorals by electron-beam (e-beam) evaporation. A schematic and picture of the Cu–Ag cathode is shown in Fig. 6.8.

The Ag foil substrate will have limited influence on the plasmonic and photocurrent properties of the Cu–Ag cathode because it is a relatively flat surface. Kim et al. showed that Ag foil required intentional surface roughening through cyclic voltammetry to high anodic potentials to achieve even a small photocurrent.[51] Comparing the CO_2 reduction product distribution results of Gurudayal et al. (bare Cu nanocorals deposited on a Ag foil) to those of Kuhl et al. (Cu foil), the similar Faradaic efficiencies (FE) of CO demonstrate that the Ag foil substrate also has a limited impact on the catalytic activity of the Cu nanocorals.[2,189]

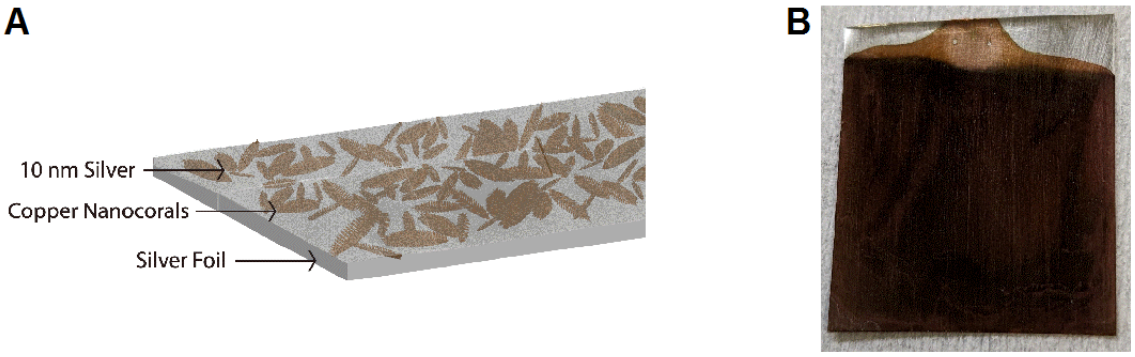

Figure 6.8: (A) Cathode schematic and (B) cathode picture. Cu nanocorals are electrochemically deposited on a Ag foil. 10 nm of Ag is deposited by e-beam on the Cu nanocorals.

Cathode Surface Imaging

Scanning electron microscopy (SEM) and energy-dispersive X-ray spectroscopy (EDS) images are shown in Fig. 6.1, 6.9, and 6.10. Multiple images at different locations were taken on each cathode to ensure that presented images are representative of the entire surface.

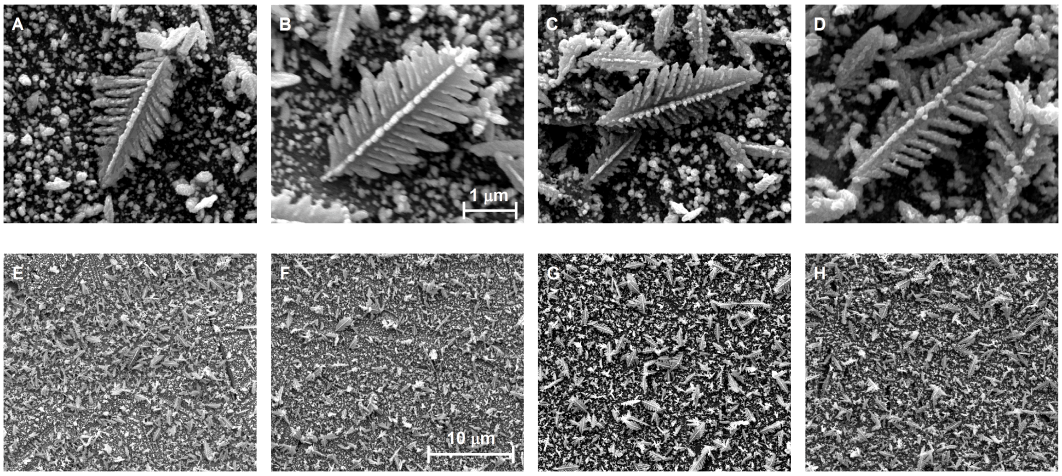

Figure 6.9: Scanning electron microscopy (SEM) images of the cathode surface (A and E) as-deposited and after (B and F) 2 days, (C and G) 3 days, and (D and H) 4 days of electrochemical experiments. The scale bar in (B) applies to (A–D) and the scale bar in (F) applies to (E–H). Different cathodes were imaged for each day.

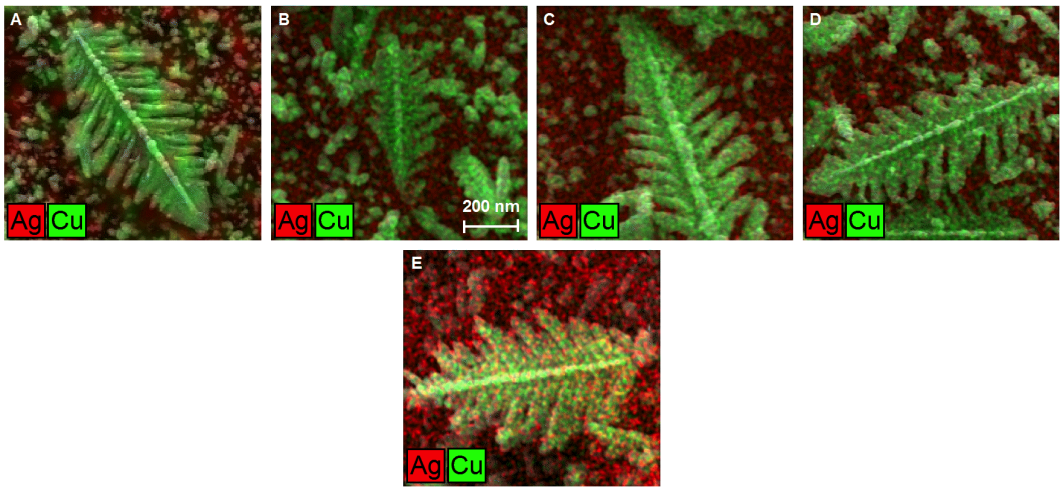

Figure 6.10: Energy-dispersive X-ray spectroscopy (EDS) images of the cathode surface (A) as-deposited and after (B) 2, (C) 3, and (D–E) 4 days of electrochemical experiments. The cathode surface in (E) was tilted at 60°. The scale bar in (B) applies to all of the images in this figure. Different cathodes were imaged for each day.

XRD Measurements

The crystalline structure of the cathode was analyzed by X-ray diffraction (XRD) with a Rigaku Smartlab diffractometer using Cu Kα radiation. The grazing incidence angle was fixed at 0.5°, 1.0°, or 1.5° and the detector angle was scanned between 25° and 75°. Peaks were observed for Cu, Cu_2O, and Ag at all grazing incidence angles as shown in Figure 6.11. Both Ag and Cu are polycrystalline.

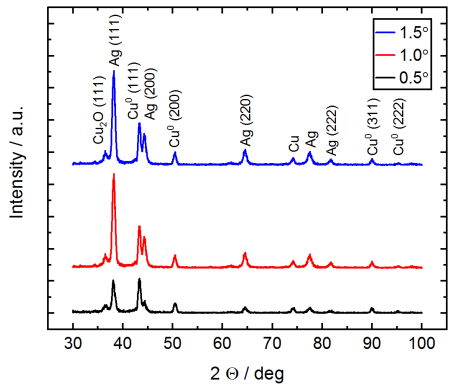

Figure 6.11: XRD pattern of a cathode after 1 day of electrochemical experiments. The grazing incidence angle was 0.5° (black), 1.0° (red), or 1.5° (blue).

XPS Measurements

The surface compositions were probed using X-ray photoelectron spectroscopy (XPS) acquired by a Kratos Axis Ultra spectrometer using an Al K-Alpha X-ray source (hν = 1486.69 eV) operated at 75 W with a hemispherical electron energy analyzer (Fig. 6.12). Parameters used for the measurements of Ag3d3/2, Ag3d5/2, Cu2p1/2, and Cu2p3/2 were: pass energy, 20 eV; energy step size, 0.05 eV; dwell time, 300 ms; 6 scans.

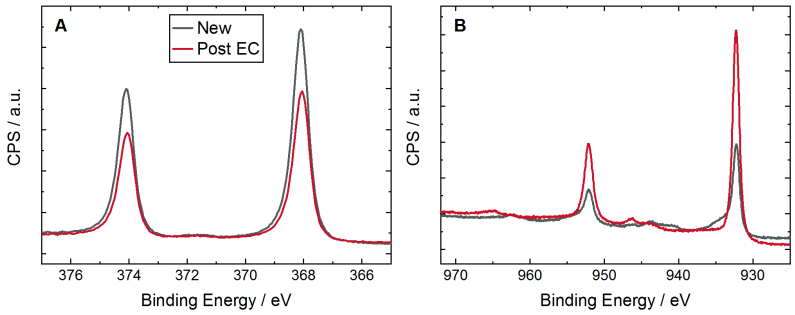

Figure 6.12: XPS spectra of a new cathode (black) and the same cathode after 180 minutes of chronoamperometry (CA) at -1.0 V_{RHE} (red). Peaks shown are (A) Ag (3d3/2 and 3d5/2) and (B) Cu (2p1/2 and 2p3/2). The ratio of the sum of the peak areas of Ag3d3/2 and Ag3d5/2 to the peak area of Cu2p3/2 is normalized to 1 for the new cathode and decreases to 0.35 after electrolysis.

Electrochemical Measurements

0.05 M potassium carbonate (K_2CO_3) (Alfa Aesar 10838, Puratronic 99.997%) was prepared with Millipore water. Upon saturation with carbon dioxide (CO_2) the solution became 0.1 M potassium bicarbonate ($KHCO_3$) (pH 6.8). Electrochemical measurements were performed in a leak-tight polyether ether ketone (PEEK) compression cell described by Corson et al.[43] CO_2 was continuously bubbled through the electrolyte at 5 sccm. A leak-free Ag/AgCl reference electrode (Innovative Instruments, Inc. LF-1) was located in close proximity to the cathode. All potentials in this study are reported versus the reversible hydrogen electrode (RHE). A thermistor (Micro Lab 103) covered with a fluorinated ethylene propylene (FEP) heat shrink cap was in contact with the catholyte. A peltier device (Ferrotec 72008/131/150B) in contact with the back of the cathode, heat sink with fan, and a proportional-integral-derivative (PID) controller maintained the catholyte at the desired set point ±0.1°C. An anion exchange membrane (Asahi Glass, Selemion AMV) separated the cathode and anode chambers. A platinum (Pt) foil was used as the anode. The cathode and anode were each compressed against an o-ring (Ace Seal 2-015, Kalrez 6375) exposing a 1 cm^2 geometric surface area.

CO_2 was bubbled through the electrolyte for 10 minutes before the start of an electrochemical experiment to ensure saturation. Electrochemical experiments were performed with a Biologic SP-300 potentiostat. Impedance spectroscopy was performed at the open circuit potential from 100 to 1 kHz with a 10 mV amplitude and the resulting resistance was used to apply an 85% IR correction to each electrochemical measurement. Typical resistance values ranged from 40 to 50 Ω. The cathode was front-illuminated through a quartz window primarily using a 365 nm ultra-high-power light-emitting diode (LED) (Mightex Systems LCS-0365-48-22) with a light intensity of 170 mW cm^{-2} at the surface of the cathode. Other LEDs in this study include 405 nm (Mightex Systems LCS-0405-50-22), 470 nm (Mightex Systems LCS-0470-50-22), and 525 nm (Mightex Systems LCS-0525-6022). The light intensity was measured with a Coherent PowerMax PM10 power meter.[36]

Product Measurements

The product analysis experiments were conducted in a temperature-controlled cell described by Corson et al.[43] The gaseous products were quantified using an in-line Multiple Gas Analyzer #5 SRI Instruments gas chromatography (GC) analyzer with a 12 ft HayeSep D (divinylbenzene) column, thermal conductivity detector (TCD), flame ionization detector (FID) preceded by a methanizer, and Ar carrier gas. Each product analysis run was a single potential and temperature applied to the cell for 64 minutes with GC injections at 3, 15, 27, 39, 51, and 63 minutes with the data from 15–63 minutes averaged and reported. The concentration of each gas was calculated using a calibration curve with points from at least 3 different concentrations. Liquid products remaining in the electrolyte were analyzed using proton nuclear magnetic resonance (^{1}H NMR) spectroscopy on a Bruker Avance III 500 MHz magnet. Concentrations in the electrolyte were determined using phenol and dimethyl sulfoxide (DMSO) as internal standards, while using a water suppression method.[2] More details on the NMR and GC analysis can be found in our previous paper.[43] A list of all products detected in this study is shown in Table 6.1.

Table 6.1: CO_2 Reduction Products

Product	Chemical Formula	Carbons	Electrons	State
Carbon Monoxide	CO	C_1	2	Gas
Formate	$HCOO^-$	C_1	2	Liquid
Methane	CH_4	C_1	8	Gas
Glycolaldehyde	$C_2H_4O_2$	C_2	8	Liquid
Acetaldehyde	C_2H_4O	C_2	10	Liquid
Ethanol	C_2H_6O	C_2	12	Liquid
Ethylene	C_2H_4	C_2	12	Gas
Ethane	C_2H_6	C_2	14	Gas
Hydroxyacetone	$C_3H_6O_2$	C_3	14	Liquid
Acetone	C_3H_6O	C_3	16	Liquid
Allyl Alcohol	C_3H_6O	C_3	16	Liquid
Propionaldehyde	C_3H_6O	C_3	16	Liquid
n-Propanol	C_3H_8O	C_3	18	Liquid

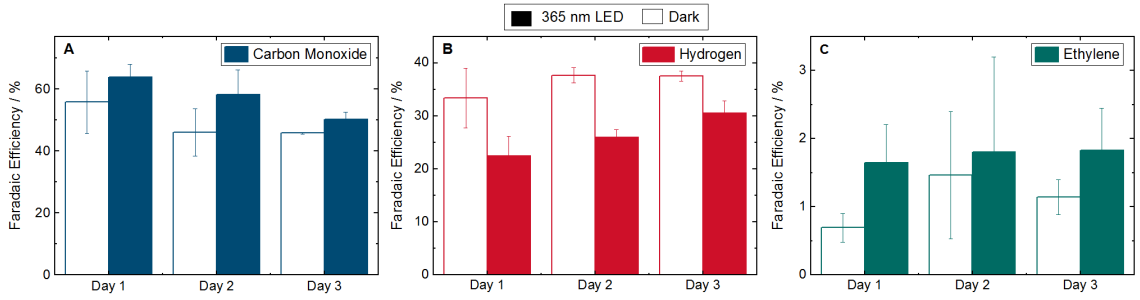

Figure 6.13: Faradaic efficiencies (FE) of gaseous products demonstrating electrode stability over time. Gaseous products (A) carbon monoxide, (B) hydrogen, and (C) ethylene were measured at -0.8 V_{RHE} in the dark (unfilled columns) and under 365 nm LED illumination at 170 mW cm^{-2} (filled columns) after 1, 2, and 3 days of cathode use for electrochemical experiments. One-way ANOVA analysis showed no statistically significant difference for any of the results over time within a confidence interval of 95%. Error bars represent one standard deviation of experiments performed in triplicate.

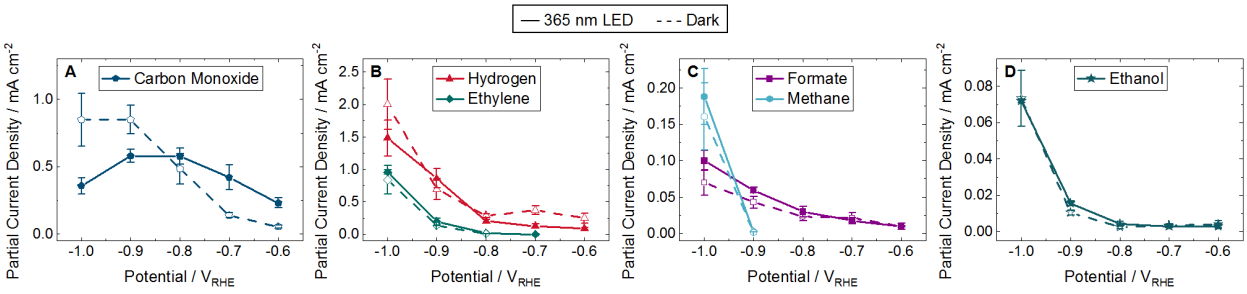

Figure 6.14: Partial current densities of major products from -0.6 to -1.0 V_{RHE} at 22°C corresponding to the Faradaic efficiencies (FE) shown in Fig. 6.2. Dashed lines with unfilled symbols show results performed in the dark and solid lines with filled symbols show results performed under continuous illumination using a 365 nm LED with an intensity of 170 mW cm^{-2}. No points are plotted if the product was not detected. Products shown are (A) carbon monoxide, (B) hydrogen and ethylene, (C) formate and methane, and (D) ethanol. The FE and partial current densities of the minority products methanol, glycolaldehyde, acetaldehyde, ethane, hydroxyacetone, acetone, allyl alcohol, propionaldehyde, and n-propanol are shown in Fig. 6.16 and 6.17, respectively. Error bars represent one standard deviation of experiments performed in triplicate.

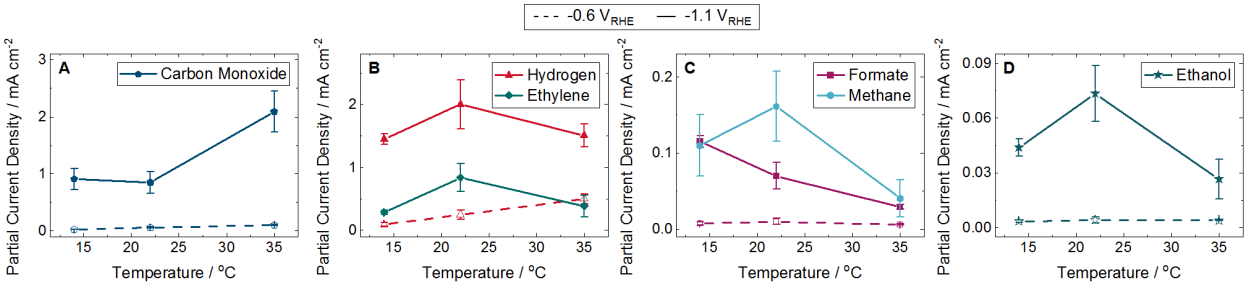

Figure 6.15: Partial current densities of major products at 14, 22, and 35°C in the dark. Dashed lines with unfilled symbols show results performed at -0.6 V_{RHE} and solid lines with filled symbols show results performed at -1.0 V_{RHE}. Products shown are (A) carbon monoxide, (B) hydrogen and ethylene, (C) formate and methane, and (D) ethanol. Fig. 6.3 shows the Faradaic efficiencies (FE) for these major products. Ethylene and methane were not detect at any temperature at -0.6 V_{RHE}. The FE and partial current densities of the minority products methanol, glycolaldehyde, acetaldehyde, ethane, hydroxyacetone, acetone, allyl alcohol, propionaldehyde, and n-propanol are shown in Fig. 6.18 and 6.19, respectively. Error bars represent one standard deviation of experiments performed in triplicate.

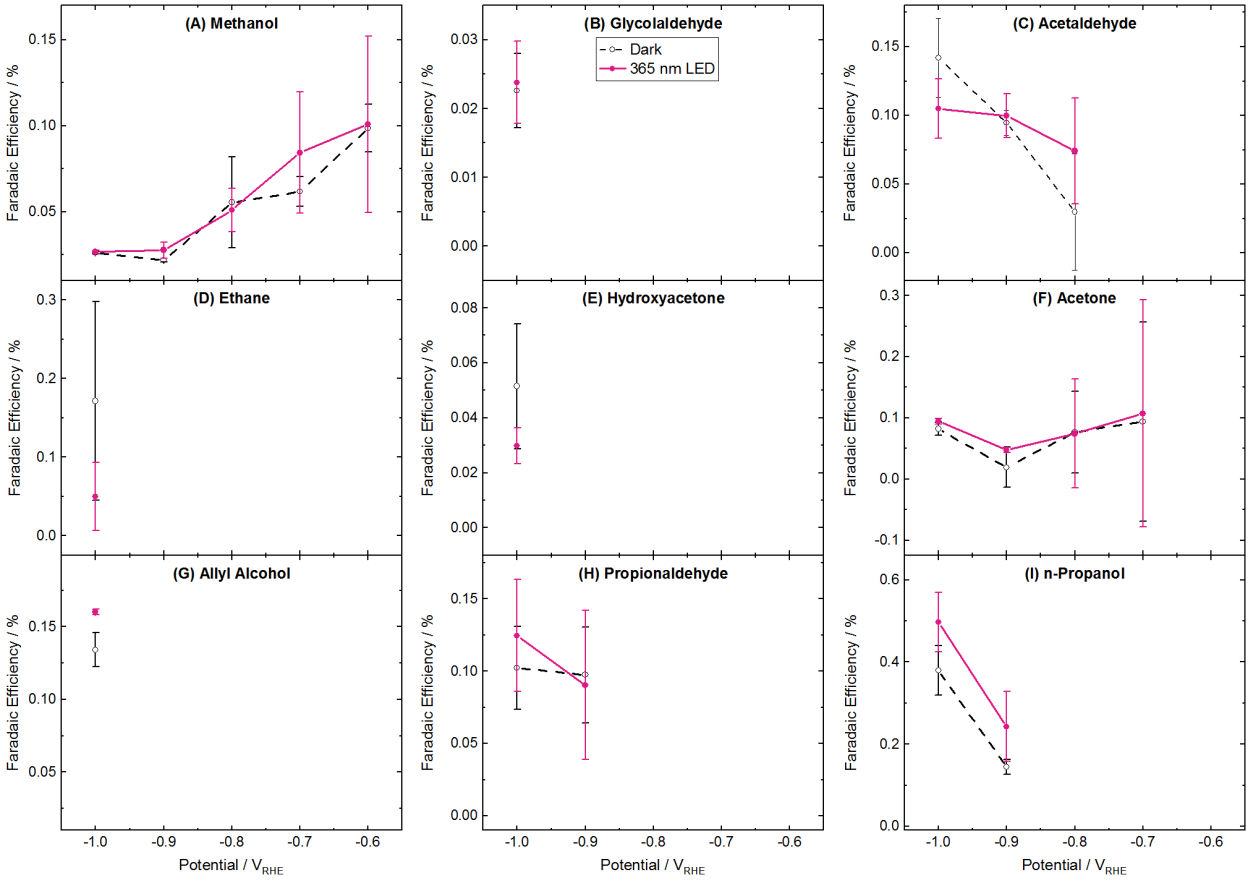

Figure 6.16: Faradaic efficiencies (FE) of minor products from -0.6 to -1.0 V_{RHE} at 22°C. FE of (A) methanol, (B) glycolaldehyde, (C) acetaldehyde, (D) ethane, (E) hydroxyacetone, (F) acetone, (G) allyl alcohol, (H) propionaldehyde, and (I) n-propanol. Dashed lines with unfilled symbols show results performed in the dark and solid lines with filled symbols show results performed under continuous illumination using a 365 nm LED with an intensity of 170 mW cm^{-2}. No points are plotted if the product was not detected. Corresponding major products are shown in Fig. 6.2 ((FE) and 6.14 (partial current densities). Fig. 6.17 shows the partial current densities for these minor products. Error bars represent one standard deviation of experiments performed in triplicate.

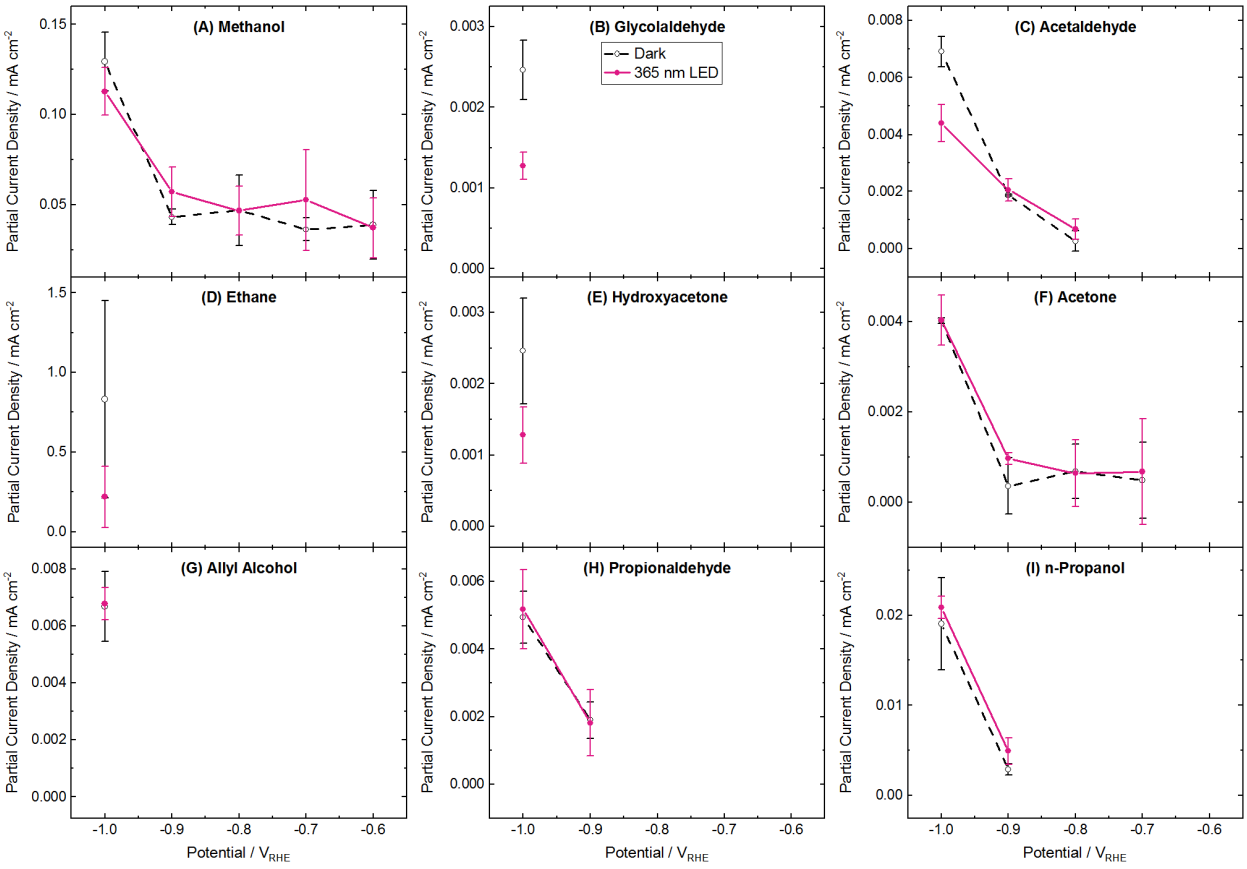

Figure 6.17: Partial current densities of minor products from -0.6 to -1.0 V_{RHE} at 22°C. Partial current densities of (A) methanol, (B) glycolaldehyde, (C) acetaldehyde, (D) ethane, (E) hydroxyacetone, (F) acetone, (G) allyl alcohol, (H) propionaldehyde, and (I) n-propanol. Dashed lines with unfilled symbols show results performed in the dark and solid lines with filled symbols show results performed under continuous illumination using a 365 nm LED with an intensity of 170 mW cm^{-2}. No points are plotted if the product was not detected. Corresponding major products are shown in Fig. 6.2 (Faradaic efficiencies (FE)) and 6.14 (partial current densities). Fig. 6.16 shows the FE for these minor products. Error bars represent one standard deviation of experiments performed in triplicate.

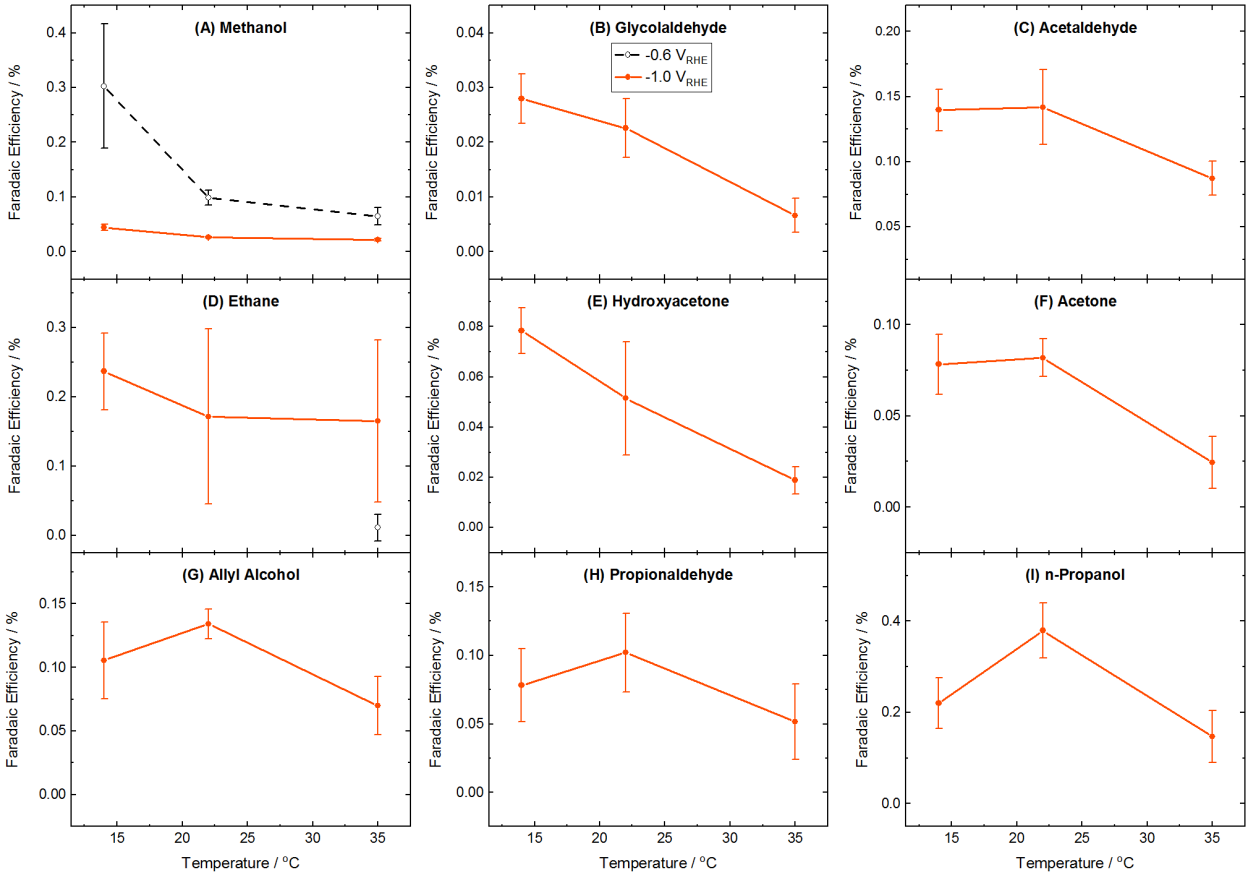

Figure 6.18: Faradaic efficiencies (FE) of minor products at 14, 22, and 35°C in the dark. FE of (A) methanol, (B) glycolaldehyde, (C) acetaldehyde, (D) ethane, (E) hydroxyacetone, (F) acetone, (G) allyl alcohol, (H) propionaldehyde, and (I) n-propanol. Dashed lines with unfilled symbols show results performed at -0.6 V_{RHE} and solid lines with filled symbols show results performed at -1.0 V_{RHE}. No points are plotted if the product was not detected. Corresponding major products are shown in Fig. 6.3 (FE) and 6.15 (partial current densities). Fig. 6.19 shows the partial current densities for these minor products. Error bars represent one standard deviation of experiments performed in triplicate.

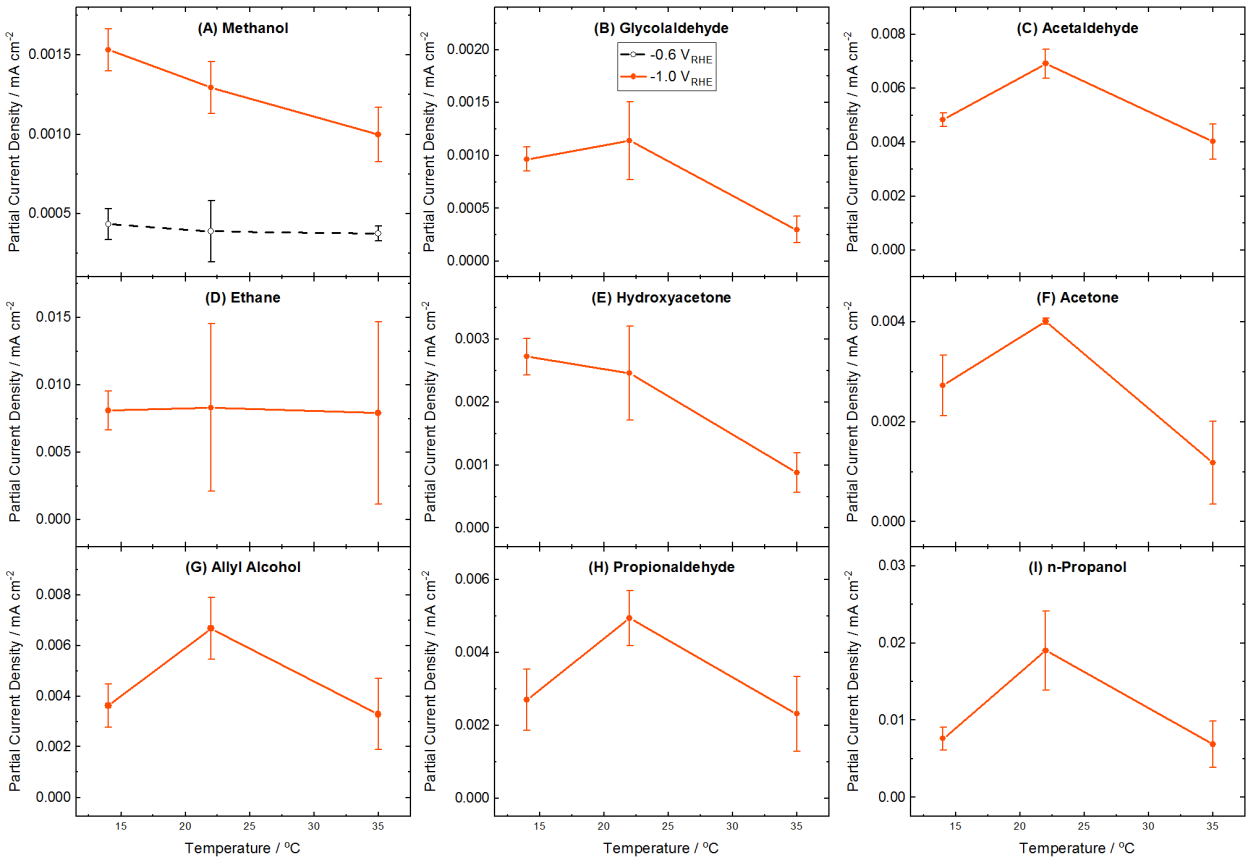

Figure 6.19: Partial current densities of minor products at 14, 22, and 35°C in the dark. Partial current densities of (A) methanol, (B) glycolaldehyde, (C) acetaldehyde, (D) ethane, (E) hydroxyacetone, (F) acetone, (G) allyl alcohol, (H) propionaldehyde, and (I) n-propanol. Dashed lines with unfilled symbols show results performed at -0.6 V_{RHE} and solid lines with filled symbols show results performed at -1.0 V_{RHE}. No points are plotted if the product was not detected. Corresponding major products are shown in Fig. 6.3 (Faradaic efficiencies (FE)) and 6.15 (partial current densities). Fig. 6.18 shows the FE for these minor products. Error bars represent one standard deviation of experiments performed in triplicate.

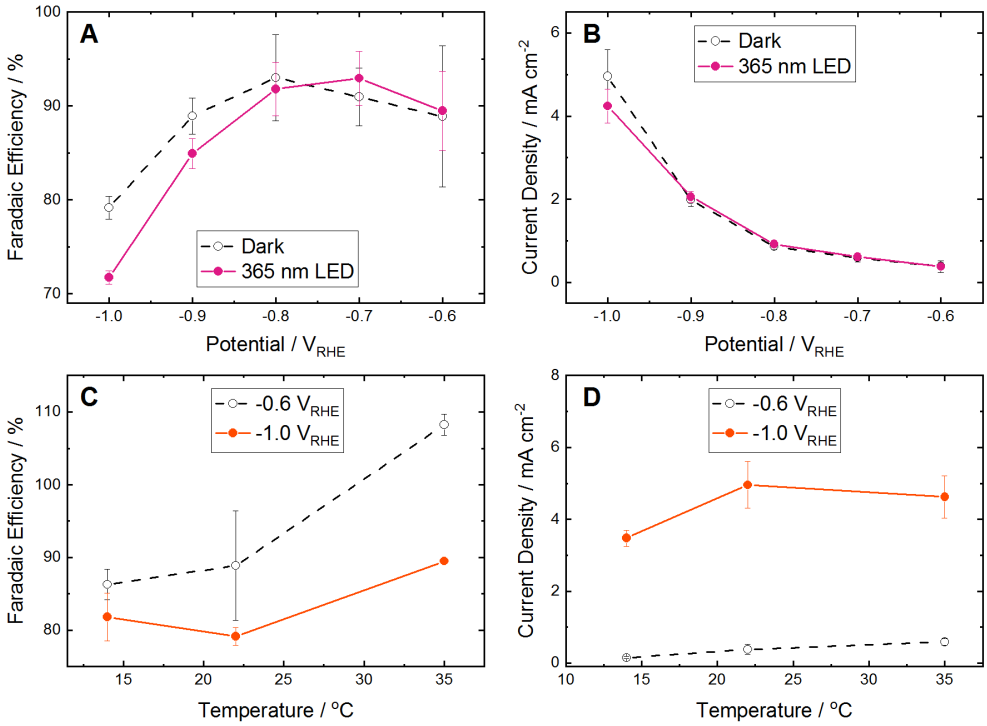

Figure 6.20: (A) The total Faradaic efficiencies (FE) from -0.6 to -1.0 V_{RHE} at 22°C for results shown in Fig. 6.2 and 6.16. (B) The total current densities from -0.6 to -1.0 V_{RHE} at 22°C for results shown in Fig. 6.14 and 6.17. Dashed lines in (A) and (B) with unfilled symbols show results performed in the dark and solid lines with filled symbols show results performed under continuous illumination using a 365 nm LED with an intensity of 170 mW cm^{-2}. (C) The total FE at 14, 22, and 35°C in the dark for results shown in Fig. 6.3 and 6.18. (D) The total current densities at 14, 22, and 35°C in the dark for results shown in Fig. 6.15 and 6.19. Dashed lines in (C) and (D) with unfilled symbols show results performed at -0.6 V_{RHE} and solid lines with filled symbols show results performed at -1.0 V_{RHE}. Error bars in all plots represent one standard deviation of experiments performed in triplicate.

Plasmonic Mechanisms

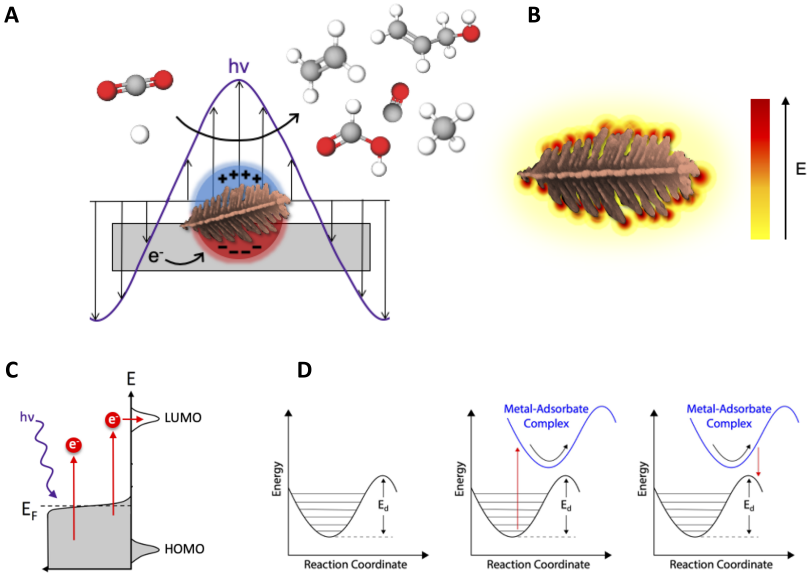

Figure 6.21: (A) Incident light ($h\nu$) on the cathode surface results in a collective oscillation of the electrons, a phenomenon known as localized surface plasmon resonance (LSPR). In this study, illumination of the Cu–Ag cathode during CO_2 reduction resulted in the plasmon-enhanced formation of carbon monoxide, ethylene, methane, formate, and allyl alcohol. Adapted with permission from ref. 195. Copyright 2003, American Chemical Society. Possible plasmonic mechanisms are (B) the enhancement of the local electric field or (C) a permanent or (D) temporary hot electron transfer. (B) LSPR can generate strong local electric fields which can influence the bond energy of adsorbates at the cathode surface. The electric field is expected to be maximized at the tips of the nanocorals.[51] (C) LSPR can also decay to form energetic electron–hole pairs. In the schematic, a hot electron is permanently transferred to an unoccupied molecular orbital (MO) of an adsorbate, where E_F is the Fermi level, E is the energy level, HOMO is the highest occupied molecular orbital of an adsorbate, and LUMO is the lowest unoccupied molecular orbital of an adsorbate. Adapted with permission from ref. 6. Copyright 2015, Springer Nature. (D) In the desorption induced by electronic transitions (DIET) mechanism, a hot electron can temporarily transfer to an unoccupied MO of an adsorbate, forming an excited metal–adsorbate complex with a different potential energy surface (PES). On this new PES, the energy of the donated charge carrier is converted to the kinetic energy of the metal–adsorbate complex. After a short time, the donated electron decays back to the metal E_F and the adsorbate returns to the ground state PES. If the energy transfer exceeds the activation barrier for desorption (E_d), the adsorbate will leave the surface. Adapted with permission from ref. 9. Copyright 2011, Springer Nature.

Chapter 7
Outlook

The scale of global carbon dioxide (CO_2) emissions is too great to address through electrochemical CO_2 reduction alone, but it can be an important part of the solution. However, new technologies are needed to make the conversion of CO_2 to useful products a reality. Plasmon-enhanced electrochemical conversion (PEEC) is a promising approach to address the challenges associated with CO_2 reduction.

This dissertation has shown that nanostructured electrodes can enhance the localized surface plasmon resonance (LSPR) effect and selectively promote electrochemical CO_2 reduction at lower overpotentials. This was first shown at electrochemically roughened silver (Ag) film cathodes when formation of carbon monoxide (CO), formate, and methanol were enhanced in the light while hydrogen production was suppressed. Strikingly, methanol was produced only upon illumination, representing a 100-fold increase in selectivity and a 550 mV decrease in overpotential when compared with dark electrocatalysis at a silver cathode.[17] CO_2 reduction selectivity was also impacted upon illumination at a copper–silver (Cu–Ag) cathode when CO, ethylene, methane, formate, and allyl alcohol were promoted and hydrogen activity was again suppressed. While these improvements in selectivity and efficiency show the promise of plasmon-enhanced electrochemical CO_2 reduction, we are quite far from the ultimate goal of a plasmonic cathode that is highly selective for a single product at a low overpotential.

To achieve this goal we must understand the plasmonic mechanisms that drive these changes in selectivity and efficiency. This dissertation has conclusively shown that plasmonic heating is not a significant contributor to plasmon-enhanced CO_2 reduction. For both the Ag and Cu–Ag cathodes, the photocurrent increased linearly with light intensity, where we would expect an exponential dependence in the case of heating. Temperature-dependent product analysis of the Ag and Cu–Ag cathodes provided further evidence against a photothermal mechanism as the changes in selectivity due to heating were opposite of those observed upon illumination. The in situ ATR–SEIRAS (attenuated total reflectance–surface-enhanced infrared absorption spectroscopy) study provided further insight into the selectivity and efficiency changes at the Ag cathode, demonstrating that different plasmonic mechanisms were likely at play. To explain the observed increase in selectivity and decrease in onset potential for CO formation, we concluded that the light must be assisting the desorption of CO from the surface through the temporary transfer of a plasmonically excited hot electron in a desorption induced by electronic transitions (DIET) mechanism. We also found that the bicarbonate bond was likely strengthened by the plasmonically enhanced local electric field, increasing the local pH and suppressing hydrogen formation.

The ATR–SEIRAS study was limited by our inability to detect formate, methanol, and reaction intermediates. In future work we could develop a cathode with greater surface enhancement to improve species detection, employ time-resolved step-scan spectroscopy to observe species with short lifetimes, or use a cathode that produces formate and methanol at higher concentrations. In addition, designing an ATR–SEIRAS cell with temperature control and a shorter path length for light to reach the cathode surface would enable the use of higher light intensities to increase the plasmonic effects and permit a wider variety of

photoelectrochemical experiments.

Other experimental techniques are of interest to probe plasmonic mechanisms. In situ X-ray spectroscopy could be used to identify species in the electric double layer and how their concentration, orientation, and structure changes upon illumination. In situ Raman spectroscopy may enable us to observe species that cannot be detected by IR spectroscopy. Scanning electrochemical microscopy (SECM) could permit us to connect structure to function by measuring electrochemical behavior at individual nanofeatures. The field of PEEC would greatly benefit from an in situ method for plasmon mapping to identify active sites for plasmon-enhanced conversion.

With a better understanding of the plasmonic mechanisms that result in plasmon-enhanced CO_2 reduction we could rationally design cathodes that target a specific CO_2 reduction product. These cathodes will likely combine a plasmonic metal with a catalyst and have uniform, densely packed nanofeatures on the surface. For practical application there are still open questions about the electrolyzer design. Gas diffusion electrodes overcome the low solubility of CO_2 in water, resulting in much higher current densities. How to incorporate light, and the source of that light, is another challenge. Sunlight is low-cost but intermittent and low intensity at any single wavelength, although this could be partially addressed through solar concentration. Depending on the absorbance of the cathode in the visible range and the plasmonic mechanism, it may be necessary to use a single-wavelength light-emitting diode (LED) light source, especially if continuous operation is desired.

To make the greatest impact in CO_2 utilization we should expand the global markets for CO_2 reduction products. Ethanol could replace 85% of gasoline used in flexible-fuel vehicles today without any infrastructure or technology change, and could eventually replace 100% of gasoline and diesel used in vehicles by changing to vehicles with engines optimized for ethanol. By developing fuel cells that use formate or methanol we could also offset gasoline and diesel used for transportation and replace fossil fuels that are used for power generation. CO and hydrogen could be converted to synthetic fuel and lubrication oil through the Fischer-Tropsch process, replacing fuels and lubricants derived from petroleum.

To make this vision a reality we must first address the key challenges of low selectivity and efficiency in CO_2 reduction. This dissertation has shown that plasmon-enhanced electrochemical conversion can positively impact both of these challenges. The next steps are to gain a fundamental understanding of the plasmonic mechanisms that drive plasmon-enhanced CO_2 reduction and optimize cathodes to be highly selective and efficient for a single product.

Bibliography

1. Contribution of Working Groups I, II and III to the Fifth Assessment Report of the Intergovernmental Panel on Climate Change [Core Writing Team, R.K. Pachauri and L. A. Meyer (eds.)], Report, 2014.

2. Kuhl, K. P.; Cave, E. R.; Abram, D. N.; Jaramillo, T. F. New Insights into the Electrochemical Reduction of Carbon Dioxide on Metallic Copper Surfaces. *Energy Environ. Sci.* **2012**, *5*, 7050–7059.

3. De Luna, P.; Hahn, C.; Higgins, D.; Jaffer, S. A.; Jaramillo, T. F.; Sargent, E. H. What Would it take for Renewably Powered Electrosynthesis to Displace Petrochemical Processes? *Science* **2019**, *364*.

4. Kostecki, R.; Augustynski, J. Unusually Strong Cathodic Photoeffect at Silver in Contact with Aqueous Solutions Containing Carbon Dioxide. *Chem. Phys. Lett.* **1992**, *194*, 386–390.

5. Kostecki, R.; Augustynski, J. Effect of the Surface Roughness on the Spectral Distribution of Photoemission Current at the Silver/Solution Contact. *J. Appl. Phys.* **1995**, *77*, 4701–4705.

6. Linic, S.; Aslam, U.; Boerigter, C.; Morabito, M. Photochemical Transformations on Plasmonic Metal Nanoparticles. *Nat. Mater.* **2015**, *14*, 567–576.

7. Kreibig, U.; Vollmer, M. *Optical Properties of Metal Clusters*; Springer: Berlin, DE, 1995.

8. Link, S.; El-Sayed, M. A. Size and Temperature Dependence of the Plasmon Absorption of Colloidal Gold Nanoparticles. *F. Phys. Chem. B.* **1999**, *103*, 4212–4217.

9. Linic, S.; Christopher, P.; Ingram, D. B. Plasmonic-Metal Nanostructures for Efficient Conversion of Solar to Chemical Energy. *Nat. Mater.* **2011**, *10*, 911–921.

10. Lu, X.; Rycenga, M.; Skrabalak, S. E.; Wiley, B.; Xia, Y. Chemical Synthesis of Novel Plasmonic Nanoparticles. *Annu. Rev. Phys. Chem.* **2009**, *60*, 167–192.

11. Mukherjee, S.; Libisch, F.; Large, N.; Neumann, O.; Brown, L. V.; Cheng, J.; Lassiter, J. B.; Carter, E. A.; Nordlander, P.; Halas, N. J. Hot Electrons do the Impossible: Plasmon-Induced Dissociation of H_2 on Au. *Nano Lett.* **2013**, *13*, 240–247.

12. Christopher, P.; Xin, H.; Linic, S. Visible-Light-Enhanced Catalytic Oxidation Reactions on Plasmonic Silver Nanostructures. *Nat. Chem.* **2011**, *3*, 467–472.

13. Shi, F. et al. Plasmonic-Enhanced Oxygen Reduction Reaction of Silver/Graphene Electrocatalysts. *Nano Lett.* **2019**, *19*, 1371–1378.

14. Wilson, A. J.; Mohan, V.; Jain, P. K. Mechanistic Understanding of Plasmon-Enhanced Electrochemistry. *J. Phys. Chem. C* **2019**, *123*, 29360–29369.

15. Amendola, V.; Meneghetti, M. Laser Ablation Synthesis in Solution and Size Manipulation of Noble Metal Nanoparticles. *Phys. Chem. Chem. Phys.* **2009**, *11*, 3805–3821.

16. Kuhl, K. P.; Hatsukade, T.; Cave, E. R.; Abram, D. N.; Kibsgaard, J.; Jaramillo, T. F. Electrocatalytic Conversion of Carbon Dioxide to Methane and Methanol on Transition Metal Surfaces. *J. Am. Chem. Soc.* **2014**, *136*, 14107–14113.

17. Hatsukade, T.; Kuhl, K. P.; Cave, E. R.; Abram, D. N.; Jaramillo, T. F. Insights into the Electrocatalytic Reduction of CO_2 on Metallic Silver Surfaces. *Phys. Chem. Chem. Phys.* **2014**, *16*, 13814–13819.

18. Sundararaman, R.; Narang, P.; Jermyn, A. S.; Goddard, W. A.; Atwater, H. A. Theoretical Predictions for Hot-Carrier Generation from Surface Plasmon Decay. *Nat. Commun.* **2014**, *5*, 5788.

19. Kortlever, R.; Shen, J.; Schouten, K. J.; Calle-Vallejo, F.; Koper, M. T. M. Catalysts and Reaction Pathways for the Electrochemical Reduction of Carbon Dioxide. *J. Phys. Chem. Lett.* **2015**, *6*, 4073–4082.

20. Lange, J.-P.; Sushkevich, V. L.; Knorpp, A. J.; van Bokhoven, J. A. Methane-to-Methanol via Chemical Looping: Economic Potential and Guidance for Future Research. *Ind. Eng. Chem. Res.* **2019**, *58*, 8674–8680.

21. Corson, E. R.; Creel, E. B.; Kostecki, R.; McCloskey, B. D.; Urban, J. J. Important Considerations in Plasmon-Enhanced Electrochemical Conversion at Voltage-Biased Electrodes. *iScience* **2020**, *23*, 100911.

22. Becquerel, E. Recherches Sur Les Effets de La Radiation Chimiquede La Lumière Solaire, Au Moyen Des Courants électriques. *Compt. Rend. Acad. Sci.* **1839**, *9*, 145–149.

23. Gerischer, H.; Delahay, P. *Advances in Electrochemistry and Electrochemical Engineering*; Wiley: New York, NY, 1961.

24. Boddy, P. J. Oxygen Evolution on Semiconducting TiO_2. *J. Electrochem. Soc.* **1968**, *115*, 199–203.

25. Fujishima, A.; Honda, K. Electrochemical Photolysis of Water at a Semiconductor Electrode. *Nature* **1972**, *238*, 37–38.

26. Grätzel, M. Photoelectrochemical Cells. *Nature* **2001**, *414*, 338–344.

27. Bak, T.; Nowotny, J.; Rekas, M.; Sorrell, C. Photo-Electrochemical Hydrogen Generation from Water Using Solar Energy. Materials-Related Aspects. *Int. J. Hydrogen Energ.* **2002**, *27*, 991–1022.

28. Kudo, A.; Miseki, Y. Heterogeneous Photocatalyst Materials for Water Splitting. *Chem. Soc. Rev.* **2009**, *38*, 253–78.

29. Ganesh, I. Conversion of Carbon Dioxide to Methanol Using Solar Energy - A Brief Review. *Mater. Sci. Appl.* **2011**, *2*, 1407–1415.

30. Kumar, B.; Llorente, M.; Froehlich, J.; Dang, T.; Sathrum, A.; Kubiak, C. P. Photochemical and Photoelectrochemical Reduction of CO_2. *Annu. Rev. Phys. Chem.* **2012**, *63*, 541–569.

31. Zhao, J.; Wang, X.; Xu, Z.; Loo, J. S. C. Hybrid Catalysts for Photoelectrochemical Reduction of Carbon Dioxide: a Prospective Review on Semiconductor/Metal Complex Co-Catalyst Systems. *J. Mater. Chem. A* **2014**, *2*, 15228–15233.

32. Lianos, P. Production of Electricity and Hydrogen by Photocatalytic Degradation of Organic Wastes in a Photoelectrochemical Cell: the Concept of the Photofuelcell: a Review of a Re-Emerging Research Field. *J. Hazard. Mater.* **2011**, *185*, 575–590.

33. Georgieva, J.; Valova, E.; Armyanov, S.; Philippidis, N.; Poulios, I.; Sotiropoulos, S. Bi-Component Semiconductor Oxide Photoanodes for the Photoelectrocatalytic Oxidation of Organic Solutes and Vapours: a Short Review with Emphasis to TiO_2–WO_3 Photoanodes. *J. Hazard. Mater.* **2012**, *211–212*, 30–46.

34. Sass, J. K.; Sen, R. K.; Meyer, E.; Gerischer, H. Effect of Surface Plasmon Excitation on Photoemission and Photooxidation Processes at a Silver-Electrolyte Interface. *Surf. Sci.* **1974**, *44*, 515–528.

35. Kostecki, R.; Augustynski, J. Electrochemical Reduction of CO_2 at an Activated Silver Electrode. *Phys. Chem.* **1994**, *98*, 1510–1515.

36. Creel, E. B.; Corson, E. R.; Eichhorn, J.; Kostecki, R.; Urban, J. J.; McCloskey, B. D. Directing Selectivity of Electrochemical Carbon Dioxide Reduction Using Plasmonics. *ACS Energy Lett.* **2019**, *4*, 1098–1105.

37. Zheng, Z.; Xie, W.; Li, M.; Ng, Y. H.; Wang, D.-W.; Dai, Y.; Huang, B.; Amal, R. Platinum Electrocatalysts with Plasmonic Nano-Cores for Photo-Enhanced Oxygen-Reduction. *Nano Energy* **2017**, *41*, 233–242.

38. Zhang, H. X.; Li, Y.; Li, M. Y.; Zhang, H.; Zhang, J. Boosting Electrocatalytic Hydrogen Evolution by Plasmon-Driven Hot-Electron Excitation. *Nanoscale* **2018**, *10*, 2236–2241.

39. Guo, X.; Li, X.; Kou, S.; Yang, X.; Hu, X.; Ling, D.; Yang, J. Plasmon-Enhanced Electrocatalytic Hydrogen/Oxygen Evolution by Pt/Fe–Au Nanorods. *J. Mater. Chem. A* **2018**, *6*, 7364–7369.

40. Chen, Z.; Dinh, H. N.; Miller, E. *Photoelectrochemical Water Splitting Standards, Experimental Methods, and Protocols*; Springer: New York, NY, 2013.

41. Döscher, H.; Geisz, J. F.; Deutsch, T. G.; Turner, J. A. Sunlight Absorption in Water – Efficiency and Design Implications for Photoelectrochemical Devices. *Energy Environ. Sci.* **2014**, *7*, 2951–2956.

42. Xiang, C.; Walczak, K.; Haber, J.; Jones, R.; Beeman, J. W.; Guevarra, D.; Karp, C.; Liu, R.; Shaner, M.; Sun, K.; West, W.; Zhou, L. In *Integrated Solar Fuel Generators*; Sharp, I. D., Atwater, H. A., Lewerenz, H.-J., Eds.; Royal Society of Chemistry: London, UK, 2019; pp 387–453.

43. Corson, E. R.; Creel, E. B.; Kim, Y.; Urban, J. J.; Kostecki, R.; McCloskey, B. D. A Temperature-Controlled Photoelectrochemical Cell for Quantitative Product Analysis. *Rev. Sci. Instrum.* **2018**, *89*, 055112.

44. Haussener, S.; Hu, S.; Xiang, C.; Weber, A. Z.; Lewis, N. S. Simulations of the Irradiation and Temperature Dependence of the Efficiency of Tandem Photoelectrochemical Water-Splitting Systems. *Energy Environ. Sci.* **2013**, *6*, 3605–3618.

45. Brown, A. M.; Sundararaman, R.; Narang, P.; Goddard, W. A.; Atwater, H. A. Nonradiative Plasmon Decay and Hot Carrier Dynamics: Effects of Phonons, Surfaces, and Geometry. *ACS Nano* **2016**, *10*, 957–966.

46. Dias, P.; Lopes, T.; Meda, L.; Andrade, L.; Mendes, A. Photoelectrochemical Water Splitting using WO_3 Photoanodes: the Substrate and Temperature Roles. *Phys Chem Chem Phys* **2016**, *18*, 5232–43.

47. Zavarine, I. S.; Kubiak, C. P. A Versatile Variable Temperature Thin Layer Reflectance Spectroelectrochemical Cell. *J. Electroanal. Chem.* **2001**, *495*, 106–109.

48. Chen, Z.; Jaramillo, T. F.; Deutsch, T. G.; Kleiman-Shwarsctein, A.; Forman, A. J.; Gaillard, N.; Garland, R.; Takanabe, K.; Heske, C.; Sunkara, M.; McFarland, E. W.; Domen, K.; Miller, E. L.; Turner, J. A.; Dinh, H. N. Accelerating Materials Development for Photoelectrochemical Hydrogen Production: Standards for Methods, Definitions, and Reporting Protocols. *J. Mater. Res.* **2010**, *25*, 3–16.

49. Shi, Z.; Wen, X.; Guan, Z.; Cao, D.; Luo, W.; Zou, Z. Recent Progress in Photoelectrochemical Water Splitting for Solar Hydrogen Production. *Ann. Phys.-New York* **2015**, *358*, 236–247.

50. Robatjazi, H.; Bahauddin, S. M.; Doiron, C.; Thomann, I. Direct Plasmon-Driven Photoelectrocatalysis. *Nano Lett.* **2015**, *15*, 6155–6161.

51. Kim, Y.; Creel, E. B.; Corson, E. R.; McCloskey, B. D.; Urban, J. J.; Kostecki, R. Surface-Plasmon-Assisted Photoelectrochemical Reduction of CO_2 and NO_3^- on Nanostructured Silver Electrodes. *Adv. Energy Mat.* **2018**, *8*, 1800363.

52. Jang, J. W.; Cho, S.; Magesh, G.; Jang, Y. J.; Kim, J. Y.; Kim, W. Y.; Seo, J. K.; Kim, S.; Lee, K. H.; Lee, J. S. Aqueous-Solution Route to Zinc Telluride Films for Application to CO_2 Reduction. *Angew. Chem. Int. Ed. Engl.* **2014**, *53*, 5852–5857.

53. Abdi, F. F.; Savenije, T. J.; May, M. M.; Dam, B.; van de Krol, R. The Origin of Slow Carrier Transport in $BiVO_4$ Thin Film Photoanodes: A Time-Resolved Microwave Conductivity Study. *J. Phys. Chem. Lett.* **2013**, *4*, 2752–2757.

54. Boerigter, C.; Aslam, U.; Linic, S. Mechanism of Charge Transfer from Plasmonic Nanostructures to Chemically Attached Materials. *ACS Nano* **2016**, *10*, 6108–6115.

55. Tian, Y.; Tatsuma, T. Plasmon-Induced Photoelectrochemistry at Metal Nanoparticles Supported on Nanoporous TiO_2. *Chem. Commun.* **2004**, *16*, 1810–1811.

56. van de Krol, R.; Grätzel, M. *Photoelectrochemical Hydrogen Production*; Springer: New York, NY, 2012.

57. Döscher, H.; Young, J. L.; Geisz, J. F.; Turner, J. A.; Deutsch, T. G. Solar-to-Hydrogen Efficiency: Shining Light on Photoelectrochemical Device Performance. *Energy Environ. Sci.* **2016**, *9*, 74–80.

58. May, M. M.; Lackner, D.; Ohlmann, J.; Dimroth, F.; van de Krol, R.; Hannappel, T.; Schwarzburg, K. On the Benchmarking of Multi-Junction Photoelectrochemical Fuel Generating Devices. *Sustain. Energy Fuels* **2017**, *1*, 492–503.

59. Kale, M. J.; Avanesian, T.; Christopher, P. Direct Photocatalysis by Plasmonic Nanostructures. *ACS Catal.* **2014**, *4*, 116–128.

60. Shen, S.; Chen, J.; Wang, M.; Sheng, X.; Chen, X.; Feng, X.; Mao, S. S. Titanium Dioxide Nanostructures for Photoelectrochemical Applications. *Prog. Mater. Sci.* **2018**, *98*, 299–385.

61. Wu, S. L.; Wen, L.; Cheng, G. A.; Zheng, R. T.; Wu, X. L. Surface Morphology-Dependent Photoelectrochemical Properties of One-Dimensional Si Nanostructure Arrays Prepared by Chemical Etching. *ACS Appl. Mater. Inter.* **2013**, *5*, 4769–4776.

62. Manjavacas, A.; Liu, J. G.; Kulkarni, V. K.; Nordlander, P. Plasmon-Induced Hot Carriers in Metallic Nanoparticles. *ACS Nano* **2014**, *8*, 7630–7638.

63. Link, S.; El-Sayed, M. A. Shape and Size Dependence of Radiative, Non-Radiative and Photothermal Properties of Gold Nanocrystals. *Int. Rev. Phys. Chem.* **2000**, *19*, 409–453.

64. Hodnik, N.; Dehm, G.; Mayrhofer, K. J. J. Importance and Challenges of Electrochemical In Situ Liquid Cell Electron Microscopy for Energy Conversion Research. *Accounts Chem. Res.* **2016**, *49*, 2015–2022.

65. Tao, F.; Salmeron, M. In situ Studies of Chemistry and Structure of Materials. *Science* **2011**, *331*, 171–174.

66. Sato, K.; Fujii, K.; Koike, K.; Goto, T.; Yao, T. Anomalous Time Variation of Photocurrent in GaN During Photoelectrochemical Reaction for H_2 Gas Generation in NaOH Aqueous Solution. *Phys. Status Solidi C* **2009**, *6*, S635–S638.

67. Tong, H.; Ouyang, S.; Bi, Y.; Umezawa, N.; Oshikiri, M.; Ye, J. Nano-Photocatalytic Materials: Possibilities and Challenges. *Adv. Mater.* **2012**, *24*, 229–51.

68. Hori, Y.; Kikuchi, K.; Suzuki, S. Production of CO and CH_4 in Electrochemical Reduction of CO_2 at Metal Electrodes in Aqueous Hydrogencarbonate Solution. *Chem. Lett.* **1985**, 1695–1698.

69. Hori, Y.; Kikuchi, K.; Murata, A.; Suzuki, S. Production of Methane and Ethylene in Electrochemical Reduction of Carbon Dioxide at Copper Electrode in Aqueous Hydrogencarbonate Solution. *Chem. Lett.* **1986**, *15*, 897–898.

70. Mukherjee, S.; Zhou, L.; Goodman, A. M.; Large, N.; Ayala-Orozco, C.; Zhang, Y.; Nordlander, P.; Halas, N. J. Hot-Electron-Induced Dissociation of H_2 on Gold Nanoparticles Supported on SiO_2. *J. Am. Chem. Soc.* **2014**, *136*, 64–67.

71. Govorov, A. O.; Zhang, H.; Demir, H. V.; Gun'ko, Y. K. Photogeneration of Hot Plasmonic Electrons with Metal Nanocrystals: Quantum Description and Potential Applications. *Nano Today* **2014**, *9*, 85–101.

72. Lobaccaro, P.; Singh, M. R.; Clark, E. L.; Kwon, Y.; Bell, A. T.; Ager, J. W. Effects of Temperature and Gas-Liquid Mass Transfer on the Operation of Small Electrochemical Cells for the Quantitative Evaluation of CO_2 Reduction Electrocatalysts. *Phys. Chem. Chem. Phys.* **2016**, *18*, 26777–26785.

73. Chan, G. H.; Zhao, J.; Hicks, E. M.; Schatz, G. C.; Duyne, R. P. V. Plasmonic Properties of Copper Nanoparticles Fabricated by Nanosphere Lithography. *Nano Lett.* **2007**, *7*, 1947–1952.

74. West, A. C. *Electrochemistry and Electrochemical Engineering: An Introduction*; Columbia University: New York, NY, 2013.

75. Azuma, M.; Hashimoto, K.; Hiramoto, M.; Watanabe, M.; Sakata, T. Carbon Dioxide Reduction at Low Temperature on Various Metal Electrodes. *J. Electroanal. Chem.* **1989**, *260*, 441–445.

76. Azuma, M.; Hashimoto, K.; Hiramoto, M. Electrochemical Reduction of Carbon Dioxide on Various Metal Electrodes in Low-Temperature Aqueous $KHCO_3$ Media. *J. Electrochem. Soc.* **1990**, *137*, 1772–1778.

77. Kudo, A.; Nakagawa, S.; Tsuneto, A.; Sakata, T. Electrochemical Reduction of High Pressure CO_2 on Ni Electrodes. *J. Electrochem. Soc.* **1993**, *140*, 1541–1545.

78. Mizuno, T.; Ohta, K.; Sasaki, A.; Akai, T.; Hirano, M.; Kawabe, A. Effect of Temperature on Electrochemical Reduction of High-Pressure CO_2 with In, Sn, and Pb Electrodes. *Energ. Source.* **1995**, *17*, 503–508.

79. Gennaro, A.; Isse, A. A.; Severin, M.; Vianello, E.; Bhugun, I.; Saveant, J. Mechanism of the Electrochemical Reduction of Carbon Dioxide at Inert Electrodes in Media of Low Proton Availability. *J. Chem. Soc., Faraday Trans.* **1996**, *92*, 3963–3968.

80. Kaneco, S.; Iiba, K.; Ohta, K.; Mizuno, T.; Saji, A. Electrochemical Reduction of CO_2 at an Ag Electrode in KOH-Methanol at Low Temperature. *Electrochim. Acta* **1998**, *44*, 573–578.

81. Kaneco, S.; Iiba, K.; Ohta, K.; Mizuno, T.; Saji, A. Electrochemical Reduction of CO_2 on Au in KOH + Methanol at Low Temperature. *J. Electroanal. Chem.* **1998**, *441*, 215–220.

82. Chaplin, R.; Wragg, A. Effects of Process Conditions and Electrode Material on Reaction Pathways for Carbon Dioxide Electroreduction with Particular Reference to Formate Formation. *J. Appl. Electrochem.* **2003**, *33*, 1107–1123.

83. Kostecki, R.; Augustynski, J. Photon-Driven Reduction Reactions on Silver. *J. Appl. Electrochem.* **1993**, *23*, 567–572.

84. Hou, W.; Hung, W. H.; Pavaskar, P.; Goeppert, A.; Aykol, M.; Cronin, S. B. Photocatalytic Conversion of CO_2 to Hydrocarbon Fuels via Plasmon-Enhanced Absorption and Metallic Interband Transitions. *ACS Catal.* **2011**, *1*, 929–936.

85. Liu, E.; Kang, L.; Wu, F.; Sun, T.; Hu, X.; Yang, Y.; Liu, H.; Fan, J. Photocatalytic Reduction of CO_2 into Methanol over Ag/TiO_2 Nanocomposites Enhanced by Surface Plasmon Resonance. *Plasmonics* **2013**, *9*, 61–70.

86. Wang, C.; Ranasingha, O.; Natesakhawat, S.; Ohodnicki, J., P. R.; Andio, M.; Lewis, J. P.; Matranga, C. Visible Light Plasmonic Heating of Au-ZnO for the Catalytic Reduction of CO_2. *Nanoscale* **2013**, *5*, 6968–74.

87. Choi, K.; Kim, D.; Rungtaweevoranit, B.; Trickett, C. A.; Barmanbek, J. T. D.; Yang, P.; Yaghi, O. M. Plasmon-Enhanced Photocatalytic CO_2 Conversion within Metal-Organic Frameworks Under Visible Light. *J. Am. Chem. Soc.* **2017**, *139*, 356–362.

88. Zhang, X.; Li, X.; Zhang, D.; Su, N. Q.; Yang, W.; Everitt, H. O.; Liu, J. Product Selectivity in Plasmonic Photocatalysis for Carbon Dioxide Hydrogenation. *Nat. Commun.* **2017**, *8*, 14542.

89. Seborg, D. E.; Edgar, T. F.; Mellichamp, D. A. *Process Dynamics and Control*; Wiley: Hoboken, NJ, 2003; p 736.

90. Corson, E. R.; Creel, E. B.; Kostecki, R.; Urban, J. J.; McCloskey, B. D. Effect of Pressure and Temperature on Carbon Dioxide Reduction at a Plasmonically Active Silver Cathode. *Electrochim. Acta* **2020**, Submitted.

91. Stocker, T. F.; Qin, D.; Plattner, G.-K.; Tignor, M. M. B.; Allen, S. K.; Boschung, J.; Nauels, A.; Xia, Y.; Bex, V.; Midgley, P. M. *Intergovernmental Panel on Climate Change, 2013. The Physical Science Basis. Contribution of Working Group I to the Fifth Assessment Report of the Intergovernmental Panel on Climate Change*; IPCC, Cambridge University Press: Cambridge, UK, 2013.

92. Hori, Y. In *Modern Aspects of Electrochemistry*; Vayenas, C. G., White, R. E., Gamboa-Aldeco, M. E., Eds.; Springer: New York, NY, 2008; Chapter 3, pp 89–189.

93. White, J. L.; Baruch, M. F.; Pander Iii, J. E.; Hu, Y.; Fortmeyer, I. C.; Park, J. E.; Zhang, T.; Liao, K.; Gu, J.; Yan, Y.; Shaw, T. W.; Abelev, E.; Bocarsly, A. B. Light-Driven Heterogeneous Reduction of Carbon Dioxide: Photocatalysts and Photoelectrodes. *Chem. Rev.* **2015**, *115*, 12888–935.

94. Yu, S.; Wilson, A. J.; Kumari, G.; Zhang, X.; Jain, P. K. Opportunities and Challenges of Solar-Energy-Driven Carbon Dioxide to Fuel Conversion with Plasmonic Catalysts. *ACS Energy Lett.* **2017**, *2*, 2058–2070.

95. Thomann, I.; Pinaud, B. A.; Chen, Z.; Clemens, B. M.; Jaramillo, T. F.; Brongersma, M. L. Plasmon Enhanced Solar-to-Fuel Energy Conversion. *Nano Lett.* **2011**, *11*, 3440–6.

96. Lee, J.; Mubeen, S.; Ji, X.; Stucky, G. D.; Moskovits, M. Plasmonic Photoanodes for Solar Water Splitting with Visible Light. *Nano Lett.* **2012**, *12*, 5014–9.

97. Ingram, D. B.; Linic, S. Water Splitting on Composite Plasmonic-Metal/Semiconductor Photoelectrodes: Evidence for Selective Plasmon-Induced Formation of Charge Carriers near the Semiconductor Surface. *J. Am. Chem. Soc.* **2011**, *133*, 5202–5.

98. Kumari, G.; Zhang, X.; Devasia, D.; Heo, J.; Jain, P. K. Watching Visible Light-Driven CO_2 Reduction on a Plasmonic Nanoparticle Catalyst. *ACS Nano* **2018**, *12*, 8330–8340.

99. Yu, S.; Wilson, A. J.; Heo, J.; Jain, P. K. Plasmonic Control of Multi-Electron Transfer and C-C Coupling in Visible-Light-Driven CO_2 Reduction on Au Nanoparticles. *Nano Lett.* **2018**, *18*, 2189–2194.

100. Brongersma, M. L.; Halas, N. J.; Nordlander, P. Plasmon-Induced Hot Carrier Science and Technology. *Nat. Nanotechnol.* **2015**, *10*, 25–34.

101. Aslam, U.; Rao, V. G.; Chavez, S.; Linic, S. Catalytic Conversion of Solar to Chemical Energy on Plasmonic Metal Nanostructures. *Nat. Catal.* **2018**, *1*, 656–665.

102. Marimuthu, A.; Zhang, J.; Linic, S. Tuning Selectivity in Propylene Epoxidation by Plasmon Mediated Photo-Switching of Cu Oxidation State. *Science* **2013**, *339*, 1590–1593.

103. Robatjazi, H.; Zhao, H.; Swearer, D. F.; Hogan, N. J.; Zhou, L.; Alabastri, A.; McClain, M. J.; Nordlander, P.; Halas, N. J. Plasmon-Induced Selective Carbon Dioxide Conversion on Earth-Abundant Aluminum-Cuprous Oxide Antenna-Reactor Nanoparticles. *Nat. Commun.* **2017**, *8*, 27.

104. DuChene, J. S.; Tagliabue, G.; Welch, A. J.; Cheng, W. H.; Atwater, H. A. Hot Hole Collection and Photoelectrochemical CO_2 Reduction with Plasmonic Au/p-GaN Photocathodes. *Nano Lett.* **2018**, *18*, 2545–2550.

105. Maier, S. A. *Plasmonics Fundamentals and Applications*; Springer: New York, NY, 2007.

106. Hori, Y.; Murata, A.; Kikuchi, K.; Suzuki, S. Electrochemical Reduction of Carbon Dioxide to Carbon Monoxide at a Gold Electrode in Aqueous Potassium Hydrogen Carbonate. *J. Chem. Soc.* **1987**, *10*, 728–729.

107. Kyriacou, G. Z.; Anagnostopoulos, A. K. Influence of CO_2 Partial Pressure and the Supporting Electrolyte Cation on the Product Distribution in CO_2 Electroreduction. *J. Appl. Electrochem.* **1993**, *23*, 483–486.

108. Hara, K.; Tsuneto, A.; Kudo, A.; Sakata, T. Electrochemical Reduction of CO_2 on a Cu Electrode under High Pressure: Factors that Determine the Product Selectivity. *J. Electrochem. Soc.* **1994**, *141*, 2097–2103.

109. Hara, K.; Kudo, A.; Sakata, T. Electrochemical Reduction of Carbon Dioxide Under High Pressure on Various Electrodes in an Aqueous Electrolyte. *J. Electroanal. Chem.* **1995**, *391*, 141–147.

110. Noda, H.; Ikeda, S.; Yamamoto, A.; Einaga, H.; Ito, K. Kinetics of Electrochemical Reduction of Carbon Dioxide on a Gold Electrode in Phosphate Buffer Solutions. *Bull. Chem. Soc. Jpn.* **1995**, *68*, 1889–1895.

111. Todoroki, M.; Hara, K.; Kudo, A.; Sakata, T. Electrochemical Reduction of High Pressure CO_2 at Pb, Hg and In Electrodes in an Aqueous $KHCO_3$ Solution. *J. Electroanal. Chem.* **1995**, *394*, 199–203.

112. Li, J.; Prentice, G. Electrochemical Synthesis of Methanol from CO_2 in High-Pressure Electrolyte. *J. Electrochem. Soc.* **1997**, *144*, 4284–4288.

113. Morris, A. J.; McGibbon, R. T.; Bocarsly, A. B. Electrocatalytic Carbon Dioxide Activation: the Rate-Determining Step of Pyridinium-Catalyzed CO_2 Reduction. *ChemSusChem* **2011**, *4*, 191–196.

114. Chen, S.; Wang, L.-W. Thermodynamic Oxidation and Reduction Potentials of Photocatalytic Semiconductors in Aqueous Solution. *Chem. Mater.* **2012**, *24*, 3659–3666.

115. Hansen, H. A.; Varley, J. B.; Peterson, A. A.; Norskov, J. K. Understanding Trends in the Electrocatalytic Activity of Metals and Enzymes for CO_2 Reduction to CO. *J. Phys. Chem. Lett.* **2013**, *4*, 388–392.

116. Lu, Q.; Rosen, J.; Zhou, Y.; Hutchings, G. S.; Kimmel, Y. C.; Chen, J. G.; Jiao, F. A Selective and Efficient Electrocatalyst for Carbon Dioxide Reduction. *Nat. Commun.* **2014**, *5*, 3242.

117. Rosen, J.; Hutchings, G. S.; Lu, Q.; Rivera, S.; Zhou, Y.; Vlachos, D. G.; Jiao, F. Mechanistic Insights into the Electrochemical Reduction of CO_2 to CO on Nanostructured Ag Surfaces. *ACS Catal.* **2015**, *5*, 4293–4299.

118. Wuttig, A.; Yaguchi, M.; Motobayashi, K.; Osawa, M.; Surendranath, Y. Inhibited Proton Transfer Enhances Au-Catalyzed CO_2-to-Fuels Selectivity. *Proc. Natl. Acad. Sci. U.S.A.* **2016**, *113*, E4585–93.

119. Rybchenko, S. I.; Touhami, D.; Wadhawan, J. D.; Haywood, S. K. Study of Pyridine-Mediated Electrochemical Reduction of CO_2 to Methanol at High CO_2 Pressure. *ChemSusChem* **2016**, *9*, 1660–1669.

120. Quan, F.; Xiong, M.; Jia, F.; Zhang, L. Efficient Electroreduction of CO_2 on Bulk Silver Electrode in Aqueous Solution via the Inhibition of Hydrogen Evolution. *Appl. Surf. Sci.* **2017**, *399*, 48–54.

121. Singh, M. R.; Goodpaster, J. D.; Weber, A. Z.; Head-Gordon, M.; Bell, A. T. Mechanistic Insights into Electrochemical Reduction of CO_2 over Ag Using Density Functional Theory and Transport Models. *Proc. Natl. Acad. Sci. U.S.A.* **2017**, *114*, E8812–E8821.

122. Williams, K.; Corbin, N.; Zeng, J.; Lazouski, N.; Yang, D.-T.; Manthiram, K. Protecting Effect of Mass Transport During Electrochemical Reduction of Oxygenated Carbon Dioxide Feedstocks. *Sustain. Energy Fuels* **2019**, *3*, 1225–1232.

123. Shehzad, N.; Tahir, M.; Johari, K.; Murugesan, T.; Hussain, M. A Critical Review on TiO_2 Based Photocatalytic CO_2 Reduction System: Strategies to Improve Efficiency. *J. CO_2 Util.* **2018**, *26*, 98–122.

124. Lais, A.; Gondal, M. A.; Dastageer, M. A.; Al-Adel, F. F. Experimental Parameters Affecting the Photocatalytic Reduction Performance of CO_2 to Methanol: A Review. *Int. J. Energy Res.* **2018**, *42*, 2031–2049.

125. Zhou, L.; Swearer, D. F.; Zhang, C.; Robatjazi, H.; Zhao, H.; Henderson, L.; Dong, L.; Christopher, P.; Carter, E. A.; Nordlander, P.; Halas, N. J. Quantifying Hot Carrier and Thermal Contributions in Plasmonic Photocatalysis. *Science* **2018**, *362*, 60–72.

126. Vreeland, E. C.; Watt, J.; Schober, G. B.; Hance, B. G.; Austin, M. J.; Price, A. D.; Fellows, B. D.; Monson, T. C.; Hudak, N. S.; Maldonado-Camargo, L.; Bohorquez, A. C.; Rinaldi, C.; Huber, D. L. Enhanced Nanoparticle Size Control by Extending LaMer's Mechanism. *Chem. Mater.* **2015**, *27*, 6059–6066.

127. Alonso, C.; Salvarezza, C.; Vara, J. M.; Arvia, A. J. The Evaluation of Surface Diffusion Coefficients of Gold and Platinum Atoms at Electrochemical Interfaces from Combined STM-SEM Imaging and Electrochemical Techniques. *J. Electrochem. Soc.* **1990**, *137*, 2161–2166.

128. Boerigter, C.; Campana, R.; Morabito, M.; Linic, S. Evidence and Implications of Direct Charge Excitation as the Dominant Mechanism in Plasmon-Mediated Photocatalysis. *Nat. Commun.* **2016**, *7*, 10545.

129. Boerigter, C.; Aslam, U.; Linic, S. Mechanism of Charge Transfer from Plasmonic Nanostructures to Chemically Attached Materials. *ACS Nano* **2016**, *10*, 6108–6115.

130. Ho, W. Reactions at Metal Surfaces Induced by Femtosecond Lasers, Tunneling Electrons, and Heating. *J. Phys. Chem.* **1996**, *100*, 13050–13060.

131. Dunwell, M.; Yang, X.; Yan, Y.; Xu, B. Potential Routes and Mitigation Strategies for Contamination in Interfacial Specific Infrared Spectroelectrochemical Studies. *J. Phys. Chem. C* **2018**, *122*, 24658–24664.

132. Peterson, A. A.; Abild-Pedersen, F.; Studt, F.; Rossmeisl, J.; Norskov, J. K. How Copper Catalyzes the Electroreduction of Carbon Dioxide into Hydrocarbon Fuels. *Energy Environ. Sci.* **2010**, *3*, 1311–1315.

133. Cheng, T.; Xiao, H.; Goddard, W. A. Reaction Mechanisms for the Electrochemical Reduction of CO_2 to CO and Formate on the Cu(100) Surface at 298 K from Quantum Mechanics Free Energy Calculations with Explicit Water. *J. Am. Chem. Soc.* **2016**, *138*, 13802–13805.

134. Lee, C. W.; Cho, N. H.; Yang, K. D.; Nam, K. T. Reaction Mechanisms of the Electrochemical Conversion of Carbon Dioxide to Formic Acid on Tin Oxide Electrodes. *ChemElectroChem* **2017**, *4*, 2130–2136.

135. Albo, J.; Alvarez-Guerra, M.; Castaño, P.; Irabien, A. Towards the Electrochemical Conversion of Carbon Dioxide into Methanol. *Green Chem.* **2015**, *17*, 2304–2324.

136. Li, K.; Hogan, N. J.; Kale, M. J.; Halas, N. J.; Nordlander, P.; Christopher, P. Balancing Near-Field Enhancement, Absorption, and Scattering for Effective Antenna-Reactor Plasmonic Photocatalysis. *Nano Lett.* **2017**, *17*, 3710–3717.

137. Bard, A. J.; Faulkner, L. R. *Electrochemical Methods: Fundamentals and Applications*; Wiley: New York, NY, 2001.

138. Corson, E. R.; Kas, R.; Kostecki, R.; Urban, J. J.; Smith, W. A.; McCloskey, B. D.; Kortlever, R. In Situ ATR–SEIRAS of Carbon Dioxide Reduction at a Plasmonic Silver Cathode. *J. Am. Chem. Soc.* **2020**, *142*, 11750–11762.

139. Oda, I.; Ogasawara, H.; Ito, M. Carbon Monoxide Adsorption on Copper and Silver Electrodes during Carbon Dioxide Electroreduction Studied by Infrared Reflection Absorption Spectroscopy and Surface-Enhanced Raman Spectroscopy. *Langmuir* **1996**, *12*, 1094–1097.

140. Firet, N. J.; Smith, W. A. Probing the Reaction Mechanism of CO_2 Electroreduction over Ag Films via Operando Infrared Spectroscopy. *ACS Catal.* **2017**, *7*, 606–612.

141. Dunwell, M.; Yang, X.; Setzler, B. P.; Anibal, J.; Yan, Y.; Xu, B. Examination of Near-Electrode Concentration Gradients and Kinetic Impacts on the Electrochemical Reduction of CO_2 using Surface-Enhanced Infrared Spectroscopy. *ACS Catal.* **2018**, *8*, 3999–4008.

142. Gattrell, M.; Gupta, N.; Co, A. A Review of the Aqueous Electrochemical Reduction of CO_2 to Hydrocarbons at Copper. *J. Electroanal. Chem.* **2006**, *594*, 1–19.

143. Gunathunge, C. M.; Li, X.; Li, J.; Hicks, R. P.; Ovalle, V. J.; Waegele, M. M. Spectroscopic Observation of Reversible Surface Reconstruction of Copper Electrodes under CO_2 Reduction. *J. Phys. Chem. C* **2017**, *121*, 12337–12344.

144. Yang, K.; Kas, R.; Smith, W. A. In Situ Infrared Spectroscopy Reveals Persistent Alkalinity Near Electrode Surfaces during CO_2 Electroreduction. *J. Am. Chem. Soc.* **2019**, *141*, 15891–15900.

145. Kas, R.; Ayemoba, O.; Firet, N. J.; Middelkoop, J.; Smith, W. A.; Cuesta, A. In-situ Infrared Spectroscopy Applied to the Study of the Electrocatalytic Reduction of CO_2: Theory, Practice and Challenges. *ChemPhysChem* **2019**, *20*, 2904–2925.

146. Sato, S.; Ueda, K.; Kawasaki, Y.; Nakamura, R. In Situ IR Observation of Surface Species during the Photocatalytic Decomposition of Acetic Acid over TiO_2 Films. *J. Phys. Chem. B* **2002**, *106*, 9054–9058.

147. Nakamura, R.; Nakato, Y. Primary Intermediates of Oxygen Photoevolution Reaction on TiO_2 (Rutile) Particles, Revealed by In Situ FTIR Absorption and Photoluminescence Measurements. *J. Am. Chem. Soc.* **2004**, *126*, 1290–1298.

148. Zandi, O.; Hamann, T. W. Determination of Photoelectrochemical Water Oxidation Intermediates on Haematite Electrode Surfaces using Operando Infrared Spectroscopy. *Nat. Chem.* **2016**, *8*, 778–783.

149. Ekstrom, G. N.; McQuillan, A. J. In situ Infrared Spectroscopy of Glyoxylic Acid Adsorption and Photocatalysis on TiO_2 in Aqueous Solution. *J. Phys. Chem. B* **1999**, *103*, 10562–10565.

150. Nishikawa, Y.; Nagasawa, T.; Fujiwara, K. Silver Island Films for Surface-Enhanced Infrared Absorption Spectroscopy: Effect of Island Morphology on the Absorption Enhancement. *Vib. Spectrosc.* **1993**, *6*, 43–53.

151. Delgado, J. M.; Orts, J. M.; Rodes, A. A Comparison Between Chemical and Sputtering Methods for Preparing Thin-Film Silver Electrodes for In Situ ATR-SEIRAS Studies. *Electrochim. Acta* **2007**, *52*, 4605–4613.

152. Chandra, R.; Taneja, P.; John, J.; Ayyub, P. Synthesis and TEM Study of Nanoparticles and Nanocrystalline Thin Films of Silver by High Pressure Sputtering. *Nanostruct. Mater.* **1999**, *11*, 1171–1179.

153. Del Re, M.; Gouttebaron, R.; Dauchot, J.; Leclère, P.; Lazzaroni, R.; Wautelet, M.; Hecq, M. Growth and Morphology of Magnetron Sputter Deposited Silver Films. *Surf. Coat. Tech.* **2002**, *151-152*, 86–90.

154. Zippel, E.; Breiter, M. W.; Kellnert, R. Fourier-Transform Infrared, Attenuated Total Reflection Spectroscopy: A Complementary Tool for the Investigation of the Adsorption of CO on Thin Metal Layers. *J. Chem. Soc. Faraday Trans.* **1991**, *87*, 637–642.

155. Toney, M. F.; Howard, J. N.; Richer, J.; Borges, G. L.; Gordon, J. G.; Melroy, O. R.; Wieslert, D. G.; Vee, D.; Sorensen, L. B. Voltage-Dependent Ordering of Water Molecules at an Electrode-Electrolyte Interface. *Nature* **1994**, *368*, 444–446.

156. Schultz, Z. D.; Shaw, S. K.; Gewirth, A. A. Potential Dependent Organization of Water at the Electrified Metal-Liquid Interface. *J. Am. Chem. Soc.* **2005**, *127*, 15916–15922.

157. Ataka, K.-i.; Osawa, M. In Situ Infrared Study of Water-Sulfate Coadsorption on Gold(111) in Sulfuric Acid Solutions. *Langmuir* **1998**, *14*, 951–959.

158. Iwasita, T.; Nart, F. C. In Situ Infrared Spectroscopy at Electrochemical Interfaces. *Prog. Surf. Sci.* **1997**, *55*, 271–340.

159. Ikezawa, Y.; Saito, H.; Matsubayashi, H.; Toda, G. Comparative Study of CO Adsorbed on Pt, Pd, Au and Ag Electrodes in Neutral Solution by IR Reflection Absorption Spectroscopy. *J. Electroanal. Chem. Interfacial Electrochem.* **1988**, *252*, 395–402.

160. Bewick, A. In-situ Infrared Spectroscopy of the Electrode/Electrolyte Solution Interphase. *J. Electroanal. Chem. Interfacial Electrochem.* **1983**, *150*, 481–493.

161. Dunwell, M.; Wang, J.; Yan, Y.; Xu, B. Surface Enhanced Spectroscopic Investigations of Adsorption of Cations on Electrochemical Interfaces. *Phys. Chem. Chem. Phys.* **2017**, *19*, 971–975.

162. Koper, M. T. M.; van Santen, R. A.; Wasileski, S. A.; Weaver, M. J. Field-Dependent Chemisorption of Carbon Monoxide and Nitric Oxide on Platinum-Group (111) Surfaces: Quantum Chemical Calculations Compared with Infrared Spectroscopy at Electrochemical and Vacuum-Based Interfaces. *J. Chem. Phys.* **2000**, *113*, 4392–4407.

163. Blyholder, G. Molecular Orbital View of Chemisorbed Carbon Monoxide. *J. Phys. Chem.* **1964**, *68*, 2772–2777.

164. Osawa, M.; Ataka, K.-i. Electromagnetic Mechanism of Enhanced Infrared Absorption of Molecules Adsorbed on Metal Island Films. *Surf. Sci. Lett.* **1992**, *262*, L118–L122.

165. Zhang, X.-G.; Liu, Y.; Zhan, C.; Jin, X.; Chi, Q.; Wu, D.-Y.; Zhao, Y.; Tian, Z.-Q. Reaction Selectivity for Plasmon-Driven Carbon Dioxide Reduction on Silver Clusters: A Theoretical Prediction. *J. Phys. Chem. C* **2019**, *123*, 11101–11108.

166. Qiu, J.; Wei, W. D. Surface Plasmon-Mediated Photothermal Chemistry. *J. Phys. Chem. C* **2014**, *118*, 20735–20749.

167. Qu, Z.; Cheng, M.; Huang, W.; Bao, X. Formation of Subsurface Oxygen Species and its High Activity Toward CO Oxidation over Silver Catalysts. *J. Catal.* **2005**, *229*, 446–458.

168. Prybyla, J. A.; Heinz, T. F.; Misewich, J. A.; Loy, M. M.; Glownia, J. H. Desorption Induced by Femtosecond Laser Pulses. *Phys. Rev. Lett.* **1990**, *64*, 1537–1540.

169. Prybyla, J. A.; Tom, H. W.; Aumiller, G. D. Femtosecond Time-Resolved Surface Reaction: Desorption of CO from Cu(111) in ¡325 fsec. *Phys. Rev. Lett.* **1992**, *68*, 503–506.

170. Bartels, L.; Meyer, G.; Rieder, K.-H. Dynamics of Electron-Induced Manipulation of Individual CO Molecules on Cu(111). *Phys. Rev. Lett.* **1998**, *80*, 2004–2007.

171. Denzler, D. N.; Frischkorn, C.; Hess, C.; Wolf, M.; Ertl, G. Electronic Excitation and Dynamic Promotion of a Surface Reaction. *Phys. Rev. Lett.* **2003**, *91*, 226102.

172. Robatjazi, H.; Zhao, H.; Swearer, D. F.; Hogan, N. J.; Zhou, L.; Alabastri, A.; McClain, M. J.; Nordlander, P.; Halas, N. J. Plasmon-Induced Selective Carbon Dioxide Conversion on Earth-Abundant Aluminum-Cuprous Oxide Antenna-Reactor Nanoparticles. *Nat. Commun.* **2017**, *8*, 27.

173. Hirota, K.; Song, M.-B.; Ito, M. In-situ Infrared Spectroscopy of Water and Electrolytes Adsorbed on a Pt(111) Electrode Surface in Acid Solution. Structural Changes of Adsorbed Water Molecules upon an Electrode Potential. *Chem. Phys. Lett.* **1996**, *250*, 335–341.

174. Dunwell, M.; Yan, Y.; Xu, B. A Surface-Enhanced Infrared Absorption Spectroscopic Study of pH Dependent Water Adsorption on Au. *Surf. Sci.* **2016**, *650*, 51–56.

175. Ataka, K.-i.; Yotsuyanagi, T.; Osawa, M. Potential-Dependent Reorientation of Water molecules at an Electrode/Electrolyte Interface Studied by Surface-Enhanced Infrared Absorption Spectroscopy. *J. Phys. Chem.* **1996**, *100*, 10664–10672.

176. Ito, M.; Yamazaki, M. A New Structure of Water Layer on Cu(111) Electrode Surface during Hydrogen Evolution. *Phys. Chem. Chem. Phys.* **2006**, *8*, 3623–3626.

177. Davis, A. R.; Oliver, B. G. A Vibrational-Spectroscopic Study of the Species Present in the CO_2—H_2O System. *J. Solution Chem.* **1972**, *1*, 329–339.

178. Oliver, B. G.; Davis, A. R. Vibrational Spectroscopic Studies of Aqueous Alkali Metal Bicarbonate Carbonate Solutions. *Can. J. Chem.* **1973**, *51*, 698–702.

179. Rudolph, W. W.; Fischer, D.; Irmer, G. Vibrational Spectroscopic Studies and Density Functional Theory Calculations of Speciation in the CO_2—Water System. *Appl. Spectrosc.* **2006**, *60*, 130–144.

180. Stefánsson, A.; Lemke, K. H.; Bénézeth, P.; Schott, J. Magnesium Bicarbonate and Carbonate Interactions in Aqueous Solutions: An Infrared Spectroscopic and Quantum Chemical Study. *Geochim. Cosmochim. Acta* **2017**, *198*, 271–284.

181. Garand, E.; Wende, T.; Goebbert, D. J.; Bergmann, R.; Meijer, G.; Neumark, D. M.; Asmis, K. R. Infrared Spectroscopy of Hydrated Bicarbonate Anion Clusters: $HCO_3^-(H_2O)_{1–10}$. *J. Am. Chem. Soc.* **2010**, *132*, 849–856.

182. Rotzinger, F. P.; Kesselman-Truttmann, J. M.; Hug, S. J.; Shklover, V.; Gratzel, M. Structure and Vibrational Spectrum of Formate and Acetate Adsorbed from Aqueous Solution onto the TiO_2 Rutile (110) Surface. *J. Phys. Chem. B* **2004**, *108*, 5004–5017.

183. Ayemoba, O.; Cuesta, A. Spectroscopic Evidence of Size-Dependent Buffering of Interfacial pH by Cation Hydrolysis during CO_2 Electroreduction. *ACS Appl. Mater. Interfaces* **2017**, *9*, 27377–27382.

184. Singh, M. R.; Clark, E. L.; Bell, A. T. Effects of Electrolyte, Catalyst, and Membrane Composition and Operating Conditions on the Performance of Solar-Driven Electrochemical Reduction of Carbon Dioxide. *Phys. Chem. Chem. Phys.* **2015**, *17*, 18924–18936.

185. Dai, Q.; Gellman, A. J. A HREELS Study of C_1—C_5 Straight Chain Alcohols on Clean and Pre-Oxidized Ag(110) Surfaces. *Surf. Sci.* **1991**, *257*, 103–112.

186. Kim, B.; Ma, S.; Molly Jhong, H.-R.; Kenis, P. J. A. Influence of Dilute Feed and pH on Electrochemical Reduction of CO_2 to CO on Ag in a Continuous Flow Electrolyzer. *Electrochim. Acta* **2015**, *166*, 271–276.

187. Yang, H.; He, L. Q.; Hu, Y. W.; Lu, X.; Li, G. R.; Liu, B.; Ren, B.; Tong, Y.; Fang, P. P. Quantitative Detection of Photothermal and Photoelectrocatalytic Effects Induced by SPR from Au@Pt Nanoparticles. *Angew. Chem. Int. Ed. Engl.* **2015**, *54*, 11462–11466.

188. Corson, E. R.; Subramani, A.; Cooper, J. K.; Kostecki, R.; Urban, J. J.; McCloskey, B. D. Reduction of Carbon Dioxide at a Plasmonically Active Copper—Silver Cathode. *Chem. Commun.* **2020**, *56*, 9970–9973.

189. Gurudayal,; Bullock, J.; Srankó, D. F.; Towle, C. M.; Lum, Y.; Hettick, M.; Scott, M. C.; Javey, A.; Ager, J. Efficient Solar-Driven Electrochemical CO_2 Reduction to Hydrocarbons and Oxygenates. *Energy Environ. Sci.* **2017**, *10*, 2222–2230.

190. Gurudayal,; Beeman, J. W.; Bullock, J.; Wang, H.; Eichhorn, J.; Towle, C.; Javey, A.; Toma, F. M.; Mathews, N.; Ager, J. W. Si Photocathode with Ag-Supported Dendritic Cu Catalyst for CO_2 Reduction. *Energy Environ. Sci.* **2019**, *12*, 1068–1077.

191. Hori, Y.; Takahashi, R.; Yoshinami, Y.; Murata, A. Electrochemical Reduction of CO at a Copper Electrode. *J. Phys. Chem. B* **1997**, *101*, 7075–7081.

192. Perez-Gallent, E.; Marcandalli, G.; Figueiredo, M. C.; Calle-Vallejo, F.; Koper, M. T. M. Structure- and Potential-Dependent Cation Effects on CO Reduction at Copper Single-Crystal Electrodes. *J. Am. Chem. Soc.* **2017**, *139*, 16412–16419.

193. Yoon, Y.; Hall, A. S.; Surendranath, Y. Tuning of Silver Catalyst Mesostructure Promotes Selective Carbon Dioxide Conversion into Fuels. *Angew. Chem. Int. Ed.* **2016**, *55*, 15282–15286.

194. Hori, Y.; Murata, A.; Takahashi, R. Formation of Hydrocarbons in the Electrochemical Reduction of Carbon Dioxide at a Copper Electrode in Aqueous Solution. *J. Chem. Soc.* **1989**, 2309–2326.

195. Kelly, K. L.; Coronado, E.; Zhao, L. L.; Schatz, G. C. The Optical Properties of Metal Nanoparticles: The Influence of Size, Shape, and Dielectric Environment. *J. Phys. Chem. B* **2003**, *107*, 668–677.